

Laser-induced fluorescence on organic tracers for gas mixing studies in trans- and supersonic flows

Von der Fakultät für Ingenieurwissenschaften,
Abteilung Maschinenbau und Verfahrenstechnik
der
Universität Duisburg-Essen

zur Erlangung des akademischen Grades
eines
Doktors der Ingenieurwissenschaften
Dr.-Ing.

genehmigte Dissertation

von

Matthias Beuting

aus

Wesel

Gutachter: Prof. Dr. rer. nat. Christof Schulz
Prof. Dr.-Ing. Bernhard Weigand

Tag der mündlichen Prüfung: 21.12.2021

Preface

The research presented in this work is based on the joint research project *Experimental and Numerical Mixing Investigations in Compressible Jet Flows* between the Institute of Combustion and Gas Dynamics (IVG, University Duisburg-Essen) headed by Prof. Christof Schulz and the Institute of Thermodynamics in Aerospace (ITLR, University Stuttgart) headed by Professor Weigand. Funding by the German Research Foundation (DFG, project number 250957080) is gratefully acknowledged.

First and foremost, I would like to thank my supervisor Prof. Christof Schulz for the outstanding support, guidance, and many encouragements. I am grateful for your patience and the many freedoms you gave me in exploring my ideas. Thank you for giving me the opportunity to write my dissertation in the excellent research and working environment that you have created here at the IVG. I am proud and honored to have been part of your team.

I would also like to express my great gratitude Prof. Bernhard Weigand, the second examiner of this dissertation, for his extraordinary support. I thank you for the many fruitful discussions and your scientific guidance especially during the joint measurement campaigns. It was always a pleasure to work with your outstanding team in the excellent research facilities at the ITLR.

I am especially grateful to Judith Richter who was my counterpart at the ITLR. Without you, this work would not have been possible. In the most difficult and exhausting phases of our measurement campaigns, your optimism often saved the day. I always look back with delight to our ski trips and other outings, joint conference visits, and, of course, the occasional after-work drink.

I would like to thank Prof. Thomas Dreier who, as my group leader, supported me with his inexhaustible expertise during my first years at the IVG. Thank you for all the ideas and pushes in the right direction.

A very special thanks goes to Torsten Endres. Not only as my group leader over the last few years but also as a friend, your support and encouragement has been invaluable. Inspired by your perceptiveness and eager to try new approaches I dared to do many things I would never have done otherwise and learnt so much on the way.

Many thanks also to Prof. Sebastian Kaiser for his support on the other projects and side projects I worked on during my time at IVG. I have enjoyed our often fruitful but always interesting brainstorming sessions. I appreciated your open and direct words, which helped me not to lose sight of the goal.

A special thanks must go to Erdal Akyildiz. Without being asked, you were ready to help, day or night. You provided a solution to every problem with absolute reliability (together with a pointed comment and perhaps an encouraging insult or two). Many thanks for that!

I would like to thank all current and former colleagues who have created this great and inspiring working environment at IVG. Although you all really deserve to be mentioned here, I would

especially like to thank Birgit Nelius, Natascha Schlösser, Beate Endres, Ludger Jerig and Jörg "Aldi" Albrecht, who were always there for me when a technical problem had to be solved or something had to be built or modified on short notice.

I would also like to make a very special mention of Barbara Nota. I firmly believe that no one has ever managed to solve bureaucratic problems so creatively and efficiently. I don't know what I would have done without you!

A huge thank you also goes to the final year students who supported me directly or indirectly in the context of their bachelor or master theses.

Finally, I would like to thank my family for their unconditional moral support. Thank you for taking on my moods, especially in the final stages of my dissertation!

Abstract

Laser-induced fluorescence (LIF) is an established technique for spatially resolved imaging of temperature, pressure, density, and gas composition in complex flows. Because the measurement is quasi-instantaneous, it is particularly useful in turbulent and high-velocity flows. While in many applications either already existing species or species created during the process (e.g., fuels, products, or intermediates in practical combustion) are excited to fluoresce, so-called fluorescence tracers are added in inert flows or for answering specific questions via tracer LIF. Their photophysical characterization is crucial for quantitative analysis of measurements in practical applications.

This work focuses on the advancement and application of the tracer LIF technique for the investigation of mixing processes in accelerated transonic and supersonic flows under conditions that occur, e.g., in supersonic combustion of air-breathing hypersonic propulsion systems or in proposed supersonic reactors for the synthesis of nanoparticles. For the chemical reactions that take place in both cases, efficient mixing of reactants at the molecular level within the short time scales available in the fast flows is crucial. To assess mixing at the molecular level, the sensitivity of aromatic tracers to collisional quenching by molecular oxygen was exploited.

In a purpose-built air-driven modular flow channel at the ITLR in Stuttgart, the macroscopic and microscopic mixing behavior in the transonic wake of a central injector was measured by imaging in joint measurement campaigns as part of a collaborative project. The transonic mixing boundary layers encountered are associated with strong pressure and temperature gradients. In particular, the strong cross-dependence of the LIF signal of the applied tracers on these flow conditions represents a major challenge for the quantitative signal evaluation. Because the temperature range in the specific applications is below the previously explored conditions, hardly any photophysical data was previously available. To determine the missing spectroscopic information, two experiments, a cooled fluorescence flow cell and an optically accessible miniature flow channel, were developed. While the flow cell enabled precise and independent adjustment of pressure and temperature, conditions similar to those in the Stuttgart flow channel could be created in the miniature flow channel. In addition to the development and application-oriented testing of LIF measurement strategies, the miniature flow channel is also suited for spectroscopic measurements, since it can be operated with pure nitrogen containing variable amounts of oxygen.

In this work, two fluorescence tracers, anisole and toluene, were characterized in detail for low temperatures with particular emphasis on mixing studies at the molecular level. In addition, the mixing behavior in the transonic wake was analyzed using toluene LIF.

Zusammenfassung

Laser-induzierte Fluoreszenz (LIF) hat sich als bildgebende Messtechnik zur räumlich aufgelösten Bestimmung von Temperatur, Druck, Dichte und Zusammensetzung in Gasströmungen bewährt. Insbesondere in turbulenten Strömungen bietet sich der Einsatz an, da die Messung schneller als die relevanten Zeitskalen und damit quasi instantan erfolgt. Während bei vielen Anwendungen entweder bereits vorhandene oder während des Prozesses entstehende Spezies zur Fluoreszenz angeregt werden können (z.B. Kraftstoffe, Produkte oder Intermediate bei der technischen Verbrennung), werden bei inerten Strömungen oder bei spezifischen Fragestellungen sogenannte Tracer hinzugegeben (Tracer LIF). Deren photophysikalische Charakterisierung ist sowohl für das grundlegende Verständnis und Modellbildung als auch für die Kalibrierung der Messtechnik für die technische Anwendung entscheidend.

Diese Arbeit beschäftigt sich mit der Weiterentwicklung und Einsatz der LIF-Technik zur Untersuchung von Mischungsvorgängen in beschleunigten Trans- und Überschallströmungen unter Bedingungen, die z.B. bei der Überschallverbrennung bei luftatmenden Triebwerken in der Raumfahrt oder in speziellen Überschallreaktoren zur Synthese von Nanopartikeln herrschen. Ziel war es dabei, den in beiden Anwendungsfällen entscheidenden Mischungszustand von Edukten auf molekularer Ebene bildgebend zu messen. Um auch Mischungsprozesse unterhalb der Auflösung der eingesetzten Kamerasystem sichtbar zu machen, wurde die Empfindlichkeit aromatischer Tracer auf das Vorhandensein von molekularem Sauerstoff ausgenutzt.

In einem speziell für Mischungsuntersuchungen entwickelten mit Luft betriebenen modularen Strömungskanal des ITLR in Stuttgart wurden in gemeinsamen Messkampagnen im Zuge eines Kooperationsprojekts das makroskopische und mikroskopische Mischungsverhalten in der transsonischen Nachlaufströmung eines Zentralinjektors bildgebend gemessen. Die dabei auftretenden transsonischen Mischungsgrenzschichten zeichnen sich durch starke Druck- und Temperaturgradienten aus. Insbesondere die starken Querabhängigkeiten des LIF-Signals eingesetzter Tracer von diesen Strömungsbedingungen stellen deshalb eine große Herausforderung für dessen quantitative Auswertung dar. Weil der für die Anwendung relevante Temperaturbereich deutlich unterhalb der bisher untersuchten Bedingungen liegt, sind bisher kaum photophysikalische Daten vorhanden. Zum Schließen dieser Wissenslücken wurden in dieser Arbeit zwei Tracer detailliert charakterisiert. Dazu wurden zwei Experimente, eine gekühlte Fluoreszenz-Durchflusszelle und ein optisch zugänglicher Überschall-Miniatur-Strömungskanal, entwickelt. Während die Durchflusszelle die präzise und unabhängige Einstellung von Druck und Temperatur erlaubte, konnten in dem Miniatur-Strömungskanal ähnliche Bedingungen wie in dem Stuttgarter Strömungskanal geschaffen werden. Der Miniatur-Strömungskanal eignet sich, neben der Entwicklung und anwendungsnahen Erprobung von LIF-Messstrategien, auch für spektroskopische Messungen, da er mit reinem Stickstoff und beliebigem Sauerstoffanteil betrieben werden kann.

Im Rahmen dieser Arbeit wurden zwei Fluoreszenztracer, Anisol und Toluol, für niedrige Temperaturen mit besonderem Hinblick auf Mischungsuntersuchungen auf molekularer Ebene detailliert charakterisiert. Zusätzlich wurde das Mischungsverhalten in der transsonischen Nachlaufströmung mithilfe der LIF-Technik bildgebend analysiert.

Table of contents

Preface	II
Abstract	IV
Zusammenfassung	V
Table of contents	VII
Symbols and Acronyms	X
1 Introduction	1
2 Background	4
2.1 Application of LIF to supersonic flows.....	4
2.2 Anisole and toluene as fluorescence tracers.....	5
2.2.1 Toluene	6
2.2.2 Anisole	9
2.3 Quantitative imaging of mixing states	10
3 Theory	15
3.1 Fluid mechanics	15
3.1.1 Speed of sound.....	15
3.1.2 Compressible isentropic nozzle flow	17
3.1.3 Transonic wakes.....	19
3.2 Photophysics of organic fluorescence tracers	21
3.2.1 Interaction of matter and light.....	21
3.2.2 Absorption	23
3.2.3 Emission.....	25
3.2.4 Laser-induced fluorescence in the gas phase	28
4 Experimental methods	36
4.1 Quantitative LIF	36
4.1.1 LIF Imaging	38
4.1.2 Spectrally and temporally integrated measurements.....	38
4.1.3 Single-color excitation and two-color detection schemes.....	39
4.1.4 Two-color excitation and single-color detection schemes.....	40
4.1.5 Temporal measurement schemes	41
4.1.6 Other strategies	42
4.2 Schlieren imaging	43
4.3 Flow experiments.....	45
4.3.1 Full-scale modular flow channel.....	45
4.3.2 Cooled flow cell.....	46
4.3.3 Miniature supersonic flow channel.....	46
5 Macroscopic mixing	47
5.1 Introduction.....	47
5.2 Wake flow characteristics	48
5.3 Flow channel.....	49

5.4	Flow conditions.....	50
5.5	Laser-induced fluorescence.....	51
5.6	Results.....	53
5.7	Conclusions.....	55
6	Molecular mixing	56
6.1	Introduction.....	56
6.2	Theory.....	57
6.3	Experiment.....	59
6.4	Results.....	61
6.5	Conclusions and outlook.....	64
7	Tracer characterization	66
7.1	Introduction.....	66
7.2	Photophysics.....	68
7.3	Experiment.....	71
7.3.1	Continuous flow cell.....	71
7.4	Optical setup.....	73
7.4.1	Fluorescence lifetime measurements.....	73
7.4.2	Fluorescence spectra.....	75
7.5	Results.....	76
7.5.1	Anisole.....	76
7.5.2	Toluene.....	79
7.6	Implications for temperature measurements.....	81
7.7	Conclusions.....	83
8	Miniature flow channel.....	85
8.1	Introduction.....	85
8.2	Theory.....	87
8.2.1	Fluid dynamics.....	87
8.2.2	Laser-induced fluorescence.....	88
8.3	Flow channel experiment.....	89
8.3.1	Geometry.....	89
8.3.2	Mechanical design.....	91
8.3.3	Flow facility.....	92
8.3.4	Boundary conditions.....	94
8.4	Computational fluid dynamics.....	94
8.5	Optical diagnostics.....	95
8.5.1	Schlieren imaging.....	96
8.5.2	Fluorescence lifetime thermometry.....	96
8.5.3	LIF imaging.....	99
8.6	Characterization of the flow channel.....	99
8.6.1	Qualitative analysis of the supersonic flow field.....	100
8.6.2	Temperature and pressure.....	103
8.6.3	Influence of the boundary layer.....	104
8.6.4	Tracer condensation.....	106
8.6.5	Flow instabilities.....	106

8.7	Demonstration: measurement of oxygen quenching on toluene LIF	108
8.8	Conclusions	110
9	Outlook.....	112
10	Summary and conclusions	116
	Bibliography	119
	Appendix.....	129
A.	Effective fluorescence lifetimes of toluene and anisole.....	129
B.	Error estimation for the fluorescence lifetime thermometry method	130
C.	Schlieren images	131
D.	Fluorescence lifetime fit for nanosecond excitation of toluene LIF	132
E.	Temperature at different vertical positions in the miniature flow channel	133
F.	Estimated temperature dependence of toluene LIF at low temperature	134
G.	CFD simulation results of the miniature flow channel	137

Symbols and Acronyms

Latin symbol	Meaning	Typical unit
A	Area	m^2
A_{21}	Upper-level spontaneous emission rate constant	s^{-1}
b	Absorption and stimulated emission rate constant	s^{-1}
B	Einstein B coefficient	-
c	Speed of light	m s^{-1}
c_s	Speed of sound	m s^{-1}
c_p	Isobaric specific heat	$\text{J kg}^{-1} \text{K}^{-1}$
c_V	Isochoric specific heat	$\text{J kg}^{-1} \text{K}^{-1}$
C	Scaling factor	-
C_λ	Conversion factor	depends
E	Energy	J
h	Planck constant	$\text{m}^2 \text{kg s}^{-1}$
h_s	Specific enthalpy	J kg^{-1}
I_{laser}	Laser intensity	J
k	Deactivation rate	s^{-1}
k_B	Boltzmann constant	J K^{-1}
k_{GD}	Gladstone-Dale coefficient	$\text{m}^3 \text{kg}^{-1}$
\tilde{k}_q	Quenching rate constant	$\text{s}^{-1} \text{bar}^{-1}$
k_{SV}	Stern-Volmer coefficient	bar^{-1}
m	Mass	kg
M	Mach number	-
${}^n\text{M}$	Fluorescing molecule, n indicating spin configuration	-
n	Refractive index	-
n_{tracer}	Tracer number density	cm^{-3}
p	Pressure	bar
p_q	Quencher partial pressure	bar
Q_{12}	Upper-level quenching rate constant	s^{-1}
${}^n\text{Q}$	Quencher, n indicating spin configuration	-
R	Signal ratio	-
Re	Reynolds number	-
R_s	Specific ideal gas constant	$\text{J kg}^{-1} \text{K}^{-1}$
s	Specific entropy	$\text{J kg}^{-1} \text{K}^{-1}$

S	Signal intensity	arb. u.
T	Temperature	K
u	Velocity	m s^{-1}
V_m	Measurement volume	m^3
x, y, z	Spatial coordinates	mm

Greek symbol	Meaning	Typical unit
α	Opening angle	$^\circ$
γ	Arbitrary independent variable	-
Γ	Arbitrary dependent variable	-
$\delta_{1/2}$	Profile half-width	mm
δ_{99}	Boundary layer thickness	mm
δ^*	Displacement thickness	mm
Δ	Growth rate	$\text{mm}^{0.5}$
ε	Deflection angle	$^\circ$
ζ	Combined detection efficiency	-
η_e	Detector quantum efficiency	-
η_{ex}	Excitation efficiency	-
κ	Ratio of specific heats	-
λ	Wavelength	nm
ξ	Ratio of signal ratios	-
ρ	Density	kg m^{-3}
σ_{abs}	Absorption cross-section	cm^{-2}
τ	Lifetime	ns
ϕ_{fl}	Fluorescence quantum yield	-
ω	Vibrational frequency	s^{-1}
Ω	Solid angle	$^\circ$

Acronym	Meaning
BG	Background image
CCD	Charge-coupled device (camera sensor chip)
CFD	Computational fluid dynamics
CMOS	Complementary metal-oxide semiconductor (camera sensor chip)
FF	Flat field image

FL	Fluorescence
FQY	Fluorescence quantum yield
FWHM	Full width at half maximum
HOMO	Highest occupied molecular orbital
IC	Internal conversion
ISC	Intersystem crossing
IVR	Intramolecular vibrational relaxation
LCD	Liquid crystal display
LED	Light-emitting diode
LIF	Laser-induced fluorescence
LITA	Laser-induced thermal acoustics
LUMO	Lowest unoccupied molecular orbital
MFC	Mass flow controller
ND	Neutral density
Nd:YAG	Neodymium-doped yttrium aluminum garnet
PH	Phosphorescence
PIV	Particle image velocimetry
PMT	Photo multiplier tube
RANS	Reynolds-averaged Navier Stokes
S	Image
TCSPC	Time-correlated single-photon counting
UV	Ultraviolet
VR	Vibrational relaxation

1 Introduction

Predictable mixing behavior of reactants is crucial for many processes involving chemical reactions in the gas phase. The limits of the current understanding are challenged for example by optimizing practical combustion in the complex flow field of internal combustion piston engines and gas turbines. Also, in air-breathing hypersonic engines for aerospace propulsion, fuel injection, mixing, and combustion take place under supersonic conditions. The short time available makes efficient mixing crucial. While significant past work has been devoted to the study of mixing at subsonic and some at supersonic conditions, less is known about mixing in the transonic region, where sub- and supersonic gas velocities coexist in the same system. Also, outside combustion technology, rapid gas mixing can play an important role. An illustrative application are recently proposed reactors that produce nanoparticles from gas-dynamically induced gas-phase reactions (Fig. 1.1, [1]). In this reactor concept, a (potentially oxidizing) main gas flow is first heated at elevated pressure. This then expands and accelerates to supersonic velocity in a convergent-divergent nozzle. A reactant (precursor for the target particulate material) is injected through a central injector downstream into the nozzle flow, where the temperature of the surrounding gas is significantly reduced by gas-dynamic cooling. Mixing with the precursor occurs in a transonic environment until overexpansion of the flow results in rapid deceleration to subsonic velocities inducing a steep temperature rise over a normal shock system in the direction of the flow. This gas dynamic heating initiates precursor decomposition, nucleation, growth, and agglomeration of particles occurs until they are stopped by a quenching system consisting of a secondary nozzle and a water injector.

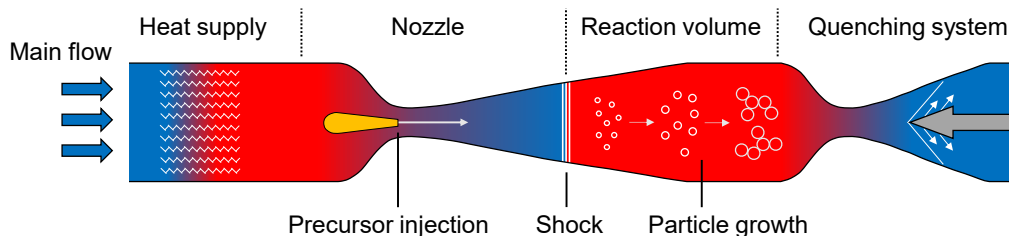


Fig. 1.1: A simplified reproduction of the operating principle of a reactor for gas phase synthesis from Grzona et al. [1].

The injection point is a compromise: On the one hand, the precursor may only be introduced into the accelerated, cooled flow, otherwise a premature reaction will occur. On the other hand, one wants the longest possible residence time to achieve sufficient mixing, which ultimately places the point of injection in the transonic region within the nozzle flow.

Whether the position of the injector trailing edge is then in the supersonic or subsonic range has severe effects on the mixing behavior. Whereas large alternating structures form in the case of subsonic injection, a complex flow field is created at the trailing edge of the injector in the case of supersonic injection. Mixing at the molecular level as required for chemical reactions between the related compounds is strongly promoted by the former, as large vortices stir the precursor-rich and oxidant-rich regions, increasing the interfacial surface between them. In the

latter case, the expansion of the mixing layer is significantly inhibited as the local Mach number increases.

In both cases, the influence of the compressibility effects especially in the transonic regime is not yet understood. This is partially due to the lack of optical measurement techniques that:

- a. Allow spatially resolved measurement of the mixing behavior on molecular level.
- b. Allow measurements of concentration, temperature, density, and pressure below room temperature.

Laser-induced fluorescence (LIF) is a powerful tool for imaging such mixing process by, e.g., replacing the injected fuel or precursor with a fluorescent substance (tracer). After excitation using a thin laser light sheet, the subsequent fluorescence is captured using cameras. The local tracer concentration can be calculated, provided corrections for other influences (temperature, pressure, bath gas composition) on the LIF signal are made. However, the spatial resolution of the cameras used in this technique is insufficient (by orders of magnitude) to detect concentration gradients on molecular length scales. Therefore, to address point a, an indirect LIF technique is applied in this work that exploits the dependence of the LIF signal of aromatic tracers on their mixing state with molecular oxygen contained in one of the mixing flows. In addition, the above-mentioned dependence of the LIF signal on flow conditions enables the imaging of, e.g., temperature fields. However, a quantitative interpretation of the LIF signal requires data on the photophysics of suitable tracers at low-temperature and low-pressure conditions. Since such data are lacking to date, suitable tracer candidates are characterized in detail in this work to address point b.

This work resulted from a joint research project of the Institute of Combustion and Gas Dynamics – Reactive Fluids (IVG) at the University of Duisburg-Essen and the Institute of Aerospace Thermodynamics (ITLR) at the University of Stuttgart aimed at identifying and fundamentally understanding the underlying mechanisms of mixing processes in compressible nozzle flows. To this end, a modular flow channel specifically designed for transonic mixing studies at practically relevant conditions was developed at the ITLR in Stuttgart allowing the investigation of wake flows behind various injectors mounted in an optically accessible Laval nozzle. In its standard configuration, the flow is accelerated through a nozzle designed for Mach 1.7 which reduces the flow temperature from about 100 °C as low as –40 °C depending on the injector geometry.

Two suitable fluorescence tracers, anisole and toluene, were identified and thoroughly analyzed at the relevant conditions. For this purpose, two experiments, a cooled fluorescence flow cell and an optically accessible miniature flow channel, were developed. While the flow cell allowed precise and independent adjustment of pressure (0.1–2 bar) and temperature (257–293 K), conditions similar to those in the flow channel of the ITLR could be created in the miniature flow channel acting as a test bed for development and testing of LIF measurement strategies. Due to the moderate mass flow rates of the miniature flow channel, it could be

operated with pure nitrogen (or arbitrary mixtures of nitrogen and oxygen) and, therefore, was also suited for spectroscopic analysis of flow tracers.

In joint measurement campaigns within the joint project, the mixing behavior in the transonic wake of two different central injectors was investigated in the modular flow channel at ITLR. The influence of a pressure gradient in the flow direction on the mixing layer was studied using toluene LIF in a single-color detection scheme. To visualize the mixing at the molecular level, a ratiometric scheme was used that exploits the oxygen-induced red shift of the toluene fluorescence spectrum. In this two-color detection method, the spectral shift was calculated from the signal from two different cameras, each equipped with different optical filters with passbands in different regions of the fluorescence spectrum.

The thesis is structured as follows: First, a review of the literature is presented covering the application of LIF to supersonic flows, previous efforts of characterizing the flow tracers used in this work, and studies on imaging the mixing behavior on the molecular level (Chapter 2). Then, the theoretical background of the fluid dynamics of the problems to be studied and the photophysics required for understanding the LIF technique are explained (Chapter 3). After that, measurement schemes for the optical diagnostics are presented before a short overview of the three different flow experiments utilized in this work is given (Chapter 4). The two subsequent chapters cover the application of LIF to the first experiment, the modular flow channel designed by Judith Richter at the ITLR in Stuttgart [2]: Chapter 5 presents a study on the mixing behavior on the macroscopic level whereas Chapter 6 is concerned with the mixing behavior on the molecular level in the transonic wake of a central injector. Chapter 7 shows the results of a thorough photophysical characterization of the fluorescence tracers anisole and toluene for low temperatures and low pressure that was performed in the second experiment, the cooled continuous flow cell. The last of the experiments, the miniature flow channel, is described in detail in Chapter 8. After a thorough characterization, it was used to investigate the effect of collisional quenching of toluene by molecular oxygen at sub-ambient temperature.

2 Background

In this thesis, each chapter that presents results (Chapters 5–8) also provides its own literature review relevant to its specific topic. To set itself apart, this section first presents a more general introduction to the challenges of applying LIF to supersonic flows. This is followed by a detailed literature review of the characterization of aromatic fluorescence tracers used in this work in a chronological order. Lastly, previous works on imaging strategies for the measurement of the extent of molecular mixing in turbulent flows are presented.

2.1 Application of LIF to supersonic flows

Laser-induced fluorescence has been used to image gas composition, temperature, and even velocity in the supersonic flows. The quantitative interpretation of the signal is met with challenges due to the complex nature of those flow fields exhibiting strong gradients of pressure, density, and temperature. Often, extreme temperature regimes are encountered, which are hard to reproduce in controlled reference experiments used for calibration of the measured data.

An excellent and recent example for this is the work of Gamba et al. [3] who applied toluene LIF to image a transverse cold jet (stagnation temperature 295 K) injected into a hot (460 K) supersonic cross flow. Strongly influenced by compression effects, the LIF image (Fig. 2.1) reveals the complex non-uniform flow pattern clearly showing a bow-shock structure, an upstream separation shock, and the turbulent wake of the jet.

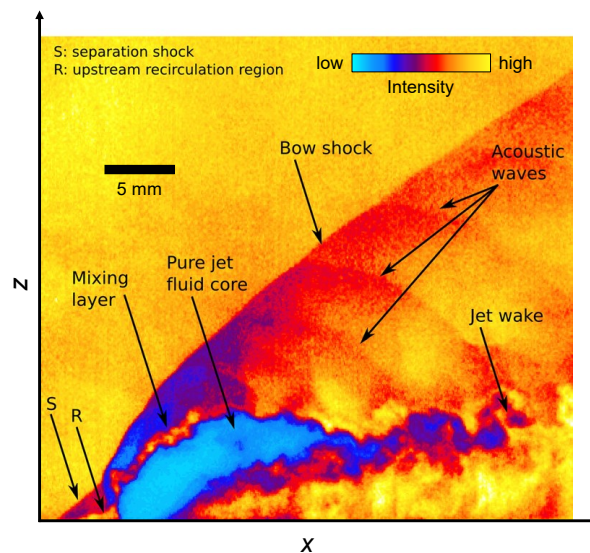


Fig. 2.1: Image showing the LIF signal intensity of toluene excited at 266 nm revealing the complex flow field of a transverse jet in a supersonic ($M = 2.3$) cross flow from Gamba et al. (Reprinted by permission from Springer Nature [3]). The cross flow (in positive x -direction) is nitrogen seeded with toluene whereas the jet (in positive z -direction) is pure hydrogen.

Using a two-color detection scheme, they were able to image the local temperature in regions where tracer was present. The temperature was established by measuring the temperature-induced red-shift from the ratio of the images of two cameras equipped with different optical filters. The temperature-dependence of the ratio was determined from LIF spectra measured by

Koban [4] allowing the calculation of the temperature field after a single-point calibration [5]. The detected temperatures ranged from 250 K in the direct wake of the jet up to 550 K in the shock-heated region just downstream of the bow shock front. Since LIF spectra were only available above room temperature, measurement of lower temperatures required extrapolation. Using the information on the temperature, they were further able to reconstruct the tracer concentration in terms of the local tracer partial pressure from single-shot LIF images.

Seeding vapor phase tracers to high-velocity gas flows can be challenging when wide temperature ranges must be covered. Strong temperature and pressure gradients may lead to local condensation in cold sections of the flow, while pyrolysis might be of concern in the same experiment in high-temperature zones [3, 6]. Combs et al. [7] used naphthalene as surrogate for the ablative heat shield to study the heat shield performance during atmospheric re-entry. They studied the concentration of ablation products in the wake of a space capsule model using naphthalene LIF which required detailed photophysical analysis under controlled conditions to correct for temperature and pressure effects [8]. This was achieved by adding naphthalene to a carrier gas (nitrogen with varying oxygen concentrations) in a sublimation seeder before gas-dynamically cooling it by expansion through a supersonic nozzle into an optically accessible test chamber [9]. This way, they were able to characterize the fluorescence properties of naphthalene, which is solid at room temperature, down to 100 K.

In a miniature rectangular flow channel (Mach number $M = 2.0$) similar but smaller in size to the one developed in this work, Handa et al. [10] used acetone LIF to measure the local variations in number density along the flow channel center line and compared the results to CFD simulations [11]. To this end, they used an expansion facility to measure the dependence of the acetone-LIF signal on local number density down to 170 K [12]. For ensuring that condensation does not occur within the test section despite the supersaturation with tracer required for sufficient signal, the maximum tolerable tracer concentration was established by monitoring the onset of condensation after a longer residence time in an extended version of the channel.

2.2 Anisole and toluene as fluorescence tracers

The selection of a suitable fluorescence tracer requires careful consideration of many of its properties, considering the boundary conditions of the particular experiment. In addition to the excitation wavelength and intensity, the LIF signal depends to varying degrees on the concentration, temperature, pressure, and composition of the bath gas. Because of these combined dependences, either a comprehensive understanding of the photophysical properties of the tracer or careful multi-parameter calibration of the LIF signal is required. For sensitive measurements, a strong dependence of the measured parameter such as the fluorescence integrated intensity, its decay curve, or its spectral distribution on the variable of interest is crucial.

In addition to the photophysical properties of the tracer candidate, other physical and chemical properties also play a decisive role. For example, evaporation properties are important if the tracer is to be used as a surrogate for fuel components for spray analysis [13-15] or its diffusion

coefficients for mixing studies [2]. Limiting the signal from tracers that are liquid at room temperature is often the temperature-dependent vapor pressure, which can cause condensation in cold flows whereas tracers may decompose at high temperatures [6]. Furthermore, the concentration is limited by the onset of self-quenching [16], which also depends on the excitation intensity. Also, the maximum laser fluence is often limited by the onset of non-linearities [17]. Finally, the availability and environmental compatibility of the tracers should not be neglected, especially in large-scale experiments.

The benzene derivatives anisole and toluene, which were used in this work, are promising candidates for measurements at low temperatures as their high quantum yield [18-21] and, especially for anisole, absorption cross-section [6] partially make up for the concentration limit imposed by their vapor pressures. Also, they are relatively environmentally safe as both are considered non-carcinogenic and non-toxic. They are suitable both for temperature measurements [3, 22-27] and, like other aromatics [28], for the measurement of local oxygen concentrations [29-32]. The latter indirectly allows measurement of the mixing behavior at the molecular level, as will be discussed in detail in section 2.3.

For both tracers, models predicting the LIF signal in the form of either semi-empirical or physical so-called step-ladder models [33] have been developed. The latter describe the deactivation of excited molecules by fluorescence and its competing processes iteratively for each of the mean vibrational energy levels in the excited state that are passed through during relaxation by a sequence of collisions (cf., section 3.2.4.1) – hence the term step-ladder. The rate constants of these deactivation processes, which depend in part on the excess energy and thus, e.g., on temperature, are determined experimentally by fitting the models to the measured data. Therefore, the confidence in the empirical models is limited to the range in which data are available. Currently, models are only valid above room temperature.

The following sections provide an overview of the photophysical data available in the literature for toluene (section 2.2.1) and anisole (section 2.2.2) in the context of their application as fluorescence tracers for quantitative LIF measurements in gas flows. The motivation of the individual authors ranges from the development of measurement techniques to solve engineering problems to fundamental research of the photophysics of fluorescence tracers.

2.2.1 Toluene

Groundbreaking work on the fluorescence properties of toluene vapor was published by Burton and Noyes [34] who studied the fluorescence and absorption properties in the ultraviolet region of its either pure or in various noble gases diluted vapor at several total pressures below 0.67 bar and a temperature range from room temperature up to 435 K. Narrowband excitation at wavelengths between 220 and 280 nm was achieved using broadband lamps in combination with a monochromator. They also studied the quenching effect of molecular oxygen on the fluorescence signal from 0 up to 9.3 mbar O₂ partial pressure.

Reboux et al. [35, 36], intending to use toluene LIF for imaging fuel/air ratios in internal combustion engines, did extensive measurements of fluorescence intensities after 248 nm excitation at higher pressure up to 8 bar for various oxygen concentrations at room temperature. They found that at air pressures of above 3 bar oxygen-quenching is the dominant deexcitation pathway. They concluded that the LIF signal only depends on the local fuel/air ratio in conditions prevalent during the engine compression stroke.

Koban et al. [4, 18, 37-39] later found by extensively studying toluene LIF at engine-related temperatures from 300–950 K and pressures from 1–15 bar at two different excitation wavelengths, 266 and 248 nm, that this assumption is limited to low vibrational energies (low temperatures and longer excitation wavelengths).

Zimmermann et al. [23, 40] measured the fluorescence lifetime of toluene after excitation fs-excitation with 248 nm for, e.g., developing an optical sensors for temperature measurements in internal combustion engines [26]. They found that the long and short lifetime components of the observed biexponential decay curve of the toluene fluorescence are differently influenced by temperature and oxygen concentration. They therefore suggested that simultaneous measurement of tracer concentration, oxygen partial pressure, and temperature might be feasible as the ratio of both lifetimes provides information in the temperature while the temporally integrated signal can be related to the concentration (after correction for temperature).

For in-cylinder temperature measurements in internal combustion engines, Devilliers et al. [41] increased the available pressure range to 1–22.3 bar by measuring the toluene fluorescence upon excitation with 248 nm in the compression stroke of an optical engine. Thus, temperature (293–773 K) was not varied independently but was rather a function of pressure.

Yoo et al. [42] and Cheung [43] measured the fluorescence quantum yields for toluene at 0–5 bar total pressure for 248 nm and 266 nm excitation. For this purpose, they used the Rayleigh calibration method described by Koch et al. [44] which allows the calculation of the absolute quantum yield while simultaneously measuring the absorption and Rayleigh scattering.

Faust et al. [21, 45] analyzed the fluorescence spectra and fluorescence lifetimes of toluene measured with a streak camera after picosecond excitation at 266 nm. They increased the available temperature range to 296–1074 K and investigated different bath gas compositions including pure N₂, N₂ with varying O₂ content, and CO₂. They found that the toluene fluorescence lifetime was almost identical for, both, N₂ and CO₂ atmospheres. Using their data, they developed an empirical model to predict the fluorescence lifetime of toluene under the conditions they studied.

Rossow [46] developed a phenomenological step-ladder model for toluene for engine-related conditions. He, therefore, measured absorption and fluorescence spectra after excitation at 266 for an extended pressure range up to 30 bar at various temperatures from 350–900 K.

Estruch-Samper et al. [47] used toluene LIF to measure temperatures as low as 68 K in cool hypersonic flows. To this end, they measured the temperature-dependent spectral shift of the

toluene fluorescence after excitation at 266 nm for pressures of 13–827 mbar. They extrapolated their results from the measured temperature range between 293–380 K results towards lower temperatures. They found the error of this technique to be within 15 % compared to the values expected in a well-studied canonical test case.

Benzler et al. [48] measured the fluorescence lifetimes of toluene among other aromatic tracers at pressures below 1 bar down to 10 mbar for a temperature range between 296–475 K. From extrapolation of their data, they were able to calculate the collision-free (vacuum) fluorescence and non-radiative rate constants which they used to develop a semi-empirical fluorescence model.

Table 2.1 provides an overview of the available literature data on toluene LIF from the studies cited in this section.

Table 2.1: Publications on the photophysical analysis of toluene with a view to its use as a tracer in the gas phase for temperature or (oxygen) concentration measurement. The table shows the measurement range (temperature T , total pressure p and oxygen partial pressure p_{O_2}) as well as the excitation wavelength λ used and the bath gas composition. The asterisk * indicates that air with a volume fraction of 21 % oxygen was used as the bath gas instead of setting the oxygen concentration separately. The entries partly summarize several publications (see references) of the respective authors.

Author (year)	λ / nm	T / K	p / bar	p_{O_2} / mbar	Bath gas	Measured parameter
Burton and Noyes (1968) [34]	220–280	293–435	0.001–0.67	0–93	He, Ar, Kr, Xe, SF ₆	Absorption and fluorescence spectra
Reboux et al. (1994, 1996) [35]	248	300	1–8	4000	N ₂ (CO ₂ , H ₂ O)	Fluorescence intensity
Koban et al. (2002–2005) [4, 18, 37-39]	248, 266	300–950	1–15	0–400	N ₂	Absorption and fluorescence spectra
Zimmermann et al. (2006) [40]	248	300–570	1	0–70	N ₂	Fluorescence lifetime
Devillers et al. (2009) [41]	248	293–773	1–22.3	*	N ₂ , air*	Fluorescence spectra
Yoo et al. (2010) [42]	248	295	0–5	0	N ₂	Fluorescence quantum yield
Cheung (2011) [43]	248, 266	295	0–5	0	N ₂	Fluorescence quantum yield
Faust et al. (2011, 2013) [21, 45]	266	296–1074	1	0–210	N ₂ , CO ₂	Fluorescence lifetimes and spectra
Rosow (2014) [46]	266	350–850	1–30	0–167	N ₂	Absorption and fluorescence spectra
Estruch-Samper (2015) [47]	266	293–380	0.01–0.83	0	N ₂	Fluorescence spectra
Benzler et al. (2015) [48]	266	296–475	0.01–1	0	CO ₂	Fluorescence lifetimes
Beuting et al. (2021) [49]	266	257–293	0.1–2	0	N ₂	Fluorescence lifetimes and spectra

2.2.2 Anisole

Hirasawa et al. [19] were committed to developing a highly sensitive but experimentally relatively simple and robust LIF thermometry method for which they screened several tracer candidates, including anisole. Their idea was to find a tracer pair that could be excited simultaneously with single laser pulse but whose fluorescence signal is spectrally separated and, therefore, can be easily detected individually. Provided that the signals from the two tracers depend very differently on temperature, the ratio of both signals can be significantly more sensitive to temperature than, e.g., the signal of ratiometric single-tracer methods. The two-tracer technique still shares the advantage of the latter of being independent of variations in tracer concentration or local laser fluence if the ratio of the two tracers does not change. Although they finally did not consider anisole because its spectral separability from the other candidates was not satisfactory, it proved promising for other applications because of its high signal intensity, which exceeded every other investigated candidate by a factor of at least 2.5.

Faust et al. [20] followed up on these findings by performing a systematic study of the anisole photophysics in the context of gas-phase tracer LIF. Having technical applications such as internal combustion engines in mind, they measured fluorescence spectra and lifetimes for elevated temperatures between 296–977 K at total pressures of 1–10 bar in an N₂ atmosphere. They also studied the influence of oxygen quenching for oxygen partial pressures between 0–210 mbar at atmospheric pressure for a similar temperature range. Faust then adapted his semi-empirical fluorescence model for toluene [21] for anisole.

Shortly after, Tran et al. [50] measured fluorescence spectra in different bath gases (N₂, CO₂, Ar) while extending the total pressure range to 2–40 bar and the oxygen partial pressure to 0–7.5 bar. They found that, with the exception of oxygen, bath gas composition had little effect on the LIF signal in the studied temperature range from 473–873 K. Based on these measurements, Wang et al. [51] developed a step-ladder model predicting the anisole fluorescence quantum yield for these conditions.

Benzler et al. [48] further extended the pressure range in the opposite direction to pressures down to 10 mbar. They found that the pressure dependence of the LIF signal intensity flips from a monotonic increase at 355 K to a monotonic decrease at 475 K with increasing pressure. They interpreted this behavior as the transition from photo-induced heating to photo-induced cooling. The implications of these findings are discussed in detail in section 6.2.

Zabeti et al. [6] investigated the maximum reasonable application temperature of anisole LIF in shock-tube experiments using mass spectroscopy finding that anisole is stable up to ~950 K before it decomposes. They measured absorption and fluorescence spectra up to this point and slightly above. Additionally, they measured the significantly different LIF spectra of the reaction products during the pyrolysis of anisole at temperatures between 1255–1620 K.

Whereas the studies on anisole LIF mentioned up to this point used 266 nm for excitation, Baranowski et al. [52] recently used a picosecond optical parametric generator and amplifier

for scanning the excitation wavelength from 256–270 nm to follow up on the findings of Benzler et al. [48]. For a temperature range between 325–525 K and pressures of 1 and 4 bar they found a unique temperature/wavelength combination at which the fluorescence lifetime became independent of pressure. These could be interpreted as wavelengths where the excitation occurs exactly to the thermalized energy level in the excited state. They found that the energy required for that is underestimated in the available models. A significant improvement was achieved by using ab initio simulations of the wavelength-dependent transition probability (i.e., absorption spectra) to provide an approximation of the ground state energy transferred to the excited state.

Table 2.2 provides an overview of the available literature data on anisole LIF from the studies cited in this section.

Table 2.2: Publications on the photophysical analysis of toluene with a view to its use as a tracer in the gas phase for temperature or (O_2) concentration measurement. The table shows the measurement range (temperature T , total pressure p and oxygen partial pressure p_{O_2}) as well as the excitation wavelength λ used and the bath gas composition.

Author (year)	λ / nm	T / K	p / bar	p_{O_2} / mbar	Bath gas	Measured parameter
Hirasawa et al. (2007) [19]	266	295	1	0	N_2	Fluorescence spectra
Faust et al. (2013) [20]	266	296–977	1–10	0–210	N_2	Fluorescence lifetimes and spectra
Tran et al. (2014) [50]	266	473–823	2–40	0–7500	N_2, CO_2, Ar	Fluorescence spectra
Benzler et al. (2015) [48]	266	296–475	0.01–1	0	CO_2	Fluorescence lifetimes
Zabeti et al. (2016) [6]	266	296, 575–980 (1255–1620)	1.5	0	Ar	Absorption and fluorescence spectra
Baranowski et al. (2019) [52]	256–270	325–525	1, 4	0	N_2	Fluorescence lifetimes
Beuting et al. (2021) [49]	266	257–293	0.1–2	0	N_2	Fluorescence lifetimes and spectra

2.3 Quantitative imaging of mixing states

In a molecularly mixed state, the probability of collisions in a binary mixture with collision partners of the same and different kind are equally likely considering an equal ratio and identical collision cross sections of both substances. This state in which the molecules are homogeneously distributed on molecular level, represents the optimum conditions for chemical reactions such as combustion since diffusion processes do not inhibit the transport, e.g., of fuel to oxidizer. The original distinction by Eckart [53] for incompressible flows that was later adapted for compressible flows [54, 55], states that stirring (or macroscopic mixing) refers to the mechanical action of distribution of fluids while (molecular) mixing describes the diffusion

of the stirred fluids across their interfacing boundaries. According to Dimotakis [56], initially segregated fluids brought together in a turbulent manner are dispersed by motion of their dissipating flow structures (stirring). As the larger eddies break down to smaller structures, molecular diffusion acts increasingly on the increasing surface of their boundaries. Therefore, molecular mixing acts on all size and time scales of the turbulence cascade and depends on the surface and, therefore, size of the flow structures. One can argue that a mixing state on molecular level is reached once molecular diffusion dominates over viscous forces, i.e., at the Batchelor length or time scale [57].

In compressible turbulent flows (turbulent Mach number > 0.5), theoretical description of the mixing behavior is complicated since compression and, in the case of supersonic flows, shocks (Fig. 2.2) introduce additional dissipation pathways [56]. It was found that increased Mach numbers stabilize turbulent flows [58] leading to less effective mixing. This is especially problematic for the production of nanoparticles in supersonic reactors, which rely on molecular-level mixing but prohibit early addition of the reactant prior to acceleration and gas-dynamic cooling to avoid premature reactions [1].

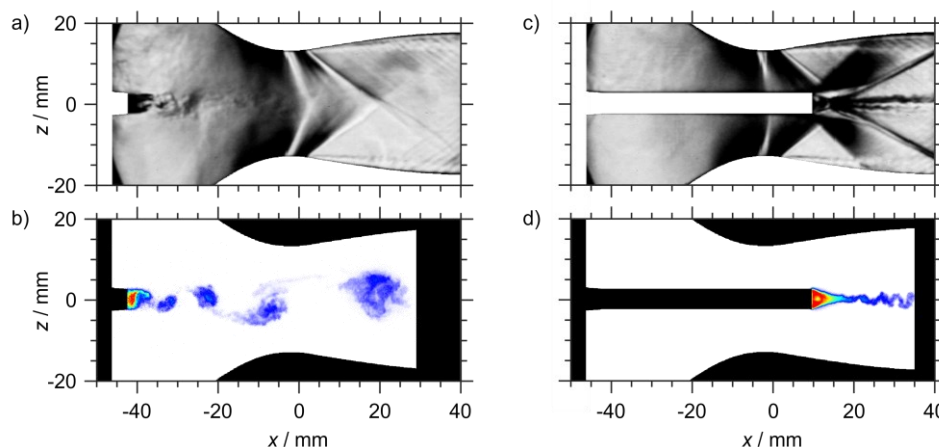


Fig. 2.2: Instantaneous schlieren (top [59]) and LIF images (bottom [60]) showing the wake of an injector whose trailing edge located in the subsonic (left) and supersonic (right) section of a nozzle flow showing inherently different macroscopic mixing behavior.

Macroscopic mixing or stirring has been extensively studied in configurations very similar to those discussed in this work by Chun [61] and Wohler [62-66]. The latter suggests that the dispersion of the flow structures for both, subsonic and supersonic injection, is self-similar in the far field (about 200 injector trailing edge heights downstream of the point of injection) of the flow independent of the angle of injection or injector geometries [66].

Although some work has investigated the molecular mixing behavior on canonical cases in and supersonic flows, the relationships are not yet fully understood [67] and the number of investigations on geometries close to the application are still limited [68, 69].

From an experimental standpoint, it is important to be able to distinguish between sub-resolution stirring and molecular mixing for, e.g., combustion applications. For illustration, consider a mixing flow of two different substances, say A and B, that is observed with an imaging

measurement system only sensitive to one of both substances, say A. The red square in the image on the left-hand side in Fig. 2.3 illustrates the limited resolution of the imaging system. In this case, the signal originating from the corresponding measurement volume is ambiguous: If for example the measured intensity would be 50 % of that expected of the measurement volume being completely filled with A, this could mean that the sub-resolution mixing state on molecular level is either completely mixed (Fig. 2.3a, gray color), completely unmixed (Fig. 2.3b), or a combination of both (Fig. 2.3c). In other words, measurement of the intensity of A only yields the mixing fraction as the dilution of a A as a passive scalar (stirring). It does not provide information on the (molecular) mixing state according to the definitions given above.

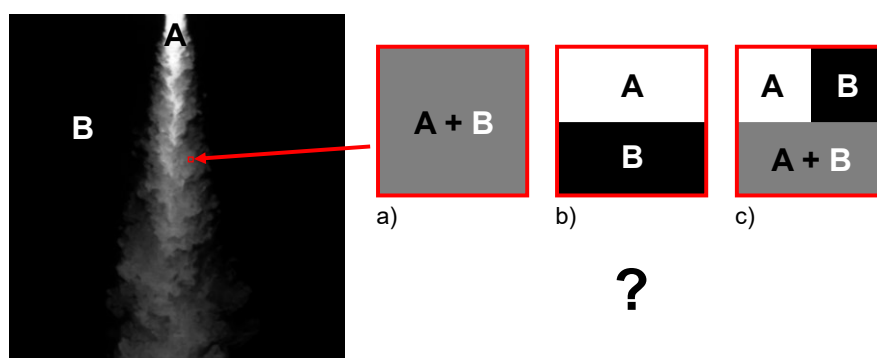


Fig. 2.3: Differentiation between sub-resolution stirring and molecular mixing. Left: Turbulent jet of fluid A injected into a quiescent fluid B. The red square represents the maximum resolution of a detection system sensitive for a signal depending on the local amount of fluid A only. If the measured intensity corresponds to 50 % of the signal expected for pure A, both fluids may be a) mixed on the molecular level, b) stirred on a sub-resolution level but completely unmixed below that, or c) a combination of both as represented in the enlarged views of the measurement volume (adapted from Meyer et al. [70] and Rossmann et al. [71]).

To overcome the resolution problem, indirect methods have been developed. For example, the local heat release of a fast chemical reaction requiring molecular mixing of two reaction partners given to A and B, respectively, was measured as a proxy for the local mixing level [55, 72]. Despite refinements of the technique [56], interpretation of the results remains not trivial and spatial resolution requires scanning of a temperature probe. Also, the heat release and the reaction products may cause undesired side effects. Winter et al. [54] demonstrated the concept of a collisional energy-transfer fluorescence technique that measured the fluorescence of biacetyl induced by energy transfer upon collisions of UV laser-excited toluene molecules with ground-state biacetyl molecules. While this signal depended directly on the mixing state of the toluene containing and the biacetyl-containing flow, the fluorescence signal of biacetyl after selective excitation at longer wavelengths was found to depend on the biacetyl concentration only and, therefore, provided information on the stirring of the flows.

The approach introduced by Paul and Clemens [73, 74] exploited the strong collisional quenching effect of molecular oxygen on the laser-induced fluorescence of nitric oxide analogous to fast chemical reactions. To this end, NO was added to a N_2 jet that was then mixed with an air co-flow. Since collisional quenching was considered having unity efficiency, the fluorescence signal only marked completely unmixed NO. By alternately injecting either the fluorescent or

quenching liquid through a nozzle into a low-velocity co-stream containing the other fluid, they were able to identify the molecularly mixed portion of the forming axisymmetric shear layer.

The limitation associated with this approach of not being able to make instantaneous measurements has been eliminated by King et al. [75]. In addition to nitric oxide, they used acetone, whose fluorescence is not quenched by oxygen, as an additional tracer to monitor stirring on the macroscopic level. Assuming that the upper-level loss rates of the excited acetone are significantly larger than its spontaneous emission rate and quenching effects and again, assuming an infinite quenching rate of NO in the presence of oxygen, they were able to calculate the mixing level on molecular level as shown in Fig. 2.4d.

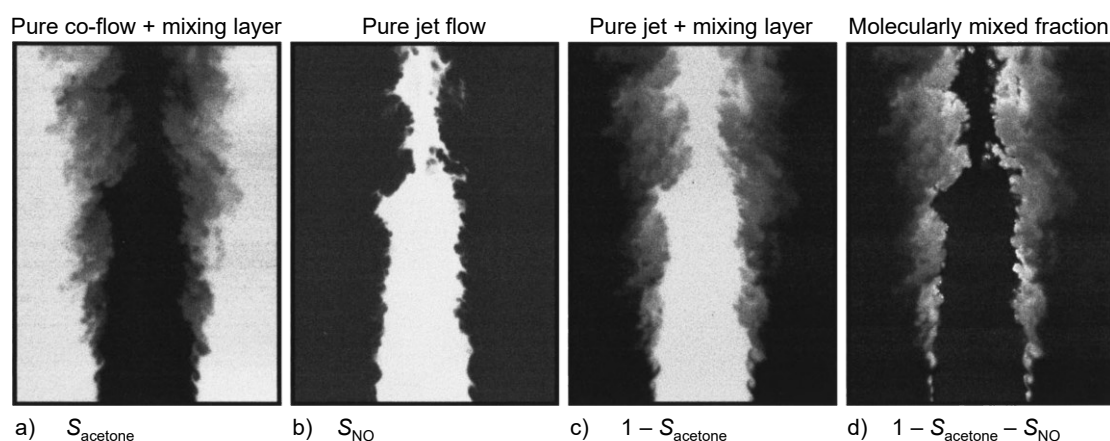


Fig. 2.4: Quantitative imaging of the molecularly mixed fraction in the mixing layer of a jet in a co-flow by King et al. (reproduced from [75], with the permission of AIP Publishing.) The co-flow is air seeded with acetone, whose fluorescence signal is insensitive to O_2 . The jet is N_2 seeded with NO, whose fluorescence is assumed to be quenched by O_2 with unity efficiency. Therefore, the a) acetone signal (S_{acetone}) represents the pure co-flow and the fraction found in the mixing layer whereas the b) NO signal (S_{NO}) only marks the pure jet flow. Since the signals are normalized by the intensity of the respective pure flow, the molecularly mixed fraction (d) can be calculated by subtracting the S_{NO} from the inverted acetone image (c).

Meyer et al. [70] followed up on this work by reviewing the validity of the theory and assumptions in detail. While they highlighted the capabilities of the approach, they pointed out that especially the in-reality finite quenching rate leads to a considerable uncertainty. Rossmann et al. [71] then developed a modeling approach using several different quenching partners accounting for the non-infinite quenching rate and the temperature dependence of the quenching cross-section.

These techniques are increasingly complex in the order they were mentioned. For the approach of King et al. [75], e.g., two lasers and two cameras are required to measure both tracers. Exact alignment of the laser beams is critical [70]. Koban et al. [29] mitigated the problem by using toluene and 3-pentanone instead, with the former being sensitive to O_2 while the latter acts as the passive scalar. Since their emission spectra overlap, both substances can be excited with a single laser. Contrary to the cold chemistry approach, both, air and N_2 , flows were seeded with the identical amount of both tracers. The ratio of the signal was then used to measure the local O_2 concentration using previously obtained calibration data. However, energy transfer and spectral cross talk between both tracers proved problematic only allowing relatively low tracer

concentrations. Yu et al. [76] recently demonstrated an almost identical technique using acetone instead of 3-pentanone while addressing and accounting for the energy transfer in detail.

A further reduction of the experimental effort was achieved by Mohri et al. [30]. They used toluene as a single tracer and exploited that quenching in the O₂-toluene system is more efficient at high energies (short excitation wavelengths), therefore, inducing an apparent red-shift of the fluorescence spectrum. Using a two-color imaging system, the spectral change was detected, and the local oxygen concentration was determined from calibration data.

A very different but noteworthy approach was developed by Hu and Koochesfahani [77] that is especially intriguing due to its experimental simplicity and robustness. Here, acetone is used as a single tracer acting as both, marker for the passive scalar and quenching partner for cold chemistry. While its fluorescence is insensitive to oxygen contained in the co flow of an N₂ jet seeded with acetone, its longer-lived (delayed) phosphorescence signal is strongly quenched. They used a single laser for excitation and a single intensified camera for detection of both signals separated by careful timing of two consecutive exposures. While the use of a single laser and single camera eliminates almost all alignment and many calibration issues, the downside of this approach were the long exposure times in the microsecond range required to capture the phosphorescence leading to spatial uncertainties of several millimeters in high-velocity flows, e.g., at the conditions studied by Chun [61], Wohler et al. [62-66], and Richter et al. [59, 60, 78-82].

3 Theory

In this chapter, the theoretical principles of fluid dynamics required for the design of supersonic flow channels and the flow phenomena to be studied are described. Additionally, the underlying photophysical processes of laser-induced fluorescence are presented. Finally, optical imaging measurement strategies and their capabilities for specific scientific objectives are discussed and compared.

3.1 Fluid mechanics

This section explains characteristics of the transonic wake flow in which the measurement techniques developed in this thesis are applied (chapters 5 and 6). It also introduces the fluid mechanical fundamentals of the nozzle flow necessary for the design of the miniature flow channel used in Chapter 8. Unless otherwise stated, the following explanations are based on the elaborations by White [83], and Weigand et al. [84] beginning with the following definition and classification.

The Mach number M is the dimensionless ratio of the flow velocity u and the speed of sound a being $M = 1$ in the case of sonic flow.

$$M = \frac{u}{a} \quad (3.1)$$

Whereas slow subsonic flows ($M < 0.2$) are considered incompressible, density effects cannot be neglected for increasing flow velocity ($0.2 < M < 1.0$). If the magnitude of the flow velocity or the velocity of an object relative to a fluid at rest reaches sonic velocity ($0.8 < M < 1.2$), we speak of transonic flow in which both supersonic and subsonic regions are present accompanied by compressibility effects, e.g., in the form of shock waves. These are wave fronts caused by sound waves originating from a body moving at supersonic speed or in an obstacle in a supersonic flow. Shock waves cause sharp gradients of the state variables leading to complex flow fields. After further acceleration, the formerly mixed flow field becomes a pure supersonic flow ($M > 1.2$) [83]. The following chapters aim at deriving a set of equations for the one-dimensional description of the frictionless transonic nozzle flow as function of Mach number.

3.1.1 Speed of sound

The speed of sound is the velocity with which an acoustic wave, i.e., a perturbation of pressure and the associated state variables, travels through a medium. For a perfect gas, the isobaric and isochoric heat capacities, c_p and c_V , are constant while the equation of state relating pressure p to density ρ and temperature T (specific ideal gas constant R_s) neglects intermolecular forces. This approximation is safe for small variations in temperature, especially since the ratio of specific heats κ is only a weak function of temperature [83].

$$p = \rho RT, \quad R_s = c_p - c_v, \quad \kappa = \frac{c_p}{c_v} \quad (3.2)$$

To derive a set of equations describing the flow through the flow channel, one can start with the fundamental equation describing the infinitesimal change in entropy s as a function of small changes in enthalpy h and pressure p .

$$T ds = dh_s - \frac{dp}{\rho}, \quad dh_s = c_p dT \quad (3.3)$$

Substituting Eq. 3.2 into Eq. 3.3 and after rearrangement and subsequent integration one obtains the following expression for the change of entropy.:

$$ds = c_p \frac{dT}{T} + R \frac{dp}{p}, \quad s_1 - s_0 = c_p \ln \left(\frac{T_1}{T_0} \right) + R \ln \left(\frac{p_1}{p_0} \right). \quad (3.4)$$

Small gradients such as caused by sound waves travelling through a medium can be considered adiabatic and reversible so that an isentropic change of state ($ds = 0$) is a fair assumption. Therefore, with the left part equaling zero and after substitution of c_p and R (Eq. 3.2), Eq. 3.4 reduces to

$$0 = \frac{\kappa}{\kappa - 1} \ln \left(\frac{T_1}{T_0} \right) + \ln \left(\frac{p_1}{p_0} \right) \quad (3.5)$$

yielding a simple relationship between pressure, temperature, and density (via Eq. 3.2) for the isentropic state change of a perfect gas.

$$\frac{p_1}{p_0} = \left(\frac{T_1}{T_0} \right)^{\frac{\kappa}{\kappa-1}} = \left(\frac{\rho_1}{\rho_0} \right)^{\kappa} \Rightarrow \frac{p}{\rho^{\kappa}} = \text{const.} \quad (3.6)$$

Considering a sound wave propagating through a medium of pressure p and density ρ with the velocity of a from the reference frame moving with the sound wave with du being the fluid velocity as shown in Fig. 3.1.

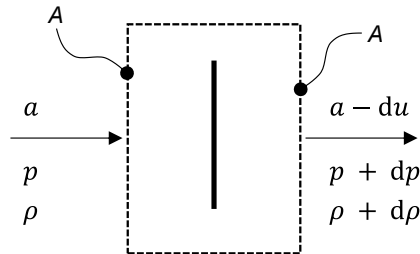


Fig. 3.1: One-dimensional sound wave propagating through a medium of pressure p and density ρ with the velocity of a . The control volume (dashed line) is attached to the sound wave so that it stands still within the reference frame. Based on drawings by White [83].

Then, assuming stationary behavior, the continuity principle dictates that the mass flow \dot{m} throughout the control volume (dashed line) remains constant for a constant control volume surface area A .

$$\dot{m} = \text{const.} = \rho a A = (\rho + d\rho)(a - du)A \quad (3.7)$$

In analogy to the mass balance, the momentum balance for the control volume can be written as follows.

$$pA + \dot{m}a = \text{const.} = (p + dp)A + \dot{m}(a - du) \quad (3.8)$$

Inserting Eq. 3.7 into Eq. 3.8 simplifies the mass balance to

$$du = \frac{dp}{\rho a}. \quad (3.9)$$

With A cancelling, the following equation can be obtained from the mass balance (Eq. 3.7) by rearranging and neglecting the second order derivatives.

$$du = \frac{1}{\rho}(a d\rho - \cancel{d\rho} du) = \frac{a d\rho}{\rho} \quad (3.10)$$

The combination of Eq. 3.9 and Eq. 3.10 then gives

$$a^2 = \frac{dp}{d\rho}. \quad (3.11)$$

Using the equation for isentropic change of state (Eq. 3.6) and the ideal gas law (Eq. 3.2), the speed of sound a of an isentropic perfect gas can be expressed in its common form.

$$a = \sqrt{\kappa \frac{p}{\rho}} = \sqrt{\kappa RT} \quad (3.12)$$

3.1.2 Compressible isentropic nozzle flow

To describe the flow through a duct with variable cross section A , it is convenient to start with the differential notations of the continuity equation (Eq. 3.7) and the momentum balance (Eq. 3.8) shown in Eqs. 3.13 and 3.14, respectively.

$$\frac{d\rho}{\rho} + \frac{dA}{A} + \frac{du}{u} = 0 \quad (3.13)$$

$$\frac{dp}{\rho} + u du = 0 \quad (3.14)$$

Inserting Eq. 3.11 into 3.14 and then into 3.13 describes the change of A required for a change in velocity as a function of the Mach number (Eq. 3.1).

$$\frac{dA}{du} = A \left(\frac{u}{a^2} - \frac{1}{a} \right) = \frac{A}{u} (M^2 - 1) \quad (3.15)$$

It becomes apparent that for subsonic flows ($M < 1$) increasing velocity requires a decreasing cross section while for supersonic flows ($M > 1$) increasing velocity requires also an increasing cross section.

$$\left. \frac{dA}{du} \right|_{M < 1} < 0, \quad \left. \frac{dA}{du} \right|_{M=1} = 0, \quad \left. \frac{dA}{du} \right|_{M > 1} > 0 \quad (3.16)$$

Consequently, to accelerate a flow from sub- to supersonic speed, the effective cross-section must be reduced and increased again after $M = 1$ is reached. This can be achieved in a convergent–divergent duct or de-Laval nozzle as shown in Fig. 3.2. The flow channels described in this work feature a rectangular cross-section with a constant width (y -direction in Fig. 3.2).

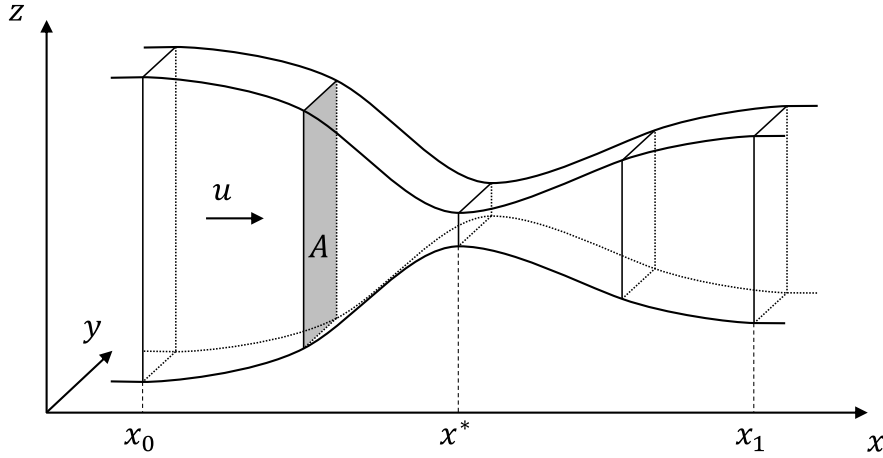


Fig. 3.2: Rectangular convergent–divergent duct (de-Laval nozzle) with constant width.

The origin of the coordinate system used in this work always resides on the flow centerline at the smallest (critical) cross-section A^* so that $x^* = 0$. Index 0 denotes the inlet and index 1 the outlet of the nozzle, respectively. Sticking to the prior assumptions (stationary, isentropic one-dimensional flow of a perfect gas) the energy balance for the nozzle reads as follows assuming that the flow at the inlet is at rest (which is approximately true for $A_0 \gg A^*$) and neglecting differences in geodesic height.

$$h_{s,0} = h_s + \frac{u^2}{2} \quad (3.17)$$

With Eq. 3.2 and Eq. 3.3 this gives

$$c_p T_0 = c_p T + \frac{u^2}{2} \quad \Leftrightarrow \quad \frac{T_0}{T} = 1 + \frac{u^2}{2c_p T} = 1 + \frac{\kappa - 1}{2} \frac{u^2}{\kappa R T}. \quad (3.18)$$

With Eq. 3.12 and Eq. 3.1, we get the temperature as a function of the Mach number.

$$\frac{T_0}{T} = \frac{\kappa - 1}{2} M^2 + 1 \quad (3.19)$$

A similar relationship for pressure and density is obtained using the equation for isentropic change of state (Eq. 3.6).

$$\frac{p_0}{p} = \left(\frac{\kappa - 1}{2} M^2 + 1 \right)^{\frac{\kappa}{\kappa - 1}}, \quad \frac{\rho_0}{\rho} = \left(\frac{\kappa - 1}{2} M^2 + 1 \right)^{\frac{1}{\kappa - 1}} \quad (3.20)$$

The parameters at the critical cross-section (superscript *) can be determined by inserting $M = 1$.

$$T^* = \frac{2T_0}{\kappa + 1}, \quad p^* = p_0 \left(\frac{2}{\kappa + 1} \right)^{\frac{\kappa}{\kappa - 1}}, \quad \rho^* = \rho_0 \left(\frac{2}{\kappa + 1} \right)^{\frac{1}{\kappa - 1}} \quad (3.21)$$

Inserting the density terms of Eq. 3.20 and Eq. 3.21 into the continuity equation 3.7 at the critical point yields an expression for A depending on the critical nozzle cross-section A^* .

$$A = \frac{A^*}{M} \left(\frac{2 + (\kappa - 1)M^2}{\kappa + 1} \right)^{\frac{\kappa + 1}{2(\kappa - 1)}} \quad (3.22)$$

This final set of equations can be used to approximate (neglecting boundary layer effects) the conditions inside and behind the nozzle at a given geometry for known inlet conditions, or vice versa. The design of the nozzle for the flow channel described in this work also accounts for boundary layer effects by incorporating computational fluid dynamics (CFD) is explained in detail in chapter 8.4.

3.1.3 Transonic wakes

In Chapters 5 and 6, mixing layers in accelerated transonic wake flows are studied using LIF. Since this work focuses on the measurement technique and less on the flow dynamics, the complex case of these frictional, turbulent shear flows and the associated compressibility effects will only be outlined roughly and phenomenologically.

For a detailed treatment of the underlying principles, the reader is kindly referred to the work of Richter [2], which deals with the aerodynamic analysis of such flows as part of the collaborative project on which this work is based.

A number of studies exist dealing with wake flows in the subsonic region ($M < 1$). Here, the wake of a blunt obstacle is dominated by large-scale spanwise vortices separating alternating for a wide Reynolds number range [85-88]. Figure 3.3 shows qualitatively the subsonic wake flow behind an obstacle with a blunt trailing edge such as of the injectors discussed later in this work. The profile of the time-averaged wake velocity deficit u_d , being the difference of the of the local velocity to the undisturbed flow velocity u_∞ (Eq. 3.23), is sketched in Fig. 3.3 on the right-hand side. Past studies showed. It was shown that its half-width $\delta_{1/2}$ increases quadratically with the distance to the point of interference which is also referred to as the $\frac{1}{2}$ -power law [89].

$$u_d = u - u_\infty, \quad \delta_{1/2} \propto \sqrt{x} \quad (3.23)$$

The shape of this velocity deficit profile was found to be self-similar in the far field wake of objects in sub- [89] and supersonic flows [68]. Self-similarity in this context means that velocity profiles, such as those shown in Figs. 3.3 and 3.4 on the right, retain their shape and scale only by their individual velocity and length scales [89] with increasing distance from the point of origin .

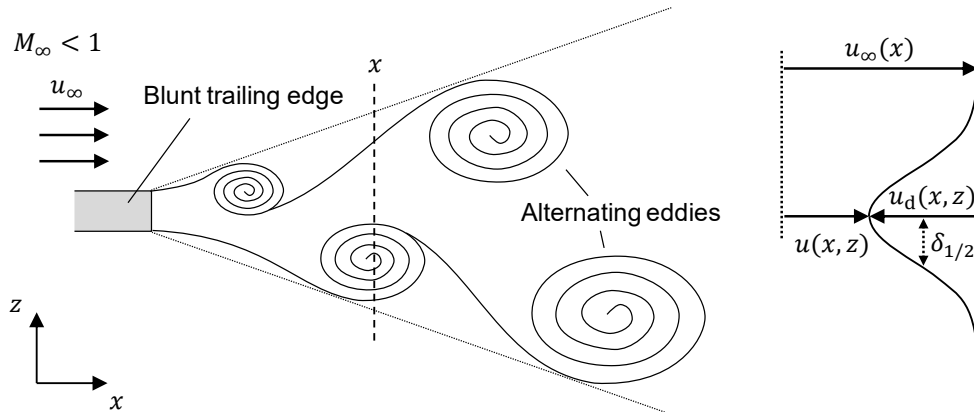


Fig. 3.3: Subsonic wake of a body with a blunt trailing edge, adapted from Nakagawa et al. [68].

The characteristics of the wake are fundamentally different for supersonic ($M > 1$) flows [68]: as shown in Fig. 3.4, first a subsonic recirculation zone forms in the closest vicinity to the blunt trailing edge accompanied by expansion fans originating from its edges. The short subsonic wake is followed by a recompression zone, recognizable by the characteristic oblique shocks that occur at its neck. These compressibility effects influence the wake significantly and inhibit its expansion with increasing Mach number while stabilizing the mixing layer [58].

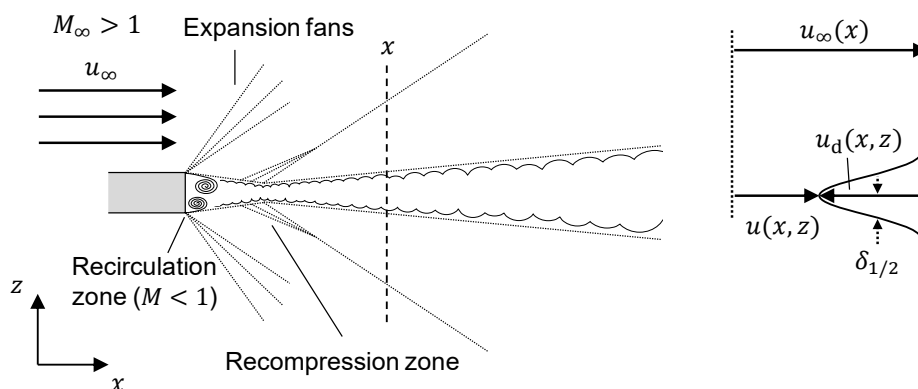


Fig. 3.4: Supersonic wake of a body with a blunt trailing edge, adapted from Nakagawa et al. [68].

All cases discussed in this thesis concern a blunt body with injection of a fluorescence tracer at the vertical trailing edge at relatively low velocity and low mass flow rate compared to the main flow. Literature refers to such low-momentum injection also as base bleed [90, 91]. The introduction of a traceable substance as base bleed provides a passive scalar whose distribution marks the mixing layer, provided that no temperature or pressure effects or mixing-induced photochemistry occur. This is on one hand of practical importance since it is analogous to fuel or precursor distribution in practical applications (Section 4) and on the other hand provides means for studying wake flows on a fundamental level [2, 66]. According to Pope [92], the lateral velocity deficit profile and the lateral concentration profile differ slightly with the latter being wider also affecting the perceived growth rate. Nevertheless, the use of concentration profiles as a proxy for the shape of the wake has become a common method for demonstrating self-similarity [59, 60, 64] since the laterally normalized mixture fraction is conserved identically to the lateral profiles of axial velocity [92].

3.2 Photophysics of organic fluorescence tracers

In this section, the photophysical background for understanding the laser-induced fluorescence of organic tracer species is explained. Emphasis is placed on the properties of the benzene derivatives anisole and toluene, which were used as fluorescence tracers. After a brief explanation of the principles of matter-light interaction, the mechanisms responsible for the influence of environmental conditions on the fluorescence signal are described.

3.2.1 Interaction of matter and light

The molecules of interest for this work are toluene and anisole (Fig. 3.5) due to their fluorescence properties and, in particular, the additional sensitivity to collisions with molecular oxygen. The energy levels of molecules are widely described by linear combinations of the atomic orbitals. Typical optically excitable transitions in both aromatic organic molecules in question are the $\pi \rightarrow \pi^*$ localized at their C=C double bonds [28]. This chapter provides the theoretical background for the understanding of laser-induced fluorescence of both aromatic tracers. Unless stated otherwise, the contents of this chapter is based on the description of Klán and Wirz [93], and Sauer [94].

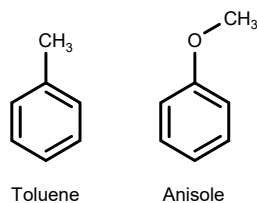
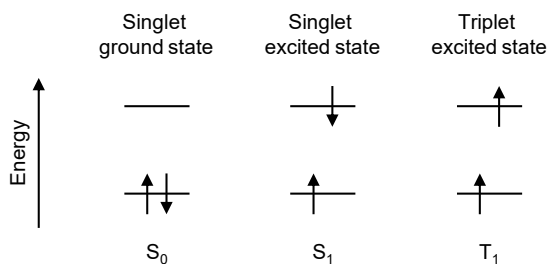


Fig. 3.5: Structural formula of toluene and anisole.

The ground-state configuration of both species is the singlet state (S_0) where the total spin is zero as shown in Fig. 3.6. After absorbing a photon of proper energy, one electron is excited from the highest occupied molecular orbital (HOMO) to the lowest unoccupied molecular orbital (LUMO). If the subsequently unpaired electron spins remain anti-parallel, the resulting spin configuration remains zero meaning that this excited state (S_1) is also a singlet state. During radiative transition from $S_1 \rightarrow S_0$, the molecule emits a photon of similar energy which can be observed as fluorescence. On the other hand, if the spins of the unpaired electrons are parallel, the excited state is called a triplet state (T_1). In contrast to the singlet state, the relaxation from the T_1 is spin-forbidden. Therefore, the radiative transition $T_1 \rightarrow S_0$ referred to as phosphorescence is several orders of magnitude slower compared to fluorescence.

Fig. 3.6: Representation of the spin configurations of the singlet ground state S_0 , the singlet excited state S_1 , and the triplet excited state T_1 , adapted from Klán and Wirz [93].

For molecules, the energy required for each transition does not only depend on the HOMO–LUMO energy difference but also on the vibrational and rotational energy level of the molecule in the ground and excited state. The potential wells of the S_0 and S_1 state for a diatomic molecule are qualitatively shown in Fig. 3.7a as Morse potentials, which also account for the anharmonicity of a diatomic oscillator. Because the electronic excitation is several orders of magnitude faster than the time scale of the molecular vibrations, the distance of the nuclei is invariant or “frozen” compared to the movement of the electrons during the excitation process, resulting in a “vertical” transition. Excitation or deactivation is much more likely if the probability density of the oscillator’s nuclear wave functions overlaps in both states. The likelihood for each such transition is shown qualitatively in Fig. 3.7b where the intensity representing the strength of the absorption and fluorescence is shown over the energy or the corresponding wavelength. The absorption and fluorescence lines result from the spatial overlap of the wave functions at the different vibrational levels also referred to as the Franck-Condon integral or factor.

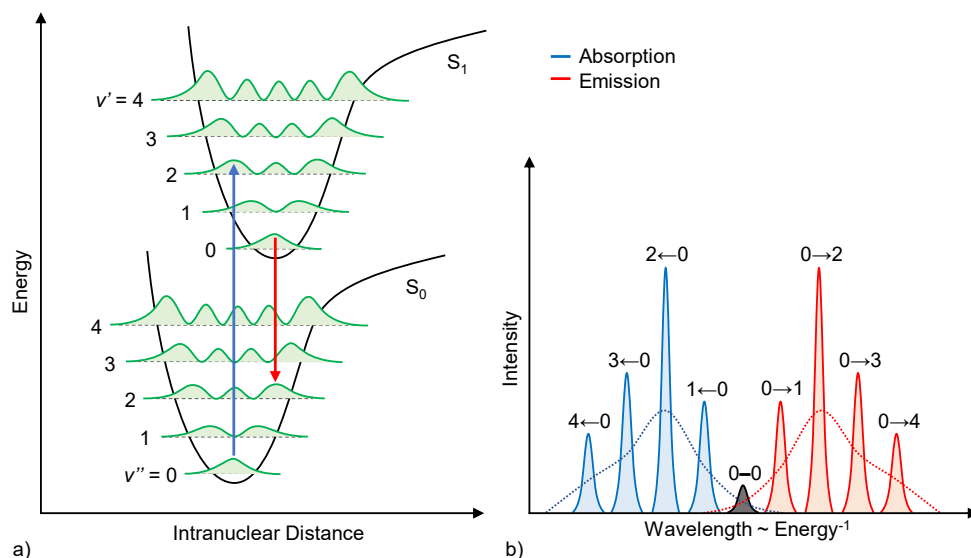


Fig. 3.7: Cartoon for explaining the Franck-Condon principle: a) Morse potentials for the S_0 and S_1 states of a diatomic oscillator where green lines depict the probability density of the oscillator wave function. b) Absorption and emission lines derived from a) favoring the $0 \rightarrow 2$ transition and the resulting absorption and fluorescence spectra (dotted lines), adapted from Sauer [94].

The shape of the final absorption and emission spectra (dotted lines) are subject to the influence of temperature, pressure, and possible bath gas composition. The initial vibrational energy population in the ground state, and hence in the excited state energy level of the molecule after absorption of a photon of a certain energy, depends on the temperature. In combination with the Franck-Condon factors this leads to multiple effects affecting the spectral shape and strength. On one hand, the number of likely transitions increases with increasing energy level (Fig. 3.7a) resulting in more broadband absorption and fluorescence spectra. On the other hand, the energy difference between the high-probability $S_1 \leftrightarrow S_0$ transitions changes due to the anharmonicity of the potential wells of the states that increases with vibrational energy. For the two tracers studied in this work, this leads to a preference of transitions with lower energy difference and, thus, a red shift of absorption and emission spectra. Finally, the overlap from S_1 to higher excited S_0 or triplet states (not shown) increases with the vibrational energy level so that losses through “horizontal” non-radiative processes (section 3.2.4.1) lead to similarly strong and near-exponential decrease of the fluorescence quantum yield with increasing temperature for anisole and toluene [95].

3.2.2 Absorption

The exponential attenuation of light along passing an optically dense medium is described by the Lambert–Beer law as illustrated in Fig. 3.8.

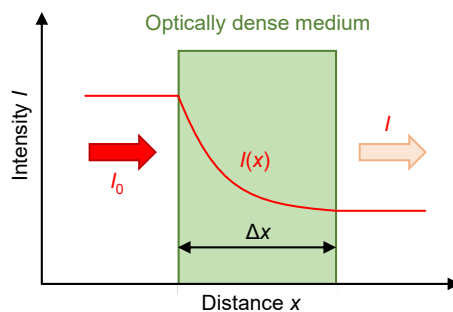


Fig. 3.8: Light absorption in an absorbing medium (green) as described by the Lamber-Beer law.

The ratio of the attenuated light intensity I_{laser} to the initial intensity $I_{\text{laser},0}$ depends on the absorber number density n_{tracer} the absorption path length Δx and the wavelength-dependent and species-specific (chapter 3.2.1) absorption cross-section σ_{abs} (Eq. 3.24)

$$\frac{I_{\text{laser}}}{I_{\text{laser},0}} = \exp(-n_{\text{tracer}}\sigma_{\text{abs}}\Delta x) \quad (3.24)$$

The gas-phase absorption spectra of the two tracers used in this work, toluene a) and anisole b), are shown in Fig. 3.9 for different bath gas temperatures. Both substances can be excited using the commonly available wavelengths 248 and 266 nm (dotted lines) of KrF-excimer and frequency-quadrupled Nd:YAG lasers, respectively. Whereas the absorption cross-section is similar at 248 nm, it is about one order of magnitude larger at 266 nm for anisole. In practical applications, this compensates for the significantly lower vapor pressure of anisole compared to toluene of 3.2 mbar vs. 29 mbar at room temperature, respectively. For toluene, the absorption cross-section is nearly independent of temperature at 248 nm so that this wavelength was chosen in this work if a low temperature dependence of the LIF signal was desired (chapters 5 and 6).

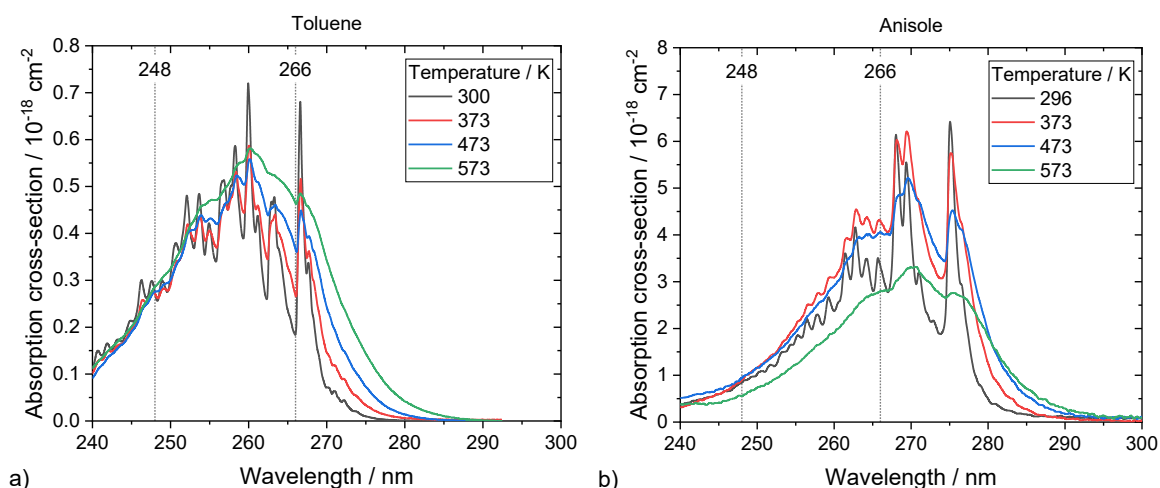


Fig. 3.9: Temperature-dependent absorption cross-section of a) toluene vapor measured in N_2 at atmospheric pressure [96] and of b) anisole measured at 120 mbar in Ar bath gas [97].

Since in this work LIF is applied to low density gases in cases, where n_{Tracer} is severely limited by the tracer vapor pressure at low temperature, the tracer concentration is so low that attenuation of laser light passing the measurement volume was neglected unless stated otherwise.

3.2.3 Emission

Spontaneous emission of light during the transition of excited molecules from a higher to a lower electronic state is referred to as luminescence. Luminescence processes can be classified according to the type of excitation, e.g., chemiluminescence, electroluminescence, thermoluminescence, photoluminescence. According to the spin configuration of the electron states involved, luminescence is further subdivided into fluorescence and phosphorescence, which will be discussed in detail in section 3.2.4.1. The LIF techniques discussed in this thesis relate to the measurement of extrinsic and intrinsic state variables from the non-saturated fluorescence signal after excitation with laser light. To explain what that means, it is useful to begin with a simple two-level energy model as shown in Fig. 3.10. Unless stated otherwise, the explanations in this section are based on the elaborations of Eckbreth [17].

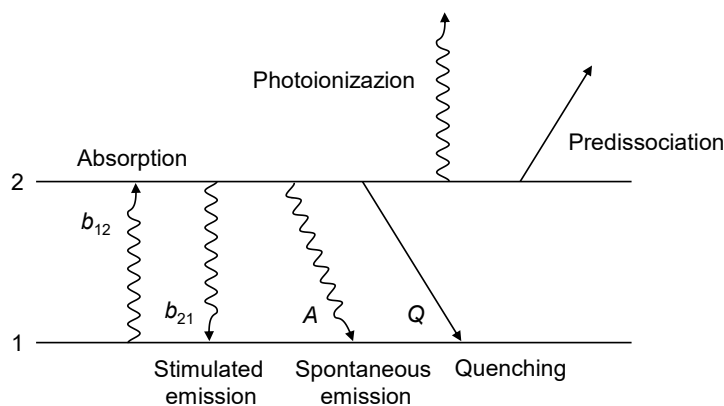


Fig. 3.10: Simple two-level energy diagram reproduced from Eckbreth [17].

Consider a gas of identical molecules, which can exist in two electronic states (1 and 2). The absorption of a photon excites molecules from 1 to 2, from which they return to 1 by spontaneous emission or by non-radiative energy transfer (quenching). With increasing population of the excited state 2, stimulated emission, i.e., the emission of another photon triggered by an absorbed photon, plays an increasingly important role. Neglecting other processes like photoionization and predissociation, which may contribute to a reduction of excited molecules but without returning them to the ground state, one can write the rate equations for describing the population of each level as follows [17].

$$\frac{dN_1}{dt} = -N_1 b_{12} + N_2 (b_{21} + A_{21} + Q_{21}) \quad (3.25)$$

$$\frac{dN_2}{dt} = N_1 b_{12} - N_2 (b_{21} + A_{21} + Q_{21}) \quad (3.26)$$

Here, N represents population density in the respective level. A_{21} is the rate constant and at the same time the Einstein A coefficient for spontaneous emission and Q_{21} is the rate constant for collisional quenching. The rate constants for absorption and stimulated emission b_{12} and b_{21} , respectively, can be calculated from the Einstein coefficient B , the incident laser intensity I_{Laser} , and C_λ a conversion factor of the same unit as I_{Laser} [98]. If the laser irradiance (e.g., in units of $\text{W m}^{-2} \text{s}^{-1}$) was used for I_{Laser} , C_λ would be equal to the speed of light c [17].

$$b = \frac{BI_{\text{laser}}}{C_\lambda} \quad (3.27)$$

If all irreversible upper-level losses are neglected (as done for Eq. 3.26), the total number of molecules is constant.

$$N_1 + N_2 = \text{const.} = N_1^0 \quad (3.28)$$

Inserting Eq. 3.28 into 3.26 eliminates N_1 yielding

$$\frac{dN_2}{dt} = N_1^0 b_{12} - N_2(b_{12} + b_{21} + A_{21} + Q_{21}). \quad (3.29)$$

Subsequent integration results in the expression

$$N_2(t) = \frac{N_1^0 b_{12}}{r} + K e^{-rt} \quad (3.30)$$

after introducing r for convenience and readability.

$$r = b_{12} + b_{21} + A_{21} + Q_{21} \quad (3.31)$$

Prior to laser excitation, the population in the upper level is negligible [17] so that the integration constant K can be determined using the initial condition $N_2(t=0) = 0$.

$$N_2(t) = \frac{N_1^0 b_{12}}{r} (1 - e^{-rt}) \quad (3.32)$$

Equation 3.32 increases rapidly until it reaches a plateau when its exponential term approaches zero for $rt \gg 1$ and, thus, achieves an equilibrium for sufficiently intense and long laser pulses [17].

$$N_2(t) = \frac{N_1^0 b_{12}}{r} \quad (3.33)$$

Rearranging Eq. 3.33 after reinserting Eq. 3.31 for r gives

$$N_2 = N_1^0 \frac{b_{12}}{b_{12} + b_{21}} \frac{1}{1 + \frac{A_{21} + Q_{21}}{b_{12} + b_{21}}}. \quad (3.34)$$

Inserting Eq. 3.27 replaces the rate constants for absorption and stimulated emission.

$$N_2 = N_1^0 \frac{B_{12}}{B_{12} + B_{21}} \frac{1}{1 + \frac{A_{21} + Q_{21}}{B_{12} + B_{21}} \frac{C_\lambda}{I_{\text{laser}}}}. \quad (3.35)$$

With the saturation laser intensity defined according to Eckbreth [17] as

$$I_{\text{laser,sat}} = \frac{A_{21} + Q_{21}}{B_{12} + B_{21}} C_\lambda, \quad (3.36)$$

Eq. 3.35 can be rewritten as

$$N_2 = N_1^0 \frac{B_{12}}{B_{12} + B_{21}} \frac{1}{1 + \frac{I_{\text{laser,sat}}}{I_{\text{laser}}}}. \quad (3.37)$$

Since the fluorescence intensity S_{fl} is proportional to spontaneous emission rate constant A_{21} times the excited state population density N_2 , it follows that

$$S_{\text{fl}} \propto N_1^0 \frac{A_{21} B_{12}}{B_{12} + B_{21}} \frac{1}{1 + \frac{I_{\text{laser,sat}}}{I_{\text{laser}}}}. \quad (3.38)$$

In the non-saturated case, i.e., $I_{\text{laser}} \ll I_{\text{laser,sat}}$, a limit analysis of Eq. 3.38 shows that the fluorescence signal is proportional to the laser intensity.

$$S_{\text{fl}} \propto I_{\text{laser}} \quad (3.39)$$

Although the two-level model is a useful way to convey the basic idea behind linear LIF, the simplification does not fully represent the photophysics of typical organic tracers. In reality, additional electronic states and loss channels must be taken into account. Depending on the boundary conditions of the experiment, the onset of nonlinearities can already occur at low excitation energies. Photoionization and predissociation may need to be considered, and self-quenching may become an issue. The following section therefore focuses on describing the photophysics of organic tracers with a view to their use as fluorescent tracers in practical applications.

3.2.4 Laser-induced fluorescence in the gas phase

Following the absorption of the laser light, the subsequent fluorescence signal recorded by a detection system such as a camera can be described using Eq. 3.40 for weak unsaturated excitation energy I_{laser} .

$$S_{\text{fl}} \propto I_{\text{laser}} n_{\text{Tracer}} \sigma_{\text{abs}}(\lambda, T, p) \phi_{\text{fl}}(\lambda, T, p, p_{\text{q}}) \quad (3.40)$$

Its intensity S_{fl} is proportional to absorption cross section σ , and fluorescence quantum yield (FQY) ϕ_{fl} , which is defined as the ratio of emitted photons to the absorbed photons (Eq. 3.41). While the former depends on the excitation wavelength λ , temperature T , and pressure p , the latter is also influenced by the bath gas composition, represented by the partial pressure p_{q} of a species potentially quenching the fluorescence signal as described further down in this chapter.

$$\phi_{\text{fl}} = \frac{\text{Number of emitted photons}}{\text{Number of absorbed photons}} = f(\lambda, T, p, p_{\text{q}}) \quad (3.41)$$

In the simple two-level energy model discussed before in section 3.2.3, the FQY can also expressed as the ratio of the spontaneous emission rate constant to the total upper-level deactivation rate constants whereas the absorption cross-section is proportional to the absorption rate constant.

$$\phi_{\text{fl}} = \frac{A_{21}}{A_{21} + Q_{21}}, \quad \sigma_{\text{abs}} \propto B_{12} \quad (3.42)$$

Thus, from equations 3.38, 3.36, and 3.42, an expression for the LIF signal intensity for stronger excitation in the non-linear case can be derived analog to Eq. 3.40. From Eq. 3.43 it is now obvious that the definition for the saturation laser intensity (Eq. 3.36) by Eckbreth [17] is chosen so that $S_{\text{fl,sat}} = 0.5 S_{\text{fl}}$ for $I_{\text{laser}} = I_{\text{laser,sat}}$.

$$S_{\text{fl}} \propto \frac{I_{\text{laser}}}{\frac{I_{\text{laser}}}{I_{\text{laser,sat}}} + 1} n_{\text{Tracer}} \sigma_{\text{abs}}(\lambda, T, p) \phi_{\text{fl}}(\lambda, T, p, p_{\text{q}}) \quad (3.43)$$

This work deals only with linear LIF in the unsaturated case. However, the LIF signal is routinely checked for linearity by measuring the S_{fl} versus I_{laser} for the laser intensities used or expected in each experiment. This is also important because other effects such as self-quenching (see 3.2.4.1), which are not taken into account by the two-level model, can lead to nonlinear behavior even at excitation energies well below $I_{\text{laser,sat}}$.

3.2.4.1 Deactivation mechanisms

Especially for larger gas molecules at temperature and pressure conditions prevalent in many practical processes, the dependence of ϕ_{fl} on pressure, temperature, and gas composition is not trivial. Before excitation, the molecules are typically in thermal equilibrium with their

environment so that the vibrational energy level in the ground state S_0 corresponds to the thermal energy level as indicated in the Jabłoński diagram in Fig. 3.11 (pink line representing the average thermal energy). After excitation with laser light, the initial vibrational level in the excited S_1 state may be higher or lower than the thermal energy level depending on the laser energy (or wavelength, Eq. 3.44 with h being the Planck constant and c the vacuum light speed) and the vibrational energy in S_0 .

$$E_{\text{laser}} = \frac{hc}{\lambda} \quad (3.44)$$

Through collisions with bath gas molecules, the excited molecules subsequently relax toward thermal equilibrium, either extracting energy from or transferring energy to their environment. As they pass through several vibration levels, this process is called (external) vibrational relaxation (VR) and has an almost unity probability of energy transfer per collision [28]. It is, therefore, extremely fast for high density media or liquids [93] so that subsequent radiative deactivation of the excited molecules occurs almost exclusively from the thermalized ensemble. In lower-density gases, however, fluorescence and other deactivation processes act while VR is active so that light is emitted from transitions that originate from various vibrational levels along the relaxation cascade. Since the deactivation processes competing with fluorescence are energy-dependent and/or directly depend on the number of collisions, as described in the following sections, temperature, pressure, and gas composition have a strong influence on ϕ_{fl} .

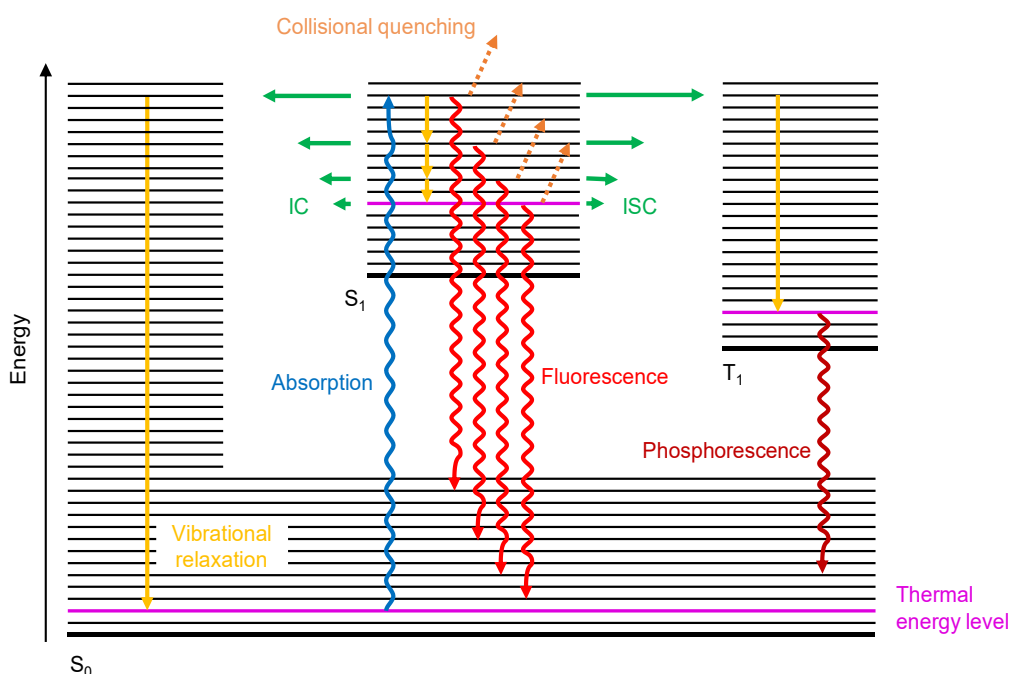


Fig. 3.11: Jabłoński diagram showing the different deactivation channels of an electronically excited molecules. Wiggly lines indicate radiative, straight lines non-radiative energy-transfer processes.

Deactivation mechanisms of the excited molecules can be subdivided into radiative and non-radiative processes. The structure reflects the way they affect the LIF measurement technique: Radiative processes provide the quantity that is measured, light. Non-radiative energy-transfer processes such as collisional quenching depend on the collider species and collision frequencies and thus on the one hand can complicate quantitative data interpretation but on the other hand can also provide additional information about these local conditions in the fluid. Unless stated otherwise, the following distinctions and considerations in this subsection are based on the elaborations of Schulz and Sick [28], and Sauer [94].

Radiative deactivation

Fluorescence (FL) is defined as the spontaneous emission of light during the transition of an excited molecule to the ground state. According to the Kasha rule, fluorescence only occurs between the lowest electronically excited state of each multiplicity (S_1 and T_1 for closed-shell organic molecules) as internal conversion (cf., Fig. 3.11) from higher excited states of the same multiplicity is typically three orders of magnitude faster than the spontaneous emission of light [93]. Fluorescence is spectrally distributed (cf. section 3.2.1) while the shape of emission spectra is also attributed of the environmental influence on the molecule's relaxation kinetics. For organic molecules, fluorescence typically occurs from $S_1 \rightarrow S_0$ on a time scale of around 10^{-9} to 10^{-7} s [28].

Phosphorescence (PH) is the spontaneous emission of a photon while relaxing from an excited state to the ground state involving a change in spin multiplicity (e.g., $T_1 \rightarrow S_0$). Since this process requires a spin change (Pauli-principle, cf. Fig. 3.6), it is quantum-mechanically forbidden and, thus, unlikely and slow in the order of 10^{-3} to 10^0 s [28]. Therefore, Fig. 3.11 shows the phosphorescence only occurring from the thermal energy level after the significantly faster vibrational relaxation in T_1 .

Non-radiative deactivation

Internal conversion (IC) is the spin-conserving non-radiative transition between two electronic states. As energy is conserved, the transition from an electronically higher state occurs to higher vibrational levels of the electronically lower state. IC acts on timescales around 10^{-12} to 10^{-6} s [93]. However, IC plays a fairly insignificant role for typical fluorescence tracers such as anisole and toluene because of their large energy gap between S_0 and S_1 . According to the energy gap law, there is less overlap of the vibrational wave functions with increasing energy difference reducing the transition probability [28]. At low vibrational excess energy in S_1 , which is the case for both tracers discussed in this work at low temperature after excitation with 266 nm as shown later (section 7.5), IC is almost negligible for aromatic tracers due to the small overlap of the wave functions in S_0 and S_1 . With excitation of higher vibrational energy levels (higher temperature or increased excitation energy), however, IC becomes more significant as the IC rate increases more steeply than the rate of intersystem crossing (see below) surpassing it at excess energies of around $\sim 10^4$ cm^{-1} [46].

Intersystem crossing (ISC) is the non-radiative transition between two electronic states of different multiplicity, e.g., $S_1 \rightarrow T_1$. During this transition, the total energy is preserved so that the molecule gains vibrational energy (cf., Jabłoński diagram in Fig. 3.11) for the aromatic tracers discussed in this work. Though ISC is symmetry-forbidden for typical aromatic tracers, it is still orders of magnitude faster than spontaneous emission [28] acting on a similar time scales around 10^{-12} to 10^{-6} s [94]. As IC is relatively insignificant at low temperature and small excess energy for the reasons being given above, ISC is the most significant decay channel for the tracers in question [46]. As discussed separately below, collisions with molecular oxygen can significantly promote ISC for benzene derivatives.

Intramolecular vibrational energy redistribution (IVR) describes the internal energy distribution within the fluorescing molecule to a large number of vibrational modes. With the high density of vibrational modes in large molecules such as the aromatics of interest for this work, IVR acts on a sub- 10^{-12} s timescale [93]. For non-near-vacuum environments, the much more efficient external VR through collisions with bath gas molecules dominates so that IVR is mostly neglected for practical applications. IVR significantly influences the shape of the fluorescence spectra in cases where few collisions happen during the fluorescence lifetime and, therefore, much of the detected signal originates from not yet collided excited molecules. This leads to a broadening of the emission spectra with decreasing fluorescence lifetime or decreasing collision frequency [99].

Collisional quenching

Different mechanisms can lead to deactivation or quenching of excited M^* molecules after close contact to or collision with a quenching molecule Q. The non-radiative electronic energy transfer can be much more efficient than the emission and subsequent absorption of a photon and occurs for certain tracer-quencher pairs, e.g., toluene and molecular oxygen with almost unity probability per collision [28]. The following paragraphs reproduce the basic principles of those mechanisms from the review paper of Schulz and Sick [28].

Dexter exchange describes the quenching of M^* by exchange of electrons with Q. Since it requires a spatial overlap of the orbitals of both species and, therefore, direct contact, it is also referred to as *short-range energy transfer*. This process is spin-allowed for the interaction of excited molecules in singlet (Fig. 3.12a) or triplet (Fig. 3.12b) state [28] with the singlet ground state quencher.

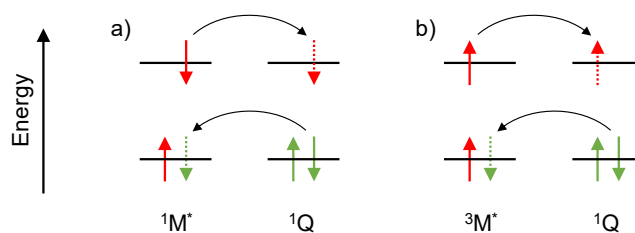


Fig. 3.12: The two spin-allowed pathways for the Dexter exchange for energy transfer from excited molecules M^* in a) singlet state and b) triplet state to a singlet ground state quencher molecule Q.

This leaves the quencher molecule in an excited singlet or triplet state, respectively, as shown in Eq. 3.45.

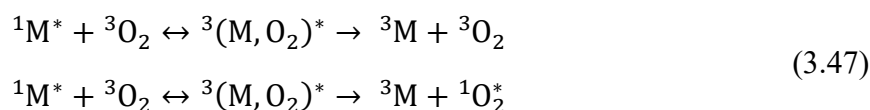


Förster resonance energy transfer (FRET) or *Coloumbic energy transfer* describes the non-radiative transfer from M^* to Q over long (several molecule diameters) distances. Here, the oscillating electric field from photo-induced dipole oscillation of M^* induces a dipole moment in Q . This requires a spectral overlap of the emission of donor M^* and absorption of the acceptor Q [28]. Since the efficiency of the dipole–dipole interaction strongly depends on the intermolecular distance, the effect is exploited for molecular rulers in, e.g., applications in biology [94]. Possible paths for the energy transfer are shown in Eq. 3.46 [28].



Quenching by molecular oxygen

Collisional quenching by molecular oxygen or, for short, *oxygen quenching*, is a special case of the Dexter short-range energy transfer [94]. Since the ground state of O_2 is a triplet state, it can facilitate the spin-forbidden intersystem crossing of organic molecules from $S_1 \rightarrow T_1$: After collision of the excited molecule with the ground state O_2 , a short-lived transition state in form of an exciplex ${}^3(M, O_2)^*$ [28] is formed. This exciplex decays as shown in Eq. 3.47 into triplet M and triplet (top) or singlet O_2 (bottom). The latter requires that the $S_1 \rightarrow T_1$ energy difference of M is larger than the energy required to excite O_2 to its singlet state [100]. This is the case, e.g., for aromatic hydrocarbons but not for ketones explaining the significantly more efficient oxygen quenching for aromatics [28].



However, literature on these mechanisms in the gas phase is sparse [4, 37, 46] and mostly phenomenological so far. Evidently, this process depends on the vibrational energy excitation energies. Koban et al. [37], e.g., found that for toluene the quenching effect was more pronounced at excitation with 248 nm compared to 266 nm. Similarly, a strong red shift of the fluorescence spectrum is noticeable at higher energies [37] which seems to diminish at lower excitation energy [3, 4, 80] though the excitation energy dependence has not been studied systematically yet.

Self-quenching

High tracer concentrations are often used for maximizing the LIF signal, sometimes only limited by the tracer vapor pressure. As collision rates of excited tracer molecules with other tracer molecules increase compared to bath gas molecules, energy transfer between tracer molecules, i.e., self-quenching (Eq. 3.48), becomes increasingly important.



Fuhrmann et al. [16] investigated it in detail for toluene. They found that the toluene fluorescence is subject to a strong self-quenching effect depending on the tracer concentration and laser fluence. While it was absent at low laser intensities and low tracer number density (small number of excited molecules), it became significant with increasing power and concentration (large number of excited molecules). Thus, they concluded that self-quenching only occurs between excited state tracer molecules and proposed the following process as the dominating quenching pathway (Eq. 3.49).



They could not establish the multiplicity n of the colliding molecules and the state of the remnant M which were left open for further study. Since the quenching cross section was 50 times smaller than the one of molecular oxygen, this effect is deemed negligible in oxygen containing bath gases.

3.2.4.2 Deactivation kinetics

For analyzing the deactivation kinetics, it is useful to introduce rate constants k for each competing deactivation channel. Here is $[M^*]$ the concentration of excited molecules.

$$-\frac{d}{dt}[M^*] = k[M^*] \quad (3.50)$$

The first-order solution of this differential equation yields the following equation where the index 0 indicates the initial concentration of excited molecules. The natural lifetime τ of the excited state, i.e., the time until the signal is decayed to e^{-1} of the initial signal, is, therefore, the reciprocal of k .

$$\frac{[M^*]}{[M^*]_0} = e^{-kt}, \quad \tau = \frac{1}{k} \quad (3.51)$$

The fluorescence quantum yield (Eq. 3.41) can also be expressed as the ratio (Eq. 3.52) of the fluorescence rate constant compared to the total rate constant k_{tot} from all relevant deactivation channels combined. Here k_{fl} is the radiative deactivation rate, and k_{ISC} and k_{IC} the non-radiative deactivation rates for intersystem crossing and internal conversion, respectively. The rate

constant of a quenching species k_q depends on the concentration (or partial pressure p_q) of the quenching species and is therefore written as the product of the rate coefficient \tilde{k}_q and p_q .

$$\phi_{fl} = \frac{k_{fl}}{k_{tot} + k_q} = \frac{k_{fl}}{k_{fl} + k_{ISC} + k_{IC} + \sum \tilde{k}_q p_q} = \frac{\tau_{eff}}{\tau_{fl}} \propto \tau_{eff} \quad (3.52)$$

With Eq. 3.52, the ratio of the rate constants can be also expressed as the ratio of the excited state lifetime τ_{fl} and effective lifetime τ_{eff} . Contrary to τ_{fl} , τ_{eff} can be measured directly from the decay curve of the fluorescence signal since it corresponds to the loss rate of the total excited population.

The Stern-Volmer equation (Eq. 3.53) describes the relationship between the fluorescence quantum yield and the concentration of a quenching species. Since the quenching rate is difficult to measure directly, the Stern-Volmer factor k_{SV} is introduced as the ratio of the quenching rate coefficient \tilde{k}_q and the total deactivation rate k_{tot} .

$$\frac{\phi_{fl,0}}{\phi_{fl}} = \frac{\tau_{eff,0}}{\tau_{eff}} = 1 + \frac{k_q}{k_{tot}} = 1 + \frac{\tilde{k}_q}{k_{tot}} p_q = 1 + k_{SV} p_q \quad (3.53)$$

The Stern-Volmer factor is the slope of the normalized quantum yield (index 0 means that no quencher is present) plotted against the tracer concentration in the so-called Stern-Volmer plot shown in Fig. 3.13. It can therefore be easily determined experimentally by measuring the fluorescence intensity (or lifetime, cf. Eq. 3.52) for various quencher concentrations or partial pressures. The Stern-Volmer factor is usually temperature dependent, decreasing by an order of magnitude between 300 and 700 K for toluene at 266 nm excitation, for example [28].

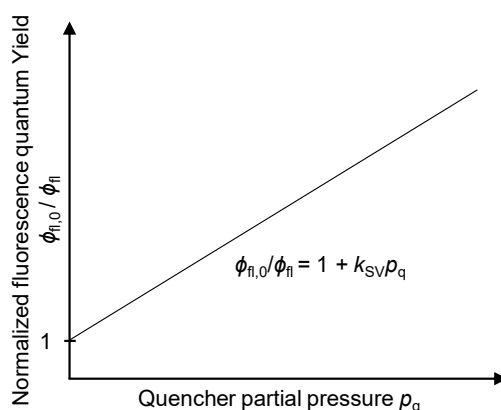


Fig. 3.13: Graphical representation of the Stern-Volmer coefficient as the slope of the normalized fluorescence signal intensity over the quencher partial pressure.

Summary

For both tracers studied in this work, toluene and anisole, collisional quenching is by far the dominant deactivation mechanism if molecular oxygen is present. It dramatically increases ISC by facilitating the otherwise spin-forbidden transition from the first excited to a triplet state

$S_1 \rightarrow T_n$ (of spin multiplicity n) with almost unity probability upon collision. Without oxygen, ISC is still the most efficient non-radiative deactivation channel being orders of magnitude faster than the rates of spontaneous emission [28]. On the other hand, IC is much less relevant due to the large energy gap from $S_1 \rightarrow S_0$ compared to $S_1 \rightarrow T_1$ under the conditions that result in low excess energy in S_1 , which is the case at temperatures below room temperature and the excitation wavelengths used in this work.

Table 3.1 summarizes the competing deactivation processes mentioned in this chapter, the underlying transitions, and their typical time scale in form of deactivation rate constants for diluted gaseous aromatics.

Table 3.1: Deactivation processes relevant for electronically excited aromatics and their time scales for gaseous states.

Classification	Process	Abbr.	Transition	Timescale / s
Radiative	Fluorescence	FL	$S_1 \rightarrow S_0$	10^{-9} – 10^{-7} [28]
	Phosphorescence	PH	$T_1 \rightarrow S_0$	10^{-3} – 10^0 [28]
Non-radiative, internal [94]	Internal conversion	IC	$S_1 \rightarrow S_0$	10^{-12} – 10^{-6} [94]
	Intersystem crossing	ISC	$S_1 \rightarrow T_1$	10^{-12} – 10^{-6} [94]
	Intramolecular vibrational redistribution	IVR	$S_1 \rightarrow S_1$	$< 10^{-12}$ [94]
Non-radiative, external	Vibrational relaxation	VR	$S_1 \rightarrow S_1$	Collision rate driven e.g., 10^{-10} – 10^{-8}
	Collisional O ₂ quenching	-	$S_1 \rightarrow T_n$	(cf., chapter 7.5)

4 Experimental methods

This chapter explains the measurement strategies either used or considered in this work and the experiments they were applied to focusing on LIF imaging techniques. It also briefly presents the schlieren imaging method which was utilized to study density gradients in the investigated supersonic flow fields. The experiments in mixing flows to which these techniques have been applied to are briefly presented.

4.1 Quantitative LIF

As explained in the introduction (chapters 1 and 2), tracer LIF can be used in a variety of ways to measure intrinsic and extrinsic quantities of gases influencing the absorption or emission properties of the fluorescing species such as gas composition, temperature, pressure, and even flow velocity. Since the LIF signal is affected to some degree by all these parameters, measurement strategies must be tailored specifically to the problem at hand to isolate the influence of the variables of interest and eliminate or compensate for cross dependencies.

For example, a temperature increase typically decreases the fluorescence quantum yield and thus the fluorescence lifetime (Fig. 4.8b), shifts the fluorescence spectrum towards longer wavelengths, increases the absorption cross-section, and broadens fluorescence and absorption spectra. Similarly, collisional quenching by oxygen also reduces the fluorescence quantum yield and lifetime, and can, depending on the excess energy after excitation, also cause a spectral red-shift and broadening (Fig. 4.8a).

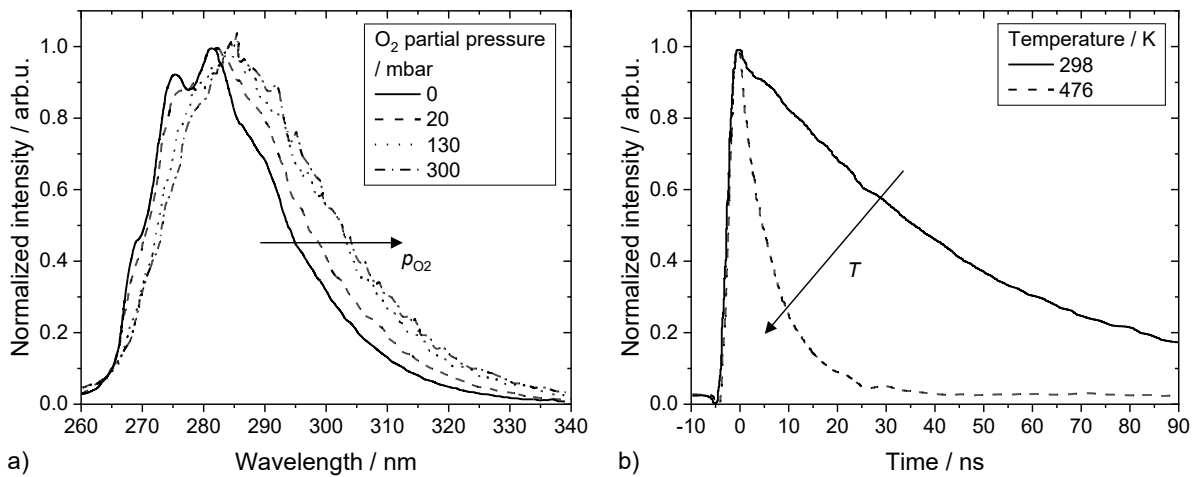


Fig. 4.1: a) Normalized toluene-LIF spectra after excitation at 248 nm showing a shift of the spectral centroid towards longer wavelengths with increasing O₂ partial pressure in N₂ at a total pressure 1 bar at room temperature. Reproduced from Koban et al. [38]. b) Time trace of the normalized spectrally integrated toluene-LIF signal after ps-excitation at 266 nm showing a reduction of fluorescence lifetime with increasing Temperature partial pressure in CO₂ at a pressure 1 bar. Reproduced from Benzler et al. [48].

Additionally, the efficiency and sensitivity of the detection system must be accounted for when applying LIF to real-world problems. To this end, the equation for the LIF signal presented in section 3.2 (cf., Eq. 3.40) can be rewritten as follows. Here, Ω stands for the detection solid angle, η_e for the detector quantum efficiency, ε for the light collecting optics transmission

efficiency, and V_m for the effective probe volume. For quantitative measurements, these parameters must be determined by calibration of the equipment or can be eliminated by suitable measurement strategies such as the ratiometric (sections 4.1.3 and 4.1.4) or temporal (section 4.1.5) schemes.

$$S_{\text{fl}}(\lambda, T, p, p_{\text{O}_2}) = \Omega \eta_e \varepsilon I_{\text{laser}} V_m n_{\text{Tracer}} \sigma(\lambda, T, p) \phi_{\text{fl}}(\lambda, T, p, p_{\text{O}_2}) \quad (4.1)$$

The experimentally accessible properties of the LIF signal, i.e., its intensity, its spectral shape, and its decay rate can be detected using various measurement strategies. The spectrally- and spatially-integrated LIF signal is relatively straightforward to measure using sensors with broadband spectral response and slow response time, such as large photodiodes or charge-coupled devices (CCDs). The spectral shape, i.e., the LIF intensity as a function of the wavelength, can be determined using, e.g., monochromators or multiple sensors with different spectral sensitivities (e.g., through optical filters). The decay rate of the fluorescence signal can be measured using fast detectors such as photomultipliers or precise timing of the data acquisition.

The underlying research question of each particular application places further demands on the measurement strategy. For example, high time resolution is often required for highly transient processes, such as turbulent mixing layers. Spatial resolution (imaging) may be required, e.g., to monitor flame fronts in steady or unsteady combustion processes. Investigations of short-lived phenomena may also require high repetitions rates to track, e.g., droplet breakdown and evaporation during fuel injection in internal combustion engines.

Since the fluorescence lifetime is typically on the order of nanoseconds, single-shot LIF measurements are quasi-instantaneous for most engineering applications. This does not apply to measurement strategies that require multiple laser pulses, such as measurements in which the absorption spectrum is probed by scanning the laser wavelength or where spatial resolution is achieved by scanning the laser over a measurement volume (e.g., confocal fluorescence microscopy).

This chapter describes and compares the measurement strategies that can be used to determine the respective variables of interest, such as temperature T , pressure p , tracer number density n_{tracer} , and oxygen partial pressure p_{O_2} . Since many of the named strategies can be used to determine different parameters which influence the LIF signal in similar manner, the generic independent variable of interest γ is introduced for the sake of argument.

$$\gamma = \begin{cases} T \\ p \\ n_{\text{tracer}} \\ p_{\text{O}_2} \end{cases} \quad (4.2)$$

4.1.1 LIF Imaging

To achieve spatial resolution, either the exciting laser beam can be scanned along the measurement volume, or the complete measurement volume can be illuminated at once while the spatial resolution is achieved using camera sensors which is also referred to as LIF imaging. The basic principle LIF imaging for measurements in gases in, e.g., combustion applications, has been introduced to in the early 1980s [101] and the basic principle has remained mostly unchanged (Fig. 4.2): A thin sheet of light is formed from a laser beam and used to excite fluorescing species in quasi-2D measurement volume. The fluorescing species are either formed in situ by chemical reactions or added as fluorescence tracers. A camera positioned perpendicular to the light sheet than captures the LIF signal and provides the two-dimensional spatial resolution.

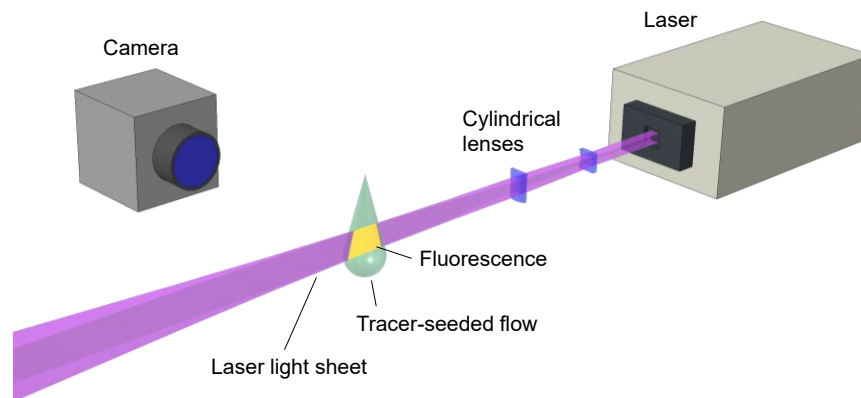


Fig. 4.2: Basic experimental setup for laser-induced fluorescence (LIF) imaging.

Typically, imaging methods require spatial calibration, i.e., mapping of the acquired image to real world coordinates. This is achieved by using calibration targets placed in the region of interest. Reference points on the target are then used with algorithms for scaling the image following corrections for image distortion by dewarping, shifting, and rotating. For measurements in the ultraviolet region, typically image intensifiers are used. Besides extending the sensitivity of the camera system to shorter wavelengths, they also provide more authority over the acquisition timing since they can be gated more quickly. This, on one hand, allows for additional measurement schemes and, on the other hand, allows short exposure times to discriminate against background signal.

4.1.2 Spectrally and temporally integrated measurements

As mentioned in the introduction of this chapter, measurement of the spectrally and temporally integrated LIF signal is the most straight forward measurement scheme but requires calibration for the detection system efficiency. This can be achieved by careful characterization of the measurement equipment and consideration of the geometric arrangement. In practice, however, a so-called flat-field corrections are often performed instead. In the context of LIF, this is typically achieved by dividing each measured image S by a flat-field image FF recorded at controlled conditions, i.e., known uniform tracer concentration, temperature, pressure, and bath-gas composition (Eq. 4.3). Prior to that, the background (BG), which corresponds to any signal

not originating from the tracer fluorescence including scattered laser light, is subtracted. The background is ideally recorded at the same conditions as the flat fields just without any tracer present. Both, background and flat-field images are usually averaged over several shots to increase signal-to-noise ratio (angle brackets indicating ensemble averages in Eq. 4.3).

$$S_{\text{FF}} = \frac{S - \langle \text{BG} \rangle}{\langle \text{FF} \rangle - \langle \text{BG} \rangle} \quad (4.3)$$

The flat-field correction achieves three things: First, it compensates for inhomogeneities of the laser light sheet intensity and the illuminated volume (I_{Laser} and V_m cancel, cf. Eq. 4.1). Secondly, it corrects for variations in detection efficiency (Ω , η_e , and ε cancel, cf. Eq. 4.1). Thirdly, it can provide a calibration for quantitative measurements by normalizing σ and ϕ_{fl} to their respective level at the flat-field conditions. For example, the local tracer concentration can be easily derived if the flat-field images were taken at a known concentration as long as the signal depends linearly on the tracer number density. This is often the case for isothermal and isobaric conditions with otherwise constant bath gas composition.

4.1.3 Single-color excitation and two-color detection schemes

Often, it is desired to perform quantitative measurements of, e.g., temperature, pressure, or a quencher concentration (i.e., the independent variable γ introduced in Eq. 4.2), independent of the local tracer number density. This is the case when a homogeneous tracer concentration cannot be achieved or the tracer concentration itself is an additional variable to be measured. If the spectral shape of the LIF signal is influenced by γ , the latter can be determined from spectrally resolved measurements. In the context of LIF imaging, this can be achieved by a ratiometric approach: To extract the spectral information, two cameras imaging the same measurement volume illuminated by the laser light sheet (Exc) are equipped with individual spectral filters (bandpass BP and longpass LP) that enable a detection of separate portions of the fluorescence emission spectra as shown in Fig. 4.3a.

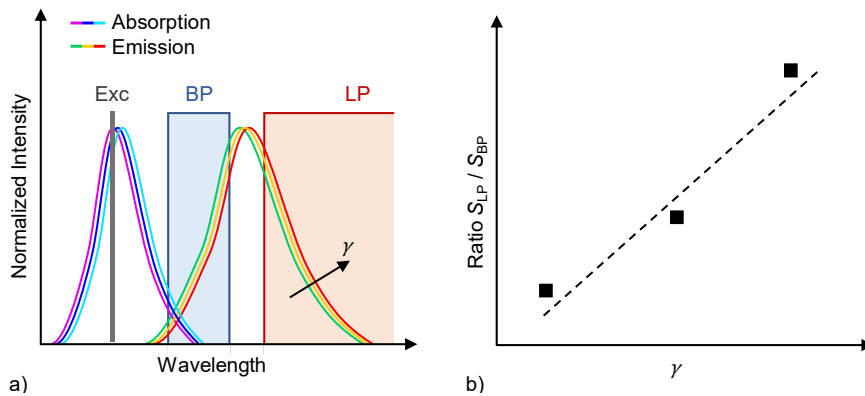


Fig. 4.3: Single-color excitation and two-color detection scheme used to measure the independent variable γ from the change it inflicts on the emission spectrum (a) by relating it to the ratio (b) of two detection channels.

The ratio of both spectrally integrated signals S_{BP} and S_{LP} depends directly on γ as shown in Fig. 4.3b. In this case, the local tracer concentration and laser fluence in Eq. 4.4 cancel out.

$$\frac{S_{LP}}{S_{BP}} = \frac{\Omega_{LP}\eta_{e,LP}\varepsilon_{LP}\phi_{LP}(\gamma)}{\Omega_{BP}\eta_{e,BP}\varepsilon_{BP}\phi_{BP}(\gamma)} = \zeta_{\text{det}} \frac{\phi_{LP}(\gamma)}{\phi_{BP}(\gamma)} \quad (4.4)$$

The different efficiencies of both detection channels can be expressed as a single parameter ζ_{det} . This parameter can be established using a less involved single-point calibration. These ratiometric approaches have been used to image temperature [22] and oxygen partial pressure [30] in the past. Based on the available spectroscopic data [49], also pressure sensing seems feasible. The disadvantage of the ratio methods compared to single-shot measurements is that the signal-to-noise ratio is usually lower because only parts of the spectrum are detected. The uncertainty increases further due to error propagation when two noisy signals are divided by each other. In addition, the sensitivity is lower because the spectral change is usually weaker than the total change in signal intensity, so multiple acquisitions must often be averaged to achieve reasonable confidence. Further, exact spatial calibration (mapping) of both detection channels is required which sometimes is a significant challenge [80].

4.1.4 Two-color excitation and single-color detection schemes

A different ratiometric approach uses two different lasers and a single detector capturing two consecutive images from fluorescence from two different excitation wavelengths (Exc1, Exc2) as shown in Fig. 4.4. This technique exploits the dependence of the absorption spectrum on the variable of interest γ . As it uses only a single camera, the detection side variables cancel out during ratioing while, analogously to the two-color detection scheme, a single parameter ζ_{ex} can be calibrated to account for the two lasers different intensities.

$$\begin{aligned} \frac{S_{\text{Exc1}}}{S_{\text{Exc2}}} &= \frac{I_{\text{Exc1}} V_{\text{m,Exc1}} \sigma(\lambda_{\text{Exc1}}, \gamma) \phi(\lambda_{\text{Exc1}}, \gamma)}{I_{\text{Exc2}} V_{\text{m,Exc2}} \sigma(\lambda_{\text{Exc2}}, \gamma) \phi(\lambda_{\text{Exc2}}, \gamma)} \\ &= \zeta_{\text{ex}} \frac{V_{\text{m,Exc1}} \sigma(\lambda_{\text{Exc1}}, \gamma) \phi(\lambda_{\text{Exc1}}, \gamma)}{V_{\text{m,Exc2}} \sigma(\lambda_{\text{Exc2}}, \gamma) \phi(\lambda_{\text{Exc2}}, \gamma)} \end{aligned} \quad (4.5)$$

Since a time delay is used to separate both frames, this method is strictly-spoken not instantaneous. However, the employment of, e.g., double-frame detection or the use of two cameras still allows for a high time resolution in the sub-microsecond region [102]. This technique has proven to provide high sensitivity for measuring temperature using ketones [102, 103] and aromatics [104] as tracers. As an additional challenge compared to the method described before, a careful alignment of both laser sheets is crucial to avoid any error stemming from non-overlapping measurement volumes V_{m} . Temporal variations in laser energy and laser-sheet inhomogeneity further reduce the precision of this technique and must be accounted for.

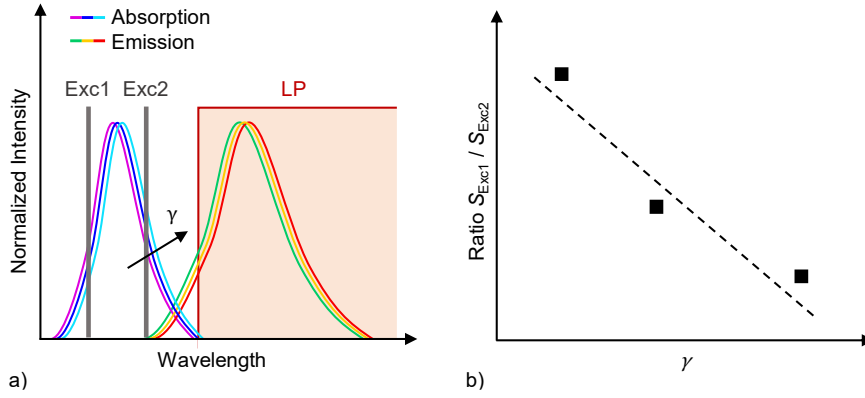


Fig. 4.4: a) Two-color excitation and single-color detection scheme for measuring a quantity of interest γ from the change it inflicts on the shape of the absorption spectrum by relating it on the b) ratio of two subsequent captured LIF signals excited from two different laser wavelengths.

4.1.5 Temporal measurement schemes

The independent variable of interest γ can be determined from the fluorescence decay curve provided its dependence on the fluorescence lifetime is known as illustrated in Fig. 4.5a. As described in section 3.2.4, the effective fluorescence lifetime is proportional to the fluorescence quantum yield. Unlike the FQY, it can be determined independently of the local concentration and the detection system efficiency making it an attractive technique for situations where calibration of the detection system is difficult to achieve. The fluorescence decay curve can be measured directly using fast detectors such as photomultipliers or using time-correlated single-photon counting (TCSPC). The latter, which is explained in detail later in section 7.4.1, is a technique that typically uses a high-repetition short-pulsed laser. Instead of measuring the resulting signal as a function of time, the time until the first photon arrives at the detector is logged. The time trace is then reconstructed from the histogram of the arrival times with respect to the laser pulses. This technique offers an extremely high sensitivity even at low laser fluences or tracer concentrations making it ideal for measurements in supersonic flows where concentrations are severely limited by the tracer vapor pressure. The downside of this approach is that for reconstructing the decay curve sufficient photon events are required so that multiple (at least on the order of thousands to millions) laser pulses are required so that this method cannot be considered instantaneous.

The effective fluorescence lifetime τ_{eff} can be interpreted as the point in time at which the signal has reached $1/e$ (Fig. 4.5a) of its original value assuming sufficiently short laser pulse and a mono-exponential decay (cf., Eq. 3.52). In practical applications, however, the response of the detector and the laser pulse width must be considered. This is often done by modeling the fluorescence signal using a convolution of the instrument response function (IRF) and an exponential decay. The IRF is often the time trace of the laser pulse measured with the same detector, e.g., from laser scattered light. The lifetime is τ_{eff} then determined from a least-squares fit of the model function to the experimental data. This procedure is explained in detail in section 7.4.1.

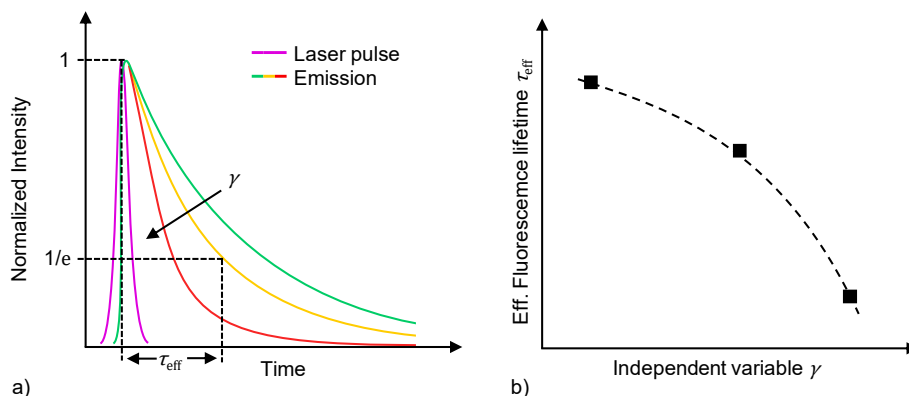


Fig. 4.5 a) Laser pulse and fluorescence signal time traces showing a b) decreasing fluorescence lifetime with increasing independent variable γ .

For both, the direct measurement of the decay curve and TCSPC, scanning of the laser beam can be used to achieve spatial resolution, which is also an established approach for, e.g., confocal microscopy. Though kinetic cameras [105] and, for certain wavelengths, high-resolution sensors exist [106], ratiometric approaches using fast gated imaging have been proven in the past for measurements in the UV range [31, 107]. The latter capture two successive frames with a certain delay during the fluorescence lifetime. From the ratio of both images the lifetime and, consequently, the variable of interest can be calculated as shown in Fig. 4.6.

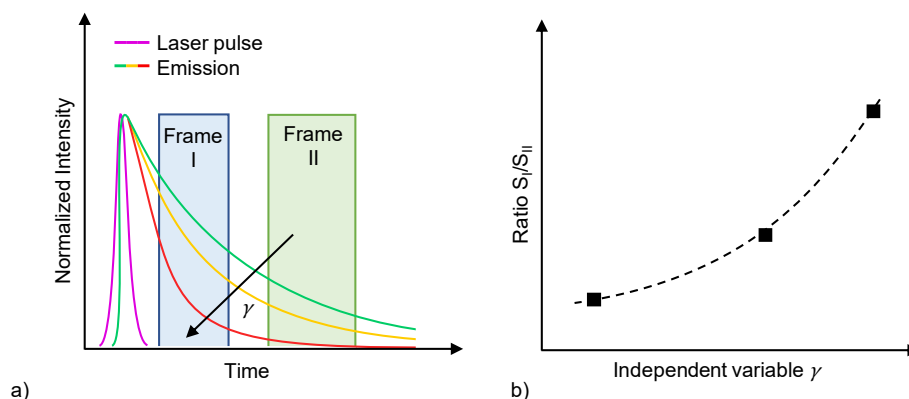


Fig. 4.6: a) Laser pulse and different fluorescence signal time traces showing the gate times of two camera frames, I and II. The ratio of both frames depends on the fluorescence lifetime and, therefore, shows b) an increase with increasing independent variable γ as the fluorescence lifetime decreases.

4.1.6 Other strategies

Multiline excitation and broadband detection

Multiline-excitation schemes use tunable lasers to excite different discrete transitions of smaller molecules. The wavelength-dependent measured fluorescence intensity is then fitted to simulated transition line spectra to determine the temperature. Therefore, this technique is calibration free, invariant to local concentration variation (stationary behavior assumed), and independent of excitation energy inhomogeneities and detection efficiency. It provides high signal-to-noise ratio even at low tracer concentrations and has been demonstrated for NO [108, 109] and SiO [110]. The downside of this technique is the low time resolution due to the slow

wavelength scanning and is therefore limited to stationary processes. Further, the requirement to be able to simulate the spectra limits the technique to diatomic molecules so far.

Multiple tracer and mixed schemes

Measurement schemes that use multiple tracers with distinct properties enable measurements with high sensitivity and/or measure multiple flow properties simultaneously. For example, NO was used together with acetone to indirectly determine the mixing ratio at the molecular level via oxygen quenching [75]. While the NO signal is strongly quenched by oxygen, the acetone signal is almost unaffected providing the local macroscopic concentration. From the ratio of both, the mixing state on molecular level could be derived. However, this required the use of two lasers and two cameras, since absorption and emission spectra of both substances are far apart, resulting in a relatively large experimental effort. This was later simplified considerably by using toluene instead, which is sensitive to oxygen present as an aromatic, and 3-pentanone as an oxygen insensitive component [29, 32]. In that case, the absorption spectra overlap while the emission spectra are still easily separable, thus, only one laser was necessary. Another approach used two tracers, a single-color excitation three-color detection scheme to measure temperature and oxygen concentration simultaneously [111]. Naphthalene and toluene were used as tracers and excited by one laser. There were three detection channels, one of which had a bandpass filter at the emission maximum of toluene, whereas the pass bands of the other two channels were on the longer wavelength emission spectrum of naphthalene. From the ratio of the latter, the temperature was determined using the spectral temperature dependence of the naphthalene. From the ratio of the toluene signal to the naphthalene signal, the local oxygen concentration was then determined exploiting the different oxygen sensitivity of the two tracers.

Multiple-tracer techniques provide means to measure multiple variables in complex flow fields. However, these schemes often require an increased experimental effort and sophisticated calibration. Further, they may suffer from radiative (absorption) and non-radiative (collisional) tracer-tracer interaction, which is not yet fully understood and, therefore, subject to ongoing research.

4.2 Schlieren imaging

In the scope this work, schlieren imaging has been applied to measure density gradients caused by oblique or normal shocks and, by some extension, of weaker flow structures in a subsonic injector wake flow [59, 60, 78, 79]. This method is well-established to verify desired flow conditions in flow channel experiments by visualizing density gradients. This method only works in a line-of-sight integrated manner, which is a lesser problem for the flow channels discussed in this work, since their width in the direction of measurement remains constant. It, therefore, allows, e.g., to image the almost two-dimensional shock patterns (cf., Fig. 2.2a) and rolling vortices (cf., Fig. 2.2a) encountered during the mixing investigations.

Schlieren are defined as spatial gradients of refractive index n in transparent media. For gases, n is linearly dependent on the local density ρ as expressed by the Gladstone–Dale relation with the Gladstone–Dale coefficient k_{GD} is approximately $0.23 \text{ m}^3/\text{kg}$ for visible wavelengths in air at standard conditions [112].

$$n - 1 = k_{GD}\rho \quad (4.6)$$

This dependence can be used to indirectly detect density gradients by measuring the deflection of light passing through the measurement volume. Practical approaches are focused (i.e., collimated [112]) shadowgraphy and schlieren imaging. The former is the slightly more direct approach: Parallel light is projected through the measurement volume onto a screen. Dark spots (hence the name) indicate non-uniform perpendicular density gradients along the line of sight as light is deflected. Schlieren imaging, on the other hand, applies additional spatial filtering: After passing the probe volume the collimated light is focused onto a knife edge or pinhole before arriving at the screen or detector (Fig. 4.7).

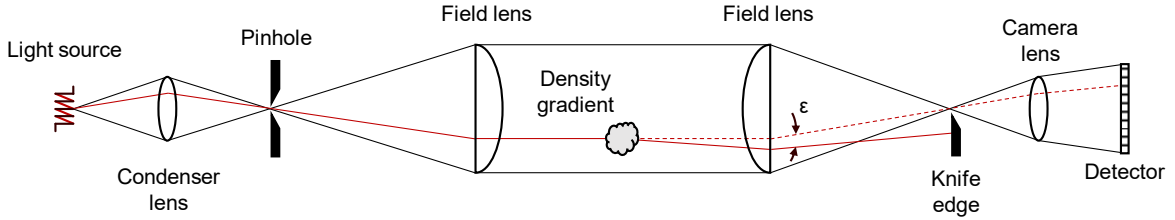


Fig. 4.7: Typical dual-field-lens schlieren setup for visualizing density gradients in one spatial direction.

Whereas the signal strength for focused shadowgraphy is proportional to the second derivative of the refractive index, schlieren imaging is more sensitive as its beam deflection angle ϵ (and, thus, contrast) depends on its first spatial derivative [112] where x_i stands for the coordinate perpendicular to the knife edge orientation.

$$E_{x_i} \propto \frac{dn}{dx_i} \propto \frac{d\rho}{dx_i} \quad (4.7)$$

While quantitative interpretation of the recorded schlieren image (e.g., the calculation of a density field) is possible provided a precisely adjusted and well characterized optical arrangement, it is nearly infeasible for the non-perfectly two-dimensional phenomena observed in this work. However, it allows us to determine shock front positions accurately and, thus, provides valuable insight into the prevalent flow conditions.

4.3 Flow experiments

Overall, three different flow experiments were used in this work. Their individual purposes are briefly outlined in this section to provide guidance for the following chapters.

4.3.1 Full-scale modular flow channel

The rectangular cross-section modular flow channel located at the ITLR at the University of Stuttgart serves as a universal test bed to study accelerating flows and wake flows on the scale of up to by allowing installation of different injector bodies (also used for the injection of tracers or precursors or fuel surrogates, hence the name) in the nozzle section of the duct. In the context of this work, it was used for the studies described in chapters 5 and 6. The general setup of the flow channel is described in detail in the dissertation by Judith Richter [2], who designed, tested, and characterized it for a $M = 1.7$ nozzle. Briefly, the experiment section consists of four modules: An inlet section, a nozzle module containing the converging-diverging nozzle, a longer test section, and an outlet diffuser. The nozzle module and the test section provide optical access on four sides allowing application various optical measurement techniques such as shadowgraphy [79] and schlieren imaging [59, 60], particle image velocimetry (PIV) [2], laser-induced thermal acoustics (LITA) [82], and laser-induced fluorescence [59, 78, 80]. Also, the vortex shedding frequency at the injector trailing edge was measured by beam steering [79].

Historically, these experiments succeed those carried out in a flow channel used by Chun [61] and Wohler [66]. The major difference is its name-giving modularity that enables the realization of multiple configurations such as nozzles with different design Mach numbers and slanted test section top and bottom walls, which has proven useful to study the influence of and/or compensate for pressure gradients in the far-field of the wake as discussed in chapter 5.

The hot gas facilities used are mostly identical (Fig. 4.8) and were described by Chun [61]: A screw compressor flows up to 1.45 kg/s air through multiple heater stages (1 MW) after stripping it from atmospheric water in an air dryer (< 0.1 % residual relative humidity). An auxiliary air supply stores approximately 8 m³ air at 100 bar in four gas cylinders to ensure a safe shut down in the unlikely case of a compressor or power failure [66].

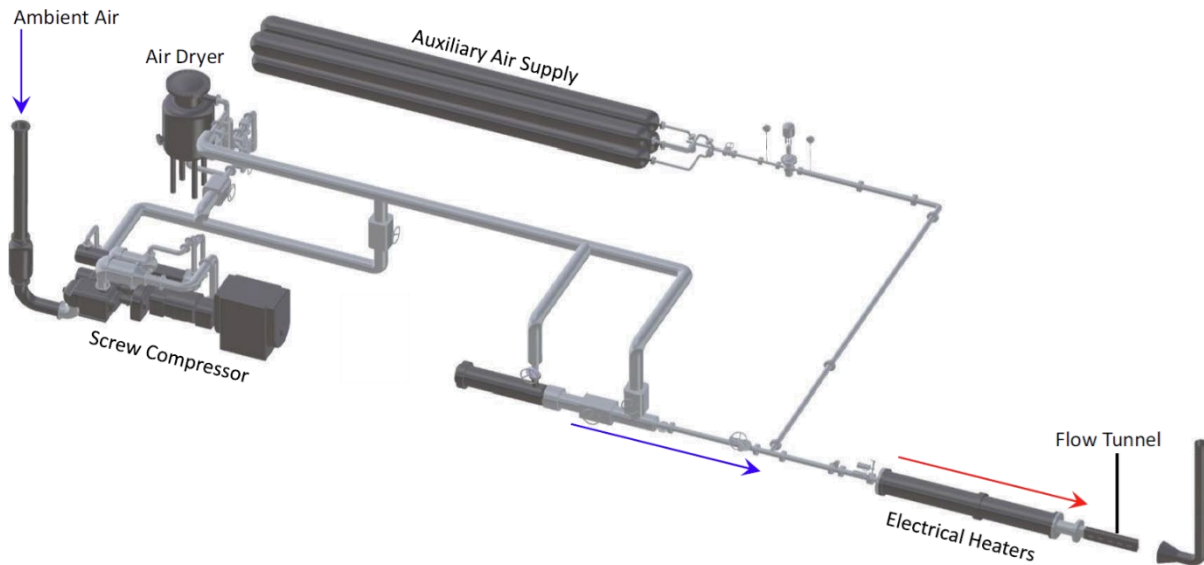


Fig. 4.8 Flow facility of the Stuttgart flow channel [78].

Despite the excellent and proven suitability of the overall system for the investigation of wake flows, it has its limitations. Firstly, the operation of the facility is costly because of the energy and manpower requirements. Secondly, the development of measurement techniques that are sensitive to oxygen requires a specific variation of the oxygen concentration, which is not possible in a system operated with air. Therefore, the two additional experiments described below were developed.

4.3.2 Cooled flow cell

The flow cell described in Chapter 7 was built on the one hand to extend of the application range of the tracer substances towards lower temperatures. Furthermore, it serves as a calibration tool for the lifetime based LIF thermometry, which was used to characterize the miniature channel (chapter 8). In this context, the cell bridges the temperature range between the highest temperature achievable in the miniature channel (and room temperature, where abundant literature data are available. In addition, it was used to estimate the temperature effect on the oxygen quenching of the toluene signal (chapter 6) before this relationship could be investigated in detail using the miniature flow channel.

4.3.3 Miniature supersonic flow channel

Chapter 8 is devoted to experiments in a miniature flow channel. It serves two purposes: Firstly, it provides conditions similar to those in the Stuttgart channel, but the total mass flow is low enough so that operation with pure nitrogen is also possible in a bench-top experiment. Thus, it allows the characterization of fluorescence tracers with respect to their sensitivity to oxygen at the relevant low temperatures and pressures. Furthermore, due to its rectangular cross-section and four-sided optical access to the measuring section, it offers the possibility to test various optical measuring methods.

5 Macroscopic mixing

The content of this chapter was published at the Aviation forum of the 2018 Fluid Dynamics Conference of the American Institute of Aeronautics and Astronautics [59] as follows.

Beuting, M., Richter, J., Weigand, B., and Schulz, C., *Experimental investigation of the influence of the pressure gradient on the transonic mixing behavior in blunt-body wakes using tracer LIF*, 2018 Fluid Dynamics Conference, Atlanta, GA, USA, 2018, 3543, doi: 10.2514/6.2018-3543

© 2018 American Institute of Aeronautics and Astronautics.

My personal contribution was the conduct and evaluation of the LIF and schlieren measurements as well as the preparation of the manuscript. The measurements have been done during a joined measurement campaign in the labs of the ITLR in Stuttgart under supervision of Prof. Bernhard Weigand. The test hardware was designed, tested, and characterized by Judith Richter [60] who also provided the figures containing the drawings and parts of the text. Prof. Christof Schulz, Prof. Bernhard Weigand., and Prof. Thomas Dreier provided scientific guidance and support during the experiments and write-up. All authors mentioned contributed to the manuscript by helping with the interpretation of the results, with the wording, and by proof-reading.

Abstract: Toluene laser induced-fluorescence (LIF) has been used to study the effect of a stream-wise pressure gradient on the mixing behavior in the transonic wake of two different types of central injectors feeding a low momentum flow into an accelerating co-flow. For this purpose, an optically-accessible, modular flow channel with a rectangular cross-section has been utilized: Following a nozzle module comprising a $M = 1.7$ convergent–divergent nozzle and the injector assembly, three interchangeable test modules imposing a pressure gradient by featuring different opening angles (0° , 0.25° , and 1.25°) can be attached. The two injectors investigated distinguish by the extent of their trailing edge into the sub- and supersonic region of the nozzle flow. It was found that the self-similarity of the mixing layer is preserved in all cases independent of the imposed pressure gradient. Calculated growth rates of the mixing layer agreed well with the half-power law.

5.1 Introduction

Mixing processes of two or more gas-phase components have been in the interest of many researchers throughout the last decades. One of the various geometries of practical interest is a central injector through which a gas is injected into a gaseous co-flow. The wake flows caused in this arrangement have been subject of many publications. However, in most of these works either incompressible or supersonic wake flows were investigated, while only little research has been done on mixing under transonic conditions. This paper aims at closing this knowledge gap by providing a profound data set from experimental and numerical investigations. Previous studies in our labs suggest that the growth of the mixing layer is self-similar for different types of central injectors at a wide range of co-flow conditions [61, 64, 78]. For the most recent

experiments [78-80, 82], a modular sub- to supersonic flow channel including a convergent–divergent nozzle was built to explore the limits of self-similarity under controlled co flow conditions. This paper focuses on the influence of the stream-wise pressure gradient downstream of the nozzle exit on mixing processes in the wake of two different central injectors. The results discussed were experimentally obtained using tracer-based laser-induced fluorescence imaging (tracer LIF).

5.2 Wake flow characteristics

Two different injector types were investigated that differ only by the extent of their trailing edges, such that the injector trailing edge is either located 42.1 mm upstream (injector A, Fig. 5.4a) or 10 mm downstream (injector B, Fig. 5.4b) of the nozzle throat (Fig. 5.3). The resulting mixing layer is dominated by distinct flow structures originating from the injector trailing edge that depend on the co-flow condition (sub- or supersonic) [68].

Subsonic wakes are typically characterized by large vortex structures originating from the trailing edge of the wake generator. These become clearly visible on short-time illuminated schlieren images in the wake of injector A (Fig. 5.1a). Their frequency, and the strength of the induced fluctuations depend on the wake generator geometry and co-flow properties and have been subject to studies for a wide range of Reynolds numbers [85]. In the case of a supersonic wake flow, expansion fans leave from the injector trailing edge followed by a recompression zone, where two oblique shock waves form. This applies to the wake of injector B (Fig. 5.1b). Like in subsonic wake flows, alternating eddies can form in the subsonic recirculation zone near the injector trailing edge. Though vortices, by definition, cannot exist in the supersonic domain, these structures persist beyond the nozzle throat. They can be interpreted as regions of alternating injectant concentration which are generated near the injector trailing edge and later transported downstream.

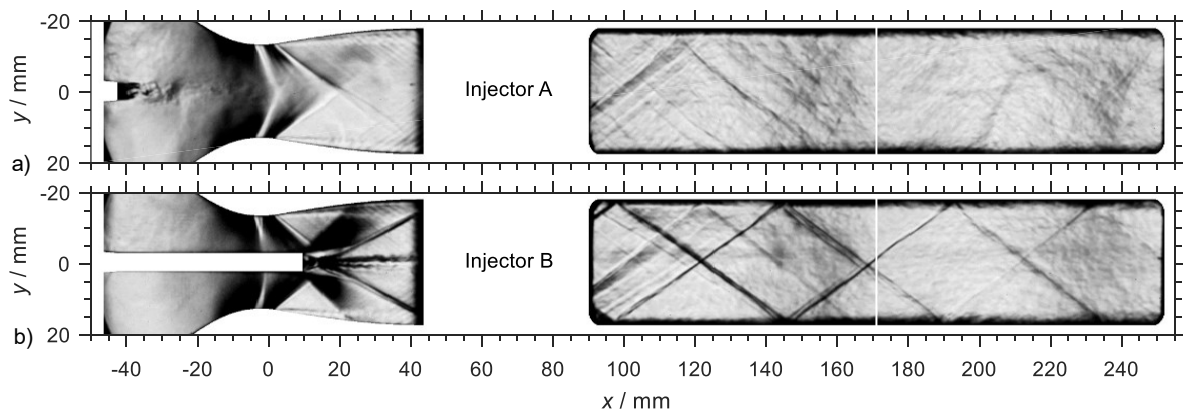


Fig. 5.1: Short-time ($5 \mu\text{s}$) illuminated schlieren images showing the fundamentally different wake flow of (a) injector A and (b) injector B both for $\alpha = 0^\circ$ channel opening angle.

5.3 Flow channel

The experiments were conducted at the high-enthalpy flow facility at the ITLR in Stuttgart that consists of a screw compressor, an air dryer, and three heater stages providing an air flow to the attached modular flow channel. (A detailed description can be found in Ref. [82].) The latter comprises a flange adapter (I), a nozzle module (II), the test section module (III), and an outlet diffuser (Fig. 5.2). Modules II and III are equipped with wall pressure taps and are optically accessible from four sides through fused silica windows. Modules II and III are equipped with wall pressure taps and are optically accessible from four sides through fused silica windows.

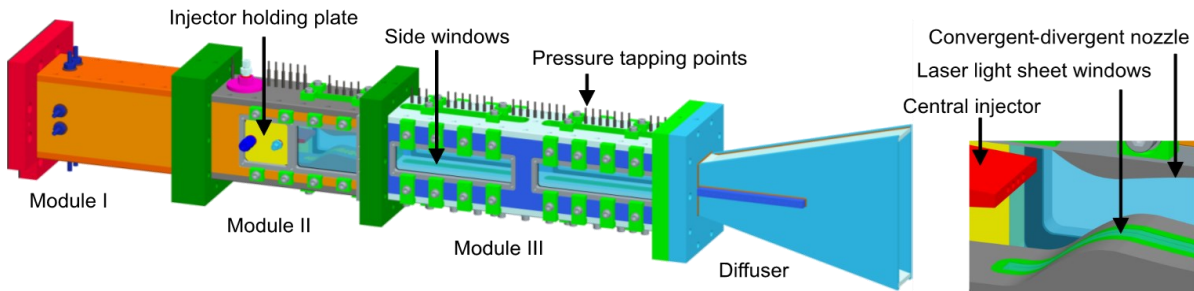


Fig. 5.2: Modular transonic flow channel.

The convergent-divergent nozzle is designed for a Mach number of 1.7 (26.3 mm throat height). To study different pressure gradients, three different versions of module III with horizontal opening angles of 0° , 0.25° , and 1.25° were designed (Fig. 5.3). The channel width is 40 mm and constant throughout the whole duct whereas its height is 35.4 mm at the nozzle exit and differs therefrom according to the duct opening angle.

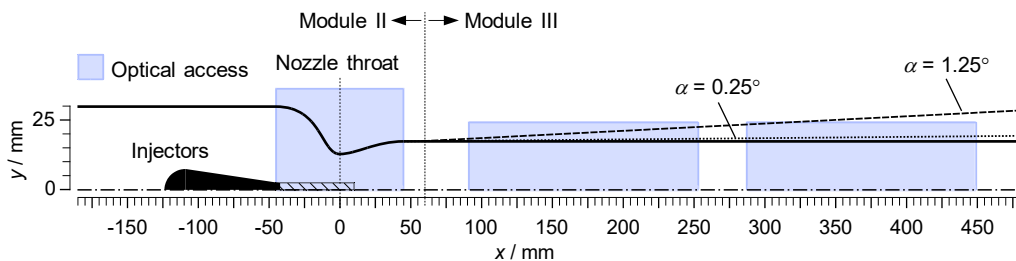


Fig. 5.3: Cross-section of the flow channel showing injector geometry and position. The opening angles of the test section α are enlarged by a factor of two for better illustration.

Both injectors are identical except for the length of their trailing section (Fig. 4): The trailing edge of injector A aligns with the nozzle inlet whereas the trailing edge of injector B reaches 10 mm past the nozzle throat ($x = 0$ mm) into the supersonic region of the nozzle flow (Fig. 3). The latter is chosen arbitrarily and mostly for reasons of comparability with previous works [65, 78]. Both trailing edges are 5 mm high whereas the width of both injectors spans over the complete channel width of 40 mm. The injectant is fed laterally through the side-way injector holding plates before it exits through four 2.5 mm holes spaced by 4.8 mm at the injector trailing edge. Two thermocouple ports allow for monitoring the injector flow temperature while the pressure is measured in both feed lines.

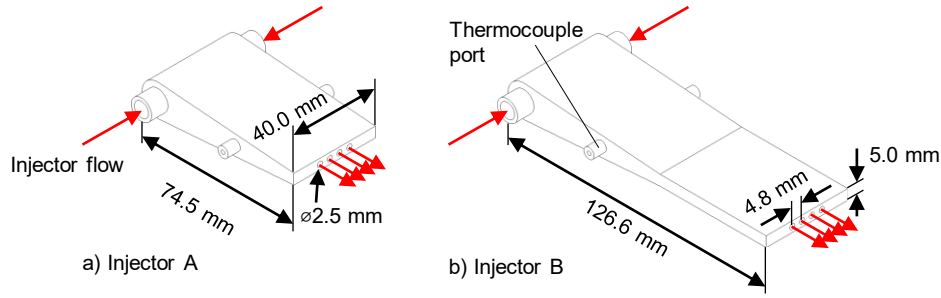


Fig. 5.4: Geometries of (a) injector A and (b) injector B.

5.4 Flow conditions

The inlet total temperature is set to 380 K for all experiments while the inlet total pressure is adjusted from 2.5 bar for injector A to 3.0 bar for injector B to maintain a constant air mass flow rate of 0.518 kg/s compensating for the reduction of the effective nozzle throat height due to the extent of injector B. The resulting nozzle exit Mach numbers (defined by the free stream velocity u_∞ and temperature T_∞ , the isentropic exponent κ , and the ideal gas constant R according to Eq. 5.1) are approximately 1.7 and 2.0. The free-stream Mach numbers at the point of injection are 0.3 and 1.4 for injectors A and B, respectively. The injector mass flow corresponds to only 0.14 % of the air mass flow. An evaporator system feeds 0.30 g/s toluene with 0.45 g/s nitrogen as carrier gas heated to 380 K.

$$M_\infty = \frac{u_\infty}{\sqrt{\kappa RT_\infty}} \quad (5.1)$$

Figure 5 shows the normalized wall pressure \tilde{p} for both injectors and the three different channel opening angles. As intended, the opening angle of 0.25° results in a nearly zero pressure gradient (Table 1) by just compensating the increasing boundary layer thickness. Analogously, the straight (0°) duct exhibits a positive pressure gradient by virtually narrowing the effective cross-section. The opening angle of 1.25° results in a negative pressure gradient until the flow decelerates due to overexpansion to subsonic speed manifesting as a shock train clearly visible in schlieren images (not shown). The resulting pressure gradients are noticeably smaller in the case of injector B compared to those of injector A. This can be attributed to the higher Mach number: First, the dependence of the pressure on the channel height is reduced according to isentropic relations. Secondly, boundary layer growth and, thus, the stream-wise decrease of the effective channel height is mitigated with increasing Mach number.

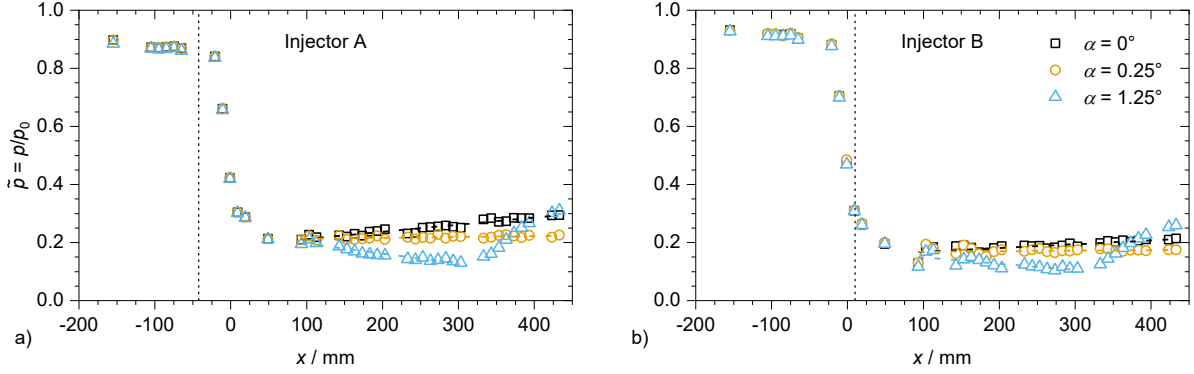


Fig. 5.5: Variation of the wall pressure p normalized by the respective inlet pressure p_0 in stream-wise direction for (a) injector A and (b) injector B depending on the channel opening angle α .

5.5 Laser-induced fluorescence

Laser-induced fluorescence (LIF) is widely used for studying mixing processes by imaging distributions of atomic or molecular tracer species in sub- or supersonic flows [3, 28, 64, 65]. The cross-sectional area of interest is illuminated by a laser light sheet and the LIF signal is recorded with intensified CCD cameras. LIF techniques using aromatic tracer species such as toluene exploit their large absorption cross-section in the ultraviolet and their high fluorescence quantum yield. The peak of the toluene absorption spectrum at room temperature is close to 250 nm; therefore, toluene LIF can be excited with 248-nm radiation from a krypton fluoride (KrF) excimer laser. The fluorescence is red shifted with a peak at approximately 280 nm [67]. The LIF signal S_{fl} (Eq. 5.2) depends on the incident laser intensity I_{laser} , the camera detection efficiency η , the tracer number density n_{tracer} the absorption cross-section σ_{abs} , and the integrated fluorescence quantum yield ϕ_{fl} . Absorption cross-section and quantum yield both depend on the incident wavelength λ and the temperature T , whereas ϕ_{fl} is also a strong function of the O_2 partial pressure p_{O_2} .

$$S_{\text{fl}} \propto I_{\text{laser}} \eta n_{\text{tracer}} \sigma_{\text{abs}}(\lambda, T) \phi_{\text{fl}}(\lambda, T, p_{\text{O}_2}) \quad (5.2)$$

The optical arrangement used for this work (Fig. 5.6a) is mounted on a traversable optical table that allows measurements along the entire flow channel. A thin (less than 0.3 mm) and 24 mm wide light sheet is formed from the rectangular beam profile of an excimer laser (Lambda Physik LPX 120, 10 Hz, 8 ns pulses) by a single $f = 500$ mm cylindrical lens. A mirror below the flow channel (Fig. 5.6b and Fig. 5.6c) redirects the laser light to enter the flow channel through the bottom laser window. The laser window in module II follows the nozzle contour on the inside of the channel and thus acts as a focusing lens. Therefore, an additional $f = -40$ mm cylindrical lens is used (Fig. 5.6b) to expand the light sheet and create a near homogeneous laser light intensity distribution in the nozzle region (module II). The laser pulse energy is monitored and attenuated to <62 mJ/cm² to avoid partial saturation of the LIF signal. The fluorescence signal is redirected with a dichroic mirror with an edge wavelength of 310 nm and passes a 280 ± 14 nm bandpass filter before it is detected by an intensified CCD camera

(LaVision Imager Intense with LaVision IRO). The mirror also acts as a beam splitter transmitting light with wavelengths larger than 310 nm which can be captured by an additional camera for experiments relying on two-color detection methods [80].

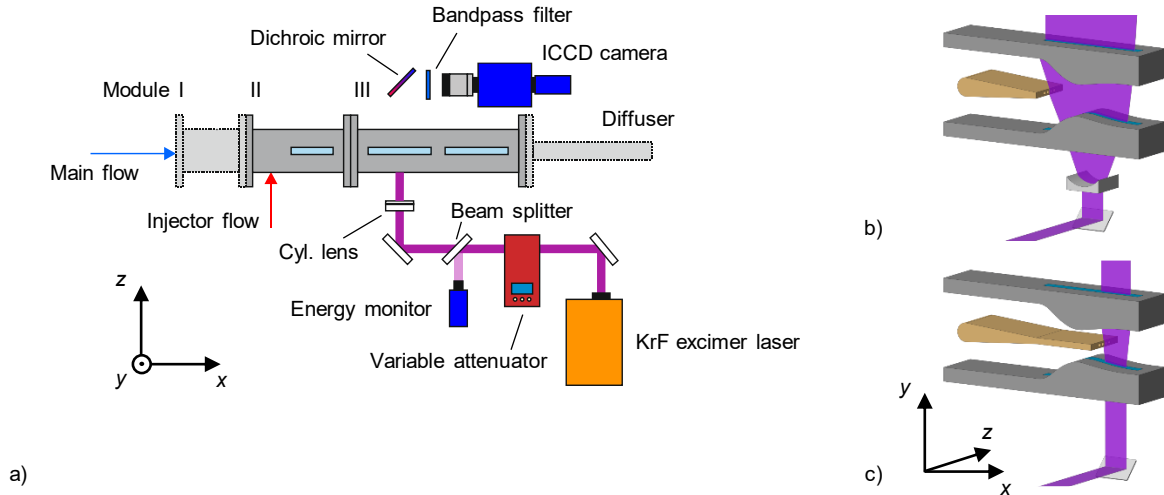


Fig. 5.6: Top view (a) on the optical setup and detail views on module II showing the light sheet position for (b) injector A and (c) injector B.

Background and flat-field images were obtained prior to the experiments to compensate for scattered laser light and light sheet and detection efficiency inhomogeneities. For the latter, toluene was added far upstream into module I to assure an even distribution in the flow channel at experimental conditions. Target images were used to correct for image distortions and to map pixels to physical dimensions resulting in a nominal resolution of approx. 14.8 px/mm. Fig. 5.7 shows averaged (200 shots) and corrected LIF images for both injectors for the straight ($\alpha = 0^\circ$) flow channel.

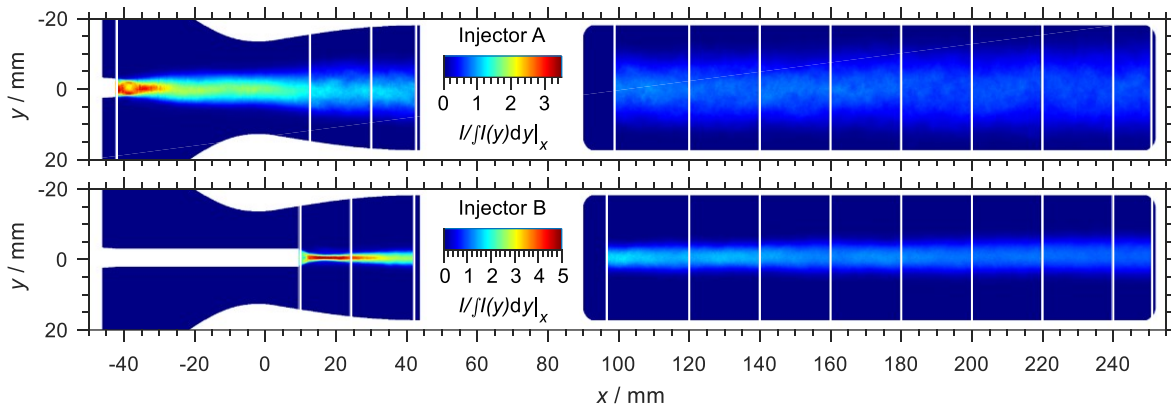


Fig. 5.7: Averaged LIF images after background and flat-field correction normalized by the integrated signal along the y -axis for (a) injector A and (b) injector B for $\alpha = 0^\circ$. White areas mask the nozzle, window, and injector contours. Both images are composed from LIF measurements at various downstream positions, with their limits indicated by vertical white lines.

Recent studies utilizing a two-color LIF technique [80] showed that fluorescence quenching by oxygen present in the main flow influences the signal in the direct vicinity of the injector

trailing edge due to incomplete mixing on molecular level. However, it was shown that the influence disappears after 7 mm (injector A) and 14 mm (injector B) downstream of the injector trailing edge in stream wise direction, respectively.

Assuming a sufficient distance and that properties affecting the fluorescence signal (Eq. 5.2) perpendicular to the direction of flow only change insignificantly [64], the signal of normalized vertical intensity profiles is proportional to the normalized injected tracer concentration. Thus, the shape and the growth of the mixing layer can be derived from averaged tracer LIF images. For this purpose, profiles along the y -coordinate (averaged over 20 pixels in x -direction) were extracted.

5.6 Results

Fig. 5.8 shows normalized LIF-intensity profiles along the vertical coordinate at selected distances d from the respective injector trailing edge. Their abscissa depicts the vertical y -coordinate normalized by the respective profile's half-maximum half-width $\delta_{1/2}$. The latter is determined by finding the intersection of the smoothed flanks with the half maximum of each profile. The near Gaussian shape of all profiles for both injector wake flows align well independently of the applied pressure gradient, thus revealing self-similarity in all cases.

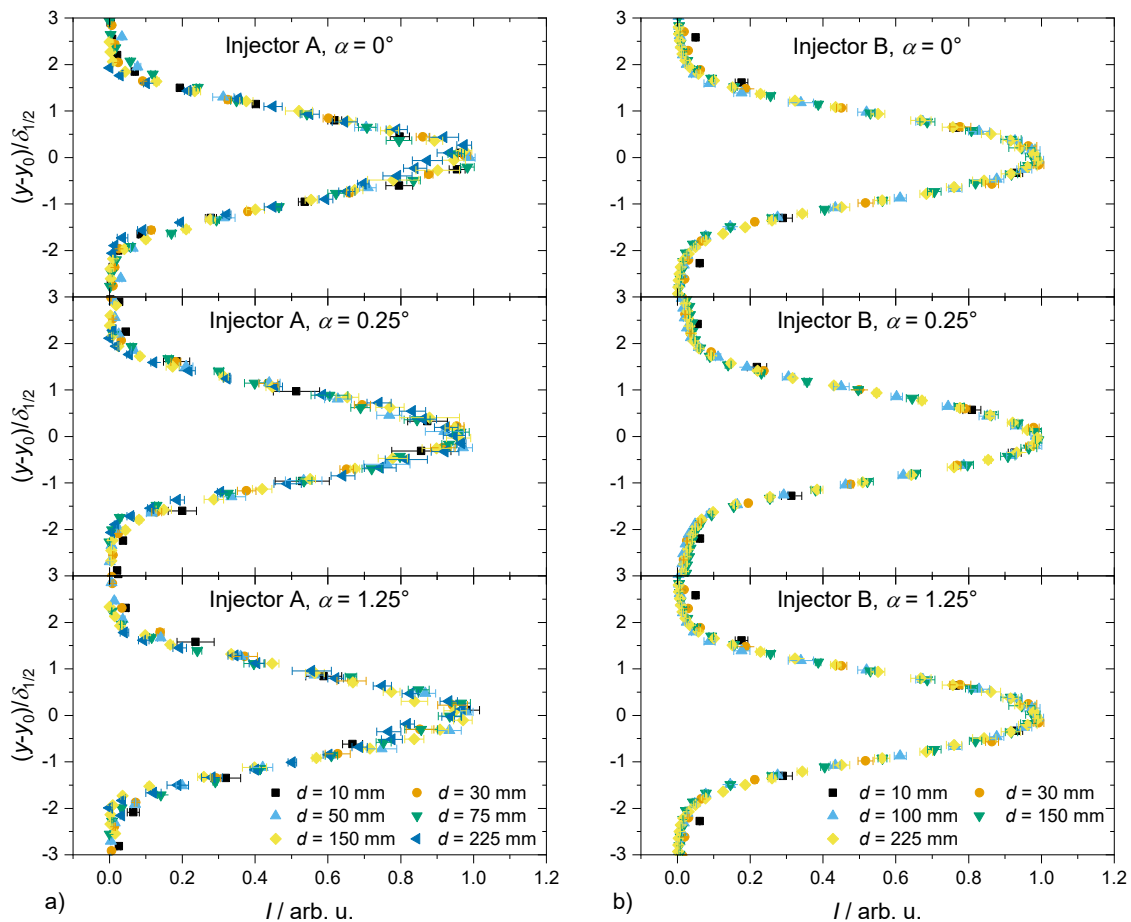


Fig. 5.8: Normalized intensity profiles scaled by the respective half-width half-maximum value $\delta_{1/2}$ at various distances d from the trailing edge of (a) injector A and (b) injector B for all three opening angles (from top to bottom: 0° , 0.25° , and 1.25°). Only every 20th point (a) or 10th point (b) is displayed for clarity.

Previous studies [64, 78] showed that the squared intensity profile half width $\delta_{1/2}$ is proportional to the square root of the distance to the origin of the wake ($1/2$ -power law) [92]. The shear layer growth rate Δ can be calculated from the squared intensity profile half width and the horizontal distance to the virtual origin x_0 .

$$\Delta = \sqrt{\frac{\delta_{1/2}^2}{x - x_0}} \quad (5.3)$$

Fig. 5.9 shows the evolution of $\delta_{1/2}$ and $(\delta_{1/2})^2$ in stream-wise direction for all investigated cases. Directly after the point of injection the growth rate increases nonlinearly along with the nozzle cross-section in the case of injector A. For injector B, the growth rate decreases before it reaches the neck of the recompression zone (cf. Fig. 5.3) before it starts increasing. In both cases, the growth rate remains nearly constant from the beginning of module III ($x = 62.2$ mm) on following the $1/2$ -power law as indicated by the straight dotted lines (Fig. 5.9b and d) representing a linear fit to the data in the test section.

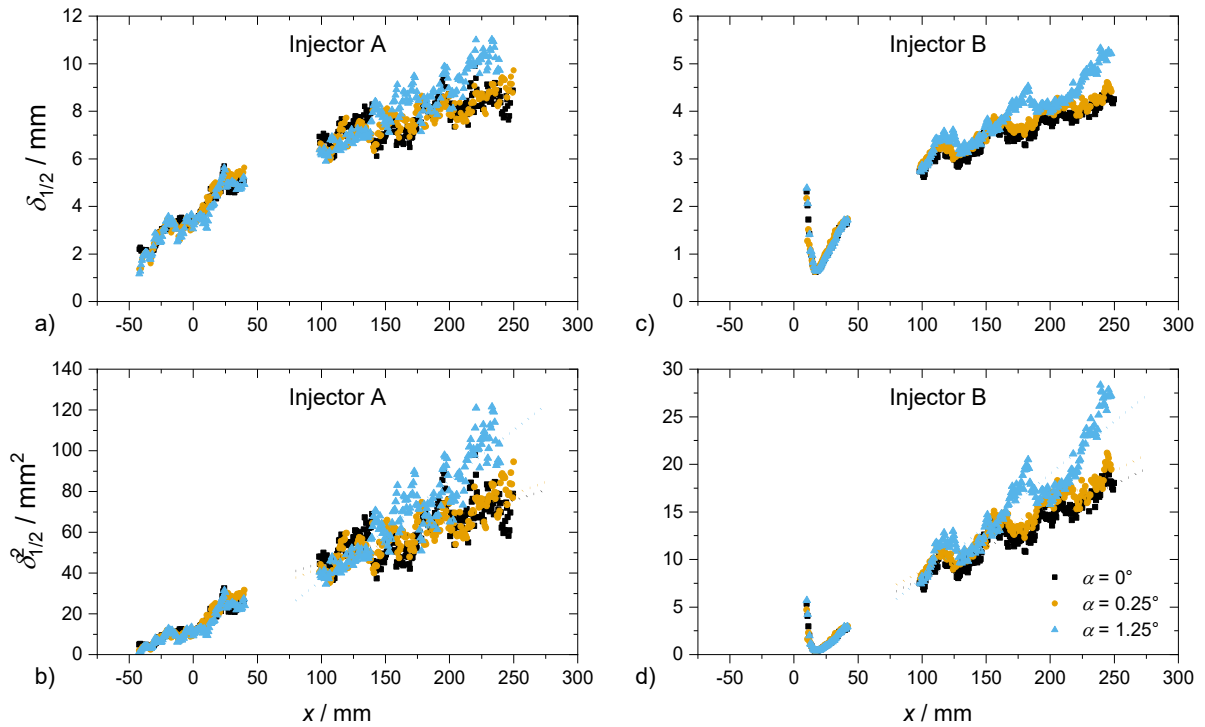


Fig. 5.9: Stream-wise evolution of $\delta_{1/2}$ (top) and $(\delta_{1/2})^2$ (bottom) for (a) injector A and (b) injector B for all opening angles. Dotted lines represent a linear fit in the window section. For clarity, only every 20th point is displayed.

In the case of injector B (Fig. 5.9c and Fig. 5.9d), $\delta_{1/2}$ decreases significantly where the reflected oblique shock waves originating from the recompression zone behind the injector trailing edge intersect. This causes a local compression accompanied by an increase in density. The positions of these contractions of the wake depend on the opening angle α and coincide well with the cross-section points of the oblique shock waves in the schlieren images as shown in

Fig. 5.10. Here, the position of the intersection after two reflections differs by about 14 mm between $\alpha = 0.25^\circ$ and $\alpha = 1.25^\circ$.

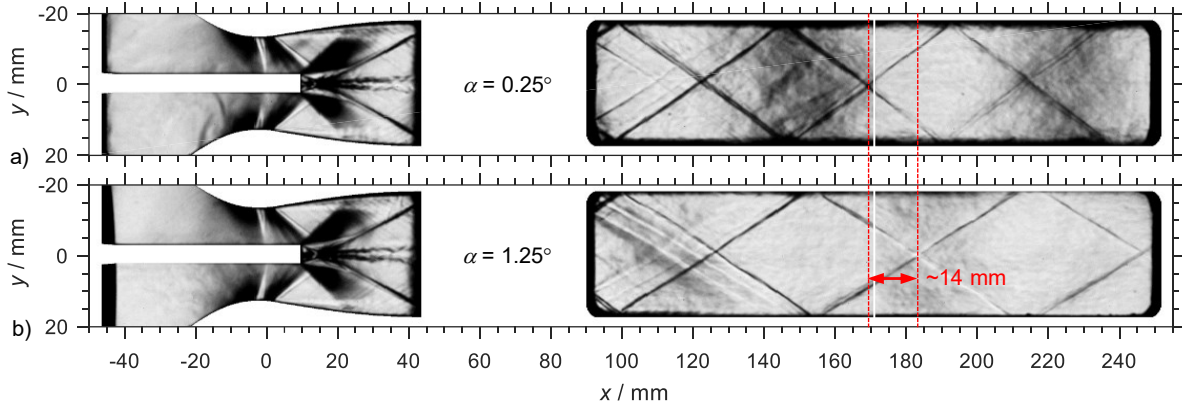


Fig. 5.10: Schlieren images of injector B comparing (a) the zero-pressure gradient case (0.25°) to (b) the maximum pressure gradient case (1.25°) showing the positions of the intersections of the reflected oblique shocks.

The growth rate of the wakes Δ , which corresponds to the slope of the lines shown in Fig. 5.9c and Fig. 5.9d, was calculated according to Eq. 3 as summarized in Table 1. It increases for both injectors with decreasing pressure gradient from $0.45 \text{ mm}^{1/2}$ to $0.70 \text{ mm}^{1/2}$ for injector A and from $0.26 \text{ mm}^{1/2}$ to $0.33 \text{ mm}^{1/2}$ for injector B, respectively. This corresponds to previous research findings that the growth rate of injection at subsonic co-flow is generally larger compared to injection at supersonic co-flow conditions of a similar straight-channel configuration due to the absence of vortex shedding [78].

Tab. 5.1: Growth rate Δ dependent on the pressure gradient for all configurations.

α / $^\circ$	Injector A		Injector B	
	$\partial\tilde{p}/\partial x$ / mbar/mm	Δ / $\text{mm}^{1/2}$	$\partial\tilde{p}/\partial x$ / mbar/mm	Δ / $\text{mm}^{1/2}$
0	0.24	0.45	0.13	0.26
0.25	0.03	0.49	0.02	0.27
1.25	-0.34	0.70	-0.22	0.33

5.7 Conclusions

The mixing behavior in a transonic wake flow of two different central injector types has been experimentally studied focused on the influence of the stream-wise pressure gradient imposed by three different flow channel geometries. Tracer LIF imaging experiments showed that self-similarity of the transonic mixing layer is preserved independently of pressure gradient or the injector configuration. The growth rate of the mixing layer was calculated finding that it follows the $\frac{1}{2}$ -power law.

6 Molecular mixing

The content of this chapter was published in Optics Express [80] as follows.

Beuting, M., Richter, J., Weigand, B., Dreier, T., and Schulz, C., *Application of toluene LIF to transonic nozzle flows to identify zones of incomplete molecular mixing*, Optics Express, 2018, **26**(8): 10266-10273

© 2018 Optical Society of America.

My personal contribution was the optical design, conduct, and evaluation of the LIF measurements as well as the preparation of the manuscript. The LIF-images has been obtained during a joined measurement campaign in the labs of the ITLR in Stuttgart under supervision of Prof. Bernhard Weigand. The test hardware was designed, tested, and characterized by Judith Richter [60]. Prof. Christof Schulz, Prof. Bernhard Weigand, and Prof. Thomas Dreier provided scientific guidance and council during the experiments and the write-up. The calibration measurements in the test cell were made independently at the IVG in Duisburg with Thomas Baranowski assisting during the experiments. All authors contributed to the manuscript by helping with the interpretation of the results, with the wording, and by proof-reading.

Abstract: Toluene laser-induced fluorescence (LIF) has been applied to image the mixing deficit on the molecular level in the transonic wake of two different blunt-body injectors in a compressible accelerated nozzle flow. A single-color excitation and two-color detection scheme is employed to measure the signal red-shift caused by the quenching effect of molecular oxygen on the fluorescence of toluene, which reduces and red-shifts the LIF signal if both substances interact on a molecular level. To this end, toluene is injected alternatingly with O₂-containing and O₂-free carrier gas into the air main flow. Differences of both signals mark regions where mixing on molecular level is incomplete. A zone of molecular mixing deficit extending several millimeters in stream-wise direction is identified. The effect of local variations in temperature on the sensitivity of this technique is discussed using photo-physical data measured in a stationary low-temperature cell.

6.1 Introduction

Efficient and fast mixing on the molecular level is essential to enable supersonic combustion and reactions in shock-wave flow reactors [1]. Practical realizations often feature central injectors that add a low-momentum feed of one reactant into a high-momentum sub- or supersonic flow containing the other [1, 62]. The fundamental understanding of mixing processes in such wake flows has been subject to fundamental research for several decades [67].

Planar laser-induced fluorescence (LIF) of organic tracers [28] has proven particularly useful for visualizing instantaneous species distributions in high-speed gas flows due to its high time resolution. The spatial resolution of the optical detectors and the light-sheet thickness, however, restrict direct measurements to macroscopic structures. These are typically orders of magnitude larger than the length scales relevant for the molecular interaction of reactants. Several

approaches to measure the level of molecular mixing have been proposed. They are based on the photo-physical sensitivity of the laser-excited species on collisions with constituents of the admixed gas, e.g., by fluorescence quenching: Clemens et al. [74] introduced an approach that exploits the quenching of nitric oxide (NO) fluorescence by O₂. They identified the level of molecular mixing in the shear layer of a coaxial jet of N₂ in air by alternately adding NO to each flow. King et al. [75] proposed a two-tracer approach. They marked the air flow with acetone, a ketone tracer insensitive to quenching by O₂, and the second O₂-free flow with NO. This method requires tracers with spectrally-separable fluorescence and, in this case, excitation at two separate wavelengths. Koban et al. [29] simplified this approach by substituting the O₂-sensitive NO with toluene, and acetone with 3-pentanone. The LIF signal intensity of aromatics like toluene strongly depends on the O₂ partial pressure [39] and is spectrally well-separated from that of 3-pentanone, while both can be excited with the same UV laser. Further simplification was introduced by Mohri et al. [30] who used toluene as single tracer and exploited the O₂-induced red-shift [29] of the LIF signal to detect micro-mixing indirectly by measuring the local O₂ distribution. The red shift was quantified by using two cameras equipped with filters for two separate portions of the fluorescence spectrum.

Knowledge about the status of molecular mixing is also relevant from a diagnostics point of view. The determination of flow composition and temperature using O₂-sensitive tracers depends on the local (molecularly mixed) O₂ partial pressure [3, 37]. A quantitative analysis of LIF signals in areas of incomplete mixing requires accurate measurement of the level of molecular mixing (and ultimately, additional photo-physical data for the dependence of the LIF signal as a combined effect of mixing state and temperature).

This work demonstrates the application of single-color excitation, two-color detection toluene LIF, similar to Ref. [30], to a transonic accelerated nozzle flow [64] to qualitatively identify zones of deficient molecular mixing in the wake of two different central injectors.

6.2 Theory

The LIF signal emitted by organic tracers after electronic excitation by a laser pulse depends on the incident laser intensity I_{laser} , the detection efficiency η_e , the tracer number density n_{tracer} , the absorption cross-section $\sigma_{\text{abs}}(\lambda, T)$, and the integrated fluorescence quantum yield $\phi_{\text{fl}}(\lambda, T, p_{\text{O}_2})$ (Eq. 1). The absorption cross-section depends on the excitation wavelength λ and the temperature T , and the quantum yield additionally depends on the O₂ partial pressure p_{O_2} .

$$S_{\text{fl}} \propto I_{\text{laser}} \eta_e n_{\text{tracer}} \sigma_{\text{abs}}(\lambda, T) \phi_{\text{fl}}(\lambda, T, p_{\text{O}_2}) \quad (6.1)$$

O₂-induced quenching has been studied for various aromatics like toluene [38], anisole [20], and naphthalene [21]. Besides reducing ϕ_{fl} by decreasing the fluorescence lifetime, O₂ also causes a red-shift of the LIF emission for certain excitation wavelengths [38] similarly to the effect caused by increasing temperature [22]. This red-shift can be sensed by measuring the ratio R of the short- and long-wavelength section of the fluorescence spectrum using two

detectors equipped with either a “red” or a “blue” filter (Eq. 6.2). The ratio is independent of the incident laser intensity, the local tracer concentration, and the absorption cross-section.

$$R = \frac{S^{\text{red}}}{S^{\text{blue}}} = \frac{\eta^{\text{red}}\phi^{\text{red}}(T, p_{\text{O}_2})}{\eta^{\text{blue}}\phi^{\text{blue}}(T, p_{\text{O}_2})} \quad (6.2)$$

Because quenching requires molecular collisions between O_2 and the tracer, R depends on the mixing state of tracer and quencher on the molecular level. Figure Fig. 6.1 shows normalized toluene-LIF spectra for various p_{O_2} at room temperature [38] and the derived signal ratio R for the filter pair used in this work.

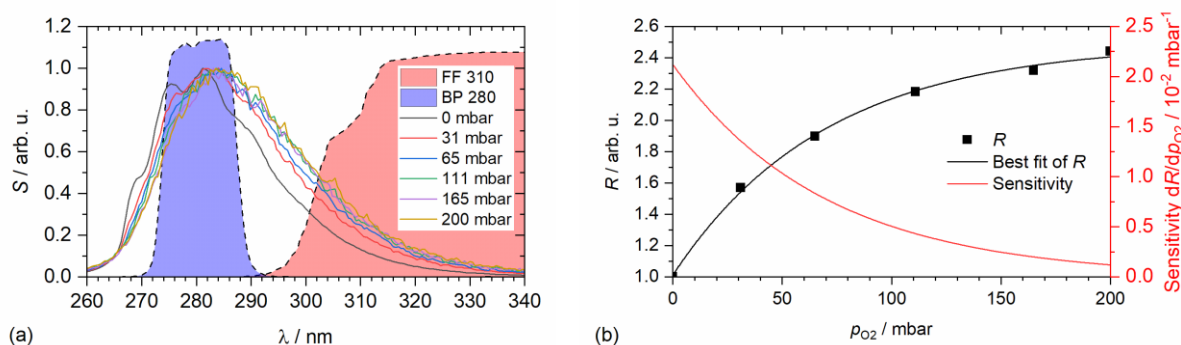


Fig. 6.1: (a) Toluene-LIF spectra at room temperature in N_2 for a series of O_2 partial pressures after excitation with 248 nm [38] and transmission curves of filters used in the present experiments. (b) Intensity ratios R (black symbols and line) and sensitivity (red line) of the two-color method.

In areas where molecular mixing has not happened, R is independent of p_{O_2} because collisions with O_2 do not occur. These areas can be identified by comparing two measurements where toluene is used either with air or with N_2 as carrier gas injected into a toluene-free air flow. R , however, also depends on temperature. Therefore, R_{air} (measured with air as carrier gas, i.e. mixing with the air main flow does not change the local p_{O_2}) is divided by R_{N_2} (obtained from measurements with N_2 as carrier gas). The resulting quotient $\zeta = R_{\text{air}}/R_{\text{N}_2}$ then only represents the O_2 -induced red-shift and, thus, marks the areas where molecular mixing is incomplete. When calculating the ratio, the detection system efficiency such as the angle-dependent filter transmission cancels. Also, the effect of T cancels, as long as it can be considered identical for both measurements, R_{air} and R_{N_2} .

To help understand the meaning of ζ , toluene-LIF spectra were measured between 264 and 295 K (cf. Fig. 6.4) for p_{O_2} between 0 and 210 mbar in a stationary cell after excitation with 248-nm laser light generated from an EXPLA PL 2413 picosecond laser in combination with an EXPLA PL 401 parametric generator. A Horiba iHR320 Spectrometer was used to capture the toluene fluorescence [48]. The measured spectral data was used to calculate the quotient ζ for the filter pair used. The results are shown in Fig. 6.2, where unity indicates full molecular mixing and a value of 3 absence of mixing. The figure also shows the error in ζ caused by varying the temperature by 30 K within the relevant (low-temperature) range of our experiment, which is below $\sim 7\%$. A more complete analysis of the low-temperature photophysics of

toluene is underway. In the context of this paper, where the aim is to qualitatively locate areas with deficient molecular mixing, this detailed analysis is not required.

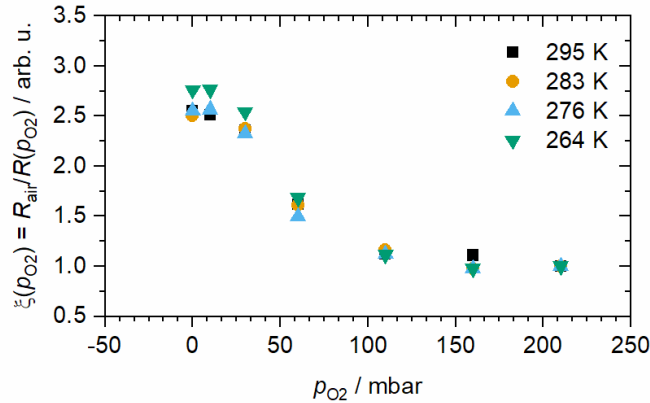


Fig. 6.2: Oxygen-dependence of ζ for the used filter pair calculated from LIF spectra obtained in a temperature-controlled static cell at atmospheric total pressure for different temperatures T within the range relevant for this paper.

6.3 Experiment

The experiments were performed at the supersonic test facility in Stuttgart. 517 g/s pressurized air was provided at a total temperature of 380 K to a modular transonic flow channel with a rectangular cross-section and a constant width of 40 mm (see Ref. [82] for details). The channel comprises a convergent-divergent nozzle (26.3 mm throat height) designed for an exit Mach number of 1.7. Optical access is provided laterally through fused silica windows and orthogonally through so-called laser slot windows whose inside polished surfaces follow the shape of the nozzle. Fig. 6.3a shows the dimensions of the nozzle and the positions of the central injectors. The wake flows of two injectors that extend over the whole channel width as shown in Fig. 6.3b were analyzed: A ‘subsonic’ (Inj A) and a ‘supersonic’ (Inj B) injector providing injection either prior or after the nozzle throat, respectively. Both injectors deliver the tracer through four 2.5-mm diameter holes spaced by 4.8 mm. In case of injector B, the nozzle throat is narrowed by the height of the injector trailing edge and, thus, the exit Mach number increases to 2.0. A constant main mass flow is ensured by setting the total pressure at the flow channel entry to 2.5 bar for injector A and 3.0 bar for injector B. The wake forming downstream of the injectors is dominated by periodic flow structures. These have been investigated in the wake of bluff bodies [89, 113] in the past. The size, the extent, and the frequency of these structures mainly depend on the free-stream Mach number (sub- or supersonic flow, compressibility effects) [91]. The detailed wake flow physics is not the topic of this paper; however, its periodic character is important to better understand the results.

forming in liquid toluene are known to fluoresce at 320 nm [114]. The absence of such a signal indicates that the local concentration is low enough or that the residence time is insufficient for nucleation.

The optical setup is sketched in Fig. 6.5(a). A rectangular beam provided by a 248-nm KrF excimer laser (8 Hz, 20 ns pulses) is formed by a $f = 500$ mm cylindrical lens to a 0.3 mm thin and 24 mm wide light sheet that is directed through the laser windows in the measurement section by a mirror below the channel as shown in Fig. 6.5(b) and Fig. 6.5(c). The light sheet is positioned in the center of the channel illuminating the flow between the second and third injector hole (cf. Fig. 6.3). In the case of injector A, the laser light passes an additional cylindrical lens ($f = -40$ mm) to expand the light sheet over the complete observable area behind the central injector (Fig. 6.5b). The laser fluence is attenuated to ~ 70 mJ/cm² before entering the channel to ensure linear signal response. An energy monitor records pulse-to-pulse energy fluctuations. A dichroic beam splitter (Semrock Brightline FF 310) divides the LIF signal into a blue and a red channel. The blue channel is further equipped with a bandpass filter (Semrock Brightline BP 280) while an additional long-pass filter is used on the red channel to suppress scattered laser light (cf. Fig. Fig. 6.1a). Two ICCD cameras (LaVision imager intense, IRO) capture the signal. All optical equipment is mounted on a three-axis translatable optical table.

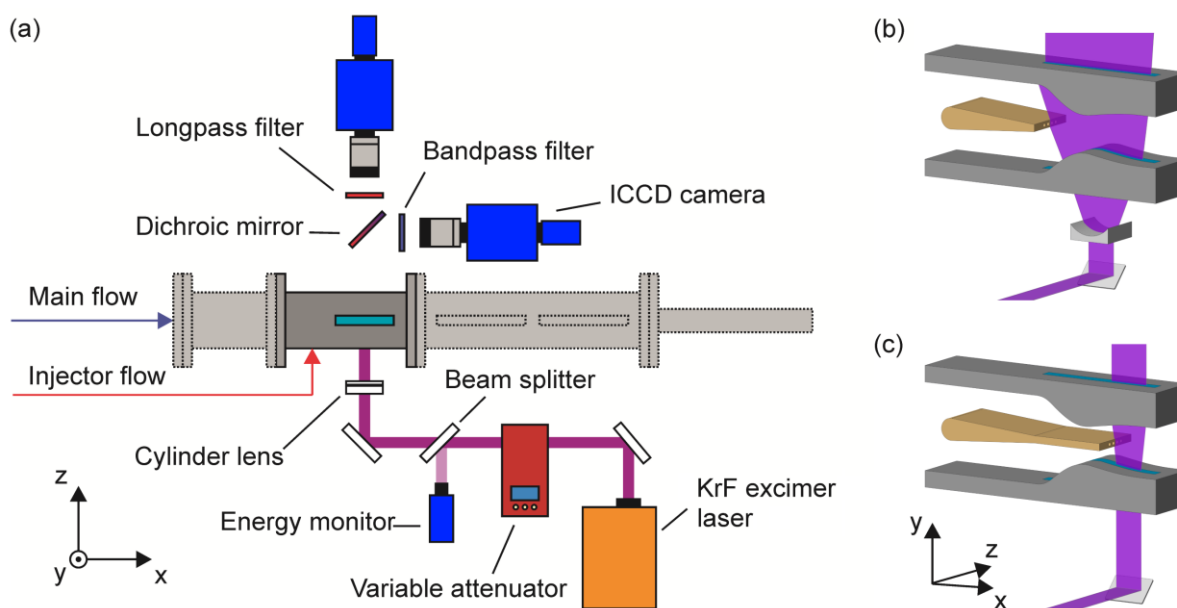


Fig. 6.5: (a) Optical setup and light sheet positions within the nozzle with (b) injector A and (c) injector B.

6.4 Results

Two-color ratioing methods require image mapping after geometric adjustment of the cameras. Since the channel shifted during the experiments due to thermal expansion, additional spatial calibration was needed: A transparent backlit target was placed on the camera-facing observation window and the optical table was moved away from the flow channel by the distance of the target to the light sheet position. The LaVision DaVis software was used to generate a mapping function with a residual error of ~ 0.8 pixels. To account for the deflections caused by

the window, the correlation between 200 pairs of LIF images was calculated and maximized iteratively after applying the mapping function.

To assess the degree of molecular mixing the ratio R of the red and the blue channel, representing the signal red-shift, is calculated according to Eq. 6.3 for each laser pulse. The signals of both channels S are corrected for pulse-to-pulse intensity variations and for background signal by subtracting averaged (200 pulse) background images $\langle \text{BG} \rangle$.

$$R = \frac{S^{\text{red}} - \langle \text{BG}^{\text{red}} \rangle}{S^{\text{blue}} - \langle \text{BG}^{\text{blue}} \rangle} \quad (6.3)$$

For comparison of the case of homogeneous O_2 concentration to the O_2 -free case, averaged ratios $\langle R_{\text{air}} \rangle$ and $\langle R_{\text{N}_2} \rangle$ are calculated from 1000 single ratios each. The results are plotted in Fig. 6.6a–d. In all cases, only regions where both channels provided sufficient signal (i.e., > 20 counts/pixel) are considered. Figures 6.6e and f show the standard deviation of R related to its average value to indicate the temporal fluctuation, where the upper half of each figure refers to R_{air} and the lower half to R_{N_2} . A measure for concentration fluctuations is provided by the relative standard deviation of the signal intensity. This is shown in Fig. 6.6g and h for the red channel (less sensitive to signal red-shift as the blue channel) for injection with homogeneous O_2 concentration. The area of strong fluctuations in the wake of injector A results from the periodic character typical for subsonic wakes that involve large coherent flow structures. In the case of injector B, the length and time scales of those structures are smaller and, thus, the fluctuations are less.

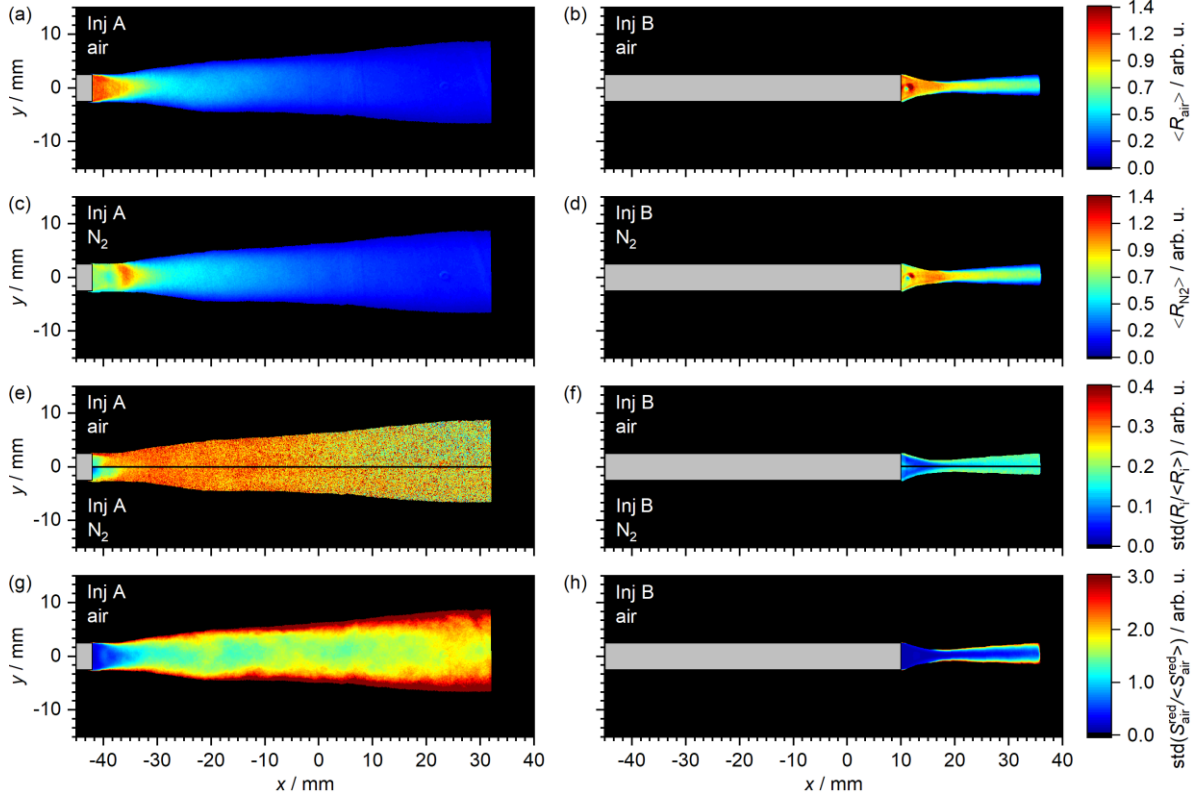


Fig. 6.6: Signal red-shift in the wake of injectors A and B after using alternately (a)–(b) air (homogeneous O_2 concentration) and (c)–(d) N_2 as carrier gas of the tracer flow, respectively. The surrounding flow is air in both cases, the grey boxes indicate the injector trailing edge position. (e)–(f) show the standard deviation of R and (g)–(h) show the standard deviation of S , each divided by the respective average value. Regions without sufficient signal (less than 20 counts/pixel in either LIF signal channel) were masked in all images S prior to the ratioing operations.

The quotient $\langle \xi \rangle$ of both averaged ratios as defined in Eq. 6.4 is shown in Fig. 5.7. This represents a measure of the degree of incomplete molecular mixing indicated by values above 1.

$$\langle \xi \rangle = \frac{\langle R_{\text{air}} \rangle}{\langle R_{\text{N}_2} \rangle} \quad (6.4)$$

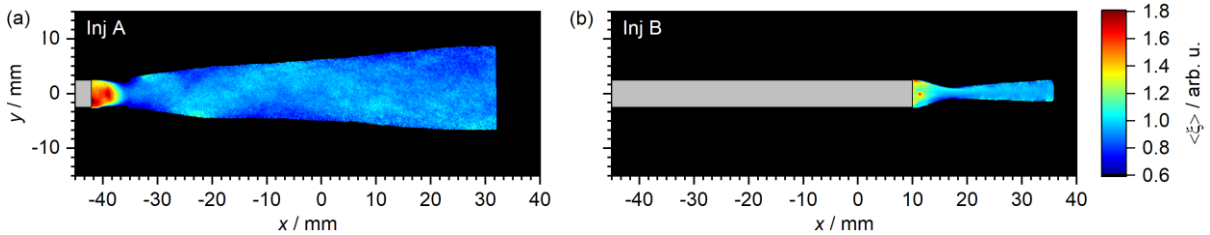


Fig. 6.7: Averaged quotient ξ as a measure for the O_2 -induced red-shift and, thus, incomplete molecular mixing for (a) injector A and (b) injector B.

To determine the extent of this zone in stream-wise direction, as relevant for technical processes requiring molecular mixed reactants at a certain point after injection [1], centerline ($y = 0$ mm) profiles of R and ξ are extracted as shown in Fig. 6.8. For both injectors, the red-shift near the trailing edge is considerably stronger if O_2 is present in the injected flow (blue lines) compared to the case with N_2 (red lines) as carrier gas. This zone extends to about 7 mm

past the trailing edge of injector A and 16 mm past injector B. Further downstream of that zone, the signal ratio is nearly independent of the injector flow composition while still decreasing. This reduction can be attributed to the blue-shift of the LIF signal due to gas-dynamic cooling (cf. Fig. 6.4).

In the wake of both injector types, ξ increases before it drops again further downstream. This can be traced back to the light sheet position that is aligned in between the two center injection holes (cf. Fig. 6.3b, Fig. 6.5b and c for details). In the very vicinity of the trailing edge the leftmost portion of the image only represents the recirculated mixture, while 3D-flow effects further downstream entrain unmixed injector flow into the image plane. In addition, in the case of injector B, two droplets (approx. 2 mm in diameter) form on each side-window inner surface about 2 mm behind the injector trailing edge. Both are visible in Fig. 6.6b and d, and Fig. 6.7b and cause a sudden drop followed by an increase of the signal around $x = 12$ mm in Fig. 6.8b. The droplets can be observed at various conditions by naked eye even without tracer flow. Thus, we suspect residual water in the main flow to condensate due to rapidly changing conditions in the recirculation zone at the trailing edge of injector B.

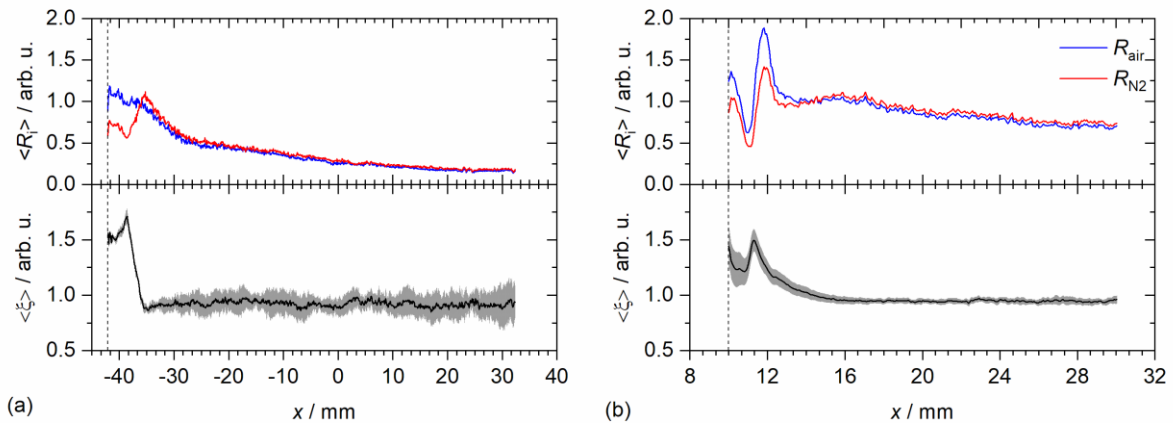


Fig. 6.8: Profiles (extracted from Fig. 6.6(a)–(d) and Fig. 6.7) of the O_2 -induced fluorescence red-shift represented by the quotient ξ (bottom) calculated from the averaged signal ratios R of both channels (top) for (a) injector A and (b) injector B along the centerline ($y = 0$ mm). The grey bands represent the standard deviation of ten 100-shot averages.

6.5 Conclusions and outlook

A single-color excitation and dual-band detection tracer LIF technique has successfully been applied to monitor the mixing deficit on molecular level in a transonic nozzle flow. The wakes of two central injectors feeding a low-momentum jet into an accelerating air flow were analyzed showing that the extend of the zone with apparent incomplete mixing depends on the point of injection: In the case of the injection into a supersonic ($M = 1.42$) main flow, it extends with approximately 16 mm more than twice the distance in stream-wise direction compared to the injection in a subsonic flow ($M = 0.26$) with 7 mm. The results presented here are of qualitative nature. For quantification, detailed photo-physical data for the complete range of conditions in the flow channel are required, which are subject to ongoing work in our lab. Further,

complementary measurement techniques are required to measure and to correct for temperature and pressure effects accordingly.

7 Tracer characterization

The content of this chapter was published in Applied Physics B [49] under the Creative Commons CC BY 4.0 license available under creativecommons.org/licenses/by/4.0/ as follows.

Beuting, M., Dreier, T., Schulz, C., and Endres, T., *Low-temperature and low-pressure effective fluorescence lifetimes and spectra of gaseous anisole and toluene*, Applied Physics B, 2021, **127**(4): 59

My personal contribution was the optical design, conduct and evaluation of the measurements as well as the preparation of the manuscript. Dr. Torsten Endres, Prof. Christof Schulz and Prof. Thomas Dreier provided scientific guidance and council during the experiments and write-up. All authors contributed to the manuscript by helping with the interpretation of the results, with the wording, and by proof-reading.

Abstract: Fluorescence spectra and lifetimes of anisole and toluene vapor in nitrogen have been measured at conditions below ambient (257–293 K and 100–2000 mbar) upon excitation with 266-nm laser light to expand the applicable range of anisole and toluene laser-induced fluorescence (LIF) for conditions below room temperature that occur in expanding flows and cases with strong evaporative cooling. Anisole fluorescence spectra broaden with decreasing pressure while fluorescence lifetimes decrease simultaneously. This is consistent with a more pronounced effect of internal vibrational redistribution on the overall fluorescence signal and can be explained by significantly reduced collision rates. In the case of toluene, the transition from photo-induced heating to photo-induced cooling was observed for the first time for 266 nm. The data confirm predictions of earlier work and is particularly important for the advancement of the available photo-physical (step-ladder) models: Since those transitions mark points where the molecules are already thermalized after excitation (i.e., no vibrational relaxation occurs during deactivation), they are important support points for fitting empirical parameters and allow analytical determination of the ground state energy transferred to the excited state. The data enables temperature and/or pressure sensing, e.g., in accelerating cold flows using laser-induced fluorescence of both tracers.

7.1 Introduction

Laser-induced fluorescence (LIF) of organic gas-phase tracer species has been widely used to measure temperature, composition, and density of various kinds of flows, often with the purpose of light-sheet based imaging [28]. While concentration and density measurements take advantage of local signal intensities [115], temperature measurements are often based on ratio-metric measurements of signal intensities detected in separate spectral regions of the fluorescence emission bands [3, 22, 27, 47]. A similar approach can also be used for the analysis of molecular interactions, when collisional quenching (and thus, e.g., local O₂ partial pressure) can be detected through modifications in the fluorescence spectra [29, 30, 73, 80, 116]. A less frequently applied technique exploits the dependence of the fluorescence lifetime on temperature, pressure or bath-gas composition for quantitative measurements [23, 26]. While the

effective fluorescence lifetime is proportional to the fluorescence quantum yield, it can be measured directly without knowledge of the tracer concentration.

The use of these effects for quantitative measurements requires detailed knowledge of the underlying spectroscopic properties under the respective environmental conditions. Most applications studied so far have focused on the application of tracer LIF at room temperature or above, e.g., for the analysis of fuel/air mixing in combustion systems and extensive data bases as well as modeling approaches have been developed for these conditions as discussed in the following sections. For temperatures below room temperature that are practically relevant, e.g., in expanding flows, in engines at cold start, or in sprays with strong evaporative cooling, the underlying spectroscopic data is missing and thus, the applicability of existing photophysical models is not validated. In this paper, this deficiency is addressed with studying fluorescence properties of two relevant species, anisole and toluene, in sub-ambient conditions and comparing the results with the state-of-the-art model understanding.

The application of tracer LIF to challenging environments such as internal combustion engines or supersonic flows requires careful choice of the best-suited fluorescence tracer and spectroscopic approach. Besides the dependence of the tracers photophysical properties on temperature, pressure, and bath-gas composition, factors like evaporation properties (i.e., for spray analysis [13, 15, 117]), high-temperature stability [6], environmental impact (especially, in the case of large-scale experiments [1, 60, 64, 80]), interaction with the reactive system (auto-igniting fuel/air mixtures [118]) and physical limits (attainable vapor pressure, onset of self-quenching [16]) must be considered for a proper choice of tracer. Applications to super- or transonic flow experiments [3, 5, 8, 60, 64, 80] pose several challenges: Firstly, due to gas-dynamic cooling, temperatures drop well below standard conditions where so far little photophysical data on typical tracers are available. Secondly, the environmental impact of the tracers used must be limited as large amounts are required for full-scale experiments ruling out the application of toxic species, e.g., nitric oxide, which would be a more obvious choice for cold gas flows as demonstrated in literature [75, 116, 119]. Aromatics such as anisole and toluene are promising candidates for tracer LIF in such flows because they, firstly, can easily be excited by standard laser wavelengths such as emitted by KrF excimer lasers (248 nm) or the 4th harmonic of Nd:YAG lasers (266 nm) [120]. Secondly, they exhibit large fluorescence quantum yields [18, 20] that enable application at low tracer concentration and that compensate for their limited vapor pressure at low temperature.

Toluene is an established and well-studied fluorescence tracer for various applications [121]. In contrast, anisole has gained attention more recently. Its advantages include an increased per-molecule signal level that enables improved signal-to-noise ratios in many applications despite its lower vapor pressure compared to toluene [15, 27]. However, most efforts studying photophysical properties of anisole [6, 48, 50, 51] and toluene [5, 23, 34, 41, 45, 48, 122] have been carried out for room temperature or above and photophysical data at low temperature and low pressure are scarcely available.

Low-temperature conditions outside the previously explored range occur frequently in transonic nozzle flows, e.g., where spatial temperature and pressure gradients are present in which our own LIF measurements have been limited to qualitative analysis [60, 80] so far. In the past, Combs et al. presented a thorough photophysical analysis of naphthalene vapor [8] for measuring flow properties in cold supersonic wake flows [9]. Using toluene LIF, Gamba et al. [3] measured temperature in supersonic flows with complex compressibility effects with a two-color detection scheme. However, since their spectral calibration data was only available above room temperature, the complete temperature range could not be covered. Estruch-Samper et al. [47] encountered the same problem while applying a similar technique in a hypersonic gun tunnel but used linear extrapolation of their above room-temperature data for toluene. Also, concentration measurements in cold supersonic flows required sophisticated calibration techniques [3, 5]. The data provided in this paper closes these gaps for anisole and toluene.

Practical applications of tracer LIF have often been supported by empirical data fits [20, 21, 48] or semi-empirical models [46, 51, 123, 124] that predict the fluorescence quantum yield for the given conditions. Both require measured data for validation in the respective temperature range. Measurements within an increased parameter range thus provide critical boundary conditions for the validation of existing models [18, 46, 51] and expand their valid range. Also, because of reduced collision rates, processes such as intramolecular vibrational energy redistribution, which are usually insignificant compared to rapid vibrational relaxation [93], are easier to study in low-density and low-temperature environments. The current state of model development is described in section 7.2 also highlighting the importance of extending the existing datasets to regions of lower temperature and pressure regions.

The primary goal of this work is to provide spectrally-resolved fluorescence intensities and fluorescence lifetimes, representing fluorescence quantum yields, for anisole and toluene in so far scarcely or not available ranges of temperature (257–293 K) and pressure (100–2000 mbar). Such data expand the applicable range of anisole and toluene LIF and also support the advancement of the most recent fluorescence quantum yield models toward the low-temperature and low-pressure regime.

7.2 Photophysics

The fluorescence signal of organic tracer species depends on the tracer number density n_{tr} , the incident laser intensity I_{Laser} , the tracer's absorption cross-section σ and fluorescence quantum yield (FQY) ϕ_{fl} . For aromatic tracers, σ_{abs} is a function of temperature T and pressure p , whereas ϕ_{fl} additionally depends on the partial pressure p_{q} of the respective quenching species q present in the gas such as oxygen [38], other organic molecules [29], or excited state molecules of the tracer itself [16].

$$S \propto n_{\text{tracer}} I_{\text{laser}} \sigma_{\text{abs}}(T, p) \phi_{\text{fl}}(T, p, p_{\text{q}}) \quad (7.1)$$

After excitation from the ground state S_0 to the first excited state S_1 , single-ring aromatics like anisole and toluene can fluoresce in the ultraviolet spectral range ($S_1 \rightarrow S_0$). The fluorescence is in strong competition with rapid non-radiative deactivation of the excited state through intersystem crossing (ISC) to the triplet state T_1 , internal conversion (IC) to highly vibrationally excited states in S_0 , and collisional quenching, while undergoing vibrational relaxation (VR) within the S_1 state due to collisions with bath gas molecules. Intramolecular vibrational energy redistribution (IVR) can often be neglected in denser gases where VR is dominant because of high collision rates.

The quantum yield of a fluorophore is defined as the ratio of the rate of spontaneous emission of light k_{fl} to the total deactivation rate k_{tot} with the latter being the sum of the rate constants for each individual deactivation channel (cf. Fig. 7.1). The rate constants for intersystem crossing k_{ISC} and internal conversion k_{IC} often are combined to the single non-radiative rate constant k_{nr} . The rate constant for collisional quenching is the product of the quenching rate k_{q} and the tracer concentration (here in the form of p_{q}). The ratio of the rate constants can further be expressed as the ratio of their reciprocals, the excited state lifetime τ_{fl} and the experimentally accessible effective lifetime τ_{eff} , respectively [28].

$$\phi_{\text{fl}} = \frac{k_{\text{fl}}}{k_{\text{tot}}} = \frac{k_{\text{fl}}}{k_{\text{fl}} + k_{\text{ISC}} + k_{\text{IC}} + \sum k_{\text{q}} p_{\text{q}}} = \frac{k_{\text{fl}}}{k_{\text{fl}} + k_{\text{nr}} + \sum k_{\text{q}} p_{\text{q}}} = \frac{\tau_{\text{eff}}}{\tau_{\text{fl}}} \propto \tau_{\text{eff}} \quad (7.2)$$

Step-ladder models as first described by Freed and Heller [33] and implemented, e.g., by Thurber et al. for ketones [124] describe the successive vibrational relaxation in the initially optically excited energy levels of the fluorophore and its competition with fluorescence emission and non-radiative deactivation processes using kinetic rate expressions. Implementations consist of a procedural model function that traverses all occupied vibrational energy levels in S_1 during VR (cf. Fig. 7.1a): After excitation to a certain energy level E_{initial} in S_1 , the contribution of each subsequent energy level to ϕ_{fl} during thermalization is calculated from the balance of all competing deactivation channels while each step corresponds to the mean time between collisions. The rate constants used for quantifying this kinetic scheme are either parameterized (energy-dependent) equations or scalar fit parameters that are determined from fitting the model function to measured fluorescence data. The starting point, E_{initial} , is determined from the laser energy E_{laser} , the ground-state thermal energy level $E_{\text{therm},0}$ and the S_0 - S_1 band gap E_0 (Eq. 7.3).

$$E_{\text{initial}} = E_{\text{laser}} + E_{\text{therm},0} - E_0 \quad (7.3)$$

The thermal energy levels E_{therm} are calculated from the vibrational frequency modes (Eq. 7.4).

$$E_{\text{therm}} = \sum_{i=1}^n \frac{\omega_i}{\exp\left(\frac{hc\omega_i}{k_b T}\right) - 1} \quad (7.4)$$

Based on these relations, attempts to model the FQY or fluorescence lifetime have been made. Thurber et al. [124] have presented a phenomenological step-ladder model describing the FQY of acetone. Rossow [46] adapted this step-ladder model for toluene between 350 and 900 K and 1–30 bar. Faust et al. [21] developed an empirical model for toluene predicting the FQY for a range of temperature ($T = 296$ – 1025 K and 296 – 977 K, respectively), pressure ($p = 1$ – 10 bar) and bath-gas composition ($p_{O_2} = 0$ – 210 mbar) by measuring fluorescence lifetimes upon picosecond laser excitation at 266 nm.

Faust et al. also developed an empirical model for anisole [20] using data obtained at similar conditions. Wang et al. adapted a more physical step-ladder model to anisole [51] using experimental normalized FQY data for $p = 2$ – 40 bar and $T = 473$ – 873 K and different bath-gas compositions. Benzler et al. [48] investigated the effective fluorescence lifetime of anisole for temperatures between 296 and 475 K at low pressure (<1 bar). They observed a switch-over of the fluorescence lifetime from increasing to decreasing with pressure occurring between ambient temperature and 355 K and explained it with the transition from photo-induced heating (PIH) to photo-induced cooling (PIC).

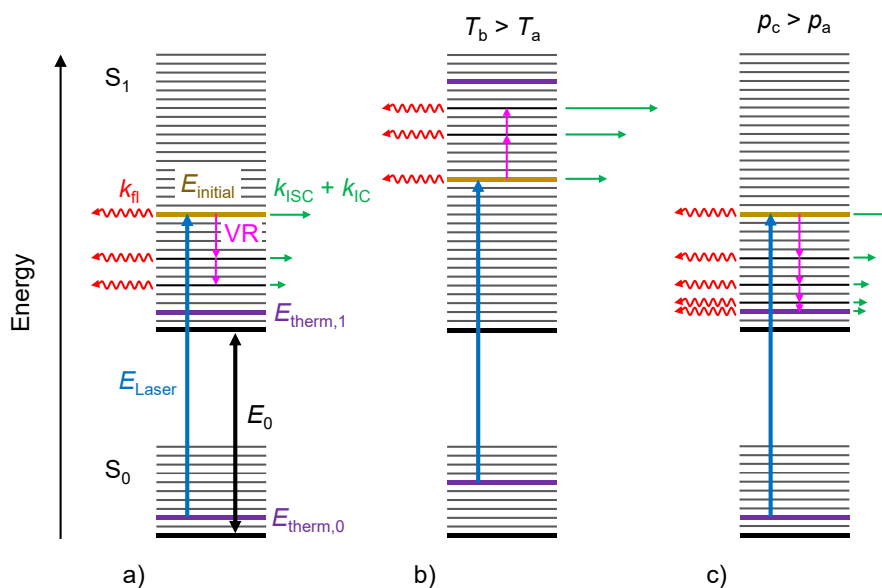


Fig. 7.1: Jablonski diagrams showing the principle of a) photo-induced heating, b) photo-induced cooling after increasing temperature, and c) photo-induced heating after increasing pressure based on the findings of Benzler et al. [48] and Baranowski et al. [52] for anisole at elevated temperatures.

Photo-induced heating (Fig. 7.1a) occurs if the initially populated vibrational energy level E_{initial} after laser excitation of the fluorophore exceeds the thermal energy level $E_{\text{therm},1}$, i.e., the most populated energy level of the thermal distribution in the excited state. Energy exchange (radiative or non-radiative) with the environment occurs while the excited molecule thermalizes to $E_{\text{therm},1}$. Photo-induced cooling (Fig. 7.1b) occurs if E_{initial} is below $E_{\text{therm},1}$ and the molecule extracts heat from the environment while relaxing through the vibrational energy levels. These effects were initially observed for naphthalene by Beddard et al. [125] and, later

thoroughly described and analyzed by Wadi et al. [126]. As the non-radiative deactivation rate k_{nr} increases with increasing vibrational energy, τ_{eff} is lower for higher excess energies for both tracers, anisole [51] and toluene [46]. Increasing pressure (Fig. 7.1c) leads to faster vibrational relaxation to $E_{therm,1}$ due to increased collision rate. This means that τ_{eff} increases with increasing pressure in the case of PIH (k_{nr} is higher at $E_{initial}$ compared to $E_{therm,1}$) and decreases in the case of PIC (k_{nr} is lower at $E_{initial}$ compared to $E_{therm,1}$).

Baranowski et al. [52] followed up on the findings of Benzler et al. [48] by systematically varying the excitation wavelength ($\lambda = 256\text{--}270$ nm) while measuring the fluorescence lifetime of anisole for moderate temperatures ($T = 335\text{--}525$ K) and pressures ($p = 1\text{--}4$ bar) above ambient conditions. By observing a vanishing pressure dependence (i.e., the tipping point where PIC switches to PIH) for a specific temperature and given excitation wavelength, they could improve the predictions of $E_{initial}$ by approximating the portion of $E_{therm,0}$ actually transferred to S_1 using the spectral overlap of the excitation wavelength with *ab initio* calculated absorption spectra. To this end, they exploited that at the tipping points, excitation occurs directly to the thermal energy level so that $E_{initial}$ equals $E_{therm,1}$. Hence, they were able to calculate the effective ground-state thermal energy $\bar{E}_{therm,0}$ from a straight-forward energy balance (Eq. 7.5) to support their assumptions.

$$\bar{E}_{therm,0} = E_{therm,1} - E_{Laser} + E_0 \quad (7.5)$$

However, there still exist uncertainties in the simulation of the absorption spectra at elevated temperatures due to unknown spectroscopic simulation parameters. Knowledge of additional tipping points, therefore, is crucial to validate the assumptions and further increase the accuracy of the predictions. One could also imagine using $\bar{E}_{therm,0}$ as additional fit parameter.

The work of Benzler et al. [48] also suggests that in the case of toluene, the PIH–PIC transition temperature for the commonly used excitation wavelength of 266 nm is below ambient conditions as the pressure dependence of the signal drops until his lowest measured temperature of 296 K. However, confirmation of this prediction has been lacking so far.

7.3 Experiment

7.3.1 Continuous flow cell

A liquid-cooled flow cell with four-way optical access was utilized for all experiments presented here (Fig. 7.2). The cell consists of the 150-mm long cylindrical test section with an inner diameter of 10 mm. Laser light enters and exits the cell through windows at its far ends while fluorescence can be collected through two side windows perpendicular to the light propagation direction in the center of the cell providing a large numerical aperture ($NA \approx 0.4$). An insulated outer jacket (inner diameter 40 mm) allows to circulate liquid coolant around all surfaces of the test section except the windows. Therefore, all windows are mounted retracted within the jacket to minimize heat losses. Threaded retainers made from low heat-conduction

plastic press the windows against o-ring seals that are supported by an inner metal ring. This permits inward and outward pressure loads for operation at below and above ambient pressure while enabling easy removal for cleaning purposes. The retainers feature tube connectors for providing a constant flush gas flow of dry N₂ to avoid condensation of atmospheric water on the outer window surfaces if the cell is operated below ambient temperature. Optionally, secondary windows can be mounted in the retainers to prevent water condensation. The temperature is measured by two thermocouples inserted approximately 2 mm into the flow through the inlet and exit lines, respectively.

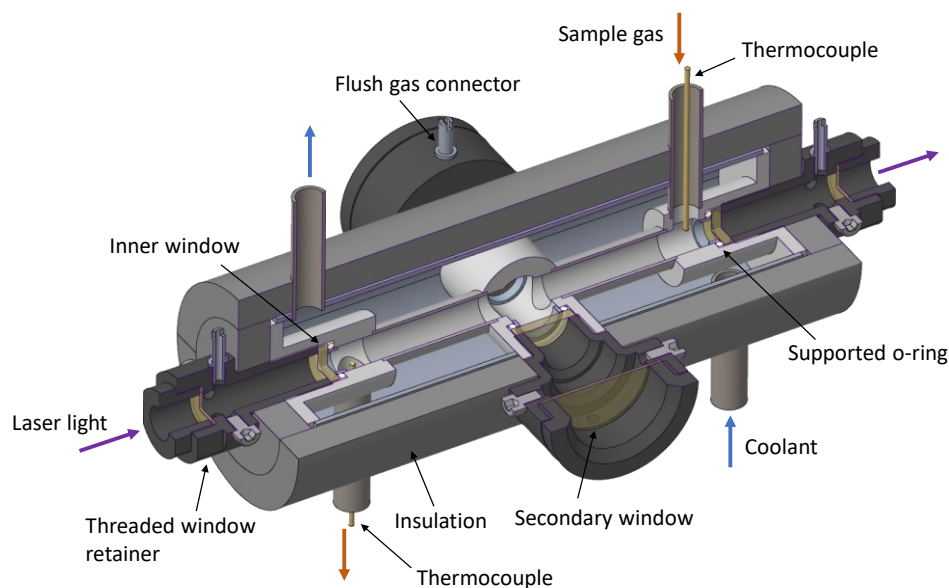


Fig. 7.2: Liquid-cooled flow cell with four-way optical access. Inner diameter along the laser light propagation direction is 10 mm, the absorption path length is 150 mm. Thermocouples are inserted through the sample-gas inlet and outlet so that their tips reach into the inner cell volume.

The sample-gas feed system consists of two mass flow controllers (MFCs) and a bubbler (Fig. 7.3). One MFC feeds the carrier gas (N₂) through a bubbler containing the tracer while the other provides a bypass flow (N₂) for dilution. The bubbler is cooled to the same temperature as the cell ensuring that the dew point temperature of the mixed gas flow is below the cell temperature to prevent condensation. The ratio of bypass-to-bubbler gas flow was 4:1, meaning that the tracer partial pressure was always below 20 % of its vapor pressure at any given temperature. This results in a maximum tracer number density (at the highest temperature and pressure investigated) of $<1.3 \times 10^{16} \text{ cm}^{-3}$ for anisole and $<1.1 \times 10^{17} \text{ cm}^{-3}$ for toluene and a lowest tracer number density (at the lowest temperature and pressure) of $<5.0 \times 10^{13} \text{ cm}^{-3}$ and $<6.8 \times 10^{14} \text{ cm}^{-3}$, respectively. A pre-cooler installed directly on top of the cell compensates for ambient heat added on the way ensuring minimal temperature variation inside the cell. In all cases, the coolant is provided by the same compressor-cooled circulating chiller (Huber Minichiller 300, cooling power 300 W at 15 °C and 70 W at -20 °C) with an operating temperature range from room temperature down to -20 °C. The total gas mass flow rate was 1000 sccm resulting in a flow velocity of approximately 0.3 up to 6 m/s. Thus, the complete cell volume is exchanged at least every second even in the worst (i.e., the highest-density) case.

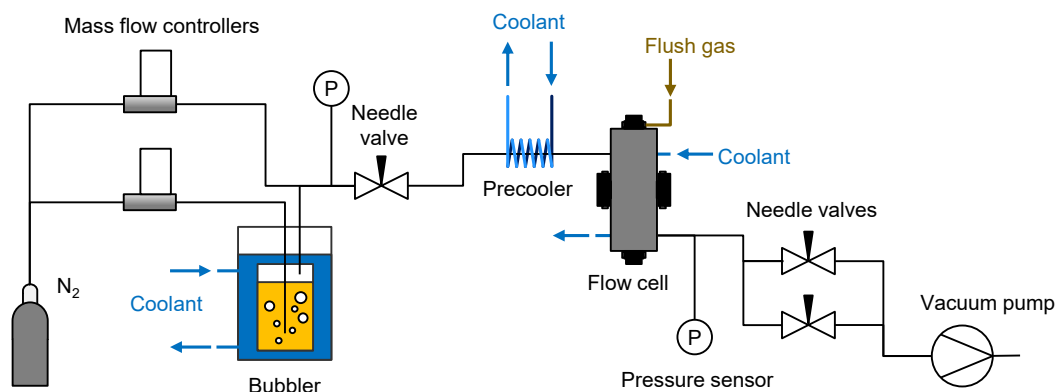


Fig. 7.3: Simplified flow diagram of the sample-gas feed system.

The pressure prior and after the flow cell is adjusted with needle valves. The first valve upstream of the flow cell is set to ensure that the pressure in the feed system before entering the cell and is above 2.5 bar monitored by a pressure transducer (Keller, 35 X HTC, 0–15 bar, accuracy 0.5 % of full scale). Maintaining this pressure ensures that ambient oxygen cannot enter the system even if small leaks exist. Two parallel needle valves downstream of the flow cell are required to set the cell pressure over the complete investigated range of 100–2000 mbar. The pressure in the flow cell is measured at the cell exit using a capacitance manometer (MKS, Baratron 722B, 0–5000 mbar, accuracy 0.5 % of reading). Prior to the experiments, the low-pressure section has been helium leak tested. The temperature is calculated from the arithmetic mean of the two thermocouples (type K, calibrated using the triple-point method) readings in the gas inlet and exit lines (Fig. 7.2). This approximation has been validated to be within the measurement error by inserting an additional thermocouple directly into the measurement plane through a stainless-steel dummy instead of one of the detection windows. Experiments were performed at five set-point temperatures with a repeatability of <0.05 K (95 % confidence interval).

7.4 Optical setup

7.4.1 Fluorescence lifetime measurements

The effective fluorescence lifetime was measured by time-correlated single photon counting (TCSPC, [127]) that has been applied to tracer LIF-related studies before [23, 26]. The TCSPC system (see Ref. [26] for details) consists of a mode-locked high repetition rate (1–20 MHz) picosecond fiber laser (Fianium, FemtoPower UVP266-PP-0.1, 266 nm, 5 nJ/pulse, 20 ps), a fast photomultiplier tube (PMT) (Hamamatsu, R3809U50, 150 ps rise time), and a TCSPC board (Becker & Hickl, SPC-130). Short excitation pulses are required because of the short fluorescence lifetimes of anisole [20, 48]. Because of the single-photon detection principle of TCSPC, experiments at very low signal levels are possible. This enables measurements with the low tracer partial pressures prevailing at the low temperatures. In addition, measurements can be carried out at low laser fluence, which prevents self-quenching by laser-excited molecules, according to the mechanism described by Fuhrmann et al. [16] for toluene. Hence,

limiting the number of excited molecules by either reducing the tracer concentration or the laser fluence eliminated any measurable non-linearities in the LIF signals vs. concentration. In our case, the laser fluence was $<0.6 \mu\text{J}/\text{cm}^2$ which is well below their established minimum $5 \text{ mJ}/\text{cm}^2$ where no non-linearities were observable at any conditions. We confirmed the linearity of the signal by systematically varying the bypass ratio from 4:1 down to 0 for both tracers.

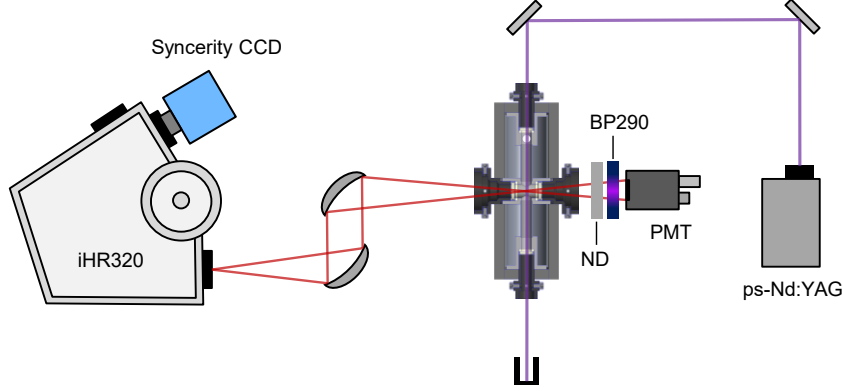


Fig. 7.4: Optical setup for simultaneous measurement of fluorescence spectra and fluorescence lifetimes.

The optical setup is shown in Fig. 7.4: The laser beam is directed centrally through the flow cell and fluorescence is detected through one of the quartz windows by the PMT mounted perpendicular to the beam propagation direction. A bandpass filter (Semrock, BP292, 292 nm, 14 nm FWHM) centered close to the peak wavelength of the fluorescence spectrum of both tracers (Fig. 7.5b) is used in front of the PMT to block residual ambient and laser stray light. For both tracers, Faust et al. established that the measured fluorescence lifetime was independent of the spectral integration window [20, 21]. Reflective UV-grade neutral-density (ND) filters (Thorlabs, NDUV, OD 0.3–3.0) are used to limit the photon count rate so that only after every 10^{th} – 200^{th} pulse a photon is detected avoiding pile-up effects [127] caused by more than one photon per laser pulse reaching the detector. The cavity in front of the laser inlet and outlet windows was deep enough to prevent interaction with moist room air by purging without an additional window, while the optical path to the PMT could be completely enclosed to ensure sufficient flushing by dry N_2 .

The fluorescence lifetime τ_{eff} is determined by the convolve-and-compare method [128]. To this end, the temporal fluorescence signal trace is modeled by the convolution (operator $*$) of the instrument response function (S_{IRF}) of the TCSPC system with a mono-exponential decay (Eq. 7.6). S_{IRF} corresponds to the elastically scattered light measured without the bandpass filter while flushing the flow cell with pure N_2 .

$$S_{\text{fl}}(t) = C_1 \left(S_{\text{IRF}}(t) * \exp\left(-\frac{t}{\tau_{\text{eff}}}\right) \right) + C_2 S_{\text{IRF}}(t) \quad (7.6)$$

The second term in Eq. 7.6 accounts for potential residual laser stray light. The scaling factors C_1 and C_2 as well as τ_{eff} are determined by fitting the model function to the temporal signal trace. The noise floor is subtracted from signal (<5 counts per channel) and S_{IRF} (<10 counts) to avoid artifacts during the convolution and preventing the need for an additional fit parameter for a constant offset. Example fits are shown for toluene at near ambient conditions in Fig. 7.5a, with the residuals between the model function and the measured data presented below the graph. Each measurement is repeated at least three times.

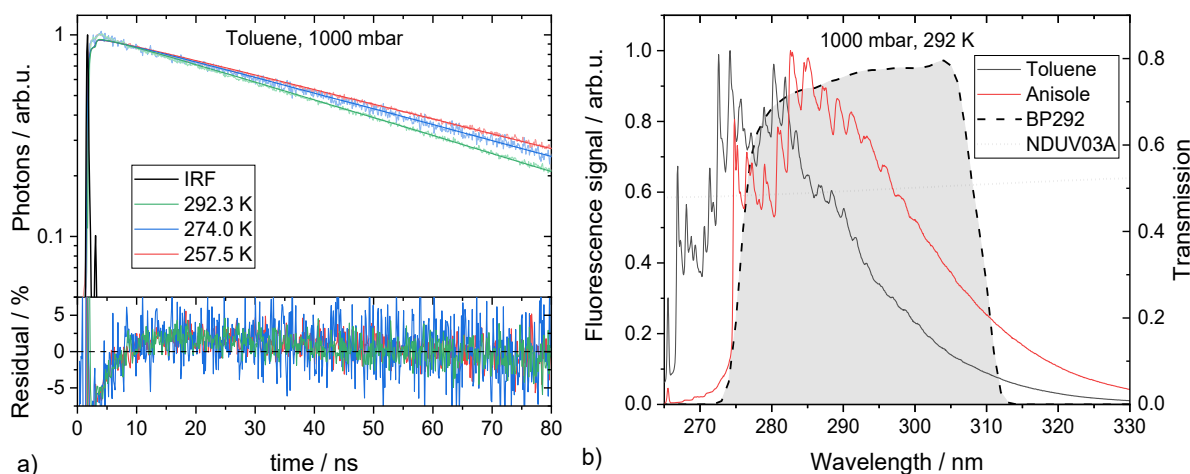


Fig. 7.5: (a) Typical TCSPC signal, IRF, and fit using the convolve-and-compare method. (b) Transmission bands of the BP292 bandpass filter and an ND filter with an optical density of 0.3 (Thorlabs, NDUV03A) for reference measured in a UV-Vis spectrophotometer (Varian, Cary 400 Scan) compared to spectra of toluene and anisole vapor in N_2 at near-ambient conditions.

7.4.2 Fluorescence spectra

Fluorescence spectra are measured following excitation with the same laser system operating at 2 MHz. Two off-axis parabolic mirrors (Fig. 7.4) image the fluorescence signal onto the entrance slit of a spectrometer (Horiba, iHR320, 320 mm focal length, 1200 groves/mm grating) with the spectrum in the exit plane dispersed on a CCD detector (Horiba, Sincerity CCD, 256×1024 pixels). The entrance slit opening is set to $100 \mu\text{m}$ while the exposure time (mechanical shutter) is varied from 1–10 s depending on the signal level. The intensity is integrated over the 256 vertical pixels. Note, that the spectra we measured for this work have not been smoothed. This was unnecessary since the integration time was chosen so that the signal level was at the maximum of the instrument's dynamic range so that signal noise is nearly imperceptible.

In a post-processing step, a previously recorded dark spectrum taken with the same exposure time (laser off) is subtracted. Outliers are removed prior to averaging individual spectra by interpolation between neighboring pixels. Spectra are then corrected for the wavelength-dependent transmission characteristics and detection sensitivity of the complete system, which was determined using an intensity-calibrated laser-driven light source (Energetiq EQ-99); the wavelength axis was calibrated using known atomic line emissions from a Hg(Ar) pen-ray lamp (LOT). The spectral resolution of the setup with the aforementioned settings was

measured to be 0.27 nm (FWHM of the 296.7-nm Hg line). To compare the measured fluorescence spectra with previously published data recorded at lower resolutions, the spectra were downsampled by convolution with a Gaussian function (Fig. 7.6), with a FWHM determined by minimizing the least-squares error to the literature data. Especially in the case of toluene, our spectra then agree well with those of Koban et al. [122]. Agreement with the spectra of Faust et al. [20], however, is not so good, which may be attributed to their significantly lower spectral resolution of ~ 3 nm of the streak camera system used in their work.

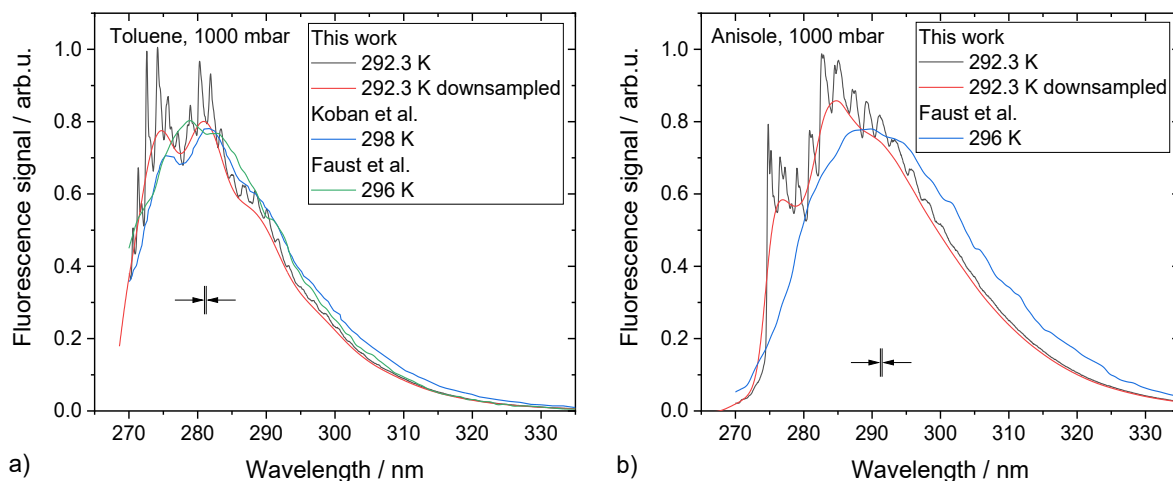


Fig. 7.6: Measured (a) toluene and (b) anisole fluorescence spectra at close-to standard conditions next to literature data from Koban et al. [122] and Faust et al. [20]. For better comparability, the new high-resolution (0.26 nm indicated by arrows) spectra were downsampled by convolution with a Gaussian with an FWHM of ~ 2.35 nm.

Each individual spectrum in Fig. 7.6 and in the following chapter is normalized by its integral value between 275–360 nm. The ordinates of each plot are then scaled arbitrarily so that $y = 1$ corresponds to the maximum intensity of each test series, thus maintaining the relative intensity of the graphs to each other. The spectral interval for the normalization was chosen so that laser stray light (visible in low-intensity measurements, cf. Fig. 7.12a on the left-hand side) would not distort the graphs ratio to each other.

7.5 Results

7.5.1 Anisole

As shown in Fig. 7.7a, for anisole, τ_{eff} decreases in the low-pressure region (< 600 mbar) with decreasing pressure thus exhibiting PIH behavior at all temperatures investigated. This is in good agreement with Benzler et al. [48] who found that $E_{\text{initial}} > E_{\text{therm},1}$ for excitation at 266 nm and temperatures from ambient to about 400 K. For higher pressures (> 800 mbar), τ_{eff} decreases slightly supposedly due to increased nitrogen bath gas quenching. A similar effect on the fluorescence lifetime has been observed by Cheung et al. for 3-pentanone [123]. At all temperatures, anisole fluorescence lifetimes exhibit a similar temperature dependence (Fig. 7.7b) decreasing by 10 % over the investigated temperature range of about 35 K.

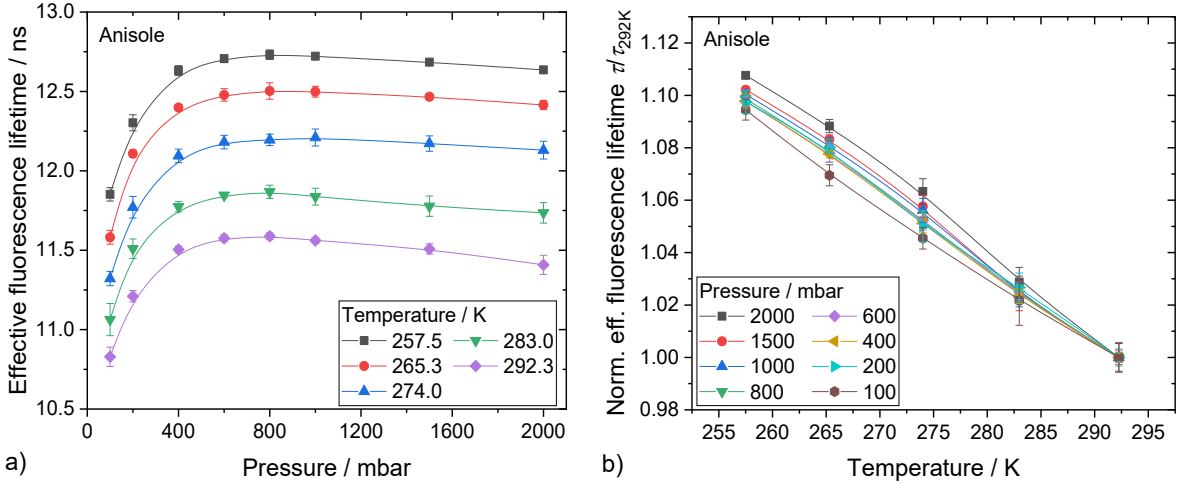


Fig. 7.7: (a) Pressure dependence of the effective fluorescence lifetimes of anisole for a range of temperatures below ambient. (b) Relative (normalized by the room temperature value) effective fluorescence lifetime showing the temperature dependence for the investigated pressure range. Error bars represent the statistical error of repeated measurements. Lines (spline fits) were added to guide the eye.

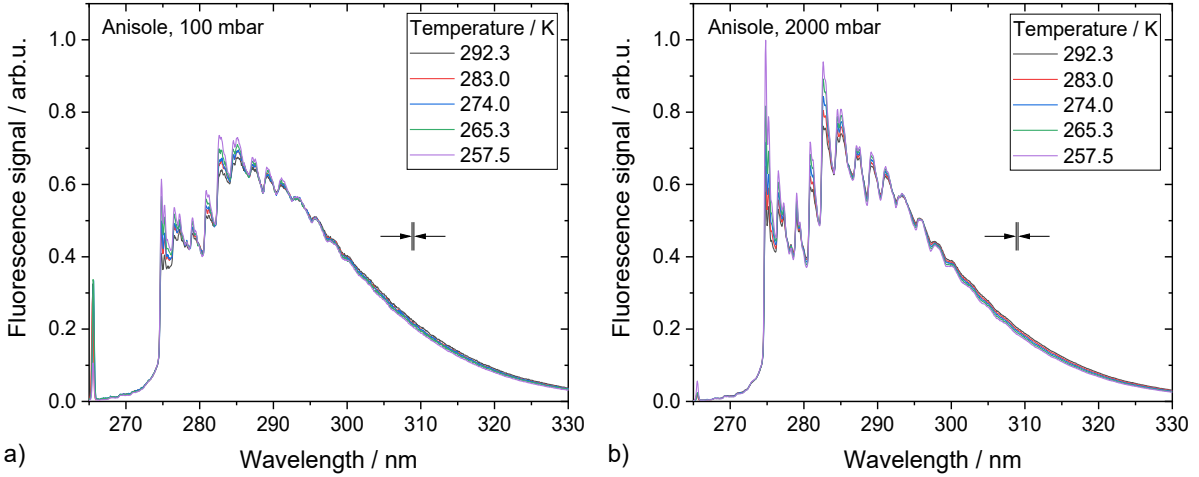


Fig. 7.8: Temperature-dependent normalized anisole fluorescence spectra for (a) the lowest (100 mbar) and (b) for the highest measured pressure (2000 mbar). Arrows indicate the spectral resolution.

Normalized fluorescence spectra for anisole are shown in Fig. 7.8 for the lowest (a) and highest (b) investigated pressure. In both cases, an increase in temperature causes a slight broadening of the spectra, which is most prominent in the sharper spectral features at shorter wavelengths. Additionally, a slight shift of the spectral centroid to longer wavelengths is visible (cf. Fig. 7.10). The spectral centroid λ_c can be interpreted as the center of the area below each intensity curve and is calculated according to Eq. 7.7.

$$\lambda_c = \frac{\int \lambda S_{fl}(\lambda) d\lambda}{\int S_{fl}(\lambda) d\lambda} \quad (7.7)$$

One needs to be careful to not confuse shifts of the spectral centroids with a shift of the fluorescence spectra. Rather, the spectral features at shorter wavelengths become weaker compared to those at longer wavelengths so that only normalized spectra appear to shift. The shift of the

anisole fluorescence spectral centroid with increasing temperature can be explained by considering the anharmonicity of S_0 and S_1 : The increase of ground state energy at increased temperature results in a population of higher vibrational levels in S_1 . If one considers only that more energy is available, one expects a shift to shorter wavelengths. However, it follows from the Franck-Condon principle that transitions are particularly strong that link similar vibration levels v' in S_1 and v'' in S_0 . As a result of an increase in anharmonicity from S_0 to S_1 , the well depth (dissociation energy) in S_1 is smaller than in S_0 , and $E(v')$ is converging faster than $E(v'')$. This and the Franck-Condon principle then cause that an increase in $E(v')$ (e.g., by temperature increase) is associated with a shift of the spectral centroid to longer wavelengths. The shift to the short wavelength by increasing p is caused by the same effect since anisole shows PIH behavior so that collisions reduce $E(v'')$. For more details, see, e.g., Uy et al. [129].

Somewhat unexpectedly, as shown in Figs. 8 and 8 for the lowest and highest temperatures investigated, a reduction in total pressure broadens the spectral features. This behavior can be explained by considering that for a molecule undergoing slow VR (long τ_{eff}), fluorescence occurs from several levels along the vibrational energy cascade (cf. Fig. 7.1a). A rapidly thermalized (short τ_{eff}) molecule, in contrast, emits light from a narrower distribution of energy levels around $E_{\text{therm},1}$.

Kimura et al. [99] observed this effect by evaluating highly time-resolved fluorescence spectra for naphthalene. Spectra measured just after (1 ns) excitation, well before the estimated mean collision time (~ 6 ns), exhibited a broadband structure while spectra measured after several collisions (up to 120 ns) were much finer structured. They concluded, that in the first case only sub-nanosecond IVR was responsible for the broader energy distribution of emitting vibrational energy levels, while in the second case molecules have already thermalized to a narrow energy distribution around $E_{\text{therm},1}$.

In the case of anisole, the mean time between collisions at room temperature has been estimated to 0.82 and 0.03 ns at 100 and 2000 mbar, respectively, by calculating the Lennard–Jones frequency using the coefficients from Wang [51] and assuming a bubbler efficiency of 75 % (actual anisole vapor pressure divided by saturation vapor pressure). This means, that especially in the low-pressure case, only few (<15) collisions occur during the fluorescence lifetime compared to the high-pressure case (>380). This explains the much broader spectral structure of the former as IVR has a larger effect on the vibrational energy distribution compared to the external (collision-driven) VR.

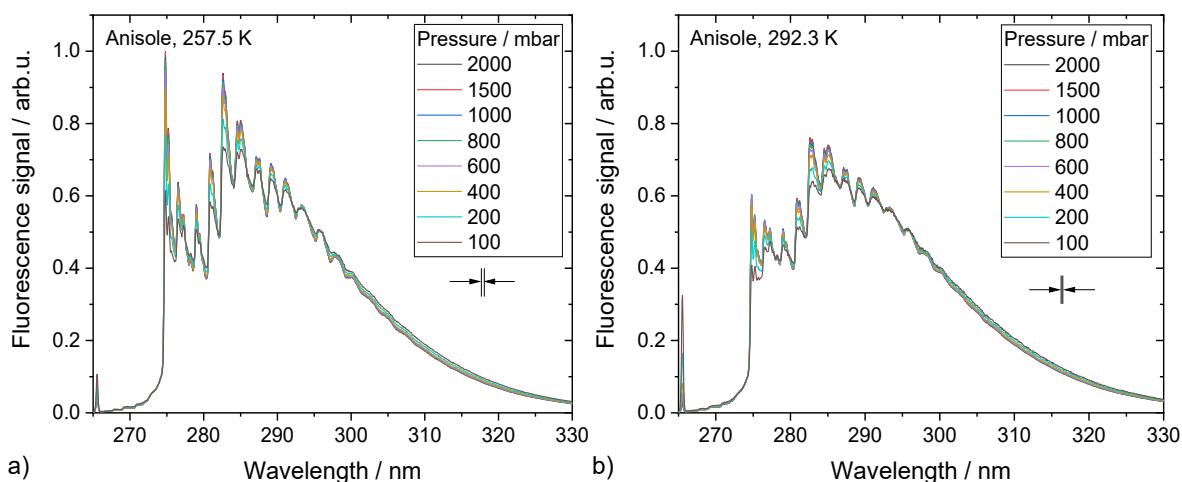


Fig. 7.9: Pressure-dependent normalized anisole fluorescence spectra for (a) the lowest (257 K) and (b) for the highest measured temperature (292 K). Arrows indicate the spectral resolution.

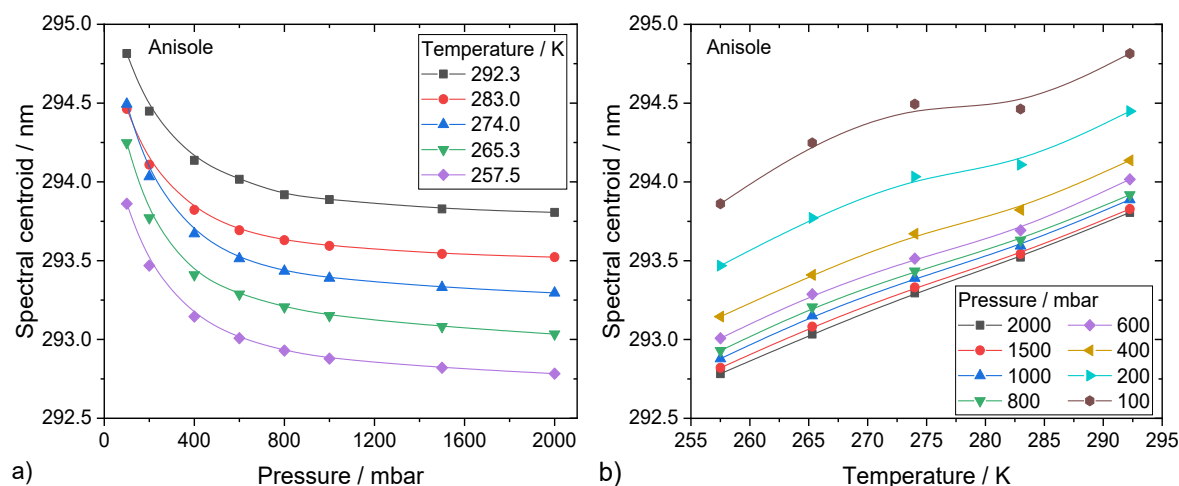


Fig. 7.10: Wavelength of the centroid of the anisole fluorescence spectra calculated for the region from 275 to 360 nm as (a) a function of pressure and (b) a function of temperature. Lines (spline fits) were added to guide the eye.

7.5.2 Toluene

As shown in Fig. 7.11a, for toluene, τ_{eff} increases monotonously with pressure in the low-pressure region (< 600 mbar) for $T \leq 274$ K but decreases for 292 K. This implies that the transition from PIC to PIH occurs between 292 K and 283 K as predicted when extrapolating the results of Benzler et al. [48]. For both cases τ_{eff} decreases slightly for higher pressures (> 800 mbar) due to increasing nitrogen quenching. Contrary to anisole (cf., Fig. 7.7b), the temperature dependence of τ_{eff} (Fig. 7.11b) differs significantly for different pressures. Whereas τ_{eff} decreases $\sim 26\%$ at 2 bar, it only drops $\sim 10\%$ at 100 mbar over the investigated temperature range of 35 K while exhibiting a more non-linear behavior.

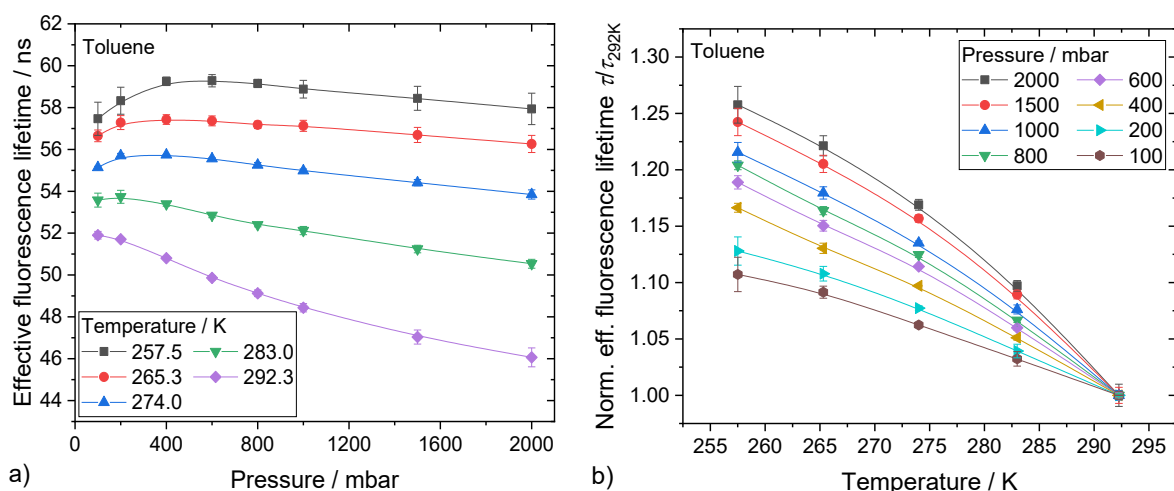


Fig. 7.11: (a) Pressure dependence of the effective fluorescence lifetimes of toluene for a range of temperatures below ambient. (b) Relative (normalized by the room temperature value) effective fluorescence lifetime showing the temperature dependence for the investigated pressure range. Error bars represent the statistical error of repeated measurements. Lines (spline fits) were added to guide the eye.

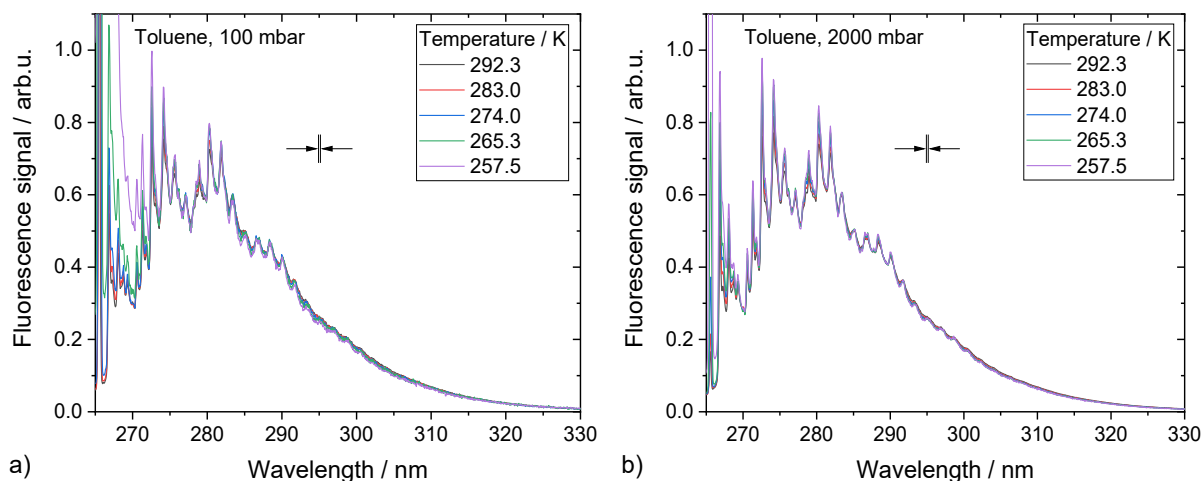


Fig. 7.12: Temperature-dependent normalized toluene fluorescence spectra for (a) the lowest (100 mbar) and (b) for the highest measured pressure (2000 mbar). Arrows indicate the spectral resolution.

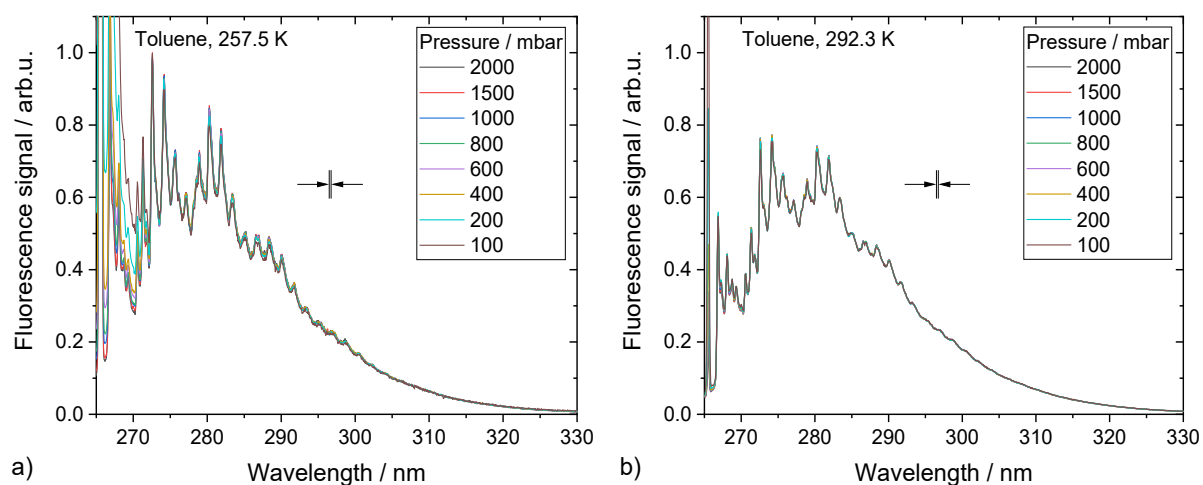


Fig. 7.13: Pressure-dependent normalized anisole fluorescence spectra for (a) the lowest (257 K) and (b) for the highest measured temperature (292 K). Arrows indicate the spectral resolution.

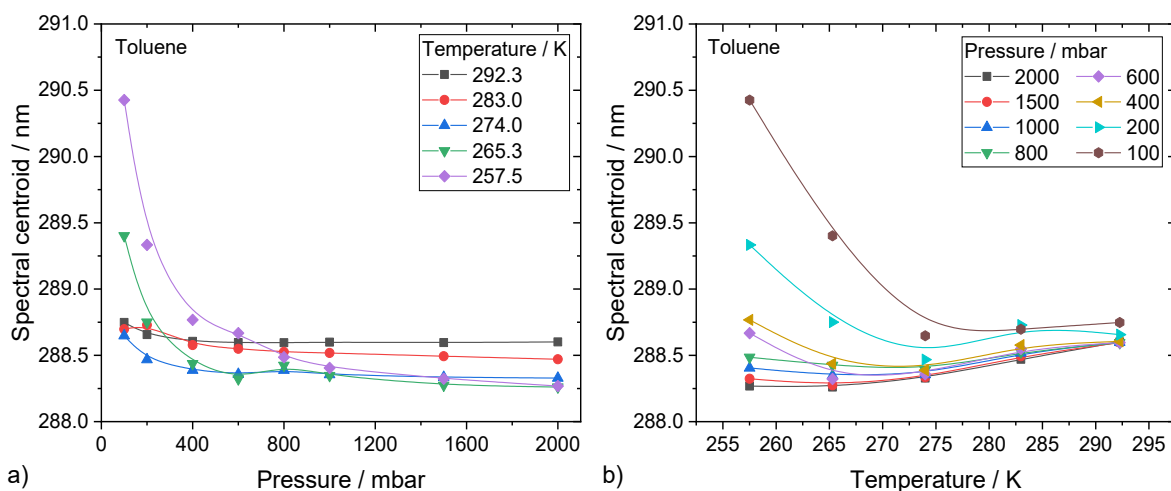


Fig. 7.14: Wavelength of the centroid of toluene fluorescence spectra calculated for the region from 275 to 360 nm as (a) a function of pressure and (b) a function of temperature. Lines (spline fits) were added to guide the eye.

Toluene fluorescence spectra are shown as a function of temperature (Fig. 7.12) and pressure (Fig. 7.13), for the lowest (panels a) and the highest (panels b) pressure and temperature, respectively. It is apparent, that the spectra are nearly invariant to changes in pressure. At the lowest temperature (Fig. 7.13a), however, the fine structure of the spectrum is more pronounced compared to the room temperature spectrum (Fig. 7.13b). The spectral intensity centroid remains nearly constant except for the low-temperature (i.e., below about 280 K) and low-pressure (i.e., below about 800 mbar) cases where it red-shifts by up to 1.5 nm (Fig. 7.14). Unfortunately, scattered laser light (Figs. 7a and 7a, left-hand side of the spectrum) affects the calculation of the centroids especially at those low-signal conditions. The absence of a significant low-pressure broadening compared to anisole can be explained by the much longer fluorescence lifetimes (Fig. 7.11) and, therefore, more dominant VR and insignificant contribution of IVR to the temporally integrated fluorescence signal.

7.6 Implications for temperature measurements

Quantitative LIF measurement techniques generally exploit that the absorption and fluorescence properties of the fluorophore, or rather the combination of both, can be related to a physical property (temperature, pressure, concentration, bath gas composition) [28]. Two-color detection schemes are often used to measure the spectral change of the fluorescence signal by spectrally separating it onto two detectors. This method is popular [121] since it allows for directly imaging a dependent variable (i.e., the ratio of both detector signals) using a relatively simple setup (single light source with two cameras with different optical filters). However, it requires at least a single-point calibration to account for differences in detection efficiency of both detection channels. This often proves difficult for experiments that only allow calibration under controlled conditions at rest. This applies, e.g., in cases where optical accesses shift spatially due to thermal expansion under operating conditions as we encountered in previous experiments [80]. Fluorescence-lifetime based methods, on the other hand, measure the

fluorescence decay time which can be detected independently of the variable sensitivity of the detection hardware. This makes them especially attractive for challenging environments [23, 26] if spatial resolution is not required or achieved otherwise (e.g., by scanning the laser beam).

To evaluate the suitability of the data for temperature measurements relying on the two measurement schemes discussed above (spectral and lifetime-based), the sensitivity of either was calculated for atmospheric pressure as an example. For the lifetime-based scheme we assumed that fluorescence lifetime is measured while the properties of interest are interpolated from the tabulated lifetime data. For the spectral method, we used the single-color excitation (266 nm) and two-color detection scheme employed by Kranz et al. [130] for anisole and Gamba et al. [3] for toluene to calculate the signal ratio based on their respective spectral filter sets. Since Gamba et al. used two independent optical paths, each camera was equipped with its own filter, a 280-nm (± 5 nm) bandpass and a 305-nm longpass (colored glass), respectively (Fig. 7.15b). Their choice was based on previous work, where the suitability of different filter sets based on sensitivity and signal-to-noise ratio was considered [5]. In the case of Kranz et al., the optical paths of both channels partly overlap until the light is separated by a dichroic beam splitter (310-nm cut-off wavelength) before it reaches the cameras individual filters, a 280-nm (± 10 nm) and a 320-nm (± 20 nm) bandpass. Additionally, each camera is equipped with a 266-nm longpass filter to block scattered laser light. The resulting filter curves (Fig. 7.15a) have been calculated from the manufacturer's (Semrock) datasheets.

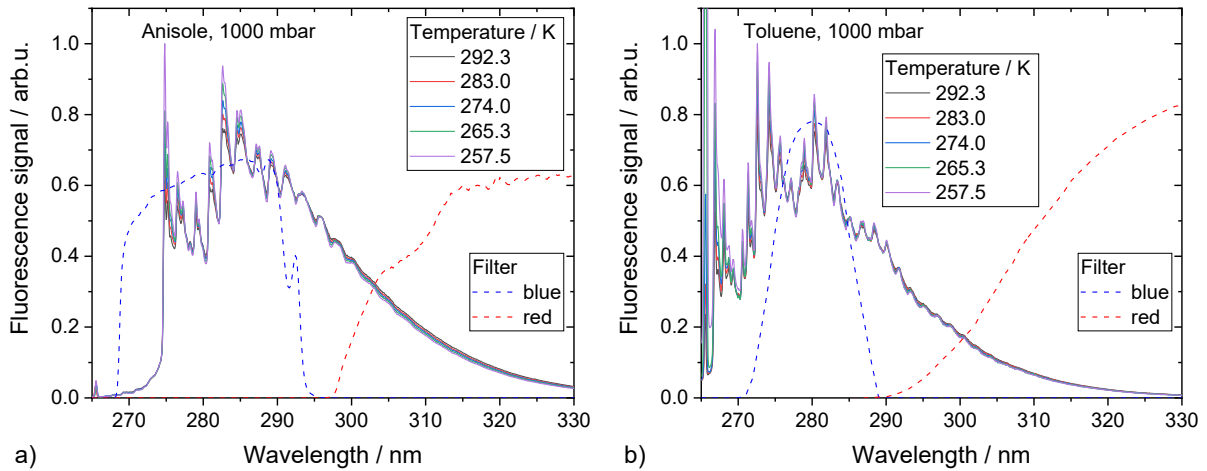


Fig. 7.15: Spectra and filter curves for a hypothetical two-color detection scheme to measure temperature based on the optical filter sets used by (a) Kranz et al. [130] for anisole and (b) Gamba et al. [3] for toluene.

The resulting signal ratios $R = S_{\text{blue}}/S_{\text{red}}$ for are shown in Fig. 7.16 for a (a) temperature variation at $p = 1000$ mbar and (b) pressure variation at $T = 274$ K. For better comparison to the evolution of the fluorescence lifetime data, both R and τ_{eff} are normalized their ambient value and are further referred to as the normalized dependent variable I . The dashed lines in Fig. 7.16a represent second-order exponential functions that have been fitted to I . These have been used to calculate the sensitivity shown in Fig. 7.16b defined as the absolute normalized change of I over the normalized change of the temperature.

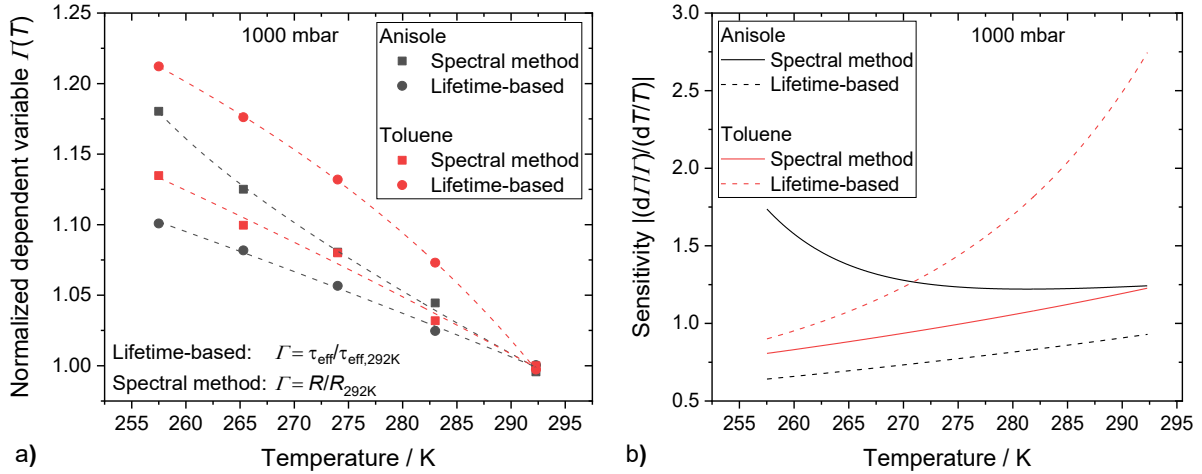


Fig. 7.16: (a) The experimentally-accessible independent variable Γ normalized to ambient conditions of a temperature series at 1000 mbar and (b) the according sensitivities of the hypothetical measurement schemes calculated from a second-order exponential fit (shown as dashed lines in (a)).

The lifetime-based method outperforms the spectral method in the case of toluene regarding its sensitivity, especially in the higher temperature region. In the lower-temperature region however, the sensitivities are similar. For anisole, the spectral method yields a higher sensitivity also showing a positive trend with decreasing temperature. In all cases, one would have to consider the achievable signal level of each method. For the spectral method, e.g., one may opt for a different filter pair to trade off some sensitivity for increased signal-to-noise ratio which is especially important for ratiometric methods [121]. For measurements in steady-state applications where averaging does introduce only minor statistical error, one may choose the opposite.

7.7 Conclusions

Effective fluorescence lifetimes (Appendix A) and higher resolution (0.27 nm) fluorescence spectra of anisole and toluene vapor in nitrogen have been studied for 266-nm excitation in a temperature range below ambient (257–293 K) for various pressures (100–2000 mbar), thus extending the available datasets for these common aromatic tracer LIF species to conditions prevalent, e.g., in trans-/supersonic flow experiments. The measured dataset enables thermometry or even pressure sensing (if temperature can be established otherwise, e.g., by laser-induced thermal acoustics [82]) under such conditions using either fluorescence lifetime-based or spectral (single-color or two-color-ratio) LIF schemes. We found that thermometry using toluene LIF with a lifetime-based measurement scheme could compete with the sensitivity achieved with a commonly applied spectral ratiometric method. It is important to note that the lifetime-based measurement scheme, contrary to the spectral-method, does not require a single-point calibration making it particularly useful in applications where controlled reference-conditions cannot be achieved easily. Further, this method allows measurements with a single light source and single detector independent of tracer concentration without the need of ratioing (i.e.,

introducing additional error), which is highly useful to measure temperature or pressure in, e.g., mixing flows.

The transition from photo-induced cooling (PIC) to photo-induced heating (PIH) behavior was observed for toluene between 283 and 292 K, confirming predictions from literature [48]. As this transition marks the point where the initial energy after excitation equals the thermal energy in the S_1 state ($E_{\text{initial}} = E_{\text{therm},1}$), no vibrational relaxation occurs during deexcitation since the molecule is already thermalized. This enables the calculation of the averaged ground state energy $\bar{E}_{\text{therm},0}$ transferred from S_0 to S_1 for the given excitation wavelength from a straightforward energy balance [52]. Baranowski et al. [52] recently identified the (usually) unknown $\bar{E}_{\text{therm},0}$ is a major cause of uncertainty in step-ladder models. Hence, these points are crucial for model validation and development.

For anisole, a broadening of fluorescence spectra correlating with decreasing fluorescence lifetimes with total pressure was observed while for toluene the spectra remained nearly invariant to pressure. This is consistent with literature [99] identifying sub-nanosecond intramolecular vibrational energy redistribution (IVR) as the responsible mechanism, which is more dominant at conditions where fewer collisions with bath gas molecules occur (i.e., in the case of short excited state lifetimes, low density, and low temperatures). Published step-ladder fluorescence models [46, 123, 124] neglect IVR since they were parameterized for above-ambient conditions. Our findings imply that accounting for IVR will be crucial for advancing these models to below-ambient conditions.

All measured effective fluorescence lifetimes measured for both tracers are summarized in Appendix A. At the present time we are preparing to launch an online database dedicated to sharing and visualizing published and unpublished spectroscopic data for gas-phase tracer LIF applications [131] to which the data including the fluorescence spectra will be uploaded.

8 Miniature flow channel

It is intended to submit the contents of this chapter as for publication as a separate research paper under the following title.

Beuting, M., Richter, J., Schulz, C., Weigand, B., Endres, T. *Miniature flow channel for spectroscopic characterization of fluorescence tracers for in situ optical diagnostics.*

My personal contribution was the mechanical design and construction of the flow channel experiment including gas conditioning, OD calculations, and design and operation of all optical and non-optical instrumentation. I planned, performed, and evaluated all experiments. Judith Richter designed the nozzle geometry and supported the design of the flow channel in the planning phase by preliminary CFD simulations and contributed the 3D CFD simulations to this publication. The manuscript was prepared by me, to which all co-authors also contributed by scientific advice, proofreading, and help with the wording.

Abstract A small-scale rectangular flow channel is introduced to provide a low-temperature environment for spectroscopic characterization of gaseous fluorescence tracers. The tracer-laden gases are cooled gas-dynamically by acceleration through a convergent-divergent nozzle to supersonic speeds before entering a four-way optically accessible test section. Its modular approach enables the variation of its internal geometry and, therefore, flow conditions. In this paper, a $M = 1.7$ nozzle was used to resemble flow conditions used in a larger-scale flow channel used in our previous works, where temperatures as low as 240 K are expected. Due to its small cross-section of $5 \times 5 \text{ mm}^2$ at the nozzle exit, the mass flows were low enough so that the miniature flow channel could be, unlike its larger counterpart, operated with pure N_2 with arbitrary O_2 concentrations. In this paper, the flow conditions in the flow channel are first characterized in detail. For this purpose, fluorescence lifetime based LIF thermometry was used in addition to CFD simulations, schlieren imaging, and LIF imaging. In an example measurement to demonstrate the suitability of the flow channel for tracer spectroscopy down to about 230 K, the influence of oxygen quenching on the LIF signal of toluene was investigated. We found that the quenching effect is independent of temperature even at O_2 concentrations as low as 1 vol.%. This implies that LIF imaging methods relying on the O_2 quenching effect for, e.g., the investigation of sub-resolution mixing processes, could be applied to transonic flows where strong temperature gradients exist.

8.1 Introduction

Despite many efforts studying transonic mixing wake flows, the underlying principles are not yet fully understood. Understanding the gas mixing in such flows both on a macroscopic level and on a molecular level on the flow conditions is important for fuel/air mixing in supersonic combustion or for mixing of reactants in supersonic nanoparticle synthesis reactors [1]. In our previous work we characterized transonic mixing wake flows using various optical methods such as schlieren or shadowgraphy [59, 60, 65, 79], particle imaging velocimetry (PIV) [2],

laser-induced thermal acoustics (LITA) [82], and laser-induced fluorescence (LIF) [59, 60, 64, 65, 80]. While LIF imaging can provide information about the mixing level on a macroscopic and a molecular level [70, 73, 75, 77, 119] of two gas flows, the spectroscopic properties under the relevant temperature and pressure conditions must be known. Toluene is frequently used for such studies as it provides a high fluorescence quantum yield. Its strong dependence on collisional quenching by molecular oxygen can be additionally used to determine mixing on a molecular level [18, 21, 38]. Toluene can be excited by commonly available laser wavelengths (e.g., 266 or 248 nm) [120] and is readily available for large-scale flow experiments, being environmentally acceptable [28]. However, very few works focus on the sub-ambient-temperature fluorescence properties of toluene [49] limiting its use to quantitative studies in the case of accelerated flows in which the temperature can be as low as 240 K [60, 80]. To fill this gap in the available spectroscopic data, we use a supersonic optically accessible miniature flow channel that provides the required conditions by gas-dynamic cooling for characterizing fluorescence tracers. The facility additionally acts a testbed for calibration and demonstration of imaging techniques.

Gas-dynamic cooling of sample gases is a common technique for accessing low-temperature regimes [132-134]. For LIF-based imaging measurements in such an environment, Combs et al. expanded a preheated sample gas containing naphthalene vapor provided by a sublimation seeder into an optically accessible evacuated chamber through different convergent-divergent nozzles covering a parameter space of 100–525 K and 10–400 mbar [8]. In a separate experiment, they used a rectangular flow channel to validate their measurement schemes in a turbulent boundary layer [9]. Later, they used the spectroscopic data to image the transport of ablation products of a heat shield approximated by a solid naphthalene layer in the wake of a space capsule during atmospheric reentry by correcting the signal for its temperature and oxygen dependence [7]. Handa et al. applied acetone LIF in a rectangular flow channel (design Mach number $M = 2.0$) to measure the local species number density as a metric for local pressure variations [11]. Their channel height was 0.5 mm whereas the width was 2.5 mm, which is more than one order of magnitude smaller than the channel presented here. They studied the influence of the inlet pressure and the flow channel length on the flow pattern, more precisely, on the shock pattern forming in high length-to-height ratio flow channels at relatively low Reynolds numbers ($Re = 3100$). They found that the relations for high Reynolds number flows did not apply: They observed a gradual pressure change instead of the normal shocks or pseudo-shocks expected in under expanded confined flows. Recently, Yu et al. used a two-tracer (acetone and toluene) approach to measure the oxygen concentration in an atmospheric nozzle flow quantitatively [76]. To this end, they first characterized the fluorescence properties of both tracers and the tracer mixture in a purpose-built static cell. The local oxygen concentration was then derived by calibration of the ratio of the individually registered LIF signals of both tracers similarly to the approach by Koban et al. [29] demonstrated for a toluene/3-pentanone mixture. They found that there is a significant quenching caused by acetone on the fluorescence signal of toluene. Ehn et al. used the fluorescence lifetime relying on precise gating of two detectors

for measuring the local oxygen concentration in an atmospheric jet containing toluene [31, 107] and for qualitative measurements in combustion processes [135].

8.2 Theory

8.2.1 Fluid dynamics

The compressible accelerated flow in the flow channel nozzle can be described by a set of equations [84]. Assuming an isentropic change of state, the local Mach number M and the geometry of the nozzle are related as follows. Here κ is the ratio of the specific heats, A is the cross-sectional area, and A^* the narrowest cross-section at which $M = 1$.

$$\frac{A}{A^*} = \left(\frac{2 + (\kappa - 1)M}{\kappa + 1} \right)^{\frac{\kappa+1}{2\kappa-2}} M^{-1} \quad (8.1)$$

The state variables such as temperature T and pressure p can also be expressed via the ideal gas law as a function of the local M .

$$\frac{T}{T_0} = \left(\frac{\kappa - 1}{2} M^2 + 1 \right)^{-1}, \quad \frac{p}{p_0} = \left(\frac{\kappa - 1}{2} M^2 + 1 \right)^{\frac{\kappa}{1-\kappa}} \quad (8.2)$$

Especially in small flow channels as discussed in this work, boundary layer effects play a significant role due to wall-to-wall interaction in the corner regions of the rectangular cross-section. While the scope of this work does not comprise boundary layer theory, we focus on the adverse effect of boundary layer growth on the usable measurement volume (i.e., the boundary layer free section of the flow) determined by numerical simulations and experimental data. To this end, we define the velocity boundary layer position $\delta_{u,99}$ at the point where the velocity u equals the asymptotic velocity u_∞ according to the following equation. The temperature boundary layer position $\delta_{T,99}$, which is particularly important for the selection of the probe volume for tracer characterization, is defined analogously.

$$u(x, z = \delta_{u,99}) = 0.99u_\infty(x) \quad (8.3)$$

$$T(x, z = \delta_{T,99}) = 0.99T_\infty(x) \quad (8.4)$$

The compressible displacement thickness δ^* is then calculated between the flow channel wall and the velocity boundary layer according to Eq. (8.5) considering the local density ρ .

$$\delta^*(x) = \int_{z_{\text{wall}}}^{\delta_{99}} \left(1 - \frac{(x, z)u(x, z)}{\rho_\infty(x)u_\infty(x)} \right) dz \quad (8.5)$$

8.2.2 Laser-induced fluorescence

In this work, laser-induced fluorescence diagnostics using toluene as tracer (tracer LIF) serves two purposes: Firstly, it is used to characterize of the flow channel by providing in situ measurement of temperature and the mixing state of the sample gases on a macroscopic level (section 8.6). Secondly, it is applied to demonstrate the flow channel's ability for spectroscopic tracer characterization and the feasibility of measuring mixing behavior on a molecular level (see section 8.7). The underlying principles are discussed in the following paragraphs.

The fluorescence signal intensity S_{fl} (Eq. 8.6) is linearly dependent on the tracer number density n_{tracer} and the exciting laser intensity I_{laser} if concentration and laser light are significantly below the onset of non-linear saturation effects or self-quenching [16]. Due to the dependence of the tracer absorption cross-section σ_{abs} and the fluorescence quantum yield ϕ_{fl} on temperature T and pressure p , one parameter can be determined directly from the LIF signal, provided the other can be determined otherwise.

$$S_{\text{fl}} \propto n_{\text{tracer}} I_{\text{laser}} \sigma_{\text{abs}}(T, p) \phi_{\text{fl}}(T, p, p_{\text{q}}) \quad (8.6)$$

Molecular oxygen quenches the fluorescence signal of aromatics efficiently leading to a significant reduction in the fluorescence signal accompanied by an apparent red shift of the fluorescence spectrum [38]. The strength of the quenching effect depends on the collision rate of the O_2 molecules with the tracer molecules and, therefore, ϕ_{fl} also depends on the local quencher species concentration expressed as the quencher partial pressure p_{q} . This allows for an indirect measurement of the mixing state on a molecular level if, e.g., an O_2 -free flow is mixed with an O_2 -containing flow using a single tracer [30].

The fluorescence quantum yield is defined as the ratio of the fluorescence rate constant k_{fl} to the total deactivation rate being the sum of all rate constants k_{tot} (Eq. (8.7)). Here, k_{nr} comprises the non-radiative deactivation rate constants for intersystem crossing and internal conversion, and k_{q} the quenching rate. The reciprocals of k_{fl} and k_{tot} are the natural fluorescence lifetime τ_{fl} and the effective fluorescence τ_{eff} , respectively. Therefore, ϕ_{fl} and, consequently, the LIF intensity S_{fl} is proportional to τ_{eff} which is experimentally accessible by measuring the fluorescence signal decay curve [28].

$$\phi_{\text{fl}} = \frac{k_{\text{fl}}}{k_{\text{fl}} + k_{\text{nr}} + \sum k_{\text{q}} p_{\text{q}}} = \frac{k_{\text{fl}}}{k_{\text{tot}}} = \frac{\tau_{\text{eff}}}{\tau_{\text{fl}}} \propto \tau_{\text{eff}} \quad (8.7)$$

The great advantage of using τ_{eff} instead of S_{fl} to measure flow properties is that it is neither dependent on the tracer concentration nor on the detection system efficiency ζ . In addition, we have found that in the case of toluene under sub-ambient conditions, a fluorescence lifetime-based scheme for temperature measurement provides some advantage in terms of sensitivity over schemes that detect spectral changes using two-color detection [49].

8.3 Flow channel experiment

The flow channel's primary purpose is to provide conditions found in larger-scale flow channels [59, 60, 64, 65] for developing and validating laser-based diagnostics such as LIF. Its smaller scale and, therefore, reduced mass flows allow to use the channel with pure nitrogen instead of compressed air. This is crucial for developing measurement strategies for determining sub-resolution mixing states by indirectly measuring the effect of oxygen quenching on the fluorescence signal [80]. The gas-dynamic cooling enables measurements for characterization of the spectroscopic properties of the tracer in an extended temperature range of our previous works [48, 49] aiming at improving the fundamental understanding of tracer photophysics to temperatures below room temperature in a continuous flow system.

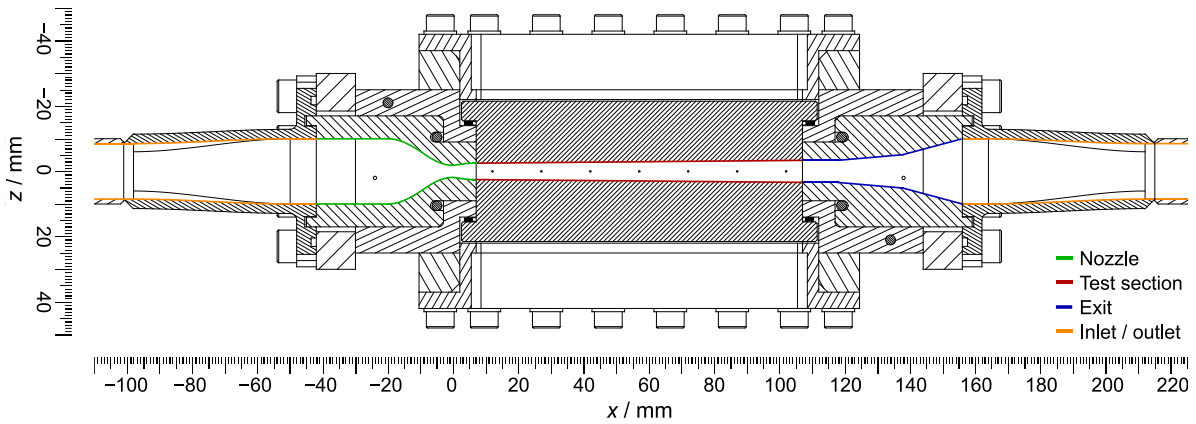


Fig. 8.1: Cross-sectional drawing of the flow channel assembly. The internal contours defining the constant-width (5 mm) flow domain in y -direction are color-coded according to the purpose of the distinct sections. The configuration shown has a metal plug with pressure taps instead of the window on the side opposite to the observer.

The flow channel (Fig. 8.1) is designed in a modular approach and parts defining the internal geometry can be replaced as needed. The following nomenclature describes the different flow channel components: The **frame** describes the main body of the channel holding all parts in place. The **nozzle** (Fig. 8.1, green contour) module is a two-part piece comprising the convergent and divergent nozzle as well as the subsonic part of the flow channel. The **test section** (red contour) begins just downstream of the nozzle and is fully optically accessible. In analogy to the nozzle, the **exit section** (blue contour) consists of a two-part transitional piece that connects between the confined test section and the outlet cross section. **Inlet** and **outlet** (orange contour) describe two identical transition pieces from the round piping of the gas delivery and exhaust system to the rectangular internal flow channel geometry. The coordinate system used throughout this work is defined relative to the center of the nozzle's critical (smallest) cross section where $x = y = z = 0$ mm with x increasing in downstream direction.

8.3.1 Geometry

The flow channel has a rectangular cross section with a constant width (yz direction) of 5 mm. The nozzle exit, i.e., the transition between nozzle and test section was set to 5×5 mm². These

geometric constraints provide enough boundary layer free flow while maintaining a manageable mass flow rate as described below.

The convergent-divergent nozzle geometry has been computed using the code of Grümmer et al. [136] that implements the method of characteristics for calculating rectangular or axisymmetric nozzles profiles for flow channel applications optimized toward a most compact (short in streamwise direction) design. The tool accounts for boundary-layer growth by calculating the displacement thickness (Eq. 8.5) assuming that the boundary layer is already turbulent at the nozzle throat before adding it to the nozzle height. The subsonic part of the geometry is modeled maintaining a monotonous height decrease and a tangential transition to the sonic part of the nozzle. Note that the resulting contour shown in Fig. 8.2 exhibits a slight discontinuity close to the critical cross section. This is due to the first-order gas-dynamic waves occurring since the program uses the Prandtl-Mayer corner flow and is therefore expected [136].

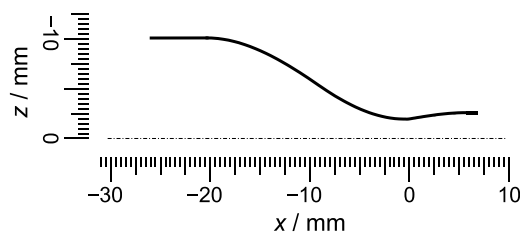


Fig. 8.2: Contour (top half) of the $M = 1.7$ nozzle used for all the measurements in this work.

The supersonic nozzle outlet height was chosen to be 5 mm so that the test section inlet cross section was a square of 5 mm x 5 mm while the subsonic nozzle inlet was arbitrarily set to 20 mm. The resulting critical height at the nozzle throat was 3.8 mm at the nozzle throat ($x = 0$ mm) for a design Mach number of $M = 1.7$.

The 100-mm long test section, i.e., the optically accessible part of the flow channel, begins right at the nozzle exit at $x = 7$ mm and has a constant width of 5 mm. The height (z -direction) at the nozzle exit is 5 mm. To compensate for boundary layer growth, the top and bottom test section walls are tapered (Fig. 8.3), thus increasing the height and therefore counteracting the boundary layer growth by increasing the internal cross-section. Relying on experience from a larger-scale flow channel [59] and CFD simulations (Fig. 8.3), a 0.5° opening angle was chosen increasing the cross section from 25 mm^2 to approximately 37.4 mm^2 throughout the test section.

However, it is neither expected nor required that this approximation fully compensates the three-dimensional boundary layer growth. Rather, it serves to avoid blocking of the flow channel by boundary layer effects. A compensation of the boundary layer growth in the direction of observation (y) would require a more complicated setup and is not required for spectroscopic measurements that were only performed close (~ 12 mm downstream of the critical cross section) to the nozzle exit.

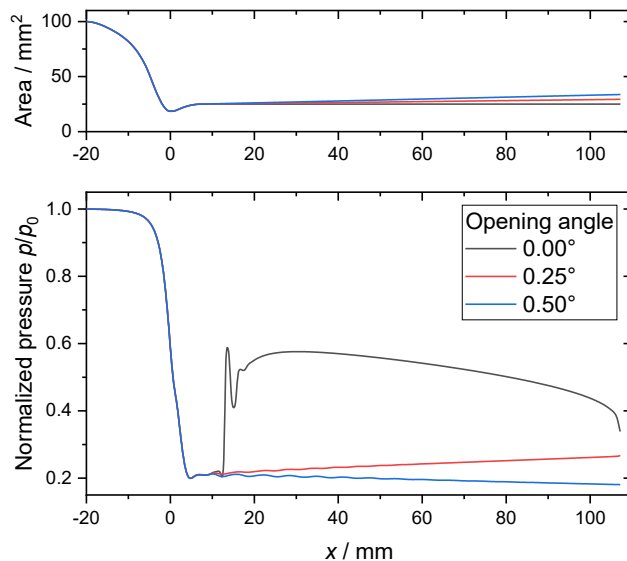


Fig. 8.3: Normalized pressure along the flow direction from CFD simulations (bottom) for channel contours (top, in the form of cross-sectional area) with opening angles of 0° , 0.25° and 0.5° for $p_0 = 3.6$ bar and $T_0 = 300$ K. The pressure profile for 0.25° shows a positive pressure gradient, whereas the pressure gradient for 0.5° is slightly negative. At 0° , the pressure profile clearly shows the presence of a normal shock in the test section and consequently a deceleration to subsonic velocities at about $x = 12$ mm.

The exit geometry continues the lower and upper window shape for 10 mm before expanding by 5° for 20 mm before again expanding by another 10° in both directions. The basic idea is to fix the streamwise position of the normal shock of the flow decelerating to subsonic velocity at this final transition by first expanding less and then more than the Prandtl-Meyer angle. However, the exit geometry did not appear to influence the CFD simulations and the experiments and, therefore, is considered optional and was omitted for the reasons given in 8.4.

8.3.2 Mechanical design

The construction of the flow channel consists essentially of a main frame, in which various interchangeable parts are inserted (Fig. 8.1). The body of the main frame was divided into two halves for manufacturing purposes, which were joined by welding after machining their internal geometries (registering pins were used for a precise fit). The external geometries were machined after joining both parts to ensure that the surfaces relate to each other as accurately as possible. Nozzle and outlet geometries each consist of two parts. Their precise fit in the main frame is ensured by registering pins and a tongue-and-groove connection to the inlet and exhaust flanges. The latter are identical and represent the transition from round pipeline of gas supply to rectangular duct cross-section. The geometry of the transition pieces was optimized to avoid sharp bends and thus additional pressure loss. Since they could not be manufactured in this way using conventional methods, they were produced by selective laser melting. The flange surfaces and O-ring groove have been finished conventionally after additive manufacturing whereas the round cross-section has been welded to a 20 mm outer diameter stainless steel pipe.

Two different kinds of windows are inserted into the main body: The horizontal observation windows that provide a large numerical aperture for the detection systems, and the vertical laser windows that provide optical access for the laser beam perpendicular to the optical path of the observation.

All windows are machined from UV-grade fused silica and exhibit a T-shaped geometry so that they provide a flange for being pressed into a gasket against the main body. That way, they can be easily replaced as is required after the windows wear out. Excessive wear is mostly found on the edges facing the channel's interior. Since the windows have been intentionally left unchamfered and sharp to avoid introducing cavities disturbing the flow, they are prone to chipping during removal and installation. Laser and side windows can each be replaced as required by an identically shaped metal plug with 0.5 mm bores for measuring the static wall pressure in the flow channel. These pressure tapping points are evenly spaced by 15 mm with the first being located 12 mm downstream of the critical nozzle cross-section. Additional pressure tapping points are located in the subsonic part of nozzle and exit geometry at $x = -24$ mm and $x = -138$ mm opposing each a through hole for a thermocouple. The adjacent bores are slightly off-center in the vertical direction and do not face each other directly.

8.3.3 Flow facility

The flow facility (Fig. 8.4) consists of the flow channel experiment itself, the main gas flow conditioning, and the evaporator system providing the toluene vapor acting as fluorescence tracer. The main gas flow is either compressed air or N_2 (purity 99.99 %) provided by a cryogenic liquefied gas evaporator, both belonging to the lab's gas supply system. The air flow is used during the startup/warmup of the flow channel and in between measurements to keep the experiment at steady temperature while saving N_2 . To further reduce the stress on the N_2 system, a gas cylinder battery of five 90-l vessels buffers enough nitrogen for a few minutes of measuring. The gas flow is fed by two mass flow controllers (Bronkhorst F-203AV (8–1000 slm) for air, and Bronkhorst D-6371 (20–1000 slm) for N_2) to the gas heater stage 1. A third mass flow controller (Brooks GF081, 0–83 slm) provides pure O_2 on demand from a gas cylinder (purity 99.995 %) to the same location.

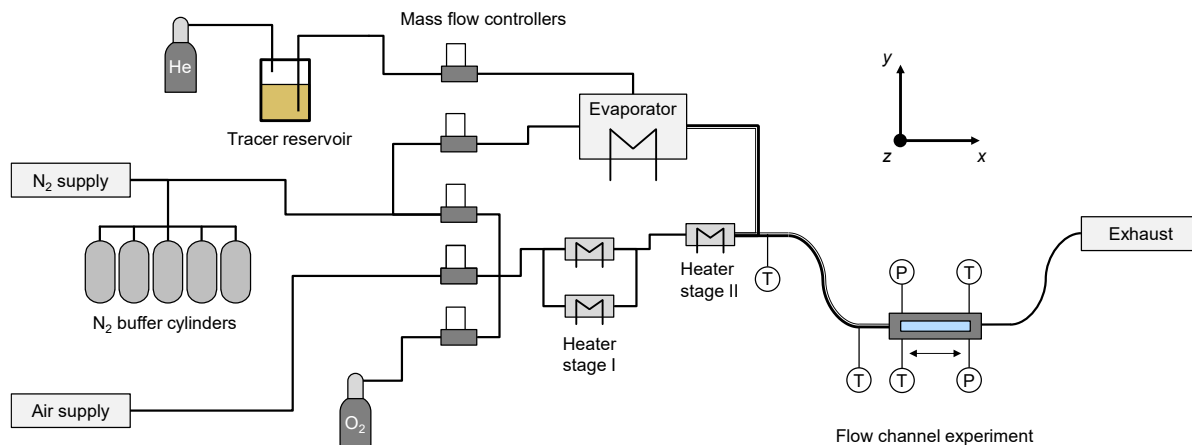


Fig. 8.4: Simplified process and instrumentation diagram (omitting, e.g., all valves) showing the flow channel and the sample gas conditioning system. Straight lines are rigid connections, curved lines are flexible connections, and double lines (bold and light) indicate heat tracing.

Heater stage 1 consists of two parallel heaters (Omega AHP-7562, 0.75 kW) and is connected through a flexible line to heater stage 2 (Leister 102.362, 3.6 kW). The second stage is only power regulated while the first stage is controlled by a closed loop controller using a dedicated thermocouple just downstream of the heater. At the same position, the main gas flow and the sample flow from the evaporator system is mixed.

The latter consists of a pressurized reservoir containing the liquid tracer which is dosed from there via a Coriolis mass-flow controller (Brooks Quantim, 0–0.36 g/s). To avoid formation of bubbles from outgassing gases dissolved in the liquid during depressurization, the reservoir is pressurized with He since its solubility in toluene is significantly lower than that of, e.g., N₂ [137, 138]. All lines conducting liquid tracer are made of PTFE, thus allowing residual He to diffuse through its walls on the way to the mass flow controller. The principle of operation of the evaporator itself (Brooks DLI) is based on the atomization of the liquid tracer of the mass flow controller into a supersonic flow of N₂ carrier gas under addition of heat (max. 1.5 kW, temperature controlled at 150 °C). The carrier gas is provided by a mass-flow controller (Brooks GF41, 0–38 slm) from the N₂ lab supply. The resulting flow from the evaporator is then fed to the aforementioned position just downstream of the second heated stage through a flexible heated line to avoid condensation on the way. After mixing with the main flow, the complete mixture is fed to the flow channel through an insulated corrugated hose.

As discussed in section 8.3.2, the flow channel provides access for thermocouples and taps for pressure sensors at inlet and exit, and, optionally, metal plugs shaped as windows or laser slots with taps for measuring pressure profiles within the flow channel test section. Each pressure sensor is connected via a flexible tube to a pressure sensor array consisting of ten piezo-resistive pressure transducers (Freescale Semiconductors, MPX5700AP, 0–7 bar, 2.5 % full-scale error). The pressure sensors are read out by a microcontroller (Atmel, ATmega32U4, 10-Bit ADC, four times oversampling). Each pressure sensor has been checked against a calibrated

precision sensor (Keller 35XHTC, 0–15 bar, 0.5%-FS error) showing no deviation out of their specified error.

8.3.4 Boundary conditions

For the characterization of the flow channel, measurements and simulations were compared for a $M = 1.7$ nozzle at total inlet temperatures ranging from $T_0 = 100\text{--}150\text{ }^\circ\text{C}$ at an inlet pressure of $p_0 = 3.1$ bar. The Mach number and the minimum inlet temperature were chosen to resemble the inlet conditions used in our previous work [60]. The upper inlet temperature yields a theoretical temperature of ~ 268 K behind the nozzle (Eq. (8.2)) and, therefore, provides some overlap with the temperature range that could be achieved in our static cell (257–293 K) [49]. The inlet pressure is somewhat of a compromise: For a pressure $p_0 < 3$ bar, the simulation showed an unstable flow within the test section. A significantly higher pressure and, therefore, flow rate, however, overstressed the nitrogen supply system leading to a rapid pressure drop and too low measurement time.

The resulting main flow mass flow ranged from 10.6–11.4 g/s depending on the inlet temperature. The evaporator system provided liquid 0.03 g/s toluene vapor in 0.2 g/s nitrogen. This limits the toluene saturation so that no condensation within the test section is expected as discussed in detail in section 1068.6.4.

8.4 Computational fluid dynamics

Computational fluid dynamics (CFD) simulations were performed to design and validate the flow channel. The 3D computational grid is a simplified version of the flow channel interior omitting the straight part of the inlet geometry and lacks the exit geometry completely. We found that the exit had no influence on the results and therefore just added to the numerical cost. The resulting structured mesh consists of 4.65×10^6 nodes and is refined near the walls so that a dimensionless wall distance of the first cell y_1^+ is < 1 everywhere.

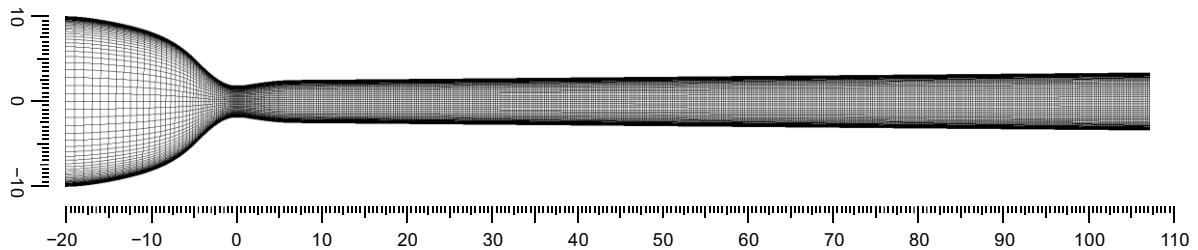


Fig. 8.5: Cross-section ($z = 0$ mm) through the 3D numerical domain.

Reynolds-averaged Navier-Stokes (RANS) equations are solved numerically in ANSYS CFX 19.0 using the $k\omega$ two-equation turbulence model. The inlet boundary condition is either constant mass flow or constant pressure, depending on the respective operating point. The channel outlet is set to a supersonic (zero gradient) boundary condition. All walls are treated as no slip and adiabatic.

8.5 Optical diagnostics

The flow channel is mounted on a motorized linear translation stage (Fig. 8.6) to enable measurements at various downstream positions and to quickly move the experiment between the three different optical diagnostics (Fig. 8.7) described in this chapter that are mounted at adjacent locations.

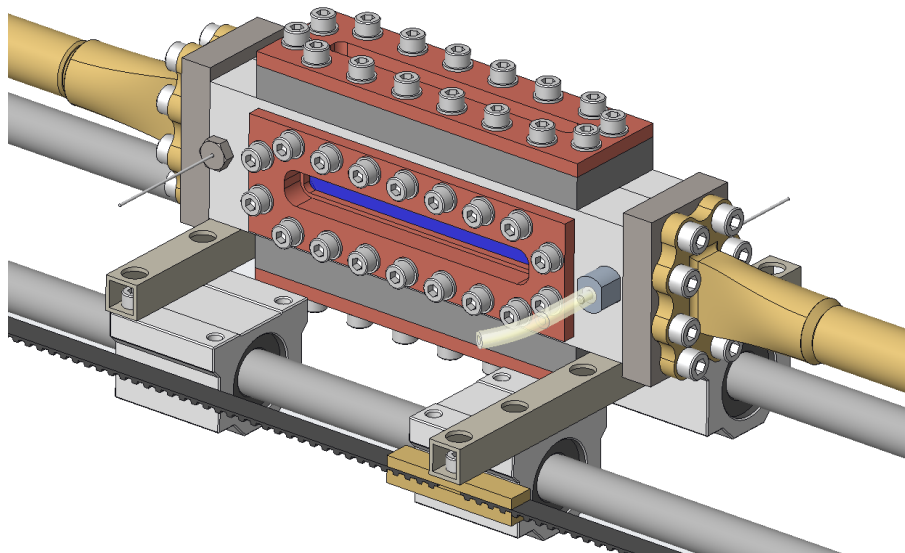


Fig. 8.6: Flow channel assembly mounted on the motorized translation stage consisting of a belt driven sled on linear rails. The unusual shape of the inlet and outlet flanges serves to minimize thermal stresses during additive manufacturing.

The translation stage consists of a sled and four linear bearings riding on two linear rails connected to a timing belt and driven by a geared stepper motor. To account for unavoidable backlash introduced by the gearing, each position is always approached in the same (positive x) direction. The repeatability of the positioning has been measured to be less than $10\ \mu\text{m}$ using a micrometer gauge. The position reference is established by a limit switch at the positive end of the travel in x -direction.

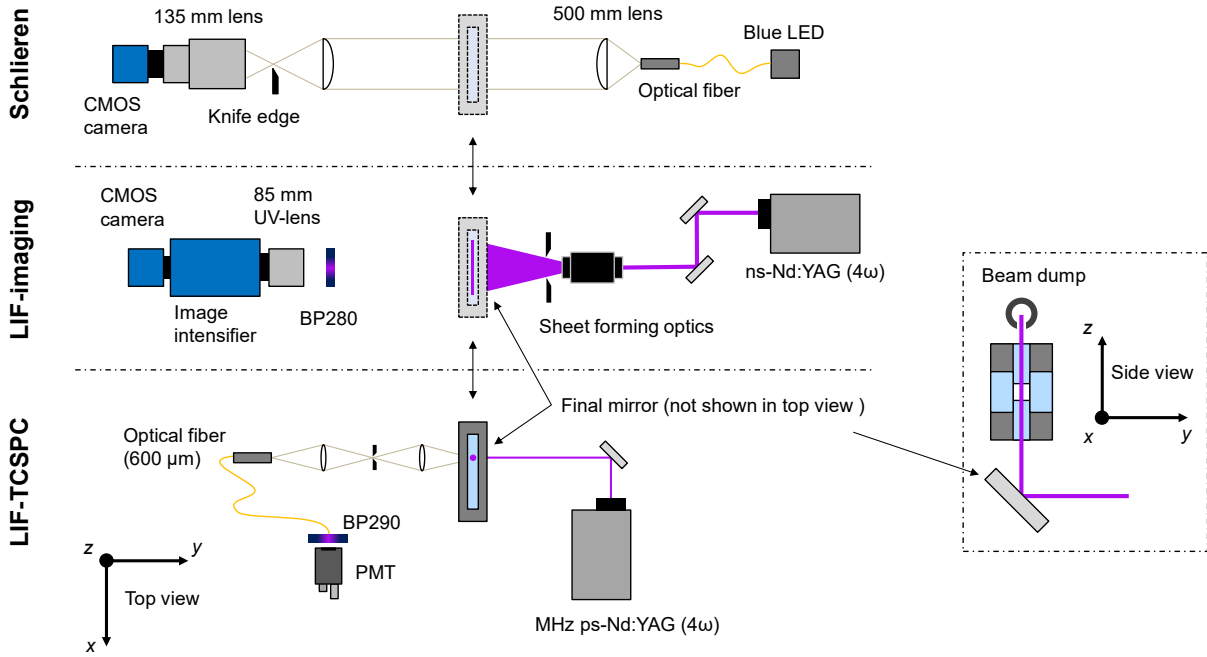


Fig. 8.7: Optical diagnostics used in this work showing a schlieren setup (top), a LIF imaging setup (center), and a scanning setup for LIF lifetime measurements. The flow channel can be moved along the x -axis (downstream direction) between the different measurement setups.

8.5.1 Schlieren imaging

For visualizing flow features such as oblique or normal shocks, a schlieren setup is used to image variations in local density. An LED (465 nm, 3 W) coupled to an optical (600 μm) fiber provides a point light source. The LED is pulsed with 10 μs pulses using a driver identical to the one Menser et al. [139] used for their work. This enables short-time illumination with detection even with consumer cameras. The light is collimated by a 50-mm diameter lens (focal length $f = 500$ mm) before it enters the flow channel. After passing the flow channel and being deflected by potential density gradients, it is focused by an identical lens on the position of a four-way aperture acting as an adjustable knife-edge before being imaged by a consumer camera lens (Samyang F2.0/135mm, $f/2.0$, $f = 135$ mm) onto a CMOS camera (LaVision, Imager M-Lite 2M).

For spatial mapping of the images, a target plate, whose outer dimensions exactly follow the divergent contour of the measuring section, is inserted into the flow channel. The opaque plate contains staggered (0.5 mm distance) holes (0.3 mm diameter), that are registered by the LaVision DaVis software for spatial calibration using the pinhole model.

8.5.2 Fluorescence lifetime thermometry

Time-correlated single photon counting (TCSPC) was used to measure the toluene fluorescence lifetime after excitation with 266-nm pico-second laser pulses. The system is identical to the one used in our previous work in which we characterized the toluene fluorescence lifetime for sub-ambient conditions in a flow-cell [49]. Laser light produced by a high repetition-rate Nd:YAG fiber laser (Fianium, FemtoPower UVP266-PP-0.1, 266 nm, 5 nJ/pulse, 20 ps pulse

width, 1–20 MHz rep rate) is directed by two mirrors (final mirror not shown in Fig. 8.7) through the bottom laser window at the centerline ($y = 0$ mm) of the flow channel. The fluorescence signal is imaged onto an optical fiber (Thorlabs M114, solarization resistant, 600 μm diameter, $\text{NA} = 0.22$) using a two-lens ($f = 35$ mm) setup with a pinhole in between providing a 1:1 magnification plus spatial filtering. On the other end of the fiber a fast photomultiplier tube (PMT) (Hamamatsu, R3809U50, 150 ps rise time, used at 3.0 kV) detects the signal after it passes a bandpass filter (Semrock, BP292/27, 292 nm center wavelength, 27 nm FWHM bandwidth) blocking ambient and scattered laser light. Laser and detector are connected to a TCSPC board (Becker & Hickl, SPC-130) registering the individual relative arrival times of the first photon arriving after a laser pulse and calculating the histograms resembling the fluorescence decay curves. See Friesen et al. [26] for further details about this method. To avoid pile-up effects arising from detecting more than a single photon at a time, the signal intensity is attenuated using neutral density filters (Thorlabs, NDUV, OD 0.3–3.0), thus only after every 10^{th} – 100^{th} laser pulse, a photon is registered. The laser repetition rate is set to 2 MHz according to the anticipated fluorescence lifetimes.

Spatial resolution in z -direction is achieved by moving the entire fiber entrance optic assembly using a vertical motorized stage. The latter consists of two linear rails and bearing and is driven by a lead screw connected to a stepper motor with a resulting repeatability of less than 10 μm .

The measurement volume is limited in y -direction (depth of the field) by the width of the laser beam (approximately 1.2 mm, measured from burn pattern) whereas in x - and z -direction the entrance optics further limit the spot size of < 1.0 mm. The latter has been measured by scanning the sharp edge between a high and low reflective surface of a target plate through the plane of focus. The spot size has then been calculated from the FWHM of the differentiated signal along the spatial coordinate.

The fluorescence lifetime is calculated analogously to previous works [26, 49] using the convolute-and-compare approach of Settersten et al. [128]. To this end, a model function is fitted to the time trace of the fluorescence consisting of the convolution of the instrument response function (IRF) and a mono-exponential decay (Eq. 8.8, the $*$ operator denotes the convolution). The IRF is measured from scattered laser light without tracer and bandpass filter. The scaling factor A is introduced to match the signal level whereas factor B scales a portion of the IRF representing residual scattered laser light still passing the bandpass filter. Prior to fitting, the background of signal and IRF is subtracted so that no additional parameter is required accounting for that.

$$S_{\text{fl}}(t) = A \left(S_{\text{IRF}}(t) * \exp\left(-\frac{t}{\tau_{\text{eff}}}\right) \right) + B S_{\text{IRF}}(t) \quad (8.8)$$

Fig. 8.8 shows a typical signal measured in the flow channel after collecting photons for 1 s at 2 MHz laser repetition rate as well as the IRF, the resulting fit, and the residual.

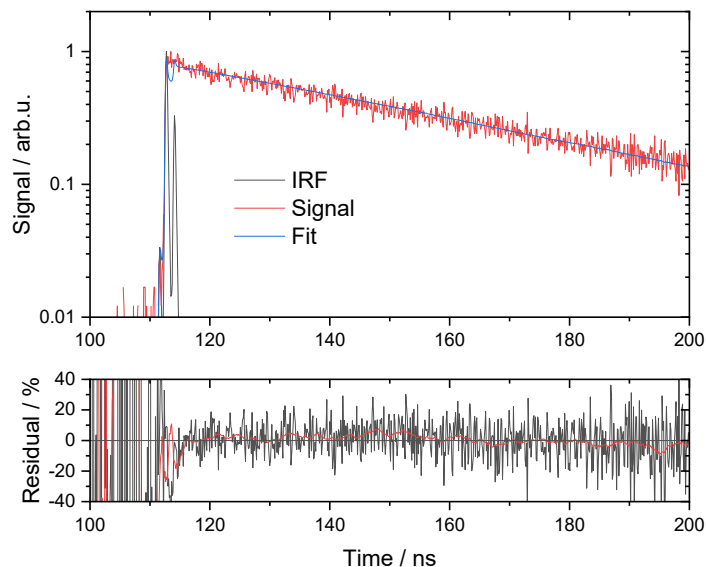


Fig. 8.8: Instrument response function IRF, a typical LIF decay curve measured by time-correlated single-photon counting (TCSPC), and data fit using the convolute-and-compare approach. The red line in the residual plot shows its moving average.

The temperature is then interpolated from the measured fluorescence lifetime data [49] graphically represented in Fig. 8.9a using the measured fluorescence lifetime and the flow channel pressure measured using the wall pressure sensors.

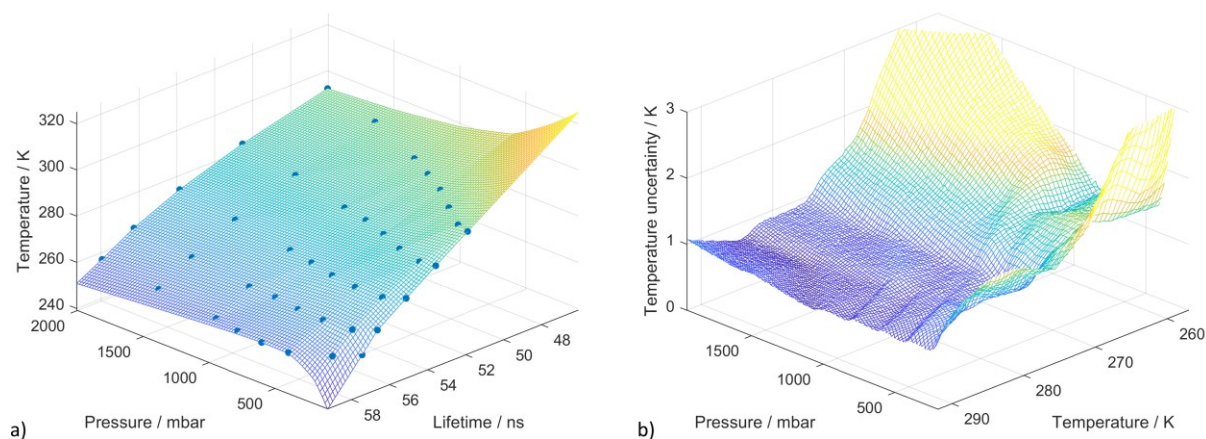


Fig. 8.9: Graphical representation of the previously measured calibration data (Beuting et al. [49]) showing a) the temperature as a function of the toluene fluorescence lifetime and local pressure (blue points) with the surface spun by interpolated splines and b) a surface plot of the systematic error of a temperature measurement from measured fluorescence lifetime and pressure using this data.

For quantification of the temperature uncertainty, a Monte-Carlo approach has been utilized accounting for the published error of the tracer characterization measurements as well as the statistical error of this measurement (see Appendix B for details). The resulting error is shown in Fig. 8.9b ranging from approximately ± 1 K at the lowest investigated temperature up to $> \pm 3$ K at the highest temperature. The temperature sensitivity of this technique, as discussed in

Beuting et al. [49], corresponds to approximately 1.25 %/K outperforming, e.g., two-color detection techniques. Another great advantage of this technique is its independence of the detection system efficiency and local tracer concentration, opposed to intensity measurements.

8.5.3 LIF imaging

The LIF imaging system serves two purposes. Firstly, it is used to qualitatively establish the local tracer concentration to assure that the tracer is evenly distributed and, therefore, the concentration in the measurement volume can be calculated exactly for spectroscopic characterization measurements. Secondly, it is used to measure the local reduction in intensity caused by oxygen quenching in mixing an oxygen containing flow with an oxygen-free flow to demonstrate indirect measurement of the mixing state on a molecular level.

As shown in Fig. 8.7 (bottom), a 45 mm wide laser light sheet at 266 nm is formed from the 4th harmonic of a nanosecond pulsed Nd:YAG laser (Quantel Q-smart 450) using a sheet forming optic (LaVision, $f = -50$ mm). It is directed through the flow channel lower laser window normal to the direction of flow at its centerline ($y = 0$ mm). The light sheet thickness is < 0.5 mm (burn pattern) with a laser fluence of ~ 60 J/cm² (energy measured using a Coherent EnergyMax energy monitor). After exciting the toluene, the fluorescence signal is imaged using an image intensifier (LaVision IRO-X) with a CMOS camera (LaVision imager M-Lite 2M) equipped with a UV lens (LaVision, $f = 85$ mm, $f/2.8$, optimized for 220–450 nm). A 280-nm bandpass filter (Semrock, BP280, 280 nm center wavelength, 14 nm FWHM bandwidth) suppresses ambient and scattered laser light.

In postprocessing, all images were corrected for shot-to-shot energy fluctuations of the laser using the energy monitor signal. Background images (100 shots average) were recorded and subtracted from all other images to account for residual ambient and scattered laser light passing the bandpass filter. To account for inhomogeneities of the laser light sheet, flat field images are recorded prior to the experiments at uniform conditions. To this end, the flow channel is only supplied by constant flow of toluene (0.6 g/min) in N₂ (24 g/min) resulting in a partial pressure of 8.7 mbar (corresponding to a total number density of 2.1×10^{17} cm⁻³) at a total temperature of 100 °C. This flow was slow enough so that no noticeable acceleration and, therefore, cooling occurs. For flat field correction, the background-corrected images were divided by the averaged (100 shots) background-corrected flat field images.

Spatial calibration is achieved using the same target plates and mapping procedure as explained in section 8.5.1. The difference is that the LIF setup required backlighting (white LCD screen) of the target placed at the light sheet position, which required temporary removal of the bandpass filter in front of the camera lens.

8.6 Characterization of the flow channel

This chapter presents the qualitative and quantitative characterization of the channel flow using the methods presented in sections 8.4 and 8.5.

8.6.1 Qualitative analysis of the supersonic flow field

Fig. 8.10 shows the a) Mach number, b) temperature, c) pressure, and d) streamwise velocity field resulting from the RANS simulation for an inlet temperature of $T_0 = 150\text{ °C}$ for the complete numerical domain. The other inlet temperature cases are presented in appendix G.

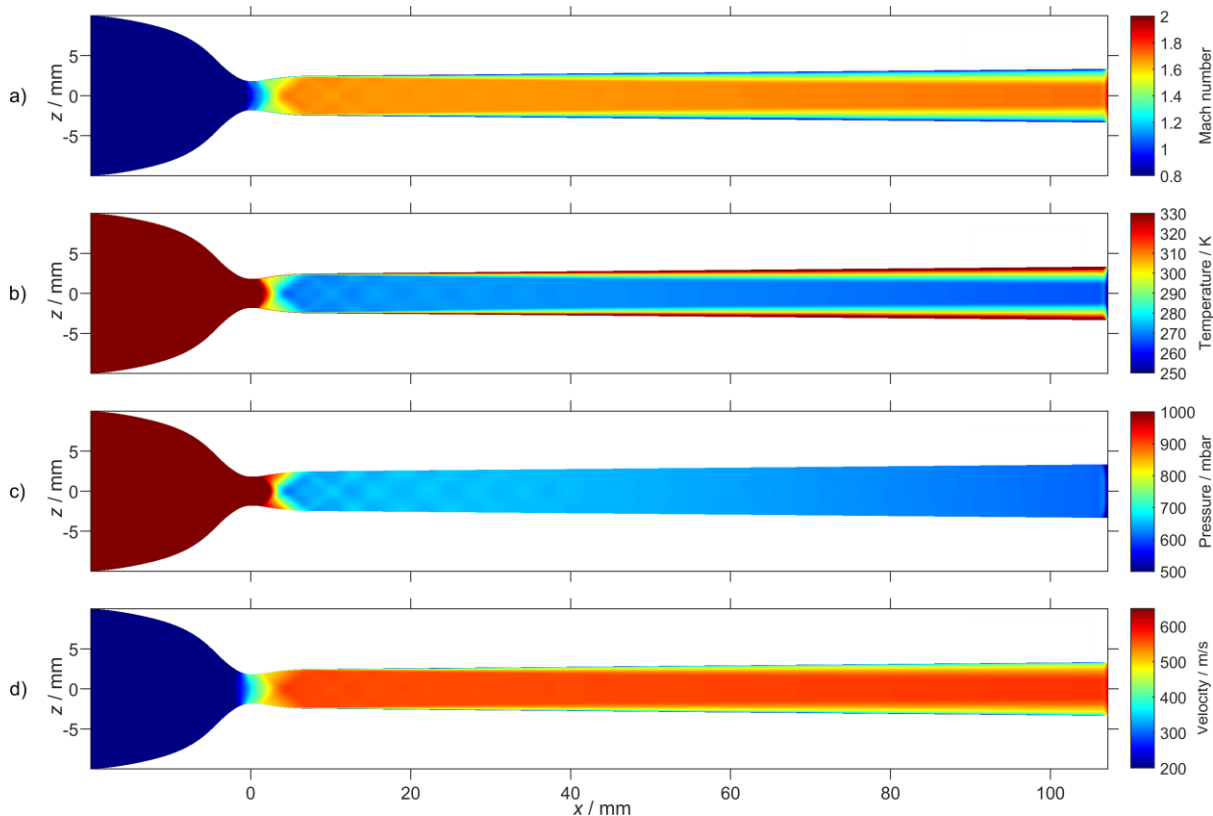


Fig. 8.10: Results of the URANS CFD simulations showing the a) Mach number, b) temperature, c) pressure, and d) streamwise velocity field on the xz -plane ($y = 0\text{ mm}$) for an inlet temperature of $T_0 = 150\text{ °C}$.

In all cases, a typical pattern of weak, oblique shocks can be seen originating in the de Laval nozzle and diminishing toward the middle of the test section as the shocks are reflected multiple times. No further structures are visible further downstream. The flow accelerates slightly throughout the test section (Fig. 8.10a and d) as the inclination of the top and bottom walls overcompensates the boundary layer growth. Consequently, pressure and temperature (Fig. 8.10b and c) decrease in downstream directions.

Such oblique shocks are also clearly visible in the Schlieren images. Fig. 8.11a shows ensemble averaged schlieren images for inlet temperatures $T_0 = 100$ and 150 °C , which are in the absence of recognizable differences representative for the complete investigated inlet temperature range. A pattern of oblique shocks is clearly recognizable up until $x = 25\text{ mm}$ where it fades in downstream direction. This shock pattern originates from the nozzle exit where the expansion fans are not completely cancelled out despite the carefully designed nozzle contour (cf., Fig. 8.1).

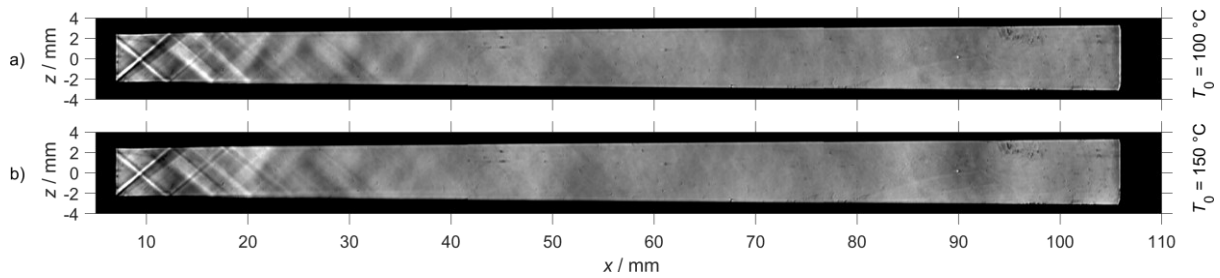


Fig. 8.11: Averaged (100 shots) Schlieren images for the a) minimum ($T_0 = 100\text{ }^\circ\text{C}$) and b) maximum ($T_0 = 150\text{ }^\circ\text{C}$) inlet temperature condition at an inlet pressure $p_0 = 3.1\text{ bar}$. The images were obtained at three positions and stitched after mapping and adjustment for increased contrast.

Fig. 8.12 shows short-time illuminated ($\sim 10\text{ }\mu\text{s}$ exposure) schlieren images taken at different uncorrelated points in time. These show high-frequency flow structures but no significant shock waves of any sort that would indicate a deceleration of the flow to subsonic speeds within the test section. The influence of these instabilities on the LIF signal is discussed in detail later (section 8.6.5).

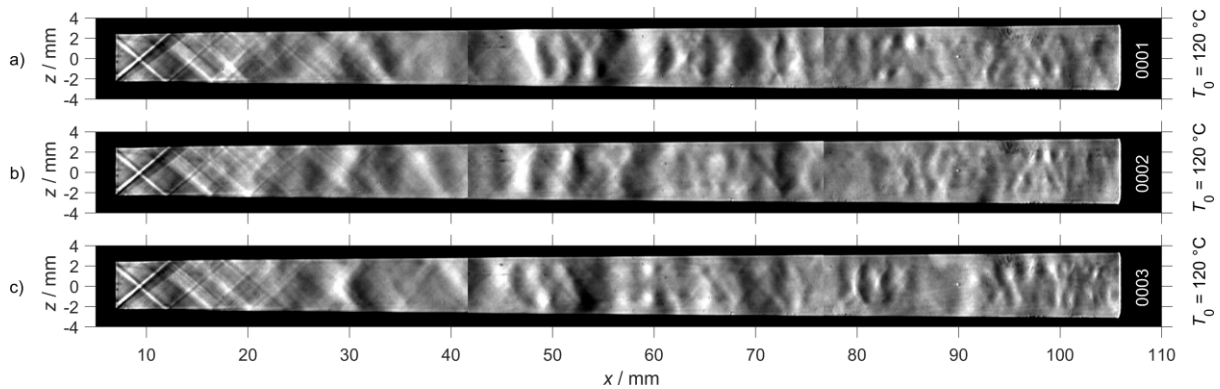


Fig. 8.12: Uncorrelated short-time illuminated ($\sim 10\text{ }\mu\text{s}$) schlieren images each stitched from three uncorrelated single images taken at different positions.

The shock pattern is also visible in ensemble-averaged flat field-corrected toluene LIF images (Fig. 8.13) obtained after excitation with a laser light sheet generated from the ns-Nd:YAG laser spanning about 80 % of the test section. The shock system influences the fluorescence intensity as the signal increases and decreases alternatingly after each shock wave before it more gradually increases downstream of the center of the test section.

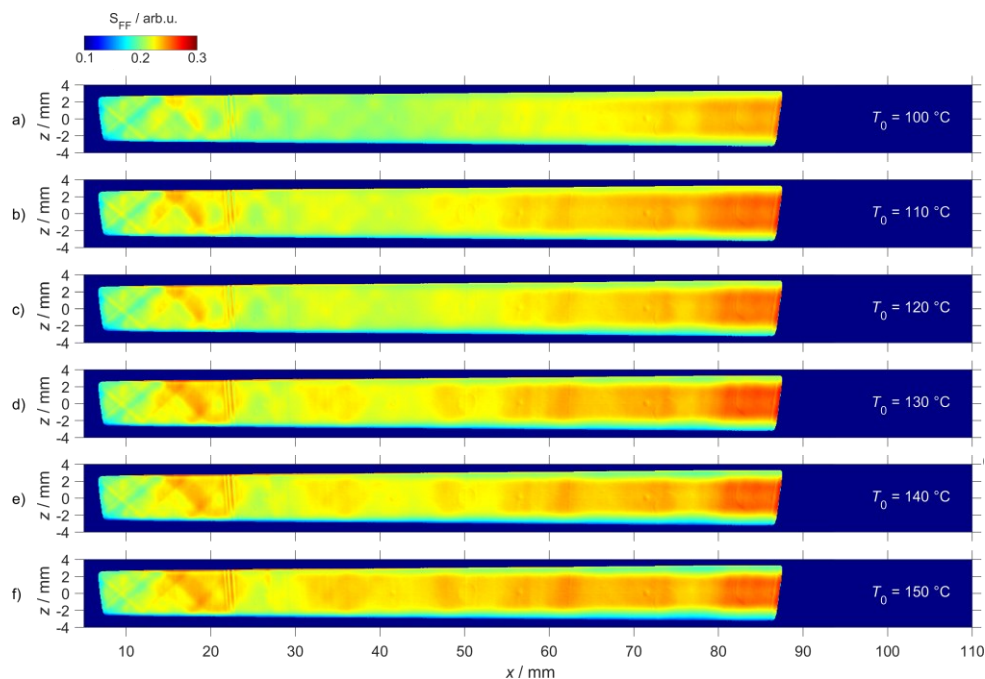


Fig. 8.13: Ensemble-averaged (100 single shots) flat-field corrected toluene-LIF images for all investigated inlet temperatures.

Considering Eq. 8.6, this increase is not trivial to explain since many effects influence the LIF signal in different ways. For example, an increase in temperature leads to reduced fluorescence quantum yield while the accompanying density increase increases the tracer number density. Also, the temperature dependence of the absorption cross-section is yet unknown in the respective temperature range. Unfortunately, the resulting LIF signal (Fig. 8.14) is ambiguous (in terms of signal intensity vs. temperature) as the considerations based on extrapolation and literature data and several assumptions shown in Appendix F suggest. Therefore, the temperature is determined using the fluorescence lifetime thermometry method discussed in 8.5.2 instead as presented in the following section.

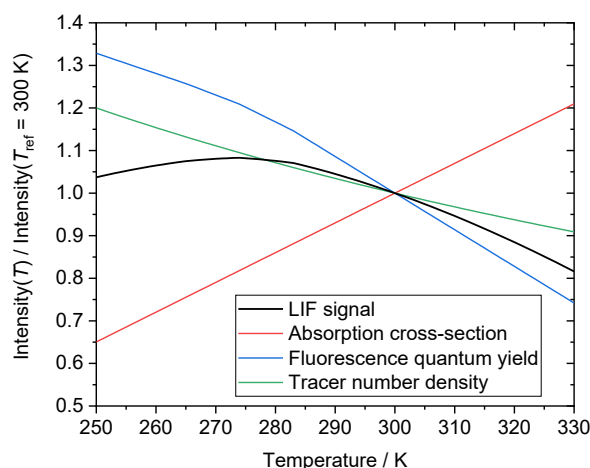


Fig. 8.14 Estimated temperature-dependent toluene-LIF signal for 266-nm excitation and the contributing factors for temperature fluctuations around a reference temperature of 300 K in an isobaric (1 bar) case. Please refer to Appendix F for a detailed derivation and discussion of the underlying assumptions.

8.6.2 Temperature and pressure

For analysis of the flow-channel performance, the wall pressure is measured during the experiments while the temperature is determined from the fluorescence lifetime measurements of toluene added as a fluorescence tracer to the flow (cf., section 7.4.1). The results of the measurements along the centerline and then compared to the CFD data. Fig. 8.15 shows the expected toluene fluorescence lifetime for $T_0 = 150\text{ }^\circ\text{C}$ calculated from the temperature (Fig. 8.10b) and pressure field (Fig. 8.10c) from the CFD using the previously measured calibration data (Fig. 8.9).

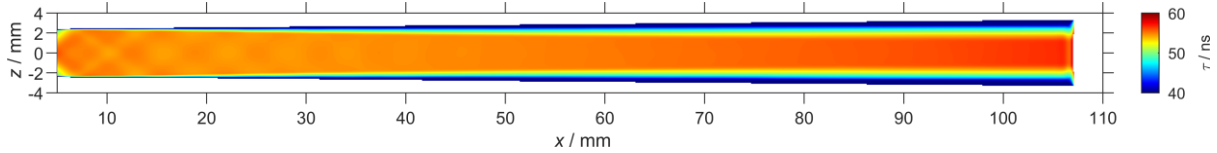


Fig. 8.15: Expected fluorescence lifetime interpolated from calibration data measured previously in a cold cell ([49], Fig. 8.9) using the temperature and pressure field from the CFD for an inlet temperature of $T_0 = 150\text{ }^\circ\text{C}$.

Figure 8.16a shows the centerline ($y, z = 0$) pressure trace extracted from the simulation compared to the wall pressure measurement and Fig. 8.16b the temperature trace compared to the temperature determined from the fluorescence lifetime measurement. There is a significant difference between experiment and simulation in both cases. While at the nozzle exit the pressure is ~ 0.16 bar higher, the measured temperature exceeds the numerical result by ~ 12 K at the nozzle exit increasing further downstream to ~ 0.4 bar and 37 K at the end of the test section. This leads to two conclusions: First, since a deviation from the predicted values is already visible at the nozzle exit, the flow velocity and Mach number is reduced, which might result from an imperfect geometry due to manufacturing inaccuracies. Second, since the deviation increases further towards the exit of the flow channel, the boundary layer growth is underestimated, possibly as a consequence of the stronger oblique shock waves originating from the nozzle exit (due to the manufacturing-related gap between the nozzle contour and the window).

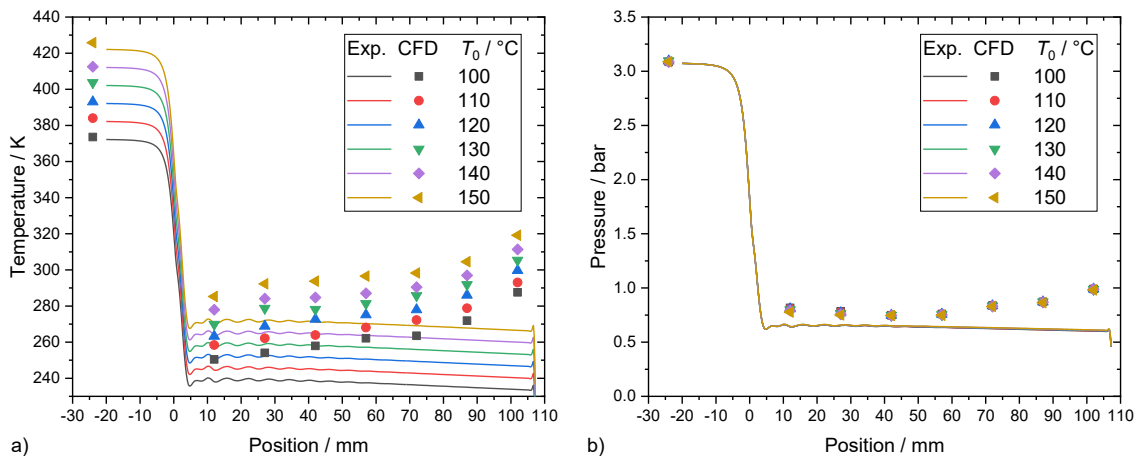


Fig. 8.16: Centerline temperature (a) and pressure (b) profiles. Solid lines show simulation data, whereas symbols are the measured temperature from the fluorescence lifetime thermometry (a) and the static wall pressure (b), respectively. The temperature data at $x = -24$ mm outside the test section stems from the reading of the thermocouple in the not yet convergent inlet part of the nozzle module.

The reduction in Mach number can be estimated from the temperature deviation by fitting the adiabatic equation for temperature (Eq. 8.2) to the experimental data from the lifetime thermometry, yielding a corresponding Mach number of $M = 1.56$ (Fig. 8.17a). The observed averaged wall pressure of approximately 0.8 bar at $x = 12$ mm (Fig. 8.17b) also matches the pressure of 0.77 bar calculated from Eq. 8.2 quite well.

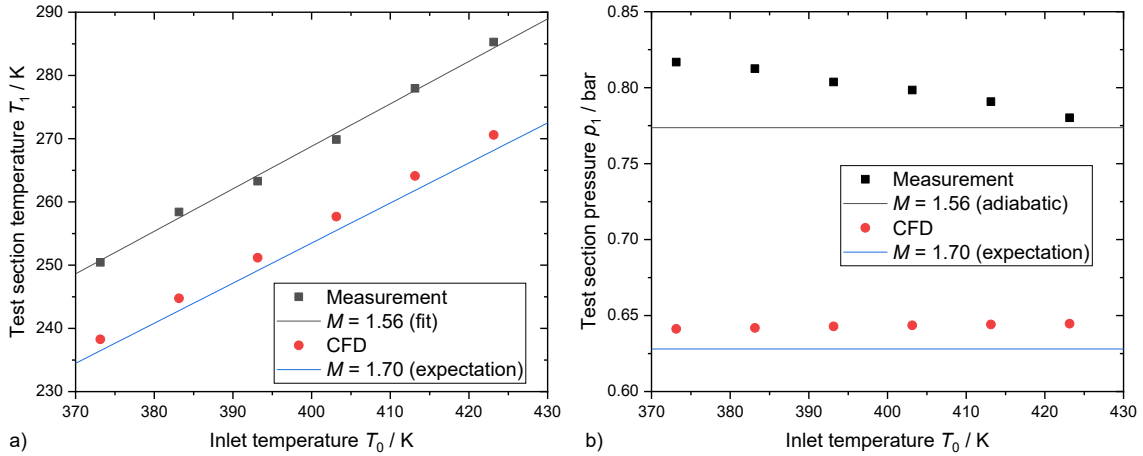


Fig. 8.17: Test section temperature (a) at $x = 12$ mm as a function of the inlet temperature. The black squares show the measurement from the lifetime thermometry, the black line is a fit of Eq. (8.2) to the measurement, the red squares are extracted from the 3D-CFD centerline, and the blue line is the expected temperature calculated from the adiabatic equation (Eq. (8.2)) for the nozzle design Mach number $M = 1.7$. Test section pressure (b) at $x = 12$ mm as a function of the inlet temperature. The falling trend shows the increasing heat losses with increasing temperature and, therefore, the deviation from the adiabatic assumption.

Fig. 8.17b, however, reveals some difference in pressure between the different inlet temperature cases, dropping slightly with increasing inlet temperature from 0.82 to 0.78 bar. This is not unexpected since the flow channel is non-adiabatic. Therefore, heat losses increasing with temperature lead to an increased pressure drop. The CFD on the other hand yields a pressure of 0.64 bar slightly above the expected value from the isentropic calculation of 0.63 bar.

8.6.3 Influence of the boundary layer

For the application of the flow channel for tracer spectroscopy, a sample region that is free of strong gradients is required. As the decreasing near-wall velocity in the flow direction in Fig. 8.18 shows, the boundary layer makes up a relatively large part of the inner cross-section of the flow channel increasing with the distance to the nozzle.

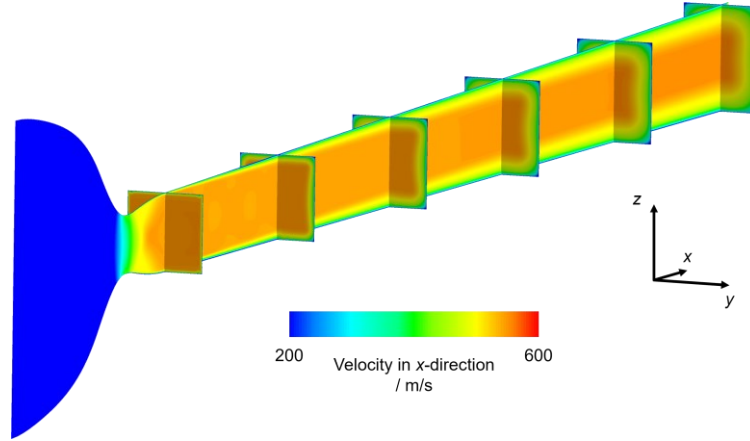


Fig. 8.18: Simulation of the velocity in x direction showing the reduction in velocity in the axial (xz) and lateral (yz) plane caused by the boundary layer growth in downstream direction. Also note the interaction of the top and side boundary layers in the corners of the rectangular duct leading to a more rounded velocity profile further downstream.

The boundary-layer-free region is determined from the temperature boundary layer as defined in Eq. 8.4. Its height (z -direction) is calculated by subtracting the boundary-layer thickness from the flow channel height. Fig. 8.19a shows the development of the boundary-layer-free height along the downstream position for the different inlet temperature conditions investigated in this work. The value drops between approximately from 4.6 mm at the nozzle exit down to 2.8 and 3.0 mm at the test section exit for the highest and lowest inlet temperature case, respectively. In all cases, some fading ripples caused by the reflected oblique shocks are clearly visible until approximately the center of the test section in downstream direction. Similarly, the displacement thickness as defined in Eq. 8.5 and shown in Fig. 8.19b rises about 0.4 mm throughout the test section with minimal difference for the different inlet temperature cases.

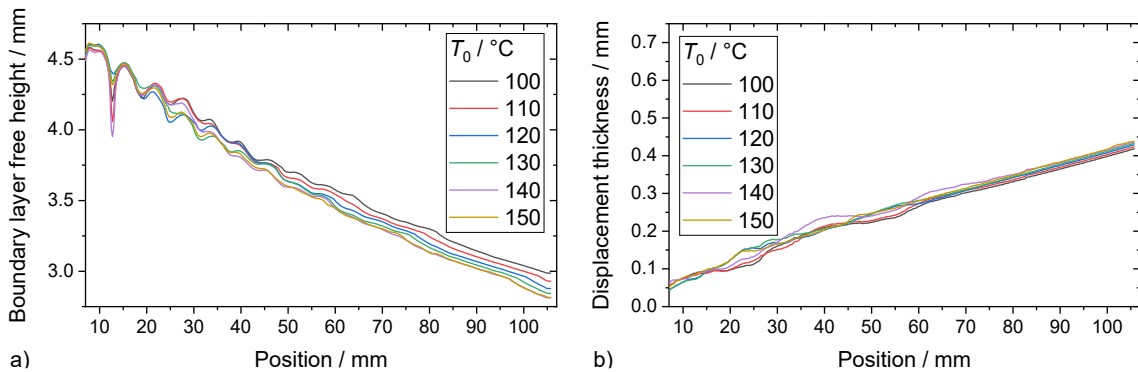


Fig. 8.19: a) Boundary-layer-free height determined using the velocity criterion as defined in Eq. 8.3 and b) the displacement thickness as defined in Eq. 8.5.

This means, that temperature-sensitive spectroscopic measurements can be performed throughout the complete test section for a region of interest of 1 mm in diameter. This is also supported by the LIF images shown in Fig. 8.13. Additionally, the TCSPC measurements were repeated at $z = +1$ mm above and $z = -1$ mm below the flow channel centerline (Appendix E) not showing significant differences.

8.6.4 Tracer condensation

For maximizing the signal, a maximum permissible tracer concentration is chosen that prevents condensation within the test section. To this end, the ratio of the local toluene partial pressure p_{tol} (from the chosen toluene mass flow rate of 0.03 g/s and the local density from the CFD) and its saturation vapor pressure $p_{\text{tol,sat}}$ (from the toluene saturation data from ref. [140] using the local temperature from CFD simulations) is calculated. Figure 8.20 shows the ratio for the lowest investigated inlet temperature investigated whereas Fig. 8.21 provides the ratio along the channel center line for all inlet temperatures. It is apparent that the saturation condition is not fulfilled except for the last ~15 mm of the test section in the case of the lowest inlet temperature of $T_0 = 100\text{ °C}$ where an oversaturation by less than 10 % occurs as the density rises towards the flow channel exit. However, no indications of condensation such as increased scattered laser light in LIF measurements or significant changes of the refractive index in schlieren images were observed. The reason for its absence are likely the short residence time of the oversaturated gas in the flow channel (~28 μs at a flow velocity of ~538 m/s), the carrier gas being free of particles that could facilitate nucleation, and the fact that the measured temperature is in reality higher than the temperature predicted by the CFD simulation (cf., Fig. 8.16).

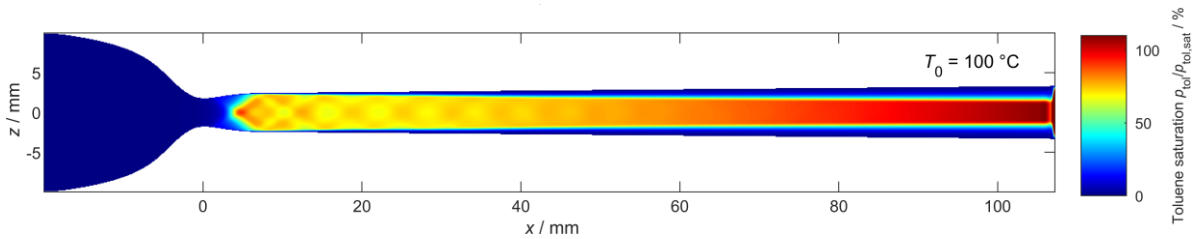


Fig. 8.20: Simulation of the toluene saturation as the ratio of the local toluene partial pressure p_{tol} and toluene saturation vapor pressure $p_{\text{tol,sat}}$ for a toluene mass flow rate of 0.03 g/s at the lowest investigated inlet temperature of $T_0 = 100\text{ °C}$.

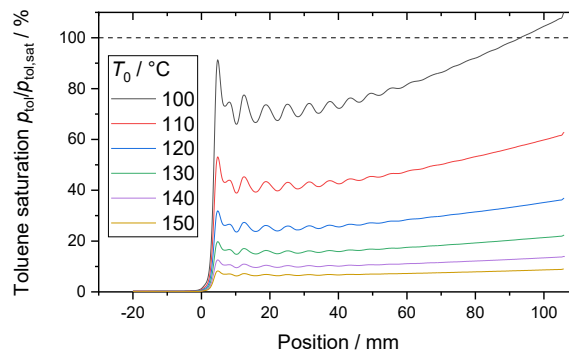


Fig. 8.21: Centerline ($y = z = 0\text{ mm}$) toluene saturation as the ratio of the local toluene partial pressure p_{tol} and its saturation vapor pressure $p_{\text{tol,sat}}$ for a toluene mass flow rate of 0.03 g/s.

8.6.5 Flow instabilities

Flow instabilities occur in the channel and are clearly visible in the quasi-instantaneous short-time illuminated schlieren images. Similar structures are also visible in the single-shot LIF images as shown in Fig. 8.22. Nevertheless, it is not obvious whether these structures originate from the boundary layer or the undisturbed main flow: While the line-of-sight integrating

schlieren images would show them in either case, the LIF images could either reflect changing flow conditions in the center of the flow channel or the deflection of the laser light sheet by density gradients only present in the boundary layer (beam steering).

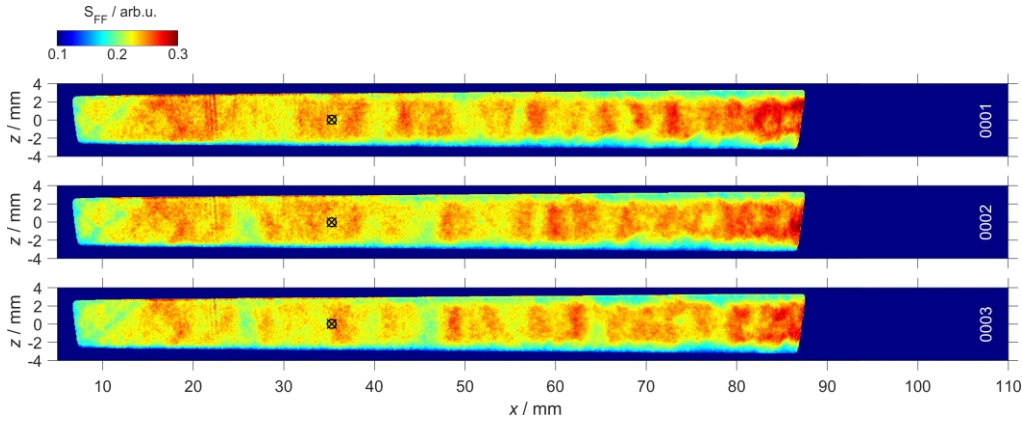


Fig. 8.22: Flat-field corrected uncorrelated single-shot LIF images showing intensity variations caused by flow structures for inlet temperature $T_0 = 150$ °C. The symbols at $x = 34.5$ mm and $z = 0$ mm mark the position where additional time-resolved fluorescence lifetime measurements were performed.

For clarification, time-resolved fluorescence lifetime measurements are performed that are independent of the local laser intensity fluctuations. To this end, the fluorescence signal decay is measured after excitation with a ns-pulse (light-sheet illumination) using the same detector and collection optics as used for the TCSPC measurements. In contrast, however, the decay curve for each individual laser shot is recorded with an oscilloscope to achieve single-shot performance. The fluorescence lifetime is then determined using the convolute-and-compare method (cf., Appendix D) analog to the method described in section 8.5.2. Here, the previously recorded time trace of scattered laser light acts as the instrument response function which is reliable for relatively long fluorescence lifetimes of toluene compared to the laser pulse width (~ 8 ns). Fig. 8.23 shows the normalized fluorescence lifetime compared to the normalized intensity extracted at the same position (as marked in Fig. 8.22) from the same measurement volume. Both measurements show a near identical standard deviation of about 5 %. As the fluorescence lifetime should be insensitive to fluctuations of the exciting laser intensity, one can conclude that the fluctuations seen in the images actually originate from temperature fluctuations in the center of the flow field and not from beam steering of the laser light sheet by the boundary layer.

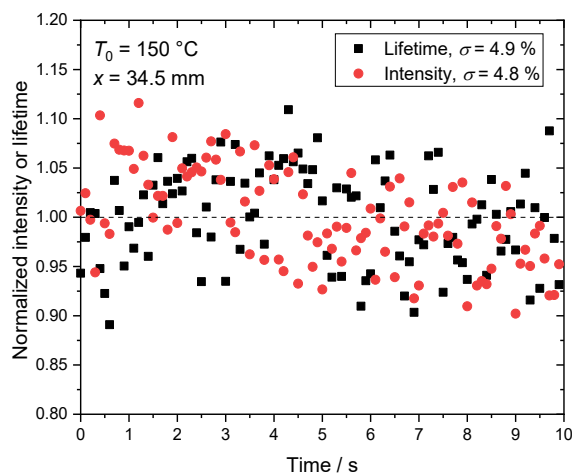


Fig. 8.23: Fluorescence intensity and fluorescence lifetime each normalized by its arithmetic mean at $T_0 = 150\text{ }^\circ\text{C}$. For time-resolved single-shot measurements, the latter is determined from the fluorescence signal decay curve measured after excitation with a ns-pulse (light-sheet illumination). The detector and collection optics are identical to those used with TCSPC (cf., section 8.5.2) while the photomultiplier signal is read using a high-speed oscilloscope (Tektronix TDS7054). The lifetime is then determined using the convolute-and-compare method with the previously recorded time trace of scattered laser light acting as the instrument response function. The signal is collected at the centerline ($z = 0\text{ mm}$) between the second and the third wall pressure bore ($x = 34.5\text{ mm}$). The fluorescence intensity corresponds to the average over a $1 \times 1\text{ mm}^2$ area at the same x -position extracted from flat-field corrected LIF images.

8.7 Demonstration: measurement of oxygen quenching on toluene LIF

The susceptibility of the toluene fluorescence signal to the local O_2 concentration allows for indirect measurement of the mixing state between a toluene-containing and an oxygen-containing gas on a molecular level. However, the cross dependence of the signal on temperature and total pressure makes the application of such measurements to accelerated transonic mixture wake flows downstream of central injectors, with their characteristically strong temperature and pressure gradients, particularly difficult [60]. Koban et al. [37] states that for low-vibrational excitation of toluene (i.e., low temperatures or relatively long excitation wavelengths) its fluorescence quantum yield depends on the O_2 partial pressure only. This was demonstrated experimentally for 266-nm excitation at room temperature, while at higher temperatures the signal showed a significant temperature dependence. This can be explained by the lower non-radiative energy losses at lower vibrational energy levels (i.e., at lower temperatures) competing with the less temperature-sensitive quenching process. Recent work [48, 52] showed that at 266-nm, excitation occurs very close to the thermal energy level in the excited state at room temperature with the exact point being between 283–292 K [49]. This means, that at the lower temperatures relevant for this work, excitation occurs to a level above the thermal energy level in the excited state. Additionally, lower pressure causes slower vibrational relaxation. Therefore, excited molecules relax more slowly and spend more time at higher vibrational levels with higher non-radiative loss rates other than quenching. The assumption that the O_2 dependence of the toluene FQY is independent of temperature has yet to be proven for the present temperature and pressure range. This is now rectified in this chapter, demonstrating the suitability of the flow channel for spectroscopic measurements at the same time.

For providing varying O_2 concentrations in the flow channel, it is fed with a main flow of nitrogen while O_2 is introduced in various amounts upstream of both heater stages. The N_2 flow is adjusted so that the inlet pressure remains constant. The flow channel is configured with two laser slots and one window while the opposing window is replaced with a metal plug with pressure tapping points. The fluorescence lifetime is then recorded using the TCSPC setup at right at the first sensor position at $x = 12$ mm enabling pressure measurements as close as possible to the measuring volume. The temperature at this point is determined previously using fluorescence-lifetime thermometry in pure tracer-seeded N_2 .

Fig. 8.24 shows the recorded fluorescence time traces for O_2 concentrations from 0–5 vol.%. The fluorescence lifetime is determined using the convolute-and-compare technique discussed in section 8.5.2 and plotted in Fig. 8.25 (left) for different temperatures.

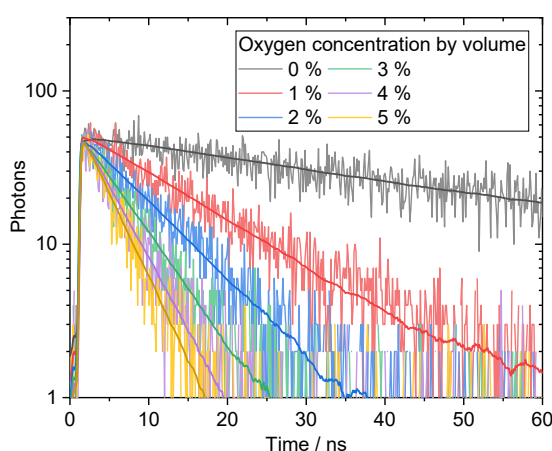


Fig. 8.24: Toluene fluorescence signal time trace for various oxygen concentrations at 265 K (determined using the fluorescence lifetime measured at 0 vol.% oxygen) at a total pressure of 0.76 bar measured at the first pressure sensor location at $x = 12$ mm.

Figure 8.25a shows that even at 1 vol.% O_2 , the fluorescence lifetime becomes invariant to temperature, confirming the assumptions made earlier. Fig. 8.25b shows the Stern–Volmer plot derived from Fig. 8.25a. The Stern–Volmer coefficients k_{SV} are determined from a linear fit and shown in the figure legend.

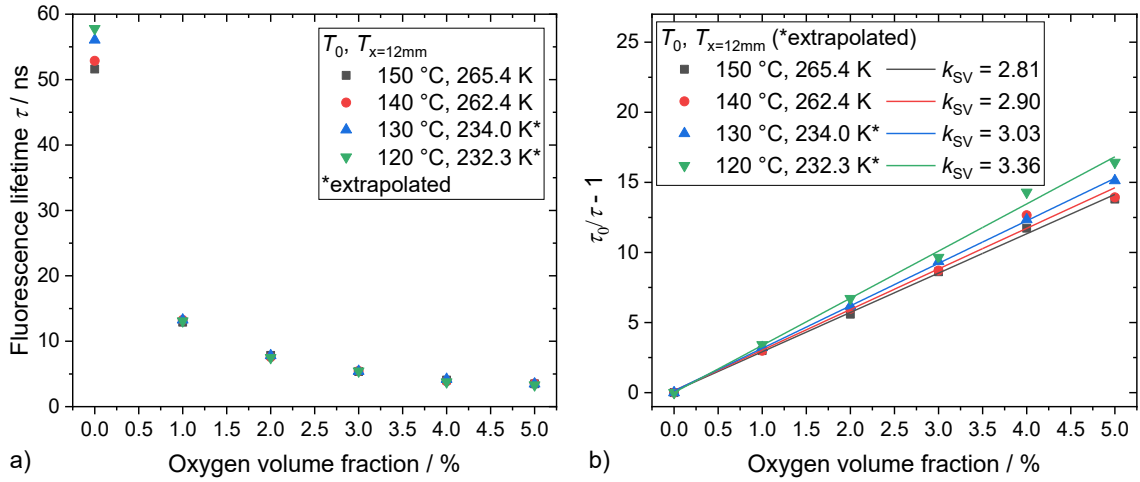


Fig. 8.25: The measured toluene fluorescence lifetime depending on the oxygen concentration (a) and the corresponding Stern-Volmer (b) plot showing the quenching effect of molecular oxygen on the toluene fluorescence signal for varying temperatures (determined using the fluorescence lifetime measured at 0 vol.% oxygen) at a total pressure of 0.76 bar measured at the first pressure sensor location at $x = 12$ mm.

8.8 Conclusions

A small-scale modular supersonic flow channel has been designed, built, and characterized. Its suitability for its two main purposes, enabling photophysical analysis of tracers and providing a testbed for LIF imaging techniques at near-application sub-ambient temperature, has been demonstrated.

The flow channel had a rectangular cross-section. Through a modular design, it is configurable in its essential sections (nozzle, test section, and outlet) by exchanging the respective parts. While the inner width of the channel is fixed at 5 mm, different Mach numbers can be set by using nozzle geometries with different throat heights. The test section consists of four elements, either fused silica windows for optical accessibility or dummies for measuring the pressure. In this work, the configuration with a $M = 1.7$ nozzle and a symmetrically widening test section increasing in height with a slope of 1° in the downstream direction was used.

Pointwise temperature measurements using the fluorescence lifetime thermometry based on data obtained in our previous work [49] were carried out. We found that the gas flow was less expanded as expected since our measured temperature (+14 K) and wall pressure (+0.16 bar) were increased compared to CFD data, which corresponds to a reduction in Mach number from 1.7 to 1.56. We attribute this deviation to two effects: First, a system of oblique shocks that is clearly visible in Schlieren and planar LIF images originating from the nozzle exit. Since a similar system is only faintly visible in the CFD data, we assume that it is more pronounced in the experiment due to manufacturing imperfections, especially at the transition from the stainless-steel nozzle geometry to the fused-silica windows of the test section. Second, since both pressure and temperature further increase in downstream direction throughout the test section, the boundary layer growth is likely either underpredicted in the CFD or it is increased due to

interactions with the shock system. Future work should address the difficulties in predicting the flow channel conditions.

An experiment was carried out to demonstrate the suitability of the flow channel for spectroscopic measurements. The effect of collisional quenching by O_2 on the toluene-LIF signal was studied by measuring the fluorescence lifetime using time-correlated single photon counting for various O_2 concentrations. The results confirmed assumptions [37] that the temperature dependence of the LIF signal disappears in the presence of O_2 even at concentrations below 1 vol.%. Therefore, we concluded that at the investigated conditions of ~ 250 K and above, mixing studies measuring the LIF signal as a function of the local mixing level of toluene and nitrogen on the molecular level can be performed even if local temperature gradients are present.

9 Outlook

In this work, the application of laser-induced fluorescence (LIF) to accelerated transonic flows was investigated, which required the extension of photophysical data sets of suitable fluorescence tracers towards lower temperatures and lower pressures. Although insights into the photophysics and fluid dynamics of transonic wakes have been gained through the application of LIF, there remain open questions or issues that have arisen throughout this work. These are summarized in this chapter.

Photophysics

The measured fluorescence lifetime data of anisole and toluene should be used for *improvement and extension of semi-empirical fluorescence step-ladder models* towards lower temperatures. For toluene, the transition from photo-induced heating to photo-induced cooling upon excitation at 266 nm was observed within the studied temperature range. These points mark transitions at which the molecules are already thermalized after excitation (i.e., no vibrational relaxation takes place during deactivation) and, therefore, allow the analytical determination of the ground state energy transferred to the excited state. The latter has recently been identified as a major uncertainty in the modeling of the fluorescence signal [52].

The *temperature range of the cooled fluorescence cell* used to measure temperature and pressure-dependent fluorescence lifetimes and pressures was only limited by the cooling capacity of the used thermostat allowing a minimum temperature of 257 K. A more potent device would enable measurements at temperatures as low as the minimum temperature of 240 K expected for the boundary conditions chosen for previous flow channel experiments [60]. In addition, the thermostat should be capable of heating to allow operating temperatures well above room temperature for providing a greater overlap with conditions used in literature.

For modeling of the LIF signal, e.g., for measurements using single-color excitation and single-color detection LIF schemes, information on the tracer *absorption cross-section* at low temperature and pressure is required. Absorption measurements of the pulsed fourth harmonic of Nd:YAG lasers were unsuccessful using the fluorescence cell developed in this work due to carbon deposits forming rapidly on the inside of the cell windows, likely due to photodissociation of adsorbed tracer molecules on the inner window surfaces. A specialized absorption cell with internal window flushing and, ideally, a long absorption path to compensate for the low tracer vapor pressure would be required for accurate measurements. Additionally, the tracer number density within the cell must be established reliably either by using a precisely metered sample gas delivery system or other means to establish the tracer concentration.

Measurements of the effect of oxygen quenching on the LIF signal of toluene were performed after excitation with 248 and 266 nm. From the literature, it appears that the quenching effect strongly depends on the vibrational energy level in the excited state, both in terms of the influence on the integrated fluorescence intensity and the spectral distribution. However, an analysis

of the energy dependence, e.g., by *systematic variation of the excitation wavelength*, is still outstanding.

Mixing studies

In this work, the extent of the mixing layer in the transonic wake of two injectors with blunt body trailing edges located in the accelerating nozzle flow was determined by LIF imaging in the modular flow channel at the ITLR in Stuttgart. In all cases, self-similar behavior of the mixing layer was observed, although the flow fields differed fundamentally depending on whether the trailing edge of the injector was located in the sub- or supersonic region of the nozzle. Despite introducing downstream pressure gradients (this work) and use of different nozzle and injector geometries (Wohler et al. [62]), self-similar behavior of the expanding mixing layer was observed. Therefore, future work should explore whether self-similar behavior of transonic mixing layers represents a universal principle and, if not, where the limits of this consideration lie. To this end, the LIF measurements should be repeated for different *different flow channel configurations* allowing more injector positions and *additional injector geometries*, which are currently under development at the ITLR.

Using a two-color detection scheme, a zone of incomplete molecular mixing was identified within the recirculation zone close to the injector trailing edge spanning several millimeters downstream of the point of injection for both injector geometries. To this end, the quenching effect of oxygen in the main air flow on the LIF signal of toluene in the oxygen-free low-momentum injector flow was exploited. It is well known that the mass flow in coaxial injection affects macroscopic mixing. Thus, an increase in the injection leads to a stabilization of the flow and less efficient mixing [90]. The *influence of the injection rate on molecular mixing*, however, has yet to be investigated.

Further, the LIF imaging experiments should include measurement of the spanwise (yz -plane) extend of the mixing layer (Fig. 9.1) for studying the *influence of the side walls* in complex flow pattern in the nozzle of the rectangular modular flow channel. To this end, a new nozzle module with larger windows extending further downstream is currently being developed at ITLR, allowing additional camera and light sheet positions. Cameras must be equipped with Scheimpflug adapters to allow imaging of the region of interest from the oblique viewing angle.

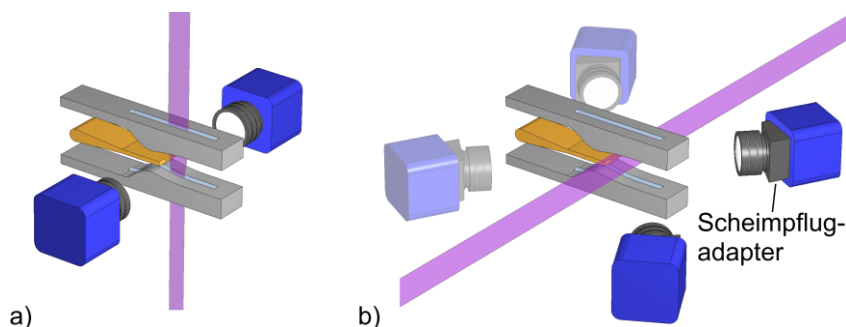


Fig. 9.1: LIF setups configured for single-color excitation and two-color detection for measurements in a) the xz -plane, as used for measurements in this work, and b) the yz -plane showing cameras equipped with Scheimpflug adapters, as proposed for future work.

The LIF images obtained in the modular flow channel, especially in the case of the two-color measurements, required ensemble averaging over several hundred shots for achieving acceptable signal levels. This was mainly due to the tracer concentration limited by its vapor pressure in the oxygen-containing main flow. To, e.g., resolve the periodic vortices present in the case of subsonic injection, either *single-shot* or *phase-locked imaging* prior to averaging would be required. For the latter, a method for measuring the vortex shedding frequency by laser beam steering was successfully demonstrated [79] which may allow triggering the LIF system in phase with vortex shedding events.

The two-color detection LIF technique, which was used in this work to analyze the mixing behavior at the molecular level from the O₂-induced red shift of the fluorescence signal, could also be used for *imaging the local density* in the flow channel independent of the local tracer number density: At constant O₂ concentration (working medium air) and homogeneous tracer distribution, the O₂ partial pressure depends on the local total density. The temperature could be determined simultaneously from the fluorescence signal intensity once corrected for the local density (and O₂ concentration) determined from the two-color ratio method. The required modifications of the flow channel to allow for homogeneous seeding of the main flow with tracers are already planned.

Mixing studies in the small-scale flow channel

For the development of the LIF measurement strategies proposed above, it would be desirable to generate a flow field with alternating periodic structures in the small-scale flow channel, similar to the injector wake flow studied in the modular flow channel at ITLR. This would require *modification of the small-scale flow channel* so that a small body (e.g., a cylinder) could be introduced into the flow. Ideally, this body would also serve as an injector for fluorescence tracers to perform basic mixing studies within the flow channel while fully controlling the composition of the main flow (i.e., pure N₂ atmosphere and/or homogeneous seeding with other tracer substances) and, therefore, also allowing techniques such as “flip” imaging [141].

Boundary layer effects and the interaction of the wall boundary layers with each other play a central role for the flow field within the small rectangular flow channel. The optical accessibility of its test section from four sides through allows to investigate the boundary layer growth and the interaction of the boundary layers, e.g., to improve the prediction by CFD simulations. To this end, the *selective visualization of the boundary layer* using LIF could be achieved by injection of tracer into the boundary layer through a slit perpendicular to the flow direction at the beginning of the test section. Additionally, analog to the proposed lateral imaging for the modular flow channel at the ITLR, the interacting boundary layers in the *yz*-plane (cf., Fig. 9.1) could be visualized by changing the light sheet position accordingly and using Scheimpflug adapters.

The suitability of the flow channel for spectroscopic measurements was demonstrated by measuring the fluorescence lifetime of toluene as a function of oxygen concentration. In the future,

these measurements should be extended to include *spectral measurements* and *additional tracers* for which no low-temperature data is available yet. The currently used evaporation system is suitable for a variety of common aromatic tracers with thermophysical properties similar to toluene, such as anisole, 1,2-xylene, 1,2,4-trimethylbenzene, and 1,4-difluorobenzene. The use of lower boiling ketones that are insensitive to the presence of O₂ such as acetone, 3-pentanone is equally possible.

10 Summary and conclusions

The work reported in this thesis is centered around a joint project of the Institute of Aerospace Thermodynamics (ITLR) at the University of Stuttgart and the Institute for Combustion and Gas Dynamics – Reactive Fluids (IVG) at the University of Duisburg-Essen. The project was motivated by the still incomplete understanding of the flow physics of transonic mixing layers – partly due to the lack of suitable measurement techniques for the relevant flow conditions. The latter result from the complex flow fields in applications where transonic mixing plays a role. For example, in supersonic combustion for hypersonic propulsion or in proposed supersonic flow-reactor concepts, reactants are added to accelerating transonic flows characterized by strong pressure and temperature gradients. Expansion of the gases and, thus, gas-dynamic cooling leads to temperatures and pressures far below standard conditions. For both applications, sufficient mixing within the short residence time in the fast flows is crucial. Measurement techniques suitable for visualizing the mixing behavior, such as laser-induced fluorescence (LIF), however, require knowledge of the photophysics of suitable fluorescence tracers which is sparse at low temperature. To combat this issue, extensive studies were carried out within this work to extend the applicability of the tracer-LIF technique which included the photophysical characterization of suitable tracer candidates. Furthermore, LIF was applied to study the mixing layer in the transonic wake of a central injector in a modular flow channel at ITLR specifically developed for transonic mixing studies. The key findings of this dissertation are listed in the following paragraphs.

Macroscopic mixing or stirring in transonic wakes was investigated in the flow channel at the ITLR using LIF imaging. For this purpose, toluene was added to the flow from two different central injectors placed at different positions in a convergent-divergent nozzle (design Mach number 1.7) so that their blunt trailing edge was either upstream (subsonic injection) or downstream (supersonic injection) of nozzle throat. The extend and growth rate of the resulting mixing layers downstream of the injector was measured from toluene concentration profiles extracted from the LIF images. Despite the inherently different characteristics of the two wake flows, self-similar behavior was observed in both cases. It is known from the literature that even small positive pressure gradients increase turbulence in the wake, which leads to an increase of the growth rate. However, it has been unclear whether or how this affects the self-similarity of the mixing layers in the transonic region or if self-similarity is a universal principle. To get closer to the answer to this question, different pressure gradients were imposed on the wake flow by equipping the modular flow channel with test sections with different sidewall inclinations. No deviations from the self-similar behavior for the resulting pressure gradients of -0.34 to 0.24 bar/m (subsonic injection) and -0.22 to 0.13 bar/m (supersonic injection) were found. In all cases, the observed growth rate of the mixing layer followed the $\frac{1}{2}$ -power law.

In the same apparatus, also the extent of *molecular mixing* in the near field after the point of injection was studied. Since the relevant length scales, i.e., where molecular diffusion dominates over viscous forces, cannot be resolved directly, the mixing state at the molecular level

was determined indirectly by the quenching effect of molecular oxygen on toluene LIF, which reduces and redshifts the fluorescence signal in the case of excitation at 248 nm. The spectral change in the region where the oxygen-free injector flow mixes with the oxygen-containing main flow was imaged using a two-color detection approach. Regions with incomplete mixing within the transonic nozzle flow were identified close to the injector trailing edge. The results showed that the region was similar in size after subsonic and supersonic injection extending only several millimeters in downstream direction, so that the flow was mixed on the molecular level before exiting the nozzle – despite an inhomogeneous macroscopic tracer distribution can be observed at the same point.

Photophysical *tracer characterization* and calibration required for quantitative measurements at the conditions prevalent in the flow channel experiments were performed in two different purpose-built experiments. Anisole and toluene vapor fluorescence spectra and fluorescence lifetimes at varying sub-ambient pressure and temperature (100–2000 mbar, 257–293 K) were studied in a cooled optical flow cell. For toluene, the reversal of the dependence of fluorescence lifetime on pressure was observed at a temperature between 283 and 292 K for 266-nm excitation. This point marks the transition point from photo-induced heating to photo-induced cooling, which was predicted to be just below room temperature but could not be observed yet. For anisole, the data showed that in the case of low collision rates (i.e., mean time between the collisions is of the same order of magnitude as the fluorescence lifetime), internal vibrational redistribution within the excited molecules significantly influences the spectral shape fluorescence causing a broadening effect of the fluorescence spectrum with decreasing pressure. These insights and the data points measured for the first time under such conditions support the generation of stepladder models for both tracers. Further, different temperature measurement schemes based on the new data were discussed and evaluated.

A *supersonic miniature flow channel* mimicking the flow conditions of the ITLR modular flow channel of the ITLR was designed, built, and thoroughly characterized. It serves two purposes: First, it is a tool for tracer characterization that extends the temperature range for spectroscopic measurements down to about 230 K by gas-dynamically cooling the tracer-laden sample gas. Secondly, its rectangular cross section, modular approach, and convenient optical access makes it a versatile testbed for validating imaging measurement techniques at low experimental cost compared to experiments in the full-scale version at the ITLR. In contrast to the latter, it could be operated with flows of pure nitrogen with any desired oxygen concentration enabling spectroscopy of fluorescence tracers, especially regarding oxygen quenching. As such, the Stern-Volmer coefficients for the oxygen quenching of toluene were determined under near-application conditions for varying sub-ambient temperatures. It was found that the signal was temperature independent under the prevailing conditions at oxygen concentrations greater than 1 vol.% when excited at 266 nm. This suggests that toluene LIF can be used to study the mixing of oxygen-free and oxygen-containing flows even under the strong temperature gradients that occur in accelerated transonic flows.

In summary, this work has addressed the application of tracer LIF techniques in transonic flows where temperatures and pressures are below standard conditions. In this context, mixing behavior was measured on the macroscopic and the molecular level using LIF imaging in a flow channel specifically designed for studying transonic wake flows. The photophysics of two suitable fluorescence tracers, anisole and toluene, were studied in detail in a purpose-built spectroscopic cooled flow cell. The data obtained can be used for quantitative measurements of temperature and pressure in cold flows which was demonstrated in miniature flow channel. Spectroscopic measurements in this miniature flow channel gave implications for measurements of the mixing behavior on the molecular level by exploiting the quenching effect of molecular oxygen on the fluorescence signal of toluene. The new extended data sets could and should be used to improve and extend the fluorescence models available for both tracers.

Bibliography

- [1] Grzona, A., Weiß, A., Olivier, H., Gawehn, T., Gülhan, A., Al-Hasan, N., Schnerr, G. H., Abdali, A., Luong, M., Wiggers, H., Schulz, C., Chun, J., Weigand, B., Winnemöller, T., Schröder, W., Rakel, T., Schaber, K., Goertz, V., Nirschl, H., Maisels, A., Leibold, W., and Dannehl, M., *Gas-phase synthesis of non-agglomerated nanoparticles by fast gasdynamic heating and cooling*, 26th International Symposium in Shock Waves, Göttingen, Germany, 2009, 857-862, doi: 10.1007/978-3-540-85181-3_10
- [2] Richter, J., *Experimentelle und numerische Mischungsuntersuchungen in kompressiblen Düsenströmungen*, PhD thesis, University of Stuttgart, Stuttgart, 2021.
- [3] Gamba, M., Miller, V. A., Mungal, M. G., and Hanson, R. K., *Temperature and number density measurement in non-uniform supersonic flowfields undergoing mixing using toluene PLIF thermometry*, Applied Physics B, 2015, **120**(2): 285-304
- [4] Koban, W., *Photophysical characterization of toluene and 3 pentanone for quantitative imaging of fuel/air ratio and temperature in combustion systems*, PhD thesis, Ruperto-Carola University of Heidelberg, 2005.
- [5] Miller, V. A., Gamba, M., Mungal, M. G., and Hanson, R. K., *Single- and dual-band collection toluene PLIF thermometry in supersonic flows*, Experiments in Fluids, 2013, **54**(6): 1169-1176
- [6] Zabeti, S., Aghsaee, M., Fikri, M., Welz, O., and Schulz, C., *Optical properties and pyrolysis of shock-heated gas-phase anisole*, Proceedings of the Combustion Institute, 2017, **36**(3): 4525-4532
- [7] Combs, C. S., Clemens, N. T., Danehy, P. M., and Murman, S. M., *Heat-shield ablation visualized using naphthalene planar laser-induced fluorescence*, Journal of Spacecraft and Rockets, 2017, **54**(2): 476-494
- [8] Combs, C. S. and Clemens, N. T., *Naphthalene laser-induced fluorescence measurements at low temperature and pressure*, Applied Optics, 2016, **55**(13): 3656-3669
- [9] Combs, C. S. and Clemens, N. T., *Measurements of Ablation-Products Transport in a Mach 5 Turbulent Boundary Layer using Naphthalene PLIF*, 53rd AIAA Aerospace Sciences Meeting, Kissimmee, FL, USA, 2015, doi: 10.2514/6.2015-1912
- [10] Handa, T., Matsuda, Y., and Egami, Y., *Phenomena peculiar to underexpanded flows in supersonic micronozzles*, Microfluidics and Nanofluidics, 2016, **20**(12): 166
- [11] Handa, T., Kitahara, K., Matsuda, Y., and Egami, Y., *Peculiarities of low-Reynolds-number supersonic flows in long microchannel*, Microfluidics and Nanofluidics, 2019, **23**(7): 88
- [12] Handa, T., Masuda, M., Kashitani, M., and Yamaguchi, Y., *Measurement of number densities in supersonic flows using a method based on laser-induced acetone fluorescence*, Experiments in Fluids, 2010, **50**(6): 1685-1694
- [13] Itani, L. M., Bruneaux, G., Di Lella, A., and Schulz, C., *Two-tracer LIF imaging of preferential evaporation of multi-component gasoline fuel sprays under engine conditions*, Proceedings of the Combustion Institute, 2015, **35**(3): 2915-2922

- [14] Cordier, M., Itani, L., and Bruneaux, G., *Quantitative measurements of preferential evaporation effects of multicomponent gasoline fuel sprays at ECN Spray G conditions*, International Journal of Engine Research, 2019, **21**(1): 185-198
- [15] Kranz, P. and Kaiser, S. A., *LIF-based imaging of preferential evaporation of a multi-component gasoline surrogate in a direct-injection engine*, Proceedings of the Combustion Institute, 2019, **37**(2): 1365-1372
- [16] Fuhrmann, D., Benzler, T., Fernando, S., Endres, T., Dreier, T., Kaiser, S. A., and Schulz, C., *Self-quenching in toluene LIF*, Proceedings of the Combustion Institute, 2017, **36**(3): 4505-4514
- [17] Eckbreth, A. C., *Laser diagnostics for combustion temperature and species*, 2 ed. New York: Taylor & Francis, 1996.
- [18] Koban, W., Koch, J. D., Sick, V., Wermuth, N., Hanson, R. K., and Schulz, C., *Predicting LIF signal strength for toluene and 3-pentanone under engine-related temperature and pressure conditions*, Proceedings of the Combustion Institute, 2005, **30**(1): 1545-1553
- [19] Hirasawa, T., Kaneba, T., Kamata, Y., Muraoka, K., and Nakamura, Y., *Temperature dependence of intensities of laser-induced fluorescences of ethylbenzene and naphthalene seeded in gas flow at atmospheric pressure*, Journal of Visualization, 2007, **10**(2): 197-206
- [20] Faust, S., Dreier, T., and Schulz, C., *Photo-physical properties of anisole: temperature, pressure, and bath gas composition dependence of fluorescence spectra and lifetimes*, Applied Physics B, 2013, **112**(2): 203-213
- [21] Faust, S., Tea, G., Dreier, T., and Schulz, C., *Temperature, pressure, and bath gas composition dependence of fluorescence spectra and fluorescence lifetimes of toluene and naphthalene*, Applied Physics B, 2012, **110**(1): 81-93
- [22] Luong, M., Koban, W., and Schulz, C., *Novel strategies for imaging temperature distribution using Toluene LIF*, Second International Conference on Optical and Laser Diagnostics, 2006, **45**(1): 133-139
- [23] Zimmermann, F. P., Koban, W., and Schulz, C., *Temperature Diagnostics Using Laser-Induced Fluorescence (LIF) of Toluene*, Laser Applications to Chemical, Security and Environmental Analysis, Incline Village, NV, USA, 2006, doi: 10.1364/LACSEA.2006.TuB4
- [24] Luong, M., Zhang, R., Schulz, C., and Sick, V., *Toluene laser-induced fluorescence for in-cylinder temperature imaging in internal combustion engines*, Applied Physics B, 2008, **91**(3-4): 669-675
- [25] Cundy, M., Trunk, P., Dreizler, A., and Sick, V., *Gas-phase toluene LIF temperature imaging near surfaces at 10 kHz*, Experiments in Fluids, 2011, **51**(5): 1169-1176
- [26] Friesen, E., Gessenhardt, C., Kaiser, S. A., Dreier, T., and Schulz, C., *In-cylinder temperature measurements via time-correlated single-photon counting of toluene laser-induced fluorescence through a fiber-based sensor*, Optics Letters, 2012, **37**(24): 5244-5246
- [27] Tran, K. H., Guibert, P., Morin, C., Bonnetty, J., Pounkin, S., and Legros, G., *Temperature measurements in a rapid compression machine using anisole planar laser-induced fluorescence*, Combustion and Flame, 2015, **162**(10): 3960-3970

- [28] Schulz, C. and Sick, V., *Tracer-LIF diagnostics: quantitative measurement of fuel concentration, temperature and fuel/air ratio in practical combustion systems*, Progress in Energy and Combustion Science, 2005, **31**(1): 75-121
- [29] Koban, W., Schorr, J., and Schulz, C., *Oxygen-distribution imaging with a novel two-tracer laser-induced fluorescence technique*, Applied Physics B, 2002, **74**(1): 111-114
- [30] Mohri, K., Luong, M., Vanhove, G., Dreier, T., and Schulz, C., *Imaging of the oxygen distribution in an isothermal turbulent free jet using two-color toluene LIF imaging*, Applied Physics B, 2011, **103**(3): 707-715
- [31] Ehn, A., Jonsson, M., Johansson, O., Aldén, M., and Bood, J., *Quantitative oxygen concentration imaging in toluene atmospheres using Dual Imaging with Modeling Evaluation*, Experiments in Fluids, 2013, **54**(1): 1433
- [32] Frieden, D., Sick, V., Gronki, J., and Schulz, C., *Quantitative oxygen imaging in an engine*, Applied Physics B, 2014, **75**(1): 137-141
- [33] Freed, K. F. and Heller, D. F., *Pressure dependence of electronic relaxation: A stochastic model*, The Journal of Chemical Physics, 1974, **61**(10): 3942-3953
- [34] Burton, C. S. and Noyes, W. A., *Electronic energy relaxation in toluene vapor*, The Journal of Chemical Physics, 1968, **49**(4): 1705-1714
- [35] Reboux, J., Puechberty, D., and Dionnet, F., *A new approach of planar Laser Induced fluorescence applied to fuel/air Ratio measurement in the Compression stroke of an optical S.I. engine*, SAE Technical Paper 1994, 941988, doi: 10.4271/941988
- [36] Reboux, J., Puechberty, D., and Dionnet, F., *Study of mixture inhomogeneities and combustion development in a SI engine using a new approach of laser induced fluorescence (FARLIF)*, SAE Technical Paper, 1996, 961205, doi: 10.4271/961205
- [37] Koban, W., Koch, J. D., Hanson, R. K., and Schulz, C., *Toluene LIF at elevated temperatures: implications for fuel–air ratio measurements*, Applied Physics B, 2005, **80**(2): 147-150
- [38] Koban, W., Koch, J. D., Hanson, R. K., and Schulz, C., *Oxygen quenching of toluene fluorescence at elevated temperatures*, Applied Physics B, 2005, **80**(6): 777-784
- [39] Koban, W. and Schulz, C., *Toluene laser-induced fluorescence (LIF) under engine-related pressures, temperatures and oxygen mole fractions*, SAE Technical Paper, 2005, 2005-01-2091, doi: 10.4271/2005-01-2091
- [40] Zimmermann, F. P., Koban, W., Roth, C. M., Herten, D.-P., and Schulz, C., *Fluorescence lifetime of gas-phase toluene at elevated temperatures*, Chemical physics letters, 2006, **426**(4-6): 248-251
- [41] Devillers, R., Bruneaux, G., and Schulz, C., *Investigation of toluene LIF at high pressure and high temperature in an optical engine*, Applied Physics B, 2009, **96**(4): 735-739
- [42] Yoo, J., Mitchell, D., Davidson, D. F., and Hanson, R. K., *Planar laser-induced fluorescence imaging in shock tube flows*, Experiments in Fluids, 2010, **49**(4): 751-759
- [43] Cheung, B. H., *Tracer-based planar laser-induced fluorescence diagnostics: quantitative photophysics and time-resolved imaging*, PhD thesis, Stanford University, Stanford, CA, USA, 2011.

- [44] Koch, J. D., Hanson, R. K., Koban, W., and Schulz, C., *Rayleigh-calibrated fluorescence quantum yield measurements of acetone and 3-pentanone*, Applied Optics, 2004, **43**(31): 5901-5910
- [45] Faust, S., Dreier, T., and Schulz, C., *Temperature and bath gas composition dependence of effective fluorescence lifetimes of toluene excited at 266 nm*, Chemical Physics, 2011, **383**(1-3): 6-11
- [46] Rossow, B., *Photophysical processes of organic fluorescent molecules and kerosene – applications to combustion engines*, PhD thesis, Université Paris Sud, Paris, France, 2014.
- [47] Estruch-Samper, D., Vanstone, L., Hillier, R., and Ganapathisubramani, B., *Toluene-based planar laser-induced fluorescence imaging of temperature in hypersonic flows*, Experiments in Fluids, 2015, **56**(6): 115
- [48] Benzler, T., Faust, S., Dreier, T., and Schulz, C., *Low-pressure effective fluorescence lifetimes and photo-physical rate constants of one- and two-ring aromatics*, Applied Physics B, 2015, **121**(4): 549-558
- [49] Beuting, M., Dreier, T., Schulz, C., and Endres, T., *Low-temperature and low-pressure effective fluorescence lifetimes and spectra of gaseous anisole and toluene*, Applied Physics B, 2021, **127**(4): 59
- [50] Tran, K. H., Morin, C., Kühni, M., and Guibert, P., *Fluorescence spectroscopy of anisole at elevated temperatures and pressures*, Applied Physics B, 2013, **115**(4): 461-470
- [51] Wang, Q., Tran, K. H., Morin, C., Bonnety, J., Legros, G., and Guibert, P., *Predicting fluorescence quantum yield for anisole at elevated temperatures and pressures*, Applied Physics B, 2017, **123**(7): 199
- [52] Baranowski, T., Dreier, T., Schulz, C., and Endres, T., *Excitation wavelength dependence of the fluorescence lifetime of anisole*, Physical Chemistry Chemical Physics, 2019, **21**(27): 14562-14570
- [53] Eckart, C., *An Analysis Of The Stirring And Mixing Processes In Incompressible Fluids*, Journal of Marine Research, 1948, **7**(3): 265-275
- [54] Winter, M., Hermanson, J., and Dobbs, G., *Imaging of molecular mixing in a gas-phase turbulent jet by collisional energy-transfer fluorescence*, 30th Aerospace Sciences Meeting and Exhibit, Reno, NV, USA, 2012, doi: 10.2514/6.1992-381
- [55] Broadwell, J. E. and Mungal, M. G., *Large-scale structures and molecular mixing*, Physics of Fluids A: Fluid Dynamics, 1991, **3**(5): 1193-1206
- [56] Bonanos, A. M., Bergthorson, J. M., and Dimotakis, P. E., *Molecular mixing and flowfield measurements in a recirculating shear flow. Part II: Supersonic flow*, Flow, Turbulence and Combustion, 2009, **83**(2): 251-268
- [57] Batchelor, G. K., *Small-scale variation of convected quantities like temperature in turbulent fluid Part I. General discussion and the case of small conductivity*, Journal of Fluid Mechanics, 2006, **5**(1): 113-133
- [58] Smits, A. J. and Dussauge, J.-P., *Turbulent Shear Layers in Supersonic Flow*, 2 ed. New York: Springer, 2006.

- [59] Beuting, M., Richter, J., Weigand, B., and Schulz, C., *Experimental investigation of the influence of the pressure gradient on the transonic mixing behavior in blunt-body wakes using tracer LIF*, 2018 Fluid Dynamics Conference, Atlanta, GA, USA, 2018, 3543, doi: 10.2514/6.2018-3543
- [60] Richter, J., Beuting, M., Schulz, C., and Weigand, B., *Mixing processes in the transonic, accelerated wake of a central injector*, Physics of Fluids, 2019, **31**(1): 016102
- [61] Chun, J., *Experimental Investigations of Injection, Mixing, and Reaction Processes in Supersonic Flow Applications*, PhD thesis, University of Stuttgart, Stuttgart, Germany, 2009.
- [62] Wohler, A., Mohri, K., Schulz, C., and Weigand, B., *Flow structures in subsonic-to-supersonic mixing processes using different injector geometries*, 4th European Conference for Aerospace Sciences (EUCASS), St. Petersburg, Russia, 2011
- [63] Mohri, K., Wohler, A., Weigand, B., and Schulz, C., *Toluene laser-induced fluorescence (LIF) imaging of supersonic flow within a diverging duct*, 28th International Symposium on Shock Waves, 2012, 509-514, doi: 10.1007/978-3-642-25688-2_78
- [64] Wohler, A., Weigand, B., Mohri, K., and Schulz, C., *Mixing processes in a compressible accelerated nozzle flow with blunt-body wakes*, AIAA Journal, 2014, **52**(3): 559-568
- [65] Mohri, K., Wohler, A., Weigand, B., and Schulz, C., *Toluene Laser-Induced Fluorescence (LIF) Imaging of Supersonic Flow within a Diverging Duct with Injectors in the Supersonic Region*, 29th International Symposium on Shock Waves, Madison, WI, USA, 2015, **1**, 471-476, doi: 10.1007/978-3-319-16835-7
- [66] Wohler, A., *Mischungsuntersuchungen in einer beschleunigten kompressiblen Düsenströmung unter Verwendung verschiedener Injektorgeometrien*, PhD thesis, University of Stuttgart, Stuttgart, Germany, 2015.
- [67] Dimotakis, P. E., *Turbulent Mixing*, Annual Review of Fluid Mechanics, 2005, **37**(1): 329-356
- [68] Nakagawa, M. and Dahm, W. J. A., *Virtual origin of incompressible and supersonic turbulent bluff-body wakes*, AIAA Journal, 2005, **43**(3): 697-700
- [69] Nakagawa, M. and Dahm, W. J. A., *Scaling properties and wave interactions in confined supersonic turbulent bluff-body wakes*, AIAA Journal, 2006, **44**(6): 1299-1309
- [70] Meyer, T. R., King, G. F., Martin, G. C., Lucht, R. P., Schauer, F. R., and Dutton, J. C., *Accuracy and resolution issues in NO/acetone PLIF measurements of gas-phase molecular mixing*, Experiments in Fluids, 2002, **32**(6): 603-611
- [71] Rossmann, T., Mungal, M. G., and Hanson, R. K., *Mixing efficiency measurements using a modified cold chemistry technique*, Experiments in Fluids, 2004, **37**(4): 566-576
- [72] Mungal, M. G. and Dimotakis, P. E., *Mixing and combustion with low heat release in a turbulent shear layer*, Journal of Fluid Mechanics, 2006, **148**: 349-382
- [73] Paul, P. H. and Clemens, N. T., *Subresolution Measurements of Unmixed Fluid Using Electronic Quenching of No-A2-Sigma*, Optics Letters, 1993, **18**(2): 161-163

- [74] Clemens, N. T. and Paul, P. H., *Scalar measurements in compressible axisymmetric mixing layers*, *Physics of Fluids*, 1995, **7**(5): 1071
- [75] King, G. F., Dutton, J. C., and Lucht, R. P., *Instantaneous, quantitative measurements of molecular mixing in the axisymmetric jet near field*, *Physics of Fluids*, 1999, **11**(2): 403-416
- [76] Yu, X., Chang, G., Peng, J., Dong, H., Yu, Y., Gao, L., Cao, Z., Yan, B., Luo, Y., and Qu, T., *Oxygen concentration distribution measurement of the nozzle flow field by toluene/acetone planar laser-induced fluorescence*, *Frontiers in Physics*, 2019, **7**: 205
- [77] Hu, H. and Koochesfahani, M. M., *A novel method for instantaneous, quantitative measurement of molecular mixing in gaseous flows*, *Experiments in Fluids*, 2002, **33**(1): 202-209
- [78] Richter, J., Beuting, M., Schulz, C., Dreier, T., and Weigand, B., *Macroscopic mixing investigation in a compressible accelerated nozzle flow using toluene tracer LIF*, 18th International Symposium on Applications of Laser and Imaging Techniques to Fluid Dynamics, Lisbon, Portugal, 2016, 2542-2559
- [79] Richter, J., Steinhausen, C., Weigand, B., Beuting, M., Dreier, T., and Schulz, C., *Non-intrusive frequency measurements of bluff-body vortex shedding at high Reynolds numbers*, 23rd International Society of Air-breathing Engines Conference, Manchester, UK, 2017, 2017-21472
- [80] Beuting, M., Richter, J., Weigand, B., Dreier, T., and Schulz, C., *Application of toluene LIF to transonic nozzle flows to identify zones of incomplete molecular mixing*, *Optics Express*, 2018, **26**(8): 10266-10273
- [81] Richter, J., Beuting, M., Schulz, C., and Weigand, B., *Numerical investigation of transonic mixing behavior in the wake of a central injector at different reynolds numbers*, AIAA Fluid Dynamics Conference, Atlanta, GA, USA, 2018, 3544, doi: 10.2514/6.2018-3544
- [82] Richter, J., Mayer, J., and Weigand, B., *Accuracy of non-resonant laser-induced thermal acoustics (LITA) in a convergent-divergent nozzle flow*, *Applied Physics B*, 2018, **124**(2): 19
- [83] White, F. M., *Fluid mechanics*, 8 ed. New York, United Sttes: McGraw Hill, 2017.
- [84] Weigand, B., Köhler, J., and von Wolfersdorf, J., *Thermodynamik kompakt*, 3 ed. Berlin, Heidelberg, Germany: Springer Vieweg, 2013.
- [85] Goldstein, S., *Modern Developments in Fluid Dynamics*, 1 ed. New York: Dover Publications, 1965.
- [86] Younis, B. A. and Przulj, V. P., *Computation of turbulent vortex shedding*, *Computational Mechanics*, 2005, **37**(5): 408-425
- [87] Brown, G. L. and Roshko, A., *On density effects and large structure in turbulent mixing layers*, *Journal of Fluid Mechanics*, 2006, **64**(4): 775-816
- [88] Cantwell, B. and Coles, D., *An experimental study of entrainment and transport in the turbulent near wake of a circular cylinder*, *Journal of Fluid Mechanics*, 2006, **136**: 321-374

- [89] Wygnanski, I., Champagne, F., and Marasli, B., *On the large-scale structures in two-dimensional, small-deficit, turbulent wakes*, Journal of Fluid Mechanics, 1986, **168**: 31-71
- [90] Bearman, P. W., *The effect of base bleed on the flow behind a two-dimensional model with a blunt trailing edge*, Aeronautical Quarterly, 1967, **18**(3): 207-224
- [91] Motallebi, F. and Norbury, J. F., *The effect of base bleed on vortex shedding and base pressure in compressible flow*, Journal of Fluid Mechanics, 1981, **110**: 273-292
- [92] Pope, S. B., *Turbulent flows*, 7 ed. Cambridge, United Kingdom: Cambridge University Press, 2000.
- [93] Klán, P. and Wirz, J., *Photochemistry of organic compounds: from concepts to practice*, 1 ed. Chichester, UK: Wiley-Blackwell, 2009.
- [94] Sauer, M., Hofkens, J., and Enderlein, J., *Handbook of Fluorescence Spectroscopy and Imaging*, 1 ed. Weinheim: Wiley-VCH, 2011.
- [95] Faust, S., Goschütz, M., Kaiser, S. A., Dreier, T., and Schulz, C., *A comparison of selected organic tracers for quantitative scalar imaging in the gas phase via laser-induced fluorescence*, Applied Physics B, 2014, **117**(1): 183-194
- [96] Benzler, T., Endres, T., Dreier, T., and Schulz, C., *Temperature, pressure, and oxygen quenching behavior of fluorescence spectra and lifetimes of gas-phase o-xylene and 1,2,4-trimethylbenzene*, Applied Physics B, 2018, **124**(4): 70
- [97] Zabeti Jahromi, S., *Optical properties and reaction kinetics of shock-heated gas-phase tracers for quantitative laser-induced fluorescence*, PhD thesis, University of Duisburg-Essen, Duisburg, Germany, 2019.
- [98] Chaze, W., Caballina, O., Castanet, G., and Lemoine, F., *The saturation of the fluorescence and its consequences for laser-induced fluorescence thermometry in liquid flows*, Experiments in Fluids, 2016, **57**(4): 58
- [99] Kimura, Y., Abe, D., and Terazima, M., *Vibrational energy relaxation of naphthalene in the S(1) state in various gases*, The Journal of Chemical Physics, 2004, **121**(12): 5794-5800
- [100] Kikuchi, K., Sato, C., Watabe, M., Ikeda, H., Takahashi, Y., and Miyashi, T., *New aspects of fluorescence quenching by molecular oxygen*, Journal of the American Chemical Society, 2002, **115**(12): 5180-5184
- [101] Hanson, R. K., *Combustion diagnostics: Planar imaging techniques*, Symposium (International) on Combustion, 1988, **21**(1): 1677-1691
- [102] Thurber, M. C. and Hanson, R. K., *Simultaneous imaging of temperature and mole fraction using acetone planar laser-induced fluorescence*, Experiments in Fluids, 2001, **30**(1): 93-101
- [103] Rothamer, D. A., Snyder, J. A., Hanson, R. K., and Steeper, R. R., *Two-wavelength PLIF diagnostic for temperature and composition*, SAE International Journal of Fuels and Lubricants, 2008, **1**(1): 520-533
- [104] Fujikawa, T., *2-D Temperature measurements of unburned gas mixture in an engine by two-line excitation LIF technique*, SAE Technical Paper, 2006, 2006-01-3336, doi: 10.4271/2006-01-3336

- [105] Cheung, B. H. and Hanson, R. K., *CW laser-induced fluorescence of toluene for time-resolved imaging of gaseous flows*, Applied Physics B, 2009, **98**(2-3): 581-591
- [106] Zickus, V., Wu, M. L., Morimoto, K., Kapitany, V., Fatima, A., Turpin, A., Insall, R., Whitelaw, J., Machesky, L., Bruschini, C., Faccio, D., and Charbon, E., *Fluorescence lifetime imaging with a megapixel SPAD camera and neural network lifetime estimation*, Scientific Reports, 2020, **10**(1): 20986
- [107] Ehn, A., Johansson, O., Arvidsson, A., Aldén, M., and Bood, J., *Single-laser shot fluorescence lifetime imaging on the nanosecond timescale using a Dual Image and Modeling Evaluation algorithm*, Optics Express, 2012, **20**(3): 3043-3056
- [108] Bessler, W. G. and Schulz, C., *Quantitative multi-line NO-LIF temperature imaging*, Applied Physics B: Lasers and Optics, 2004, **78**(5): 519-533
- [109] McDougall, C. C., Hinman, W. S., Johansen, C. T., Bathel, B. F., Inman, J. A., and Danehy, P. M., *Evaluation of nitric oxide laser-induced fluorescence thermometry techniques in a hypersonic boundary layer*, Experiments in Fluids, 2020, **61**(4): 102
- [110] Chrystie, R. S. M., Feroughi, O. M., Dreier, T., and Schulz, C., *SiO multi-line laser-induced fluorescence for quantitative temperature imaging in flame-synthesis of nanoparticles*, Applied Physics B, 2017, **123**(4): 104
- [111] Tea, G., *Development and exploitation of optical diagnostic techniques for simultaneous 2D temperature and equivalence ratio measurements for the understanding of combustion phenomena in reciprocating engine*, PhD thesis, University of Duisburg-Essen, Duisburg, Germany, 2014.
- [112] Settles, G. S., *Schlieren and shadowgraph techniques: visualizing phenomena in transparent media*. Berlin, Germany: Springer, 2001.
- [113] Matsumoto, M., *Vortex shedding of bluff bodies: A review*, Journal of Fluids and Structures, 1999, **13**(7-8): 791-811
- [114] Birks, J. B., Braga, C. L., and Lumb, M. D., *'Excimer' fluorescence. VI. Benzene, toluene, p-xylene and mesitylene*, Proceedings of the Royal Society of London. Series A, Mathematical and Physical Sciences, 1965, **283**(1392): 83-99
- [115] van Cruyningen, I., Lozano, A., and Hanson, R. K., *Quantitative imaging of concentration by planar laser-induced fluorescence*, Experiments in Fluids, 1990, **10**(1): 41-49
- [116] Meyer, T. R., Dutton, J. C., and Lucht, R. P., *Coherent structures and turbulent molecular mixing in gaseous planar shear layers*, Journal of Fluid Mechanics, 2006, **558**: 179-205
- [117] Felton, P. G., Bracco, F. V., and Bardsley, M. E. A., *On the quantitative application of exciplex fluorescence to engine sprays*, SAE Technical Paper, 1993, 930870, doi: 10.4271/930870
- [118] Herzler, J., Fikri, M., Hitzbleck, K., Starke, R., Schulz, C., Roth, P., and Kalghatgi, G. T., *Shock-tube study of the autoignition of n-heptane/toluene/air mixtures at intermediate temperatures and high pressures*, Combustion and Flame, 2007, **149**(1-2): 25-31
- [119] King, G. F., Lucht, R. P., and Dutton, J. C., *Quantitative dual-tracer planar laser-induced fluorescence measurements of molecular mixing*, Optics Letters, 1997, **22**(9): 633-635

- [120] Ginsburg, N., Robertson, W. W., and Matsen, F. A., *The Near Ultraviolet Absorption Spectrum of Toluene Vapor*, The Journal of Chemical Physics, 1946, **14**(9): 511-517
- [121] Peterson, B., Baum, E., Böhm, B., Sick, V., and Dreizler, A., *Evaluation of toluene LIF thermometry detection strategies applied in an internal combustion engine*, Applied Physics B, 2014, **117**(1): 151-175
- [122] Koban, W., Koch, J. D., Hanson, R. K., and Schulz, C., *Absorption and fluorescence of toluene vapor at elevated temperatures*, Physical Chemistry Chemical Physics, 2004, **6**(11): 2940-2945
- [123] Cheung, B. H. and Hanson, R. K., *3-pentanone fluorescence yield measurements and modeling at elevated temperatures and pressures*, Applied Physics B, 2012, **106**(3): 755-768
- [124] Thurber, M. C., Grisch, F., Kirby, B. J., Votsmeier, M., and Hanson, R. K., *Measurements and modeling of acetone laser-induced fluorescence with implications for temperature-imaging diagnostics*, Applied Optics, 1998, **37**(21): 4963-78
- [125] Beddard, G. S., Formosinho, S. J., and Porter, G., *Pressure effects on the fluorescence from naphthalene vapour*, Chemical physics letters, 1973, **22**(2): 235-238
- [126] Wadi, H. and Pollak, E., *Theory of laser cooling of polyatomic molecules in an electronically excited state*, The Journal of Chemical Physics, 1999, **110**(24): 11890-11905
- [127] Becker, W., *The bh TCSPC Handbook*, 8th ed. Becker & Hickl GmbH, 2019.
- [128] Settersten, T. B., Patterson, B. D., and Gray, J. A., *Temperature- and species-dependent quenching of NO A 2Sigma+(v'=0) probed by two-photon laser-induced fluorescence using a picosecond laser*, The Journal of Chemical Physics, 2006, **124**(23): 234308
- [129] Uy, J. O. and Lim, E. C., *Electronic relaxation in naphthalene vapor*, Chemical Physics Letters, 1970, **7**(2): 306-310
- [130] Kranz, P., Fuhrmann, D., Goschütz, M., Kaiser, S., Bauke, S., Golibrzuch, K., Wackerbarth, H., Kawelke, P., Luciani, J., Beckmann, L., Zachow, J., Schuette, M., Thiele, O., and Berg, T., *In-Cylinder LIF Imaging, IR-Absorption Point Measurements, and a CFD Simulation to Evaluate Mixture Formation in a CNG-Fueled Engine*, SAE International Journal of Engines, 2018, **11**(6): 1221-1238
- [131] Baranowski, T., Endres, T., Dreier, T., and Schulz, C. *TracerSim-Dat - Open Database for Tracer-LIF Datasets*. tracer-sim.com (accessed September 1, 2021).
- [132] Combs, C. S., *Quantitative Measurements of Ablation-Products Transport in Supersonic Turbulent Flows Using Planar Laser-Induced Fluorescence*, PhD thesis, University of Texas, Austin, TX, USA, 2015.
- [133] Hickman, C. G., Gascooke, J. R., and Lawrance, W. D., *The S1-S0(1B2-1A1) transition of jet-cooled toluene: Excitation and dispersed fluorescence spectra, fluorescence lifetimes, and intramolecular vibrational energy redistribution*, The Journal of Chemical Physics, 1996, **104**(13): 4887-4901
- [134] Mercier, X., Wartel, M., Pauwels, J. F., and Desgroux, P., *Implementation of a new spectroscopic method to quantify aromatic species involved in the formation of soot particles in flames*, Applied Physics B, 2008, **91**(2): 387-395

-
- [135] Ehn, A., Johansson, O., Bood, J., Arvidsson, A., Li, B., and Aldén, M., *Fluorescence lifetime imaging in a flame*, Proceedings of the Combustion Institute, 2011, **33**(1): 807-813
- [136] Grümmer, K., *A Computer program for the design of plane and axisymmetric supersonic wind tunnel nozzles*, Deutsche Forschungs- und Versuchsanstalt für Luft- und Raumfahrt, Cologne, Germany, Technical Report, DLR-FB 76-59, 1976.
- [137] Saylor, J. H. and Battino, R., *The solubilities of the rare gases in some simple benzene derivatives*, The Journal of Physical Chemistry, 2002, **62**(10): 1334-1337
- [138] Jabłoniec, A., Horstmann, S., and Gmehling, J., *Experimental determination and calculation of gas solubility data for nitrogen in different solvents*, Industrial & Engineering Chemistry Research, 2007, **46**(13): 4654-4659
- [139] Menser, J., Schneider, F., Dreier, T., and Kaiser, S. A., *Multi-pulse shadowgraphic RGB illumination and detection for flow tracking*, Experiments in Fluids, 2018, **59**(6): 90
- [140] Polt, A., Platzer, B., and Maurer, G., *Parameter der thermischen Zustandsgleichung von Bender fuer 14 mehratomige reine Stoffe*, Chemische Technik, 1992, **44**(6): 216-224
- [141] Koochesfahani, M. M., Dimotakis, P. E., and Broadwell, J. E., *A 'flip' experiment in a chemically reacting turbulent mixing layer*, AIAA Journal, 1985, **23**(8): 1191-1194

Appendix

A. Effective fluorescence lifetimes of toluene and anisole

Table A.1: Effective fluorescence lifetimes of toluene and anisole measured in Chapter 7 for total pressure $p = 100\text{--}2000$ mbar und temperature $T = 257\text{--}292$ K.

Pressure / mbar	Toluene					Anisole				
	Effective fluorescence lifetime / ns					Effective fluorescence lifetime / ns				
	257 K	265 K	274 K	283 K	292 K	257 K	265 K	274 K	283 K	292 K
100	57.46	56.65	55.14	53.58	51.90	11.85	11.58	11.32	11.06	10.83
200	58.33	57.28	55.70	53.74	51.71	12.30	12.11	11.77	11.51	11.21
400	59.25	57.43	55.74	53.40	50.80	12.63	12.40	12.09	11.77	11.51
600	59.28	57.36	55.56	52.85	49.86	12.71	12.48	12.18	11.85	11.58
800	59.15	57.17	55.25	52.40	49.13	12.73	12.50	12.19	11.87	11.59
1000	58.88	57.13	54.98	52.12	48.44	12.72	12.50	12.21	11.84	11.56
1500	58.44	56.69	54.41	51.24	47.04	12.68	12.47	12.17	11.78	11.51
2000	57.94	56.26	53.85	50.54	46.06	12.64	12.42	12.13	11.74	11.41

B. Error estimation for the fluorescence lifetime thermometry method

The systematic error of the fluorescence lifetime thermometry technique is determined using the statistical errors of the calibration measurement published earlier [49]. The procedure shown in Fig. B.1 starts with determining the fluorescence lifetime τ_m from the measured signal time trace $S(t)$ using the convolute-and-compare fitting method. Before looking up the corresponding temperature T_m from the calibration data (lifetime τ_c as a function of pressure p_c and temperature T_c), random Gaussian noise is added to all relevant parameters (see table in Fig. B.1). To this end, the standard deviations for the calibration pressure, $\sigma_{p,c}$, the calibration temperature, $\sigma_{T,c}$, and the calibration fluorescence lifetime, σ_τ determined in previous work [49] were used. Since different pressure sensors are used in this work, the standard deviation of the pressure measurement $\sigma_{p,m}$ is calculated from the pressure data measured in chapter 7. Because the method, equipment, and signal level for determining the fluorescence lifetime is identical to the calibration measurements, the identical standard deviation σ_τ is used for the fluorescence lifetime (hence omitting the index). After that, the interpolating plane (cf., Fig. 8.9) is calculated from the noisy calibration data (τ'_c, p'_c, T'_c). Finally, the measured temperature T_m is looked up using the noisy measured lifetime τ'_m and pressure p'_m from the interpolating plane. This is repeated 100 times for each point so that the temperature uncertainty T_{error} can be calculated from the statistics (standard deviation in this case).

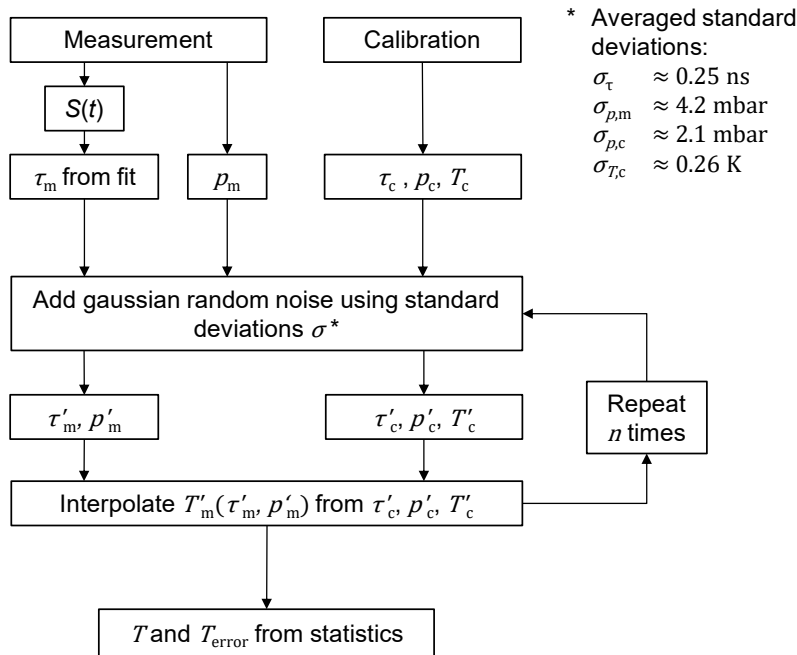


Fig. B.1: Flow chart for the systematic error determination of the fluorescence lifetime thermometry method.

C. Schlieren images

Figure C.1 shows ensemble-averaged schlieren images from the flow channel described in Chapter 7 for the different temperature inlet cases. The differences are imperceptible in all cases.

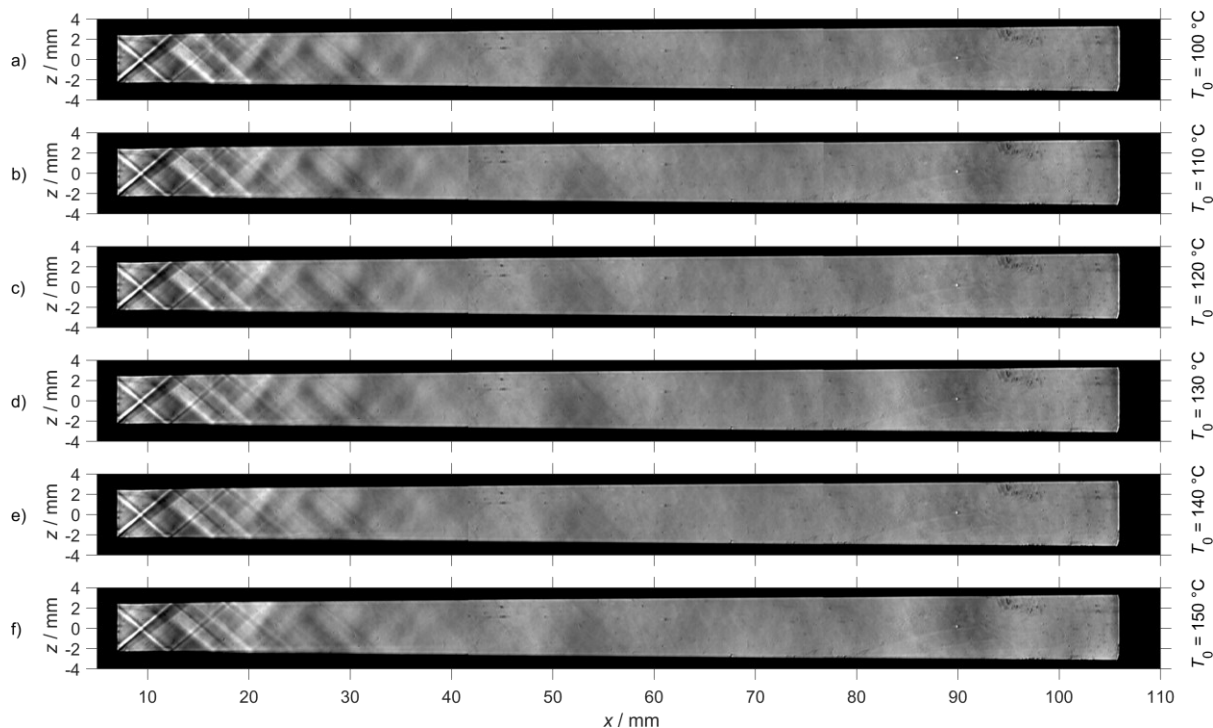


Fig. C.1: Ensemble averaged (100 shots) schlieren images obtained in the flow channel at an inlet pressure $p_0 = 3.1$ bar for all investigated inlet temperatures from $T_0 = 100$ to 150 °C (a–f).

D. Fluorescence lifetime fit for nanosecond excitation of toluene LIF

Figure D.1 shows the fit result of the convolute-and-compare method used in chapter 8.6.5 to determine the fluorescence lifetime from the toluene-LIF signal decay curve measured after excitation with a nanosecond laser pulse. The instrument response function (IRF) is determined from scattered laser light without tracer present.

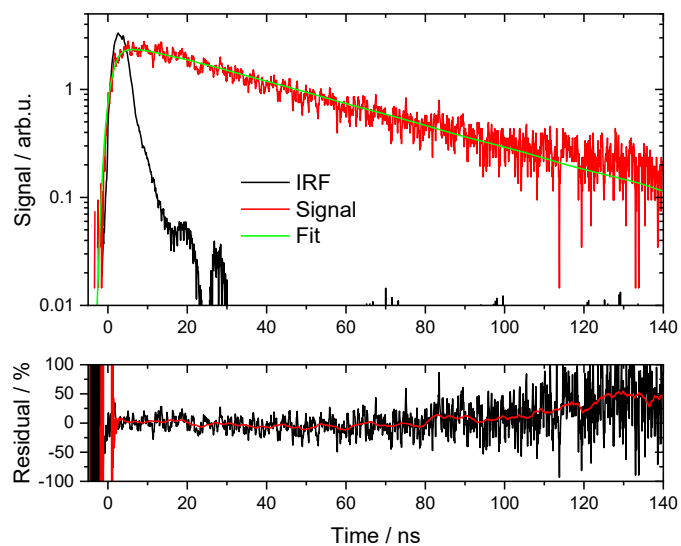


Fig. D.1: Typical fluorescence intensity time trace, instrument response function, and fit using the convolute-and-compare method for the toluene-LIF signal upon ns-excitation at 266 nm.

E. Temperature at different vertical positions in the miniature flow channel

Figure E.1 shows the temperature along the miniature flow channel center plane ($y = 0$ mm) for different vertical z positions for the highest and lowest temperature investigated (cf., chapter 8.6.2). It is apparent, that the temperature deviates only slightly at the nozzle exit and to a lesser degree further downstream

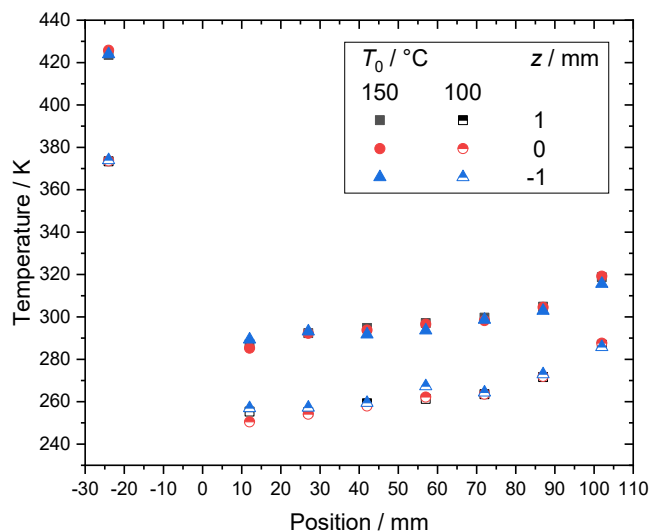


Fig. E.1: Flow temperature measured at different vertical (z) positions in the flow channel at an inlet pressure $p_0 = 3.1$ bar

F. Estimated temperature dependence of toluene LIF at low temperature

According to Eq. 8.6, the LIF signal is proportional to the in the absorption cross-section σ_{abs} , the tracer number density n_{tracer} in the probe volume, and the fluorescence quantum yield ϕ_{fl} , all of which depend on the local temperature T and, partly, on pressure p . For modeling the signal variation S_{fl} within a LIF image caused by temperature variations relative to certain reference conditions (index ref), several assumptions are made. The considerations in this chapter are made for $p_{\text{ref}} = 1$ bar, $T_{\text{ref}} = 300$ K, and an excitation wavelength of 266 nm.

$$\frac{S_{\text{fl}}(T, p)}{S_{\text{fl,ref}}} = \frac{n_{\text{tracer}}(T) \sigma_{\text{abs}}(T) \phi_{\text{fl}}(T, p)}{n_{\text{tracer,ref}} \sigma_{\text{abs,ref}} \phi_{\text{fl,ref}}} \quad (\text{F.1})$$

The absorption cross-section at the 266-nm laser line is extrapolated from the data of Koban et al. [122] as shown in Fig. F.1 using a linear fit to their lower-temperature (300–400 K) data resulting in the following relation.

$$\sigma(T) = 1.37 \times 10^{-21} T \text{ K}^{-1} \text{ cm}^{-2} - 2.15 \times 10^{-19} \text{ cm}^{-2} \quad (\text{F.2})$$

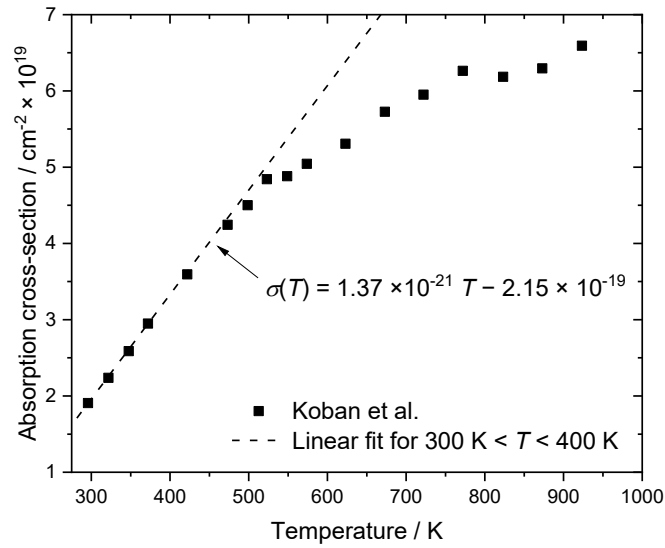


Fig. F.1: Temperature dependence of the toluene absorption cross-section at the 266-nm laser line from Koban et al. [122]. The dashed line corresponds to a linear fit to the values the linear region between 300–400 K.

The relative fluorescence quantum yield is equal to the relative fluorescence lifetime τ . The latter is interpolated from the data measured within this work.

$$\frac{\phi_{\text{fl}}(T, p)}{\phi_{\text{fl,ref}}} = \frac{\tau(T, p)}{\tau(T_{\text{ref}}, p_{\text{ref}})} \quad (\text{F.3})$$

Since the local pressure amplitudes cannot be measured independently, assumptions must be made for relationship of p to T for looking up τ and for determining the change in n_{tracer} .

There are two conceivable scenarios for the origin of temperature fluctuations in the flow channel. The first assumes that the fluctuations are caused by upstream flow effects and entrainment of gas from the boundary layer with a different temperature than the mean flow. Pockets of gas with different temperatures are then transported with the flow to the measurement point. Along the way, the pressure of the gas equalizes with the surrounding flow. The density then results from the ideal gas law assuming a constant pressure, i.e., **isobaric** conditions.

$$p = \text{const.} = p_{\text{ref}} \quad (\text{F.4})$$

$$\frac{n_{\text{tracer}}}{n_{\text{tracer,ref}}} = \frac{\rho}{\rho_{\text{ref}}} = \frac{T_{\text{ref}}}{T} \quad (\text{F.5})$$

The resulting relative LIF signal intensity can then be estimated by the product of the temperature-dependent absorption cross-section, tracer number density, and quantum yield.

$$\frac{S_{\text{fl}}(T, p)}{S_{\text{fl,ref}}} = \frac{T_{\text{ref}}}{T} \frac{\sigma(T)}{\sigma(T_{\text{ref}})} \frac{\tau(T, p_{\text{ref}})}{\tau(T_{\text{ref}}, p_{\text{ref}})} \quad (\text{F.6})$$

The second scenario assumes that the fluctuations arise from localized compression and expansion effects. The relationship of p to T can then be described assuming **isentropic** change of state, which is reasonable to assume for small fluctuations of temperature.

$$p = \left(\frac{T}{T_{\text{ref}}} \right)^{\frac{\kappa}{\kappa-1}} p_{\text{ref}} \quad (\text{F.7})$$

$$\frac{n_{\text{tracer}}}{n_{\text{tracer,ref}}} = \frac{\rho}{\rho_{\text{ref}}} = \left(\frac{T}{T_{\text{ref}}} \right)^{\frac{1}{\kappa-1}} \quad (\text{F.8})$$

The relative LIF signal intensity can then determine analogously to the isobaric case by insertion into Eq. F.1.

$$\frac{S_{\text{fl}}(T, p)}{S_{\text{fl,ref}}} = \left(\frac{T}{T_{\text{ref}}} \right)^{\frac{1}{\kappa-1}} \frac{\sigma(T)}{\sigma(T_{\text{ref}})} \frac{1}{\tau(T_{\text{ref}}, p_{\text{ref}})} \tau \left(T, \left(\frac{T}{T_{\text{ref}}} \right)^{\frac{\kappa}{\kappa-1}} p_{\text{ref}} \right) \quad (\text{F.9})$$

As shown in Fig. F.2, the relationship of LIF signal intensity and temperature is ambiguous for low temperatures as the influence of the absorption cross-section increase is counteracted by the decrease of the fluorescence quantum yield in both scenarios. In the isobaric case (Fig. F.2a), the turning point of the intensity curve is at lower temperature of ~ 273 K compared to

~ 320 K in the isentropic case (Fig. F.2b). This is mainly because in the former case the number density decreases with increasing temperature, while in the latter case it increases.

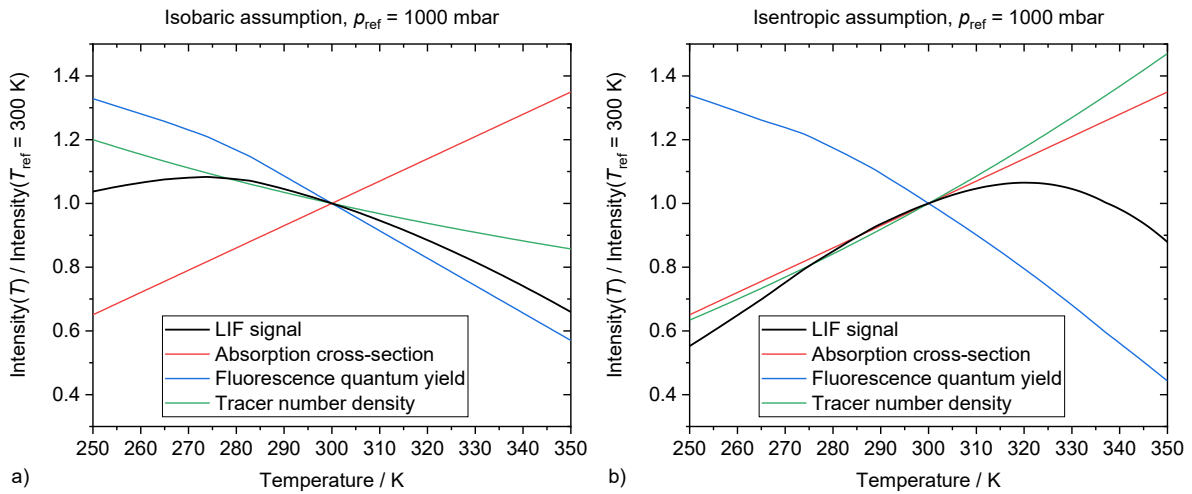


Fig. F.2: Relative LIF signal at low temperatures for a) the isobaric assumption and b) isentropic assumption for small fluctuations of flow temperature for a reference temperature of $T_{\text{ref}} = 300$ K and pressure $p_{\text{ref}} = 1$ bar.

Assuming that the extrapolated temperature dependence of the absorption cross-section is sufficiently correct, a quantitative measurement of the local flow temperature using LIF images obtained by single-color excitation and detection is not feasible for the temperature range studied. Thus, different schemes, such as fluorescence lifetime thermometry, are required.

It should be noted that the pressure dependence of the absorption cross-section of toluene was neglected due to the lack of literature data. However, an increase in pressure would likely have a similar effect on the absorption cross-section as an increase in temperature: Since the 266-nm laser line is slightly beneath one of the stronger absorption features in the toluene absorption spectrum, the absorption cross-section increases as the absorption spectrum (cf., Fig. 3.9) broadens with increasing temperature and pressure. Therefore, if the pressure dependence of the absorption cross-section was considered, the ambiguity of the signal would be similar in the isentropic case with just the turning point of the temperature-dependent signal would shift to lower temperatures.

G. CFD simulation results of the miniature flow channel

The following Figs. G.1–5 show the results of the CFD simulations of the miniature flow channel studied in Chapter 8 for all investigated inlet temperatures. As written in the synopsis of Chapter 8, the URANS simulations were performed by Judith Richter, whereas the evaluation and calculation of derived variables was performed by me.

For the two highest temperatures $T_0 = 140$ and 150 °C (Figs. G.4 and G.5), also the estimated relative LIF signal is shown as discussed in section 8.6.5 calculated using the approach presented in Appendix F. Such images would be less meaningful for the lower temperature cases since calculating the signal would have required significant extrapolation of the available fluorescence lifetime data and were, hence, omitted.

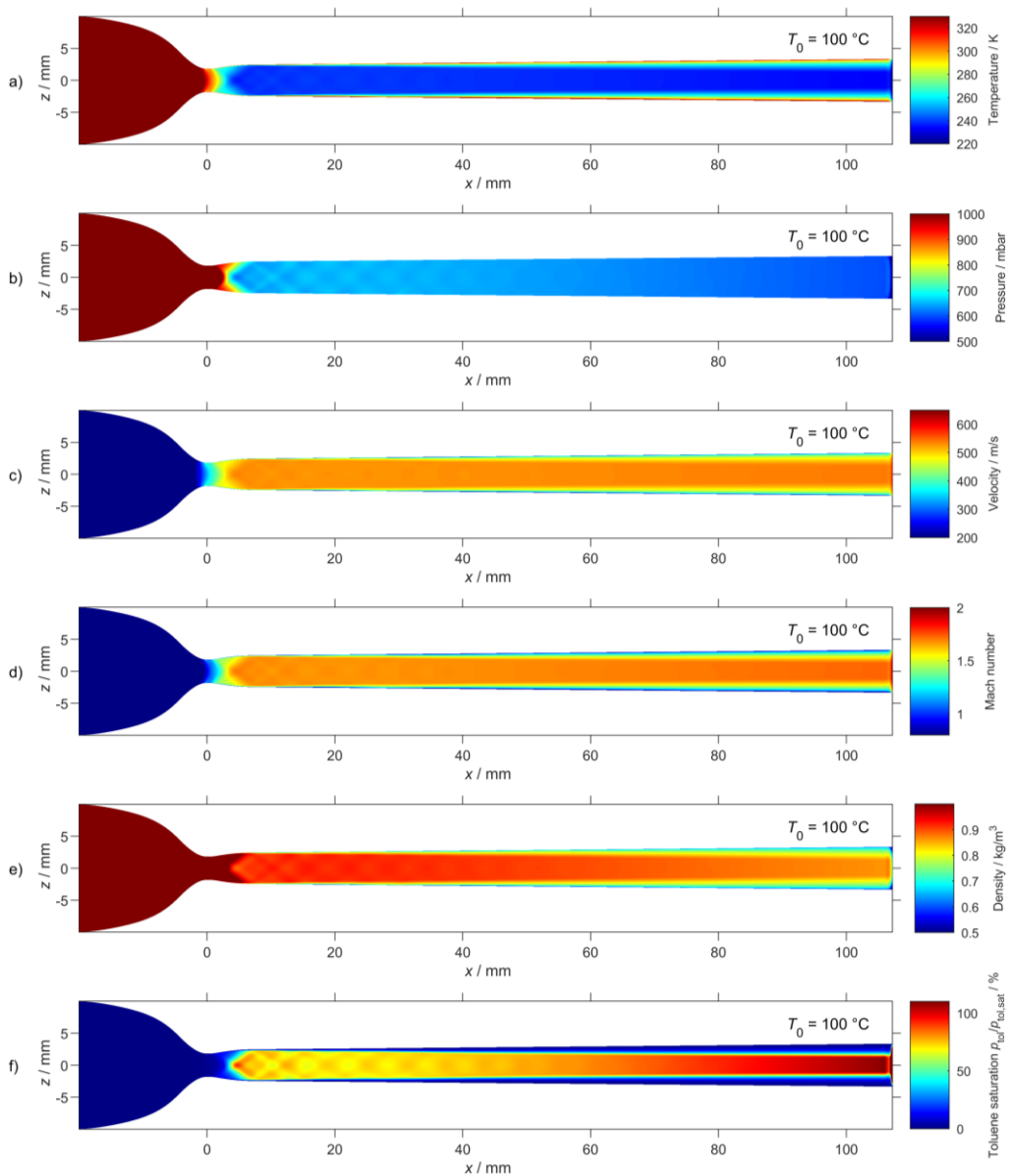


Fig. G.1: Simulation results showing a) temperature, b) pressure, c) downstream velocity, d) density, e) Mach number, and f) toluene-LIF intensity distribution on the center ($y = 0$) xz -plane for $T_0 = 100$ °C and $p_0 = 3.1$ bar.

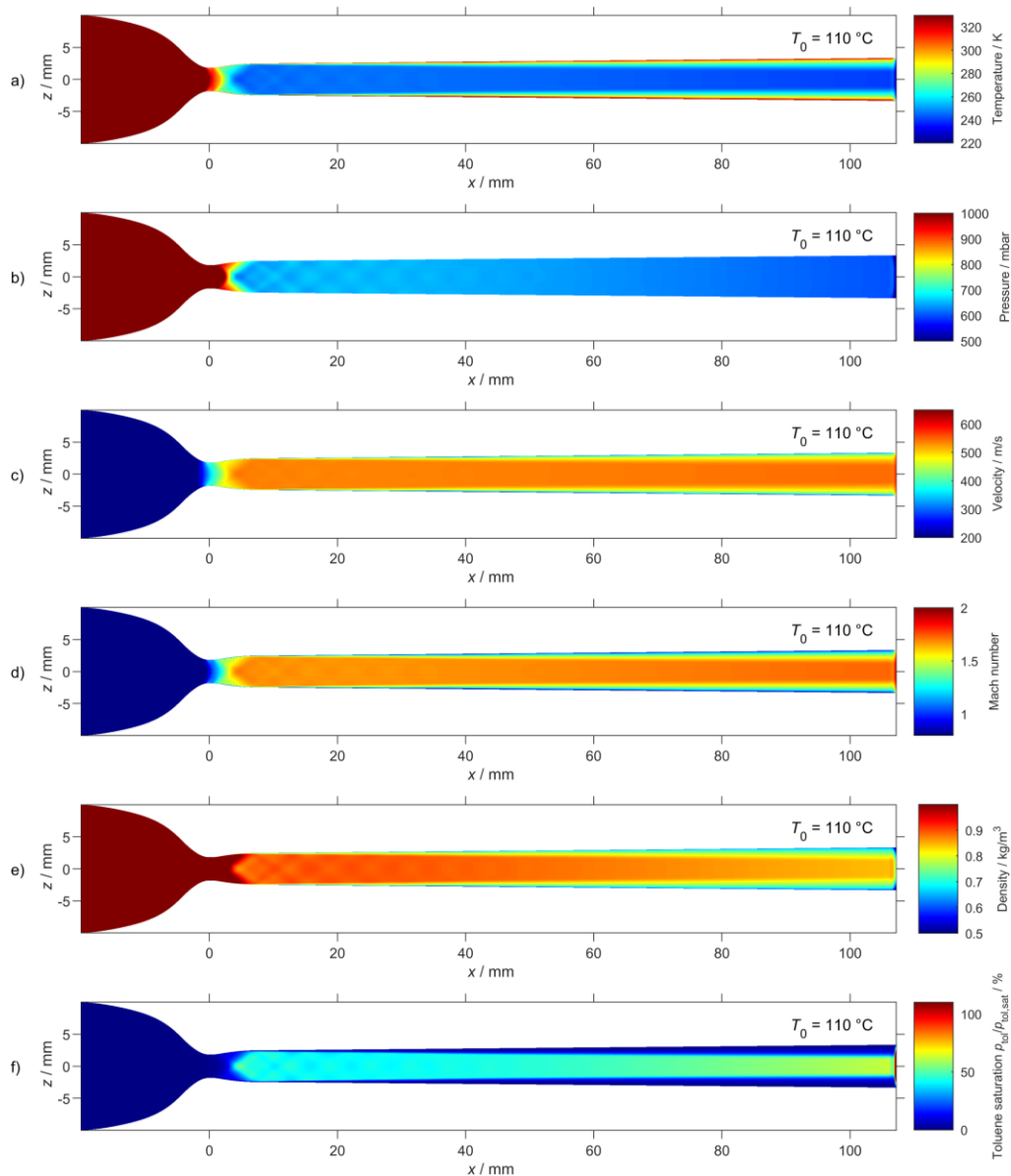


Fig. G.2: Simulation results showing a) temperature, b) pressure, c) downstream velocity, d) Mach number, e) density, and f) toluene saturation on the center ($y = 0$) xz -plane for $T_0 = 110 \text{ }^\circ\text{C}$ and $p_0 = 3.1 \text{ bar}$.

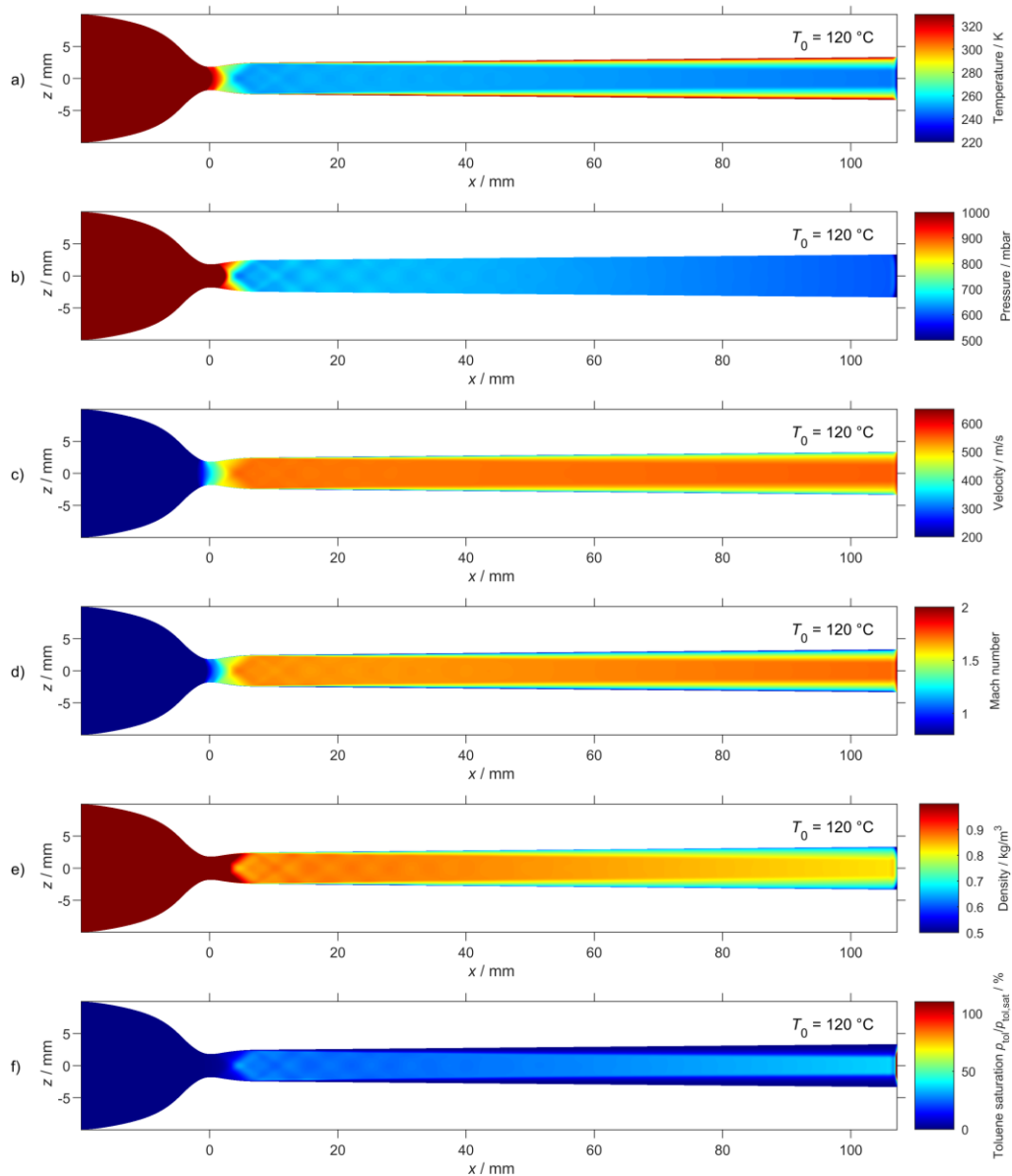


Fig. G.3: Simulation results showing a) temperature, b) pressure, c) downstream velocity, d) Mach number, e) density, and f) toluene saturation on the center ($y = 0$) xz -plane for $T_0 = 120 \text{ }^\circ\text{C}$ and $p_0 = 3.1 \text{ bar}$.

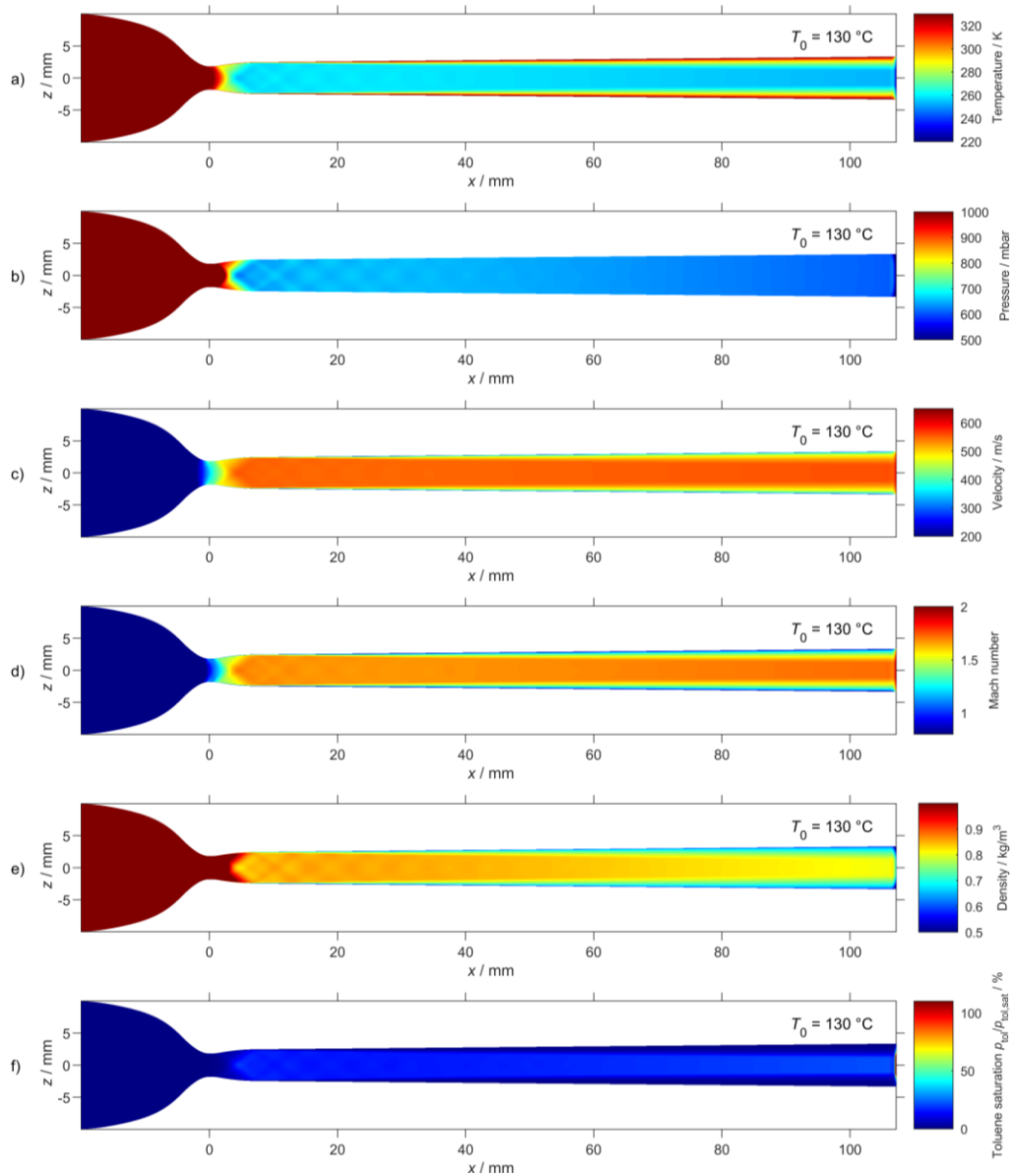


Fig. G.4: Simulation results showing a) temperature, b) pressure, c) downstream velocity, d) Mach number, e) density, and f) toluene saturation on the center ($y = 0$) xz -plane for $T_0 = 130\text{ °C}$ and $p_0 = 3.1\text{ bar}$.

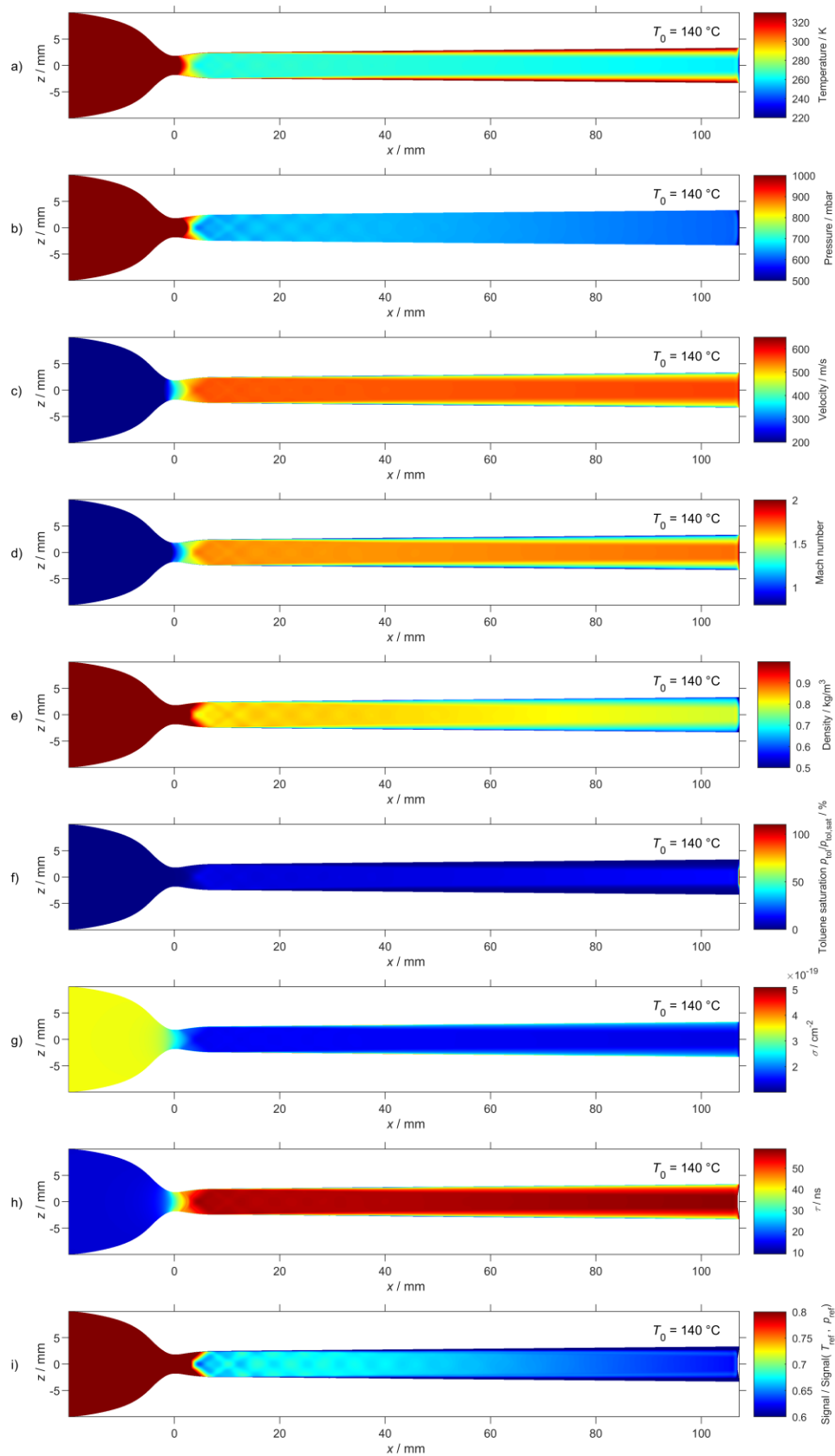


Fig. G.5: Simulation results showing a) temperature, b) pressure, c) downstream velocity, d) Mach number, e) density, and f) toluene saturation on the center ($y = 0$) xz plane for $T_0 = 140$ °C and $p_0 = 3.1$ bar. The g) toluene absorption cross-section, h) expected fluorescence lifetime, and i) expected relative toluene fluorescence signal.

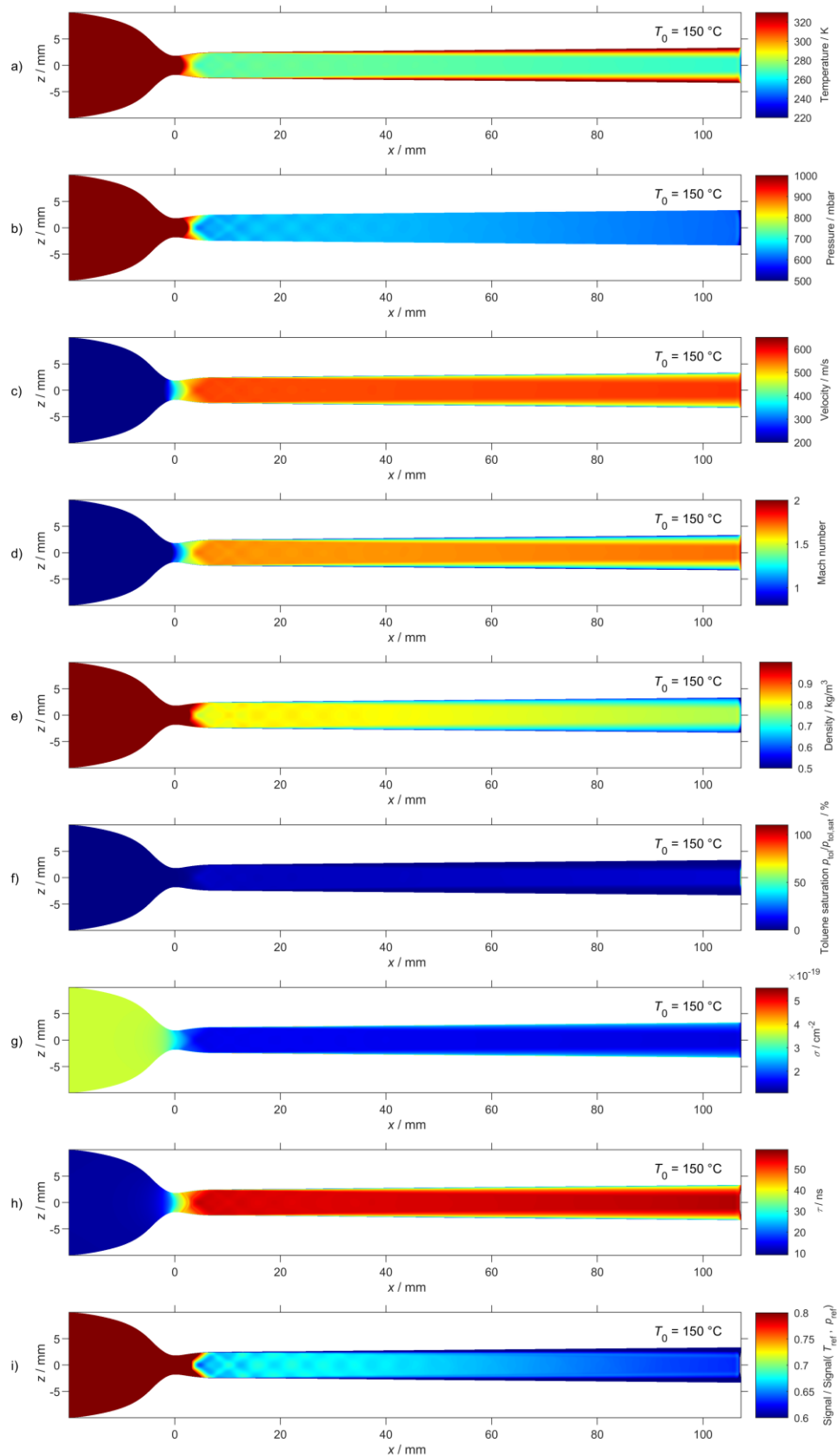


Fig. G.6: Simulation results showing a) temperature, b) pressure, c) downstream velocity, d) Mach number, e) density, and f) toluene saturation on the center ($y = 0$) xz plane for $T_0 = 150$ °C and $p_0 = 3.1$ bar. The g) toluene absorption cross-section, h) expected fluorescence lifetime, and i) expected relative toluene fluorescence signal.

DuEPublico

Duisburg-Essen Publications online

UNIVERSITÄT
DUISBURG
ESSEN

Offen im Denken

ub | universitäts
bibliothek

Diese Dissertation wird via DuEPublico, dem Dokumenten- und Publikationsserver der Universität Duisburg-Essen, zur Verfügung gestellt und liegt auch als Print-Version vor.

DOI: 10.17185/duepublico/75286

URN: urn:nbn:de:hbz:464-20220120-114633-8

Alle Rechte vorbehalten.